



N° d'ordre NNT : 2021LYSEC27

THÈSE de DOCTORAT DE L'UNIVERSITÉ DE LYON
opérée au sein de l'École Centrale de Lyon

École Doctorale N° 162
Mécanique Énergétique Génie Civil Acoustique

Spécialité de doctorat : Acoustique

Soutenue publiquement le 13/07/2021, par

Ignacio ZURBANO FERNÁNDEZ

**Reduction of the broadband noise of centrifugal fans used
for HVAC in buildings**

Devant le jury composé de :

Guédel, Alain	Docteur	CETIAT	Co-directeur de thèse
Khelladi, Sofiane	Professeur	Arts et Métiers ParisTech	Rapporteur
Lörcher, Frieder	Docteur	Ziehl-Abegg SE	Invité
Robitu, Mirela	Docteure	CETIAT	Invitée
Roger, Michel	Professeur	École Centrale de Lyon	Directeur de thèse
Sanjosé, Marlène	Professeure	ÉTS Montréal	Examinatrice
Santolaria Morros, Carlos	Professeur	Universidad de Oviedo	Rapporteur

She wanted to disappear in Rey's smoke, be dead, be him, and she tore the wax paper along the serrated edge of the box and reached for the carton of bread crumbs.

—Don DeLillo, *The Body Artist*

A mis padres y a mi hermano

Abstract

Leading-edge or trailing-edge serrations have been used with some success as a noise-reduction technique applied to fixed airfoils in wind-tunnels. More recently, this method has also been used on axial fans. This thesis extends the application of serrations to a plenum fan.

Using previous results from airfoils, several prototypes of impellers with trailing-edge or leading-edge serrations on the blades were designed and manufactured. Experimental results for the impellers with leading-edge serrations showed a pressure drop for most of the operating points with respect to the baseline unserrated configuration, with a pressure increase for the highest values of flowrate. Serrations yielded a noise reduction at mid frequencies but increased the noise at high frequencies. Overall, a slight increase for most of the operating points and geometries has been observed. Trailing-edge serrations have reduced noise for most operating points. The broadband reduction has been measured over the whole spectrum, with no noise increase at high frequencies. Furthermore, the suppression of a nearly-tonal high-frequency peak has also been reported at low flowrate.

An analytical model to predict the noise of the baseline unserrated impeller has also been developed. It is based on Amiet's model and accounts for sources on the trailing edge and the leading edge of the blades, as well as the edges of the front and back plates. The results of the prediction show that trailing-edge noise dominates over leading-edge noise. Furthermore, the edges of the impeller plates or the fan support do not contribute to the fan noise. The comparison of the analytical prediction with experimental results shows a reasonably good prediction, with a tendency to underpredict the results. There are several possible reasons behind this. First, other noise sources apart from trailing-edge and leading-edge noise could be present. Furthermore, the use of analytical and empirical models to predict the input data for the acoustic model also adds uncertainty to the prediction.

Keywords : Fan Noise, Plenum fan, Serrations, Amiet's model, Analytical model

Résumé

Des dentelures au bord d'attaque ou au bord de fuite ont été utilisées avec un certain succès comme méthode de réduction de bruit sur des profils aérodynamiques. Plus récemment, cette technique a aussi été utilisée pour des ventilateurs hélicoïdes. Cette thèse étend l'application des dentelures sur un ventilateur centrifuge à roue libre.

Des résultats précédents sur des profils ont servi à concevoir et fabriquer plusieurs prototypes avec dentelures au bord d'attaque ou au bord de fuite des pales. Des résultats expérimentaux pour les roues avec dentelures au bord d'attaque montrent à débit donné une chute de pression pour la plupart des points de fonctionnement en comparaison du ventilateur de base sans dentelures, et inversement une augmentation de la pression aux grands débits. Les dentelures entraînent une réduction du bruit aux moyennes fréquences, mais une augmentation du bruit en haute fréquence. Sur le niveau de bruit global, ceci se traduit par une légère augmentation du bruit pour la plupart des géométries et points de fonctionnement. Les dentelures au bord de fuite réduisent le bruit pour la plupart des points de fonctionnement. Cette réduction se produit sur tout le spectre, sans augmentation du bruit à haute fréquence. De plus, on a constaté également la suppression d'un bruit quasi-tonal de très forte amplitude à haute fréquence et petit débit.

Un modèle analytique de prévision du bruit du ventilateur de base, sans dentelures, a aussi été développé. Celui-ci est basé sur le modèle d'Amiet, en prenant en compte les bruits de bord d'attaque et de bord de fuite des pales, mais aussi le bruit de l'extrémité des flasques. Les résultats montrent que le bruit de bord de fuite est dominant par rapport au bruit de bord d'attaque. En outre, les flasques de la roue et le support du ventilateur ne contribuent pas au bruit global du ventilateur. Le modèle analytique arrive à prédire raisonnablement les résultats expérimentaux, avec une tendance à la sous-estimation du bruit. Il y a plusieurs raisons qui pourraient expliquer cela. D'autres sources que le bruit de bord d'attaque et le bruit de bord de fuite peuvent contribuer au bruit du ventilateur. De plus, les modèles analytiques et empiriques utilisés pour obtenir les données d'entrée du modèle acoustique ajoutent une incertitude à la prévision.

Mots clés : Bruit des ventilateurs, Ventilateur centrifuge à roue libre, Dentelures, Modèle d'Amiet, Modèle Analytique

Acknowledgments

Tout d'abord, je tiens à remercier Alain Guédel d'avoir dirigé cette thèse au CETIAT. Sans ses conseils, ses encouragements et sa bienveillance je n'y serais jamais arrivé. Je dois aussi remercier chaleureusement Michel Roger, mon codirecteur de thèse, pour la qualité de son encadrement. Il m'a aussi appris que, dans la recherche, l'humilité est une qualité aussi importante que la compétence professionnelle. De plus, je voudrais remercier Mirela Robitu, qui m'a appris à être aussi rigoureux dans la rédaction d'articles scientifiques que dans les simulations.

Je dois remercier le CETIAT de m'avoir accueilli pendant les plus de trois ans qu'a duré mon aventure, ainsi que pour le soutien économique reçu lors de la prolongation de mon contrat. Je suis très reconnaissant à tous mes collègues, qui m'ont accompagné lors de ma thèse. En particulier, je voudrais remercier Agus Ridwan, le meilleur chef de pôle qu'on puisse désirer!; Jean-Huges Salazar et Hervé Bingan, qui ont fait de très bons essais; François Durier, qui a supervisé le projet; Hervé Miler, qui m'a tant assisté avec la CFD; Benoît Savanier, qui nous a aidé avec les mesures électriques; et Alain Ginestet, avec qui je dansais quand le chat n'était pas là.

Je tiens à remercier Stéphane Moreau de m'avoir invité à faire une mission de recherche à l'Université de Sherbrooke. Malgré un contexte sanitaire incertain, on a pu travailler ensemble pour améliorer le modèle analytique. C'était un plaisir de collaborer avec lui, car en plus de son sens de l'humour, il a la rare qualité d'être très fort sur les trois piliers de la recherche en acoustique : expérimental, numérique et analytique. Je dois aussi remercier Marlène Sanjosé de nos échanges autour des simulations LBM et d'avoir accepté de présider le jury de thèse. Finalement, je voudrais remercier tous mes collègues de l'UdeS de leur accueil chaleureux au milieu de l'hiver québécois : Silouane, Pavel, Dipali, Régis, Anna, Gyuzel, Prateek, Stefanie et Yann. I would like to thank Frieder Lörcher and Walter Angelis, from Ziehl-Abegg. They kindly provided the baseline fan for the study and manufactured the serrated prototypes. I deeply enjoyed our exchanges and collaboration during the prototype design phase. Furthermore, I would like to thank Frieder for having accepted being a member of the jury.

Je voudrais aussi remercier le personnel de Valeo Systèmes Thermiques de leur accueil lors de mon stage de recherche, en particulier Manuel Henner, Maxime Laurent et Bruno Demaury. Je souhaite aussi remercier Sofiane Khelladi d'avoir accepté d'être rapporteur de ma thèse.

I would like to thank everyone from the SmartAnswer International Training Network, in particular our awesome project manager Christophe Schram and his right-hand Julien Christophe. It was also a great adventure to meet and collaborate with all the ESRs: Georgios (my favourite *μαλακας* in the whole planet), Chai (me great pal), Mad Massimo, Manu, Javed!, Alessandro, Christopher, Riccardo, Lourenço, Nilo and Thanu.

Je tiens à remercier le LMFA de m'avoir encadré pendant mon doctorat, et de m'avoir accueilli lors des derniers mois de rédaction de cette thèse. En particulier, je voudrais remercier Etienne, Daher, Elina, Igor (je ne serais pas docteur sans son câble réseau), Simon, Danny, Codor, Maroua, Mathieu, Gabriele, Mohcène et Courtney.

Me gustaría agradecer a Carlos Santolaria Morros el haberme hecho descubrir la aeroacústica, así como el haber aceptado ser *rapporteur* en mi jurado de tesis. Je voudrais aussi remercier Mejdi Azaiez de m'avoir initié au le monde de la recherche lors de mon projet de fin d'études. Tampoco me puedo olvidar de Ángel David y de Raquel, quienes me marcaron el camino a seguir en el mundo de la investigación.

Finalmente, debo agradecer a todos los amigos que me han acompañado durante este viaje, ya sea en Lyon, Ginebra o Gijón : Alexandre, Claire, Clément, Pauline, Nils, Andrea, Haris, Łukasz, Pilar, Morgane, Fritz, Dani, Blanca, Carlos, MaToni, Ángel, Villa, Joan, Ana, Marta y otros que me dejo en el tintero. En último lugar, tengo que reconocer la educación y el apoyo que mi familia me ha brindado todos estos años, ya que sin ellos no habría llegado hasta aquí.

The present work has received funding from the European Union's Horizon 2020 research and innovation program under the Marie Skłodowska-Curie SmartAnswer project (grant agreement No 722401). It has also received funds from CETIAT's industrial members which are fan manufacturers. It was performed within the framework of the Labex CeLyA of the Université de Lyon, within the program 'Investissements d'Avenir' (ANR-10-LABX-0060/ANR-11-IDEX-0007) operated by the French National Research Agency (ANR).

Nacho Zurbano Fernández

Contents

Abstract	v
Résumé	vii
Acknowledgments	ix
List of Figures	xvi
List of Tables	xxiii
Nomenclature	xxv
Introduction	1
Motivation	1
Summary of noise sources of a fan	2
Tools	3
Structure of the thesis	4
Author's contributions	4
Publications	5
1 Experimental study of serrations on a plenum fan	7
1.1 Bibliographical review	8
1.1.1 Leading-edge serrations	8
1.1.1.1 Effects on acoustics	8
1.1.1.2 Effects on aerodynamics	9
1.1.1.3 Application to fans	10
1.1.2 Trailing-edge serrations	10
1.1.2.1 Effects on acoustics	10
1.1.2.2 Application to turbomachinery	12
1.1.3 Analytical models	13

1.2	Description of the experimental setup	14
1.2.1	Description of the fan	14
1.2.2	Experimental setup	15
1.2.3	Formulas and definitions	17
1.2.3.1	Aerodynamics	17
1.2.3.2	Acoustics	19
1.3	Test of the baseline fan	20
1.3.1	Aerodynamic results	20
1.3.2	Acoustics	21
1.3.2.1	Overall Sound Power Level	21
1.3.2.2	Comparison with similar fans	22
1.3.2.3	Noise spectra at operating points with the same flow coefficient $\bar{\delta}$	22
1.3.2.4	Inlet and outlet	26
1.3.2.5	Comparison of all operating points	27
1.3.2.6	Summary of the most prominent peaks	28
1.3.2.7	Laminar-boundary-layer-vortex-shedding	29
1.3.2.8	Von Karman vortex shedding	30
1.3.2.9	Analysis of the peaks at mid to high frequencies	31
1.3.2.10	Analysis of possible resonances	32
1.4	Leading-edge serrations	34
1.4.1	Serration design	34
1.4.2	Aerodynamic results	36
1.4.3	Acoustic results	37
1.4.3.1	1440 rpm	37
1.4.3.2	720 rpm	40
1.4.4	Experiments with turbulence generator at inlet	41
1.5	Trailing-edge serrations	45
1.5.1	Serration design	45
1.5.2	Aerodynamic results	47
1.5.3	Acoustic results	49
1.6	Conclusion	54
2	Analytical modelling of the broadband noise of the baseline fan	55
2.1	Amiet's far-field models	55
2.1.1	Trailing-edge noise	56

2.1.2	Leading-edge noise	58
2.1.3	Application to a fan blade	58
2.1.4	Spanwise segmentation	59
2.1.5	Change of coordinates and rotating blades	61
2.1.6	Calculation of sound power level	64
2.1.7	Noise radiation model for front-plate and back-plate trailing edges	66
2.2	Input data	68
2.2.1	Leading edge: wavenumber spectrum of the turbulence	68
2.2.2	Trailing edge	68
2.2.2.1	Wall-pressure spectrum	69
2.2.2.1.1	Rozenberg's model	69
2.2.2.1.2	Guédel's model	69
2.2.2.1.3	Dimensionless wall pressure spectrum for flow separation	70
2.2.2.2	Correlation length	71
2.3	Conclusion	73
3	CFD simulations	75
3.1	CFD: an overview	75
3.2	Geometry description and parameters	77
3.3	Pressure-flow curves	80
3.3.1	Baseline fan	80
3.3.2	Leading-edge serrations	82
3.3.3	Trailing-edge serrations	84
3.4	Analysis of the flow features	84
3.4.1	Mean blade pressure field	84
3.4.2	Velocity field	85
3.4.2.1	Relative mean velocity magnitude through the impeller	85
3.4.2.2	Visualization between two blades	87
3.4.2.3	Flow around a blade at midspan	89
3.4.2.3.1	Minimum flow ($q_v = 1706 \text{ m}^3/\text{h}$)	89
3.4.2.3.2	Intermediate flow ($q_v = 2196 \text{ m}^3/\text{h}$)	90
3.4.2.3.3	Maximum flow ($q_v = 2584 \text{ m}^3/\text{h}$)	91
3.5	Flow parameters for serration design	92
3.5.1	Estimation of the turbulence length scale from RANS simulations	92
3.5.2	Boundary layer thickness	92

3.6	Input data for analytical model	93
3.6.1	Trailing-edge noise	93
3.6.1.1	Wall-pressure spectrum	99
3.6.1.2	Correlation length	101
3.6.2	Leading-edge noise	101
3.6.3	Front and back plates noise	103
3.7	Conclusion	104
4	Validation of the noise prediction	105
4.1	Convergence study	105
4.2	Analysis of results	110
4.2.1	Trailing-edge noise	110
4.2.2	Leading-edge noise	111
4.2.3	Combination of leading and trailing-edge noise	112
4.3	Comparison with experimental results	112
4.4	Noise prediction with empirical response of the impeller	113
4.5	Contribution of front and back plates	114
4.6	Comparison with LBM simulations	115
4.7	Conclusion	117
	Conclusion and perspectives	119
	Conclusion	119
	Perspectives	120
	Bibliography	123
	A Drawings of serrated flat blades	135
	B Impact of fan assembly on acoustics	139
B.1	Nominal speed: 1440 rpm	139
B.2	Partial speed: 720 rpm	142
B.3	Conclusion	142
	C Aeroacoustic transfer functions	143
C.1	Trailing edge	143
C.2	Leading edge	144

D Trailing-edge noise input parameters **145**

 D.1 Boundary layer 145

 D.2 Rozenberg model parameters [94] 145

E Measurement of the response of the isolated stationary impeller **147**

F Contribution of the fan support **151**

List of Figures

1	Illustration of a possible use of the fan of the study in an air handling unit. Impeller on the right (dark blue). Streamlines with general flow direction marked in red	2
1.1	Rendering of a NACA 6412 airfoil with trailing-edge serrations	8
1.2	Sinusoidal serrations with slits added to the hollow part	13
1.3	Fan of the study (credit of the picture to Ziehl-Abegg SE)	15
1.4	Main dimensions of the impeller	16
1.5	Layout of the test facility	16
1.6	Views of the reverberant rooms	17
1.7	Power conversion chain between the VFD and the impeller; notations, as per ISO/TC 117 - Fans, described in text	18
1.8	Motor efficiency versus motor input power for the fan of the study, data provided by Ziehl-Abegg	19
1.9	Baseline fan pressure curves	20
1.10	Overall efficiency versus dimensionless flowrate	21
1.11	Sound power level curves of the tested baseline fan	22
1.12	Comparison of the overall sound power of the fan of the study and other commercial plenum fans, measurements at outlet	22
1.13	Third-octave bands of sound power level at outlet as a function of the % of the nominal rotating speed, $\bar{\delta} = 0.1$	23
1.14	Third-octave bands of sound power level at outlet as a function of the % of the nominal rotating speed, $\bar{\delta} = 0.2$	23
1.15	Third-octave bands of sound power at outlet as a function of the % of the nominal rotating speed, $\bar{\delta} = 0.3$	24
1.16	Narrowband sound pressure spectra at outlet as a function of the % of the nominal rotating speed, $\bar{\delta} = 0.1$, $\Delta f = 8$ Hz	25

1.17	Narrowband sound pressure spectra in reduced variables (reference speed $N=1080$ rpm) at outlet as a function of the % of the nominal rotating speed, $\bar{\delta} = 0.1$, $\Delta f = 8$ Hz . . .	25
1.18	Narrowband sound pressure spectra at outlet as a function of the % of the nominal rotating speed, $\bar{\delta} = 0.3$, $\Delta f = 8$ Hz	26
1.19	Narrowband sound pressure spectra in reduced variables (reference speed $N=1080$ rpm) at inlet as a function of the % of the nominal rotating speed, $\bar{\delta} = 0.3$, $\Delta f = 8$ Hz . . .	26
1.20	Narrowband sound pressure spectra for inlet and outlet, $\bar{\delta} = 0.2$, $\Delta f = 8$ Hz, $N=1440$ rpm	27
1.21	Narrowband sound pressure spectra at inlet for all operating points, $\Delta f = 8$ Hz, $N=1440$ rpm	27
1.22	Narrowband sound pressure spectra in reduced variables (reference speed $N=1080$ rpm) at inlet as a function of the % of the nominal rotating speed, $\bar{\delta} = 0.1$, $\Delta f = 8$ Hz . . .	30
1.23	Dimensions considered for the assessment of standing waves	33
1.24	Sound pressure level and potential resonances for $\bar{\delta} = 0.2$ at outlet $\Delta f = 8$ Hz	34
1.25	Serrations parameters	34
1.26	Impeller prototypes with leading-edge serrations	35
1.27	Fan curves, $N=1440$ rpm	36
1.28	Fan curves, $N=720$ rpm	36
1.29	Typical averaged narrowband sound pressure spectra at outlet for $q_v = 2200 m^3/h$, $N=1440$ rpm, $\Delta f = 2$ Hz	37
1.30	Filtered narrowband sound pressure spectra at outlet for the BEP $q_v = 2200 m^3/h$, $N=1440$ rpm, $\Delta f = 2$ Hz	38
1.31	Specific narrowband sound pressure spectra at outlet for the BEP, $q_v = 2200 m^3/h$, $N=1440$ rpm, $\Delta f = 2$ Hz	38
1.32	Filtered sound pressure reduction level at outlet for the BEP $q_v = 2200 m^3/h$, $N=1440$ rpm	39
1.33	Overall specific narrowband sound pressure spectra, $N=1440$ rpm	40
1.34	Overall specific narrowband sound pressure spectra, $N=720$ rpm	40
1.35	Specific narrowband sound pressure spectra at outlet for the minimum flowrate operating point $q_v = 600 m^3/h$, $N=720$ rpm, $\Delta f = 2$ Hz	41
1.36	Filtered sound pressure reduction level at outlet for the BEP $q_v = 600 m^3/h$, $N=720$ rpm	41
1.37	Turbulence grid	42
1.38	Fan total pressure, $N=1440$ rpm	43
1.39	Fan total pressure, $N=720$ rpm	43
1.40	Overall sound power level at outlet, $N=1440$ rpm	44

1.41 Overall sound power level as a function of flowrate, N=1440 rpm	45
1.42 Narrowband sound pressure spectra at outlet for the BEP $q_v = 2200 m^3/h$, N=1440rpm, $\Delta f = 8 \text{ Hz}$	45
1.43 Iron-shaped serrations	46
1.44 Impeller prototypes with trailing-edge serrations	47
1.45 Impeller with trailing-edge serrations mounted on the shaft	47
1.46 Fan curves for impellers with trailing-edge serrations, N=1440 rpm	48
1.47 Fan curves for impellers with trailing-edge serrations, N=720 rpm	48
1.48 Overall specific narrowband sound pressure spectra, N=1440 rpm	49
1.49 Specific narrowband sound pressure spectra at outlet for the best efficiency point, $\Delta_f =$ $2Hz$, N=1440 rpm, $q_v = 2200 m^3/h$	50
1.50 Filtered sound pressure reduction level at outlet for the BEP $q_v = 2200 m^3/h$, N=1440rpm	50
1.51 Specific narrowband sound pressure spectra at outlet for $q_v = 3400 m^3/h$, $\Delta_f = 2Hz$, N=1440 rpm	51
1.52 Overall specific narrowband sound pressure spectra, N=720 rpm	51
1.53 Specific narrowband sound pressure spectra at outlet for $q_v = 585 m^3/h$, $\Delta_f = 2Hz$, N=720 rpm	52
1.54 Flat-plate sound spectra and vortex-shedding sound reduction by trailing-edge serra- tions, adapted from [15]	52
2.1 Flat plate reference frame for the trailing-edge problem, and main notations. Gust featured by the undulated surface	57
2.2 Flat plate reference frame for leading-edge problem, and main notations. Velocity gust featured by the undulated surface	58
2.3 Blade geometrical parameters for noise calculation (dimensions in mm)	59
2.4 Strips for trailing-edge noise calculation and projected observer positions	60
2.5 Strips for leading-edge noise calculation	61
2.6 Rotating (green) and fixed (red) reference frames, trailing-edge model	62
2.7 Rotating and fixed reference frames	63
2.8 Correction of sound level to account for the wall reflection	65
2.9 Two views of the area for the noise computing	66
2.10 Sides of front and back plates to be considered	67
2.11 Disk model geometry	67
2.12 Dimensionless wall pressure spectrum with Rozenberg's model. Parameters deduced from 3.6.1 and given in the main text.	69

2.13	Dimensionless wall-pressure spectrum according to Guédél's model	70
2.14	Dimensionless wall-pressure spectrum for a flat plate with detached flow	71
2.15	Dimensionless correlation length with Guedel's model	72
3.1	Overview of the simulation domain and the fan	77
3.2	Mesh around the fan assembly	78
3.3	Mesh around a blade	79
3.4	Values of y^+ over the blades, N=1440 rpm	79
3.5	Velocity magnitude inside the room, vertical cut, $q_v = 2196m^3/h$, N=1440 rpm	80
3.6	Results with coarse and refined mesh, N=1440 rpm	81
3.7	Results with refined mesh and extra layers, N=1440 rpm	81
3.8	Total pressure with $k - \epsilon$ model and refined mesh, N=720 rpm	82
3.9	Total pressure for the impellers with leading-edge serrations, $k - \epsilon$ model and refined mesh, N=1440 rpm	83
3.10	Total pressure for the TE_ L8H12 impeller, $k - \epsilon$ model and refined mesh, N=720 rpm	84
3.11	Static pressure on the blades ($q_v = 1706, 2196, 2584 m^3/h$), N=1440 rpm	84
3.12	Sections of the impeller	85
3.13	Magnitude of relative velocity 5 mm from the front plate ($q_v = 1706, 2196, 2584 m^3/h$), N=1440 rpm	86
3.14	Magnitude of relative velocity at the middle plane ($q_v = 1706, 2196, 2584 m^3/h$), N=1440 rpm	86
3.15	Magnitude of relative velocity 5 mm from the hub ($q_v = 1706, 2196, 2584 m^3/h$), N=1440 rpm	86
3.16	View of the visualization area	87
3.17	Velocity field between two blades, $q_v = 2196 m^3/h$, N=1440 rpm	87
3.18	Velocity vectors around the fan assembly, $q_v = 2196 m^3/h$, N=1440 rpm	88
3.19	Velocity field around the blade, $q_v = 1706 m^3/h$	89
3.20	Relative total pressure around a blade, $q_v = 1706 m^3/h$, N=1440 rpm	89
3.21	Velocity field around the blade, $q_v = 2196 m^3/h$, N=1440 rpm	90
3.22	Relative total pressure around a blade, $q_v = 2196 m^3/h$, N=1440 rpm	90
3.23	Velocity field around the blade, $q_v = 2584 m^3/h$, N=1440 rpm	91
3.24	Relative total pressure around a blade, $q_v = 2584 m^3/h$, N=1440 rpm	91
3.25	Area for the calculation of the turbulent length scale, $q_v = 2196 m^3/h$, N=1440 rpm	92
3.26	Estimation of the integral turbulence length scale, $q_v = 2196 m^3/h$, N=1440 rpm	93
3.27	Visualisation of boundary layer thicknes, $q_v = 2196 m^3/h$, N=1440 rpm	93

3.28	Visualisation of the effect of the turbulence model and the number of layers of the boundary layer, $q_v = 2196 m^3/h$, $N=1440$ rpm	94
3.29	Probes for boundary layer extraction	95
3.30	Components of relative velocity: streamwise (U_i), normal (U_j) and spanwise (U_k), probe 5 ($z=55.1$ mm)	96
3.31	Evolution of the relative total pressure and derivatives, probe 5 ($z=55.1$ mm)	97
3.32	Profile of streamwise velocity, pressure side and suction side, with U_{99} marked with a dashed line, probe 5 ($z=55.1$ mm)	97
3.33	Spanwise evolution of boundary layer thickness	98
3.34	Pressure and wall shear stress on the pressure side of the blade, for probe 5 ($z=55.1$ mm)	98
3.35	Wall pressure spectra on the pressure side	100
3.36	Wall pressure spectra on the suction side	100
3.37	Correlation length	101
3.38	Surface for extraction of leading-edge noise input	102
3.39	Spanwise evolution of the leading-edge turbulence parameters	102
3.40	Spanwise evolution of the velocity components upstream of the leading edge: streamwise (U_i), normal (U_j) and spanwise (U_k)	103
3.41	Visualisation of the magnitude of the axial velocity, $q_v = 2196 m^3/h$, $N=1440$ rpm	103
4.1	Definition of the angle of the circular arc ϕ	106
4.2	Effect of the circular arc angle on the convergence of the analytical model ($R_{circulararc} = 3 - m$)	106
4.3	Effect of the discretisation of the circular arc on the convergence of the analytical model	107
4.4	Effect of the the circular arc radius on the convergence of the analytical model	107
4.5	Effect of the number of strips on the convergence of the analytical trailing-edge noise model	108
4.6	Effect of the number of strips on the convergence of the analytical leading-edge noise model	109
4.7	Strips for noise calculation	109
4.8	Noise generated per strip: pressure side with Guedel's model (top left), pressure side with Rozenberg's model (top right), suction side with Guedel's model (bottom left), suction side with Rozenberg's model (bottom right)	110
4.9	Trailing-edge noise, results from analytical model	111
4.10	Noise generated per strip and global blade noise	111
4.11	Blade noise (trailing edge and leading edge)	112

4.12	Comparison with experimental results (trailing-edge and leading-edge noise)	113
4.13	Comparison of analytical model prediction, analytical model prediction including response of the impeller and experimental results (trailing edge and leading-edge noise)	114
4.14	Contribution of each side of the front and back plates and overall noise	114
4.15	Comparison of blade noise (trailing-edge and leading-edge noise) with the front and back plates noise	115
4.16	Mesh visualization of the LBM simulations, adapted from [100]	115
4.17	Comparison of the wall-pressure spectra, suction side	116
4.18	Comparison of the wall-pressure spectra, pressure side (probe 6)	117
B.1	Different fan assemblies	140
B.2	Overall sound power level at the fan inlet for the different assemblies	140
B.3	Third octave band plots for the different assemblies	141
B.4	Sound power level at inlet for the serrated impellers with different assemblies	141
B.5	Overall sound power level	142
B.6	Third octave bands for $N=720$ rpm, $\delta = 0.1$	142
E.1	Positions of the microphone	147
E.2	Example of a measurement point close to the trailing edge	148
E.3	Response of the impeller	148
E.4	Response of the impeller-response of the isolated blade	149
F.1	Fan assembly with potential noise sources highlighted	151
F.2	Velocity magnitude slightly upstream of the fan support over a cylinder coaxial with the impeller	152
F.3	Windtunnel setup	153
F.4	PSD of the noise of the support	153

List of Tables

1.1	Fan parameters	15
1.2	Blade passing frequencies for the different rotating speeds	21
1.3	Potential LBL-VS peak frequencies	29
1.4	Estimation of U_e , in m/s	31
1.5	Vortex shedding frequencies, in Hz	31
1.6	Scaling of the frequency of the peaks at mid-high frequencies, data from the outlet	32
1.7	Possible standing waves: dimensions and expected wavelength and frequency	33
1.8	Parameters for impellers with leading-edge serrations	35
1.9	Parameters for impellers with trailing-edge serrations	46
3.1	Simulation mesh parameters	78
3.2	Boundary layer values for BEP, suction side	99
3.3	Boundary layer values for BEP, pressure side	99
3.4	Boundary layer values for BEP, impeller plates	104
4.1	Parameters for analytical model	109

Nomenclature

Acronyms

BEP Best efficiency point

BPF Blade passing frequency

LBL – VS Laminar-boundary-layer-vortex-shedding

LBM Lattice Boltzmann Method

VFD Variable Frequency Drive

Greek characters

$\bar{\delta}$ Dimensionless flow coefficient

δ Boundary layer thickness

δ^* Boundary layer displacement thickness

Θ Boundary layer momentum thickness

α Free-stream to convection speed ratio

β_1 Blade angle at leading edge

β_2 Blade angle at trailing edge

$\beta,$ Compressibility parameter

η_{es} Overall static efficiency without VFD

η_e Overall efficiency without VFD

η_{mot} Motor efficiency

η_{rs} Fan impeller static efficiency

η_r Fan impeller efficiency

γ Blade leading edge angle

λ	Serration wavelength
μ	Pressure coefficient
ν	Air kinematic viscosity
Ω	Angular velocity
ω	Angular frequency
ω_e	Angular frequency of the source
Φ	Throttling coefficient
ϕ	Edge angular position
ϕ_{pp}	Wall pressure PSD
Φ_{ww}	Wavenumber spectrum of the turbulence
Π	Wake parameter
Π_0	Streamwise-integrated wavenumber spectral density of wall-pressure fluctuations
ρ	Air density
τ_w	Wall shear stress
τ_{max}	Maximum shear stress
Θ	Serration angle
ξ	Blade trailing edge angle
ξ	System resistance coefficient
u_τ	Friction velocity

Latin characters

$2h$	Serration amplitude
\bar{K}_1, \bar{K}_2	Streamwise and spanwise non-dimensional wavenumbers
\bar{u}	Streamwise fluctuating velocity
β_c	Clauser's parameter
\mathcal{I}	Aeroacoustic transfer function for the trailing edge $\mathcal{I} = \mathcal{I}_1 + \mathcal{I}_2$
\mathcal{L}	Aeroacoustic transfer function for the leading edge $\mathcal{L} = \mathcal{L}_1 + \mathcal{L}_2$
B	Number of blades

b	Half of chord length $b = c/2$, parameter used by Amiet's model
c	Chord length
c_0	Speed of sound (in quiescent medium)
D_i	Inlet diameter
D_e	Outlet diameter
K	Convective wavenumber
k	Acoustic wavenumber
K_1, K_2	Streamwise and spanwise aerodynamic wavenumbers
L	Outlet blade span length
L_p	Sound pressure level
L_t	Integral turbulence length scale
L_w	Sound power level
l_y	Spanwise correlation length
M	Mach number (free stream when it concerns the flow)
N	Rotational speed
P_e	Motor input power
P_r	Mechanical power supplied to the impeller of the fan
P_u	Fan air power generated from the static pressure
P_u	Fan air power
p_{fs}	Fan static pressure
p_f	Fan pressure
q_v	Volume flow rate
S	Fan outlet surface
S_0	Corrected distance for convection effect
$S_{ppblade}$	Far-field acoustic PSD of a fan blade
$S_{ppimpeller}$	Far-field acoustic PSD of the impeller
S_{pp}	Far-field acoustic PSD of a flat plate

Sc	Strouhal number based on the chord $Sc = \omega c / U_e$
Sh	Strouhal number based on the boundary layer and the friction velocity $Sh = \omega \delta / u_\tau$
St	Strouhal number based on the displacement thickness $St = \omega \delta^* / U_e$
St_h	Strouhal number based on half of the serration amplitude h
T	Blade thickness
U	Flow velocity
U_c	Convection velocity $U_c = \alpha U$
U_e	Free-stream velocity
U_{99}	99% of the free-stream velocity
X, Y, Z	General coordinate system
x_1, x_2, x_3	Amiet's coordinate system

Introduction

Motivation

Fan noise is becoming a growing concern in different applications, such as air-conditioning, ventilation or electronic devices. The impact of environmental concerns has made noise reduction a competitive issue in today's global market. According to the World Health Organization, "research regarding industrial noise in general is required. More specifically, there is a need to investigate stationary sources (including heat, ventilation and acclimatization devices) and their impacts on health." [32, p. 101]. Furthermore, new regulations push towards a reduction of the noise generated by fans. For instance, the version under review of COMMISSION REGULATION (EU) No 327/2011 [33], which concerns mainly fan power consumption, would reward silent equipment with lower performance requirements.

To tackle this problem, new technologies based on acoustic control have been emerging recently, both active (MEMs, micro-jet, plasma actuation), and passive (metamaterials, porous materials, serrations). The Innovative Training Network *SmartAnswer*, funded within the European Union's Horizon 2020 research and innovation programme under grant agreement No 722401, is aimed at assessing some of these solutions. The Network financed the work of 16 Early Stage Researchers, one of which is the author of this thesis (ESR 16). The Network also allowed the author to perform three secondments within other members of the consortium: *École Centrale de Lyon*, *Valeo Thermal Systems* and *Université de Sherbrooke*.

In recent years, leading-edge or trailing-edge serrations have been used with some success as a noise reduction method applied to fixed airfoils in wind-tunnels [78, 75]. More recently, this technique has also been used on axial fans [114, 12]. There are even some commercial axial fans manufactured with serrations on the blade leading edge or the trailing edge [34]. However, their effects are not yet well understood and for this reason not fully effective. Furthermore, there is a lack of research on leading-edge and trailing-edge serrations applied to centrifugal fans. This thesis aims at investigating and assessing the effectiveness of trailing-edge and leading-edge serrations on a plenum fan (i.e. centrifugal fan without volute), both from an air performance and an acoustic point of view.

The work has been carried out at CETIAT (Centre Technique des Industries Aéronautiques et Thermiques), which is an industrial R&D and technology transfer center based in Villeurbanne (France). Part of its activity is funded by HVAC manufacturers. One of these industrial members, *Ziehl-Abegg*, contributed to the study with the selection of the fan (see a rendering in Figure 1). The research has been developed under demanding industrial constraints, for both the experimental and the numerical approaches. Firstly, a full-size commercial fan has been used throughout the study. Secondly, experiments were performed in an industrial test rig, where flow measurement techniques typically present in wind tunnels (such as hot wire anemometry or laser Doppler velocimetry) were not available. Thirdly, simulations were cost-effective (RANS) and representative of the average resources available in industry. Fourthly, analytical models were used to predict the fan noise, which can be run on a desktop computer. The study is believed representative of the applicative efforts and strategies that can be developed in the context of technical centers, intermediate between advanced methodologies of research laboratories and industrial approaches.

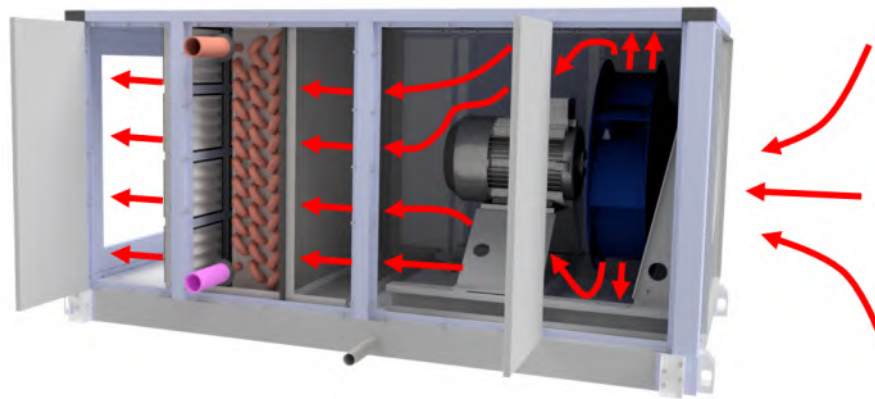


Figure 1 – Illustration of a possible use of the fan of the study in an air handling unit. Impeller on the right (dark blue). Streamlines with general flow direction marked in red

A typical plenum-fan installation is depicted in Figure 1. It includes a fan, filters, heat exchangers and a casing made of metal surfaces. Other elements, such as humidifiers, mixing chambers, instrumentation or silencers are often present but have not been depicted on the previous representation. In the present study, the fan assembly is addressed separately as an uninstalled unit.

Summary of noise sources of a fan

A fan is a turbomachine which provides an air flowrate at some pressure rise, required to overcome the pressure losses of the circuit where it is installed. Regarding the aerodynamic noise sources of fans, these can be classified on different components after the classic works of Lighthill [63, 64] and Ffowcs Williams and Hawkings [35]:

- Monopoles: directly linked to the movement of the surfaces. The noise with this origin is usually referred to as thickness noise because it originates from the volume of fluid displaced during the motion of the surfaces.
- Dipoles: originated by the interaction of solid surfaces with the flow. Mainly attributed to aerodynamic force fluctuations, it is also referred to as loading noise.
- Quadrupoles: due to the flow in the outer region of the surfaces, it characterizes the flow self-turbulence. For jet flows, it can also be referred to as shear noise.

Depending on the Mach number at which the fan is operating, some of the aforementioned sources will become dominant over others. For low-speed fans, as the focus of the current thesis, the quadrupole term becomes negligible. Furthermore, the monopole term is shown to be less efficient than the dipole, specially for thin blades. Therefore, only the dipole component is typically considered for low-speed fan applications.

A complementary classification of the noise sources accounts for their impact on the noise spectrum [42]:

- Tonal noise:
 - non-uniformity of the average velocity field at the inlet and across the fan. Note that the distortion can come from downstream.
 - interaction of the outlet flow of the impeller with nearby obstacles (e.g. volute cut-off of centrifugal fans).
- Narrowband noise:
 - Tollmien–Schlichting instability waves (it happens when the blade boundary layer is laminar)
 - vortex shedding noise (on blunt trailing edge).
- Broadband noise:
 - interaction of inflow turbulence with the blades (leading-edge noise)
 - local flow separation
 - trailing-edge noise
 - interaction of turbulent outlet flow with obstacles (e.g. outlet guide vanes of axial fans, volute cut-off of centrifugal fans)
 - tip clearance noise (only in axial fans).

Tools

In the present works, serrated prototypes are designed by modifying the blade geometry of the baseline impeller with carved serrations. This has been done with the CAD software *Autodesk Inventor* [6]. The prototypes have been manufactured by the company Ziehl-Abegg SE. Then, they have been

tested at CETIAT in a double reverberant room, which allows measuring the air performance and the sound power levels simultaneously. RANS simulations have been performed with the commercial software *STAR-CCM+* [102]. These simulations have given an insight into the flow features inside the baseline impeller and have also allowed to obtain the input data of an analytical model of fan noise prediction. The analytical model has been implemented with the commercial software *MATLAB* [72].

Structure of the thesis

This thesis has four chapters.

Chapter 1 shows a comprehensive literature review of the use of serrations as a noise-reduction technique. Results from the bibliography have been used to design several impeller prototypes with leading-edge or trailing-edge serrations. This chapter also shows experimental results for both the baseline and the serrated impellers.

Chapter 2 develops an analytical model to predict the noise of the baseline impeller. It is based on Amiet's model and accounts for sources on the blade trailing edge and leading edge, as well as the edge of the front and back plates. The required geometrical transformations to account for the rotation and the geometry of the fan are also detailed. The input data of the analytical model are obtained from different analytical and empirical models using CFD results.

Chapter 3 shows the results of CFD RANS simulations of the baseline fan. This has three objectives. First, they are used to describe and analyse the flow through the impeller and around the fan assembly. Second, some results are used to design the geometry of the serrations presented in Chapter 2. And third, flow parameters are extracted to be used as input data of the analytical model described in Chapter 3.

Chapter 4 discusses the noise prediction of the analytical model of Chapter 4. A study is performed to assess the convergence of the model based on several numerical parameters. The results allow assessing the contribution of each part of the blade, as well as the hierarchy of the noise sources. Finally, the prediction is compared with the experimental results of Chapter 2.

Author's contributions

Regarding the experimental tests described in Chapter 2, several technicians from CETIAT ensured their set up and execution. The author of the thesis carried out the post-treatment of the data and their subsequent analysis. The author also designed the fan prototypes modified with serrations, which were manufactured by the company Ziehl-Abegg SE in Künzelsau (Germany).

The works described in Chapter 2 were started during the secondment in École Centrale de Lyon.

Part of the MATLAB scripts for a flat plate was provided by CETIAT and École Centrale de Lyon and used as a basis to implement the analytical model. The spanwise segmentation, the change of coordinates and rotating blades, the calculation of sound power level and the noise of the front and back plates are original contributions. The analytical work was jointly supervised by CETIAT, École Centrale de Lyon and Université de Sherbrooke.

Staff from CETIAT's simulations team contributed to the setup and run of the CFD simulations shown in Chapter 3. The author then ensured their post-treatment and modified and rerun some of them. The author was trained in the use of the simulation software during a secondment in Valeo (La Verrière, France).

The developments discussed in Chapter 4 are original contributions of the author. The Lattice Boltzmann Method results presented in the chapter were provided by Université de Sherbrooke and ÉTS Montréal. The author post-treated the raw data and analyzed the outcome.

Publications

The content of this thesis has been partially published at the international conferences mentioned below. The author's contribution to the publications involves the design of the prototypes, the monitoring of the tests, the analysis of the experimental results, the post-processing of the CFD simulations, the implementation of the analytical models, and the drafting. Some results of the thesis are a work in progress and will be submitted to a journal in the near future.

Conference papers

- Zurbano-Fernández, I., Guédel, A., & Robitu, M. (2019). Experimental investigation of the noise reduction of a plug fan by leading-edge serrations. In M. Ochmann, V. Michael, & J. Fels (Eds.), *Proceedings of the 23rd International Congress on Acoustics: integrating 4th EAA Euroregio 2019* (p. 8256). Aachen: Zweitveröffentlicht auf dem Publikationsserver der RWTH Aachen University. <https://doi.org/10.18154/RWTH-CONV-239909>
- Zurbano-Fernández, I., Guedel, A., Robitu, M., & Roger, M. (2020). Analytical prediction of the broadband noise of a plug fan. In *ISROMAC 2020 - 18th International Symposium on Transport Phenomena and Dynamics of Rotating Machinery*.

Chapter 1

Experimental study of serrations on a plenum fan

The objective of this chapter is to show the design and present test results on impeller prototypes with leading-edge and trailing-edge serrations. Before that, the baseline fan without modifications has been extensively tested in order to determine its aerodynamic and acoustic performance.

RANS simulations on a non-serrated baseline impeller, described in Chapter 3, have been performed to define an assumed optimum geometry of leading-edge serrations to reduce the noise, in view of the predicted turbulent areas. This geometry has been used as a reference to manufacture three impeller prototypes with various geometries of sinusoidal leading-edge serrations, defined by their amplitude and wavelength. Three impellers with trailing-edge serrations were also designed, based on design criteria for fixed airfoils. These three latter impellers had an iron-shaped geometry, deemed to be better than the more prevalent sawtooth or sinusoidal shapes.

All seven impellers (the baseline and the six prototypes) have been tested in a reverberant room, where noise and air performances were measured simultaneously. For each impeller, six fan operating points were tested, and for each point, the sound levels in narrowband and one-third octave band were measured at the fan inlet and outlet, for two rotating speeds (three for the baseline configuration). This allowed assessing the effectiveness of serrations at different operating points while checking their impact on the performance curve and fan efficiency. The results were then compared with the reference fan without serrations. In order to combine aerodynamic and acoustic effects, specific noise levels, defined later in this document, have been used.

1.1 Bibliographical review

Among the noise reduction techniques studied in recent years, serrations have gained widespread attention. Inspired by the special wing characteristics which enable the silent flight of the owl [96], serrations are a geometry which can be inserted in both trailing and leading edges of an airfoil. In the simplest form their shape is sinusoidal or sawtooth, but more complex shapes have also been studied. As shown in Figure 1.1, the two main parameters that define them are the root-to-tip amplitude $2h$ and the spanwise wavelength λ . Besides, the angle ϕ can also be considered. This angle is constant for sawtooth cuts but variable for other shapes.



Figure 1.1 – Rendering of a NACA 6412 airfoil with trailing-edge serrations

Serrations can be carved on the edge of the airfoil, inserted as a flat add-on and even combined with porous materials, either as brushes or add-ons which fill the serration gap. A comprehensive bibliographic review is presented in [108].

1.1.1 Leading-edge serrations

1.1.1.1 Effects on acoustics

Inspired by the flippers of humpback whales, leading-edge serrations have been shown to improve hydrodynamic performance, especially at high angles of attack. Since [49], where it was justified by **vortices breaking the periodic structure of the wake**, the noise reduction effect has also been studied. Recent experimental works have shown an effect on the generation and control of turbulence interaction noise over a wide range of frequencies [46, 78]. Lyu *et al.* [70] attributed the noise reduction to **destructive interference of the scattered surface pressure induced by the serrations**.

For example, Narayanan *et al.* [78] showed that using sinusoidal leading-edge serrations for a flat plate and NACA-65 type airfoil leads to significant noise reduction between lower and upper frequency

limits. It was also shown that the sound power level reduction is more sensitive to the serration amplitude and less sensitive to the serration wavelength. In a more recent study, Chaitanya *et al.* [19] pointed out that the use of complex leading-edge serrations, with double wavelength, chopped-peak, slitted-root and slitted-V, can produce larger noise reductions than single wavelength serrations. Slits can be manufactured as a long and narrow shape carved into the edge of the airfoil, or as a solid strip of material added to the valleys of a sawtooth or sinusoidal serration (see 1.2 for the latter).

Clair *et al.* [24] achieved a noise reduction of 3 dB beyond 1 kHz with serrations on a NACA 65 airfoil. This value is reduced with increased flow speed or angle of attack. It was proposed that half the serration wavelength $\lambda/2$ should equal the spanwise correlation length of the incoming turbulence and that the amplitude $2h$ should be as big as possible without hindering the aerodynamics.

CFD simulations performed by Kim *et al.* [56] showed that **surface pressure fluctuations along the leading edge exhibit a cutoff effect due to the oblique edge, and that some phase-interference effect between the peaks and valleys of the serrations** is one of the reasons behind noise reduction. **Destructive interference of scattered surface pressure** induced by serrations was also observed by Narayanan *et al.* [78].

CFD simulations by Lau *et al.* [57] evidenced a significant noise reduction when the condition $2h/\lambda_{gust}$ was respected, where λ_{gust} is the streamwise wavelength of the incoming turbulence gust. Chaitanya *et al.* [18] also shown the existence of an optimum serration angle at low frequency, $\Theta_O = \tan^{-1}(2h/L_t)$, function of the turbulence integral length scale L_t . Chaitanya *et al.* [20] also found an optimum for the integral length scale $\lambda_O = 4L_t$, at which compact sources at adjacent valleys are excited incoherently. Noise reduction is a function of the Strouhal number St_h based on the serration amplitude h ($10 \log(St_h) + 10$ for optimum wavelength) and the rate of change of sound power per valley is equal to the number of valleys. Besides, PIV measurements have shown that a thicker boundary layer is present at the trailing edge, reasonably spanwise uniform.

Bampanis and Roger [11] achieved a maximum reduction of 11 dB at 4300-4500 Hz with sinusoidal leading edge on a flat-plate airfoil with the same leading edge cross-section design as a NACA-0003. Measurements off the midspan plane showed that noise reduction can be larger at 75° at lower frequencies.

1.1.1.2 Effects on aerodynamics

The aerodynamic effect of leading-edge serrations has also been analysed. It has been observed by different authors [37, 115] that stall can be delayed by the generation of streamwise vortices, attributed to enhanced momentum transfer. This results in a significant reduction of flow separation and therefore improvement in aerodynamics within the wide range of post-stalls. Corsini *et al.* [27] identified that the

main aerodynamic mechanism was the formation of a low-pressure core on the blade-suction surface at the trough of each tooth. Skillen *et al.* [105] showed that serrations generate strong spanwise pressure gradients, which results in the formation of secondary flows (additional streamwise flow along serration edge). Rostamzadeh *et al.* [92] observed a better post-stall behaviour on airfoils with serrations showing the highest amplitude and smallest wavelength. Van Nierop *et al.* [107] pointed out that the wavelength of the sinusoidal shape has a second order effect on lift and drag, whereas the amplitude directly affects lift, drag and stall angle.

1.1.1.3 Application to fans

Zenger *et al.* [114] added sinusoidal serrations to the leading edge of the blades of an axial fan. The results showed a reduction in low-frequency broadband components (implying a reduction on unsteady forces), as well as in tonal components.

Biedermann *et al.* [12], again with leading-edge serrations, achieved a maximum noise reduction of 13 dB for a certain geometry (but the noise was increased by up to 3 dB at other operating points). It was observed that the noise reduction increases with bigger values of the serration wavelength and amplitude. An interesting parameter is the ratio $\lambda/2h$: high values yield the best noise reduction performance but it rapidly degrades when going away from the BEP; low values of the ratio generate more stable noise reductions at various operating points. Double-amplitude serrations were also assessed in the same study, but they only showed small results on air performance and no impact on noise reduction, when compared with simple serrations.

Cardillo *et al.* [16] simulated a centrifugal fan without volute with leading-edge serrations, for purely aerodynamic reasons. The numerical results showed an improvement of the air performance for the serrated impeller. This was attributed to the decrease of the losses at the inflow and to a more even distribution of velocity at the outlet.

1.1.2 Trailing-edge serrations

1.1.2.1 Effects on acoustics

Whereas the study of leading-edge serrations started in the 1970s, the study of trailing-edge serrations did not start until the late 1980s. In [50, 51], Howe developed an analytical model for the potential self-noise reduction on a flat plate. According to the model, reductions of up to $10 \log_{10}(10h/\lambda)$ for sinusoidal serrations, and up to $10 \log_{10}(1 + (4h/\lambda)^2)$ for sawtooth serrations are expected, with $\phi \leq 45$ deg and $\lambda/h < 4$. Howe attributed the noise attenuation to the **reduction in the spanwise correlation associated with sound radiation**. Theoretically, it is shown that the noise reduction is more effective for sawtooth serrations. Indeed, near the tips and valleys of sinusoidal serrations, the

edge is quasi-perpendicular to the flow, and therefore it concentrates the edge noise sources.

Since then, experiments have confirmed qualitatively parts of Howe’s theory, but the measured results have never fully reached the predictions; a noise increase at some frequencies can even be observed. As part of the STENO project, Dassen *et al.* [28] reported reductions of up to 5-10 dB on flat plates and airfoils, but only results for certain frequencies were presented (1-6 kHz). To prevent increased noise at high frequencies, it was found to be critical to align the plane of the serrations with the trailing-edge flow. The applications of the same serrations to wind turbines, by Braunn *et al* [13], only yielded partial results, with a maximum noise reduction of 3.5 dB and noise increase at higher frequencies. A similar trend was observed by [79], with noise reduction up to 5 dB under 1 kHz, but a noise increase beyond this threshold.

Herr [48] added serrations as brush attachments to the trailing edge of a flat plate. This achieved to suppress the vortex shedding noise from the baseline plate, with the greatest reduction being measured for the thickest brush. A noise increase was also observed, following a U^5 power law (U being the flow velocity). Furthermore, the noise appeared to be almost non-dependant of the plate length (the boundary layer thickness does not represent a scaling parameter) and U . Similar tests were performed on a NACA 65 airfoil by Finez *et al.* [36], where the noise reduction was attributed to the porous fibers, which disorganize the turbulent structures before they radiate sound.

Gruber *et al.* [40] applied sawtooth and slitted serrations on a NACA 65 airfoil. Measurements showed a negligible impact on lift and a maximum noise reduction of 5 dB (sawtooth) and 3 dB (slitted). However, for the airfoil with slits, a noise increase of 3 dB over 700 Hz has been observed. Howe’s model was also extended to slitted trailing edges. Nevertheless, the results contradict some of Howe’s predictions: the optimal noise reduction geometry (smallest $2h$) does not match the theory and a noise increase is detected at high frequencies for slits (after a critical frequency that seems to be linked to a Strouhal number based on the boundary layer thickness of around 1.18). Other noise generation mechanisms apart from the scattering process should be involved. Avallone *et al.* [7] attributed the difference between Howe’s prediction and experimental results to the different decay rate of the spanwise correlation length with respect to a straight trailing edge.

Gruber *et al.* [41] performed a parametric study with different serration geometries on the trailing edge of a NACA 65 airfoil, aimed at increasing flow permeability. Firstly, rectangular slits achieved noise reduction when their amplitude was greater than the boundary layer thickness; best results were obtained with smaller distance between slits. Secondly, sawtooth serrations with holes exhibited a poor noise reduction and a noise increase at high frequencies; a fine tuning would be required. Thirdly, slitted sawtooth serrations work better than simple sawtooth serrations (especially at high frequencies); the longer the slits, the better. Fourthly, slits with a random geometry showed results independent of

the angle of attack and good results at high frequencies.

Moreau *et al.* [75] inserted a serrated add-on on the trailing edge of a flat plate. Some of the results disagree with Howe’s predictions, because larger serration angles appear to be more effective. The vortex shedding noise was also diminished at high frequencies, and it was proposed that the **noise reduction capability of the serrations is related to their influence on hydrodynamic field at source location**. Chong *et al.* [23] directly cut serrations in the airfoil, achieving reductions of up to 30 dB in laminar regime and 6.5 dB with a turbulent flow (but generating vortex shedding noise at high frequencies). The spectacular reduction of the laminar regime is due to the extinction of the feedback loop on laminar instabilities. Catalano *et al.* [17] compared three different serration shapes: triangular, trapezoidal and wishbone. Reductions of up to 10 dB were achieved below 5000 Hz (being the wishbone the most efficient), with a noise increase on higher frequencies.

Other shapes have also been investigated. Arce León *et al.* [5] cut streamwise slits sawtooth serrations on an airfoil, but they are less effective than simple sawtooth serrations at reducing noise. This contradicts the results from [41], but in the latter study serrations were added in the form of a supplementary flat plate instead of being carved into the airfoil. Hasheminejad *et al.* [47] added a fractal pattern to sawtooth serrations on a NACA 12 airfoil. This suppressed the vortex shedding noise generated by some simple sawtooth serrations. Lyu *et al.* [67] showed that an ogee-shaped geometry can lead to reductions up to 8 dB with respect to sawtooth serrations. This had been studied before for leading-edge serrations [69], where an asymptotic analysis outlined that noise reduction is more efficient if a shape without stationary points (in a mathematical sense) is used.

1.1.2.2 Application to turbomachinery

Trailing-edge serrations have also been applied to rotating machines, especially to wind turbines. Braun *et al.* [13] applied them to a test wind turbine, achieving a maximum noise reduction of 3.5 dB but inducing also a noise increase at high frequencies. Oerlemans *et al.* [80] also added serrations to the trailing edge of the blade of a 2.3 MW prototype test wind turbine, yielding an average noise reduction of 3.2 dB, with a slight noise increase (1-2 dB) over 1 KHz.

Weckmuller *et al.* [109] performed a numerical optimisation of trailing-edge serrations on the front-rotor of a contra-rotating open rotor, yielding a reduction of only 0.2 dB on the tonal interaction noise. Another optimisation on the same rotor by Jaron *et al.* [54] showed that tonal interaction noise could be reduced by 1 dB due to destructive interference in the radial direction, with longer serrations generating better results.

Lee *et al.* [59] simulated a ceiling fan with different serration geometries. An overall noise reduction of 9.2 dB was predicted with flat serrations, 4.7 with sawtooth, 10.9 with rectangular, 13.9 with half

flat tip (only the outer half of the blade is serrated) and 5.0 with half rectangular half flat tip. However, when tested experimentally, a reduction of only 4.1 dBA was measured with half flat tip serrations. Pagliaroli *et al.* [82] added serrations to the trailing edge of an UAV propeller. Broadband noise reduction was achieved at low frequencies, but the aerodynamic performance of the propeller was degraded (and noise increase was observed at certain angles). Polar measurements show that noise reduction is highly directional.

1.1.3 Analytical models

Roger *et al.* [91] studied the noise reduction on a NACA-12 airfoil, and tried to extend Amiet’s theory to a serrated leading edge. The mathematical challenge associated with this approach was latter solved by Ayton & Kim [9]. Azarpeyvand *et al.* [10] extended Howe’s model to study new geometries at the trailing edge, showing that they were potentially more efficient than sawtooth.

Sinayoko *et al.* [104] combined Howe’s model with Amiet’s model for rotating blades, showing that rotation has little impact on the noise effect of trailing-edge serrations. The most effective serrations are narrow relative to the boundary layer thickness δ ($\lambda < \delta$ and $h > \lambda$). The model also predicts that adding slits to serrations could provide an additional noise reduction. A possible configuration combining sinusoidal serrations with slits is depicted in Figure 1.2).

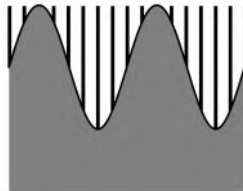


Figure 1.2 – Sinusoidal serrations with slits added to the hollow part

Lyu *et al.* [66] developed a new analytical method to predict noise reductions by trailing-edge serrations. It is more realistic and consistent than Howe’s model (this is explained by Howe’s choice of Green’s function). The noise reduction is due to **interference effects**, which is more effective at higher polar angles (thus closer to the leading edge), shows a change of directivity at high frequencies and yields a possible noise increase at low frequencies (specially for high Mach numbers or wide serrations). The noise reduction is more effective if $k_1 \cdot h_{min} \gg 1$, where k_1 is the streamwise wavenumber of the turbulent gust and h_{min} is the minimum serration amplitude for noise reduction to be effective.

Lyu *et al.* [70] also generalised Amiet’s model to account for leading-edge sawtooth serrations. An approach similar to Amiet’s was followed, based on Fourier expansion and the Schwarzschild technique, and yielded an excellent agreement with experimental results. Lyu & Azarpeyvand [65] continued the work, showing that the primary noise-reduction mechanism is the destructive interference of the

scattered pressure induced by the leading-edge serrations. A parametric study showed that serrations can reduce the overall sound pressure level at most radiation angles. The dipolar pattern of the far-field noise at low frequencies is not affected, but at high frequencies it changes from a cardioid shape to a tilted dipolar pattern.

Ayton & Kim [9] optimised the analytical prediction using several variable transformations and the Wiener-Hopf technique. They showed that increasing the serration amplitude redistributes energy from cut-on to cut-off modes, accounting for the better efficiency of longer serrations. Besides, a logarithmic dependence between the serration amplitude and the far field noise reduction was predicted. This model was also applied by Ayton & Chaitanya [8] to different shapes (sawtooth, slitted v-root, slitted u-root, chopped peak, square wave), finding a good agreement with experimental results. A secondary noise reduction mechanism, due to **nonlinear features**, was also found.

More recently, Lyu & Ayton [68] simplified the analytical models for both leading-edge and trailing-edge serrations. This is based on the fact that high order modes are cut-off and adjacent modes do not interfere in the far field except at sufficiently high frequencies. The simplification was found to dramatically reduce the computing time and opened the gate to parametric optimization studies, such as the one performed by Kholodov & Moreau [55]. Though this was not attempted in the present work, such models could be combined with classical Amiet's theory in a future work, for instance by defining a correction.

Halimi *et al.* [45] applied Lyu's *et al.* leading-edge model [70] and Lyu *et al.* trailing-edge model [66] to a propeller, using the strip theory approach. Results showed good agreement with time-domain LBM simulations at high frequencies. For the trailing-edge serrations, a noise reduction was predicted for low and middle frequencies, with a noise increase at high frequencies. Sharp serrations yield a better noise reduction. The model also predicts noise reduction at high frequencies with leading-edge serrations. Noise reduction increases with serration amplitude, whereas the wavelength has no significant effect.

1.2 Description of the experimental setup

1.2.1 Description of the fan

The fan of the study is a plenum fan, i.e. a backward-curved centrifugal fan without volute (see Figure 1.3). It was manufactured by the company Ziehl-Abegg SE in Germany (under the commercial designation ER35C-4DN.C7.1R). The impeller is mounted on a shaft coupled to an electric motor, itself mounted on a support. Also integral with the support there is an inlet nozzle, which directs the airflow towards the impeller.

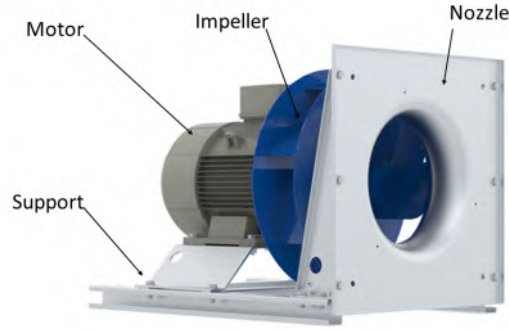


Figure 1.3 – Fan of the study (credit of the picture to Ziehl-Abegg SE)

The impeller has seven blades of a constant thickness of 2 mm and an outer blade diameter of 361 mm. The main parameters of the fan are shown in Table 1.1, whereas the geometry of the impeller is described in Figure 1.4.

Table 1.1 – Fan parameters

Designation	Value
Number of blades B	7
Blade thickness T [mm]	2
Inlet diameter D_i [mm]	224
Outlet diameter D_e [mm]	361
Outlet width L [mm]	98
Chord c [mm]	134
Blade angle at leading edge β_1 [°]	23
Blade angle at trailing edge β_2 [°]	31
Nominal speed N [rpm]	1440

1.2.2 Experimental setup

All the experiments have been carried out in CETIAT’s double reverberant room according to test category A: non-ducted at inlet and outlet (see Figure 1.5). This test facility complies with ISO/TC 117 standards. CETIAT is accredited by the *Air Movement and Control Association* (AMCA) for fan air and sound performance testing. The room on the inlet side has a volume of 500 m³. The fan is mounted in the outlet pressure chamber (volume 50 m³), with the inlet nozzle fixed on the partition between both rooms (see Figure 1.5). Downstream of the pressure chamber there is a silencer, a multiple nozzle chamber and an auxiliary fan. This setup allows to measure and control the flow, adjusting the operating point of the test fan.

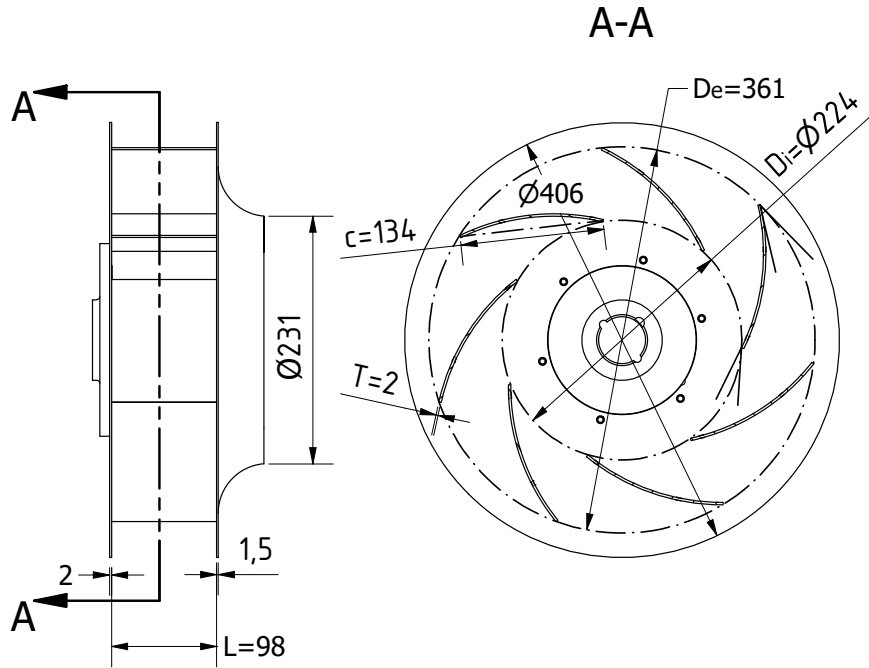


Figure 1.4 – Main dimensions of the impeller

With regards to instrumentation, according to ISO 5801 [53], the flowrate is measured in the multi-nozzle chamber and the fan pressure is obtained according to ISO 5801 [53] with pressure rings in both reverberant rooms. The fan sound power levels are determined in both rooms following ISO 13347-2 [52], using a rotating microphone in the inlet chamber and 3 fixed microphones in the smaller, outlet room to make a spatial average of the sound pressure field in each room. Figure 1.6 shows pictures of the test rig. As the rotating speed varies with the operating point, all the results are converted to the target speed (1440, 1080 or 720 rpm) and an air density $\rho = 1.2 \text{ kg/m}^3$, which are very close to the test values.

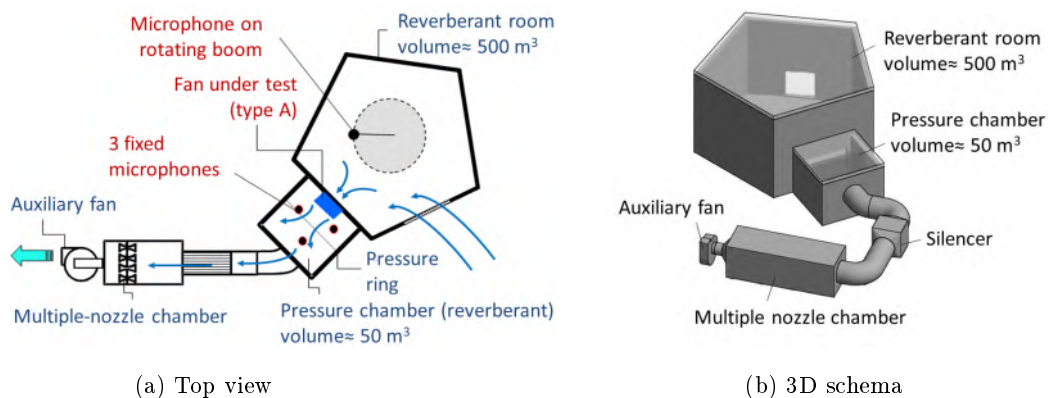


Figure 1.5 – Layout of the test facility

For each prototype, the same support (base, inlet nozzle, motor as in Figure 1.6b) has been used, with only the impeller being replaced. However, different assemblies of the fan unit have been used

during the experimental campaigns (see Annex B for more details). The motor is connected to a variable-frequency drive (VFD) which allows changing the speed between 1440 rpm (100% of the nominal speed) and 720 rpm (50% of the nominal speed).



(a) Inlet



(b) Outlet

Figure 1.6 – Views of the reverberant rooms

1.2.3 Formulas and definitions

1.2.3.1 Aerodynamics

The most commonly used fan characteristic is the pressure curve, which shows the relationship between flowrate and pressure rise. Each point on the curve is called an operating point.

There are two definitions of pressure, according to ISO 5801 [53]. The total fan pressure p_f is the difference between the total pressures at the fan outlet and inlet:

$$p_f = p_{t2} - p_{t1}$$

The static pressure is defined as the difference between the total pressure p_f and the dynamic pressure at the outlet p_{d2}

$$p_{fs} = p_f - p_{d2}$$

where

$$p_{d2} = \frac{1}{2} \rho V_2^2$$

ρ being the air density and V_2 the average air velocity at the outlet. V_2 is calculated by dividing the flow rate by the outlet surface of the impeller $V_2 = \frac{q_v}{S_2}$, with $S_2 = \pi D_e L$.

Another basic parameter to characterise a fan is its power. The power conversion chain is depicted in Figure 1.7, definitions and notations according to ISO 5801[53]. Fans are usually driven by electric motors. If the power is provided (and controlled) with a variable frequency drive (VFD), the latter

requires an input power P_{ed} . From here on, there is a successive cascade of losses: in the VFD, in the electric motor, in the transmission, in the coupling and in the impeller. Subtracting them will result in the output power at each component of the chain: the motor input power P_e , the motor output power P_o , the fan shaft power P_a and the power supplied to the fan impeller P_r . The fan finally generates the fan air power P_u , which is used to move the air through the impeller:

$$P_u = q_v \cdot p_f \quad (1.1)$$



Figure 1.7 – Power conversion chain between the VFD and the impeller; notations, as per ISO/TC 117 - Fans, described in text

In absence of a belt, a flexible transmission or bearings, we consider that $P_r = P_a = P_o$. We can define the efficiency of each element of the chain, as follows:

- Variable frequency drive: $\eta_c = \frac{P_e}{P_{ed}}$
- Motor: $\eta_{mot} = \frac{P_o}{P_e}$
- Fan impeller: $\eta_r = \frac{P_u}{P_r}$

The overall efficiency for a fan with variable speed drive η_{ed} is defined as the product of all the efficiencies, as well as the ratio between the fan air power and the drive control electrical input power:

$$\eta_{ed} = \eta_c \eta_{mot} \eta_r = \frac{P_u}{P_{ed}} \quad (1.2)$$

The overall static efficiency can be computed by replacing p_f by p_{fs} in Equation 1.1.

The motor efficiency η_{mot} was measured and provided by the fan manufacturer in the present study. The outcome (and a linear interpolation of the data) is displayed in Figure 1.8. If we neglect the losses of the VFD ($\eta_c = 1$), we obtain the impeller efficiency η_r from Equation 1.2.

To study the noise generated by a fan, both the sound pressure level L_p and the sound power level L_w are used. To compare the noise levels of different fans taking into account their differences in performance curve, we can use the concept of specific sound pressure level, which is defined as:

$$L_{p_{specific}}(f) = L_p(f) - 10 \log_{10}(q_v) - 20 \log_{10}(p_f) \quad (1.3)$$

There is a series of dimensionless numbers which will be used to compare results from different rotating speeds: the pressure coefficient μ , the flow coefficient $\bar{\delta}$, the non-dimensional system resistance coefficient (also known as throttling coefficient) Φ and the system resistance coefficient ξ .

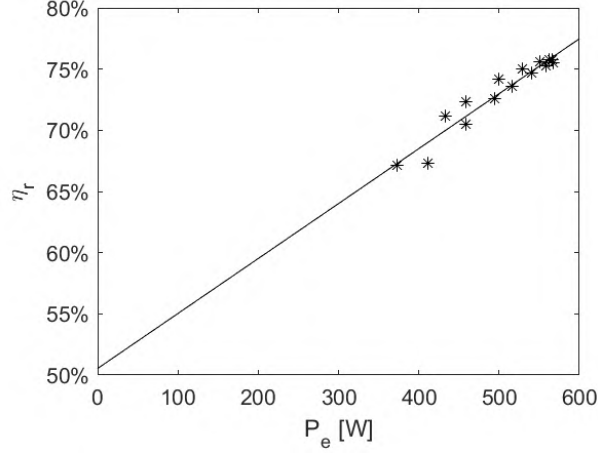


Figure 1.8 – Motor efficiency versus motor input power for the fan of the study, data provided by Ziehl-Abegg

$$\mu = \frac{p_f}{\rho U^2} \quad (1.4)$$

$$\bar{\delta} = \frac{q_v}{US} \quad (1.5)$$

$$\Phi = \frac{\bar{\delta}}{\sqrt{2\mu_{stat}}} = \frac{q_v}{S\sqrt{2p_{fs}/\rho}} \quad (1.6)$$

$$\xi = \frac{q_v}{\sqrt{2p_{fs}/\rho}} \quad (1.7)$$

with $U = \pi D_e N$, and $S = \pi D_e L$ for this type of fan. In our case, $D_e = 0.361$ m and $L = 0.098$ m.

1.2.3.2 Acoustics

Assuming that the flows are self-similar [42], there are some similarity laws which allow to convert acoustic results between fans within the same family, only differing in size (D, L) and rotational speeds (N). The basic equations, which are purely empirical, are:

$$L_{W_2}(f_2) = L_{W_1}(f_1) - 50 \log_{10}\left(\frac{N_1}{N_2}\right) - 50 \log_{10}\left(\frac{D_1}{D_2}\right) - 10 \log_{10}\left(\frac{L_1}{L_2}\right) \quad (1.8)$$

$$f_2 = f_1 \cdot \frac{N_2}{N_1} \quad (1.9)$$

As we are only changing the speed and not the geometry ($D_1 = D_2, L_1 = L_2$), Equation 1.8 then becomes:

$$L_{W_2}(f_2) = L_{W_1}(f_1) - 50 \log_{10}\left(\frac{N_1}{N_2}\right) \quad (1.10)$$

In some plots, Equation 1.9 will be normalised by the BPF to yield:

$$\frac{f_2}{BPF} = \frac{f_2}{7N_2/60} = \frac{60f_1}{7N_1} \quad (1.11)$$

1.3 Test of the baseline fan

The baseline fan was tested at three different rotating speeds N : 1440 rpm, 1080 rpm and 720 rpm. For each speed, five or six operating points have been measured, for which the most relevant aerodynamic and acoustic results have been obtained.

1.3.1 Aerodynamic results

The main air performance result is the fan curve, which shows the evolution of the pressure versus the flowrate. Figure 1.9a shows the curves for the three rotating speeds. Reducing the speed induces a reduction of the fan curve. Equations 1.4 and 1.5 can be used to check the aerodynamic similarity of the results, confirmed by the dimensionless fan curve, depicted in Figure 1.9b. Only deviations of about 0.015 in μ are found at lower flowrates.

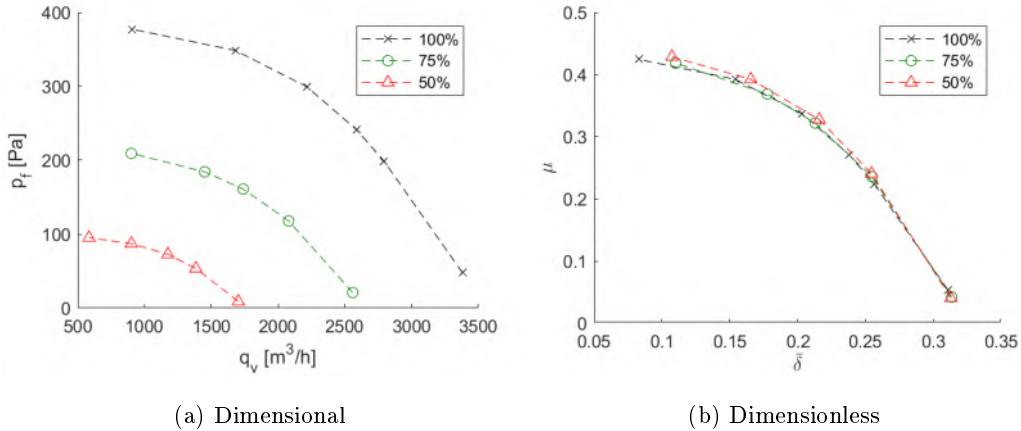


Figure 1.9 – Baseline fan pressure curves

Another important parameter is the overall efficiency of the fan assembly η_{ed} . It is plotted in Figure 1.10 versus the dimensionless flowrate $\bar{\delta}$ to see the similarity of its evolution when the rotating speed is changed. It presents a maximum around $\bar{\delta} = 0.2$, regardless of the speed. This operating point is the best efficiency point (BEP) and is quite relevant for our study. The results for 75% of the nominal speed have been omitted because there were some problems with the measurements of electric power, which is required to use Equation 1.2. As expected, the efficiency strongly decreases with speed because not only the fan efficiency, but also the combined efficiency of the motor and the VFD, decrease with speed.

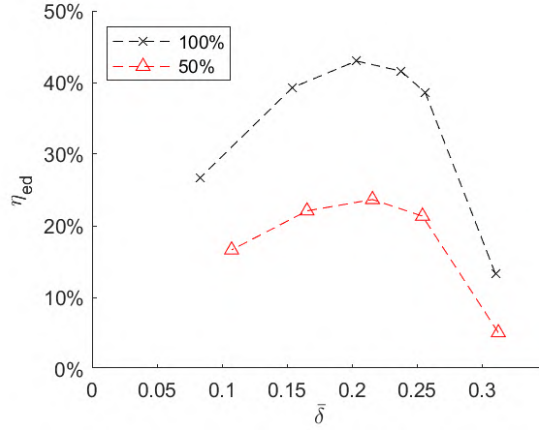


Figure 1.10 – Overall efficiency versus dimensionless flowrate

1.3.2 Acoustics

Before dealing with the acoustic results, it is useful to pay attention to the first blade passing frequencies. The result is shown in Table 1.2.

Harmonic	1440 rpm	1080 rpm	720 rpm
1	168	126	84
2	336	252	168
3	504	378	252
4	672	504	336
5	840	630	420
6	1008	756	504
7	1176	882	588
8	1344	1008	672
9	1512	1134	756
10	1680	1260	840

Table 1.2 – Blade passing frequencies for the different rotating speeds

1.3.2.1 Overall Sound Power Level

To give an overview of the acoustics of the fan, the overall sound power level in dB(A)¹ is plotted versus $\bar{\delta}$ for all speeds and operating points (in Figure 1.11a for the inlet and 1.11b for the outlet). As it is expected — and understood from fan acoustic analogies — the level increases as the fan turns faster. There is a minimum noise around the BEP, but this is not always the case.

1. The dB(A) weighting accounts for hearing sensitivity, and gives less weight to low frequencies (below a couple of hundred Hz) and maximum importance to frequencies between 1kHz and 6 kHz

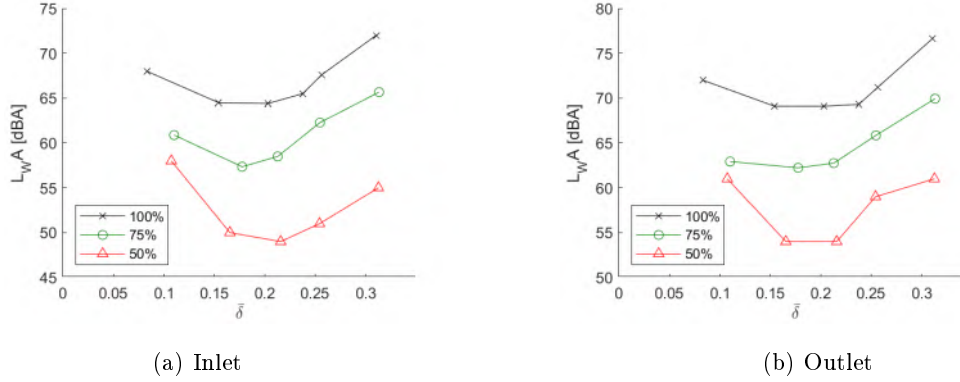


Figure 1.11 – Sound power level curves of the tested baseline fan

1.3.2.2 Comparison with similar fans

Using information from an internal database from CETIAT, the noise signature of the fan has been compared with plenum fans of other manufacturers. Their commercial designations have been removed due to confidentiality issues. As the dimensions and rotating speed may differ, all the results have been transposed to a diameter $D_2=300$ mm, a span $L_2=75$ mm and a rotating speed $N_2=3000$ rpm, using equations 1.8, 1.9, 1.10 and 1.11. The comparison of the overall sound levels in dB is plotted in Figure 1.12.

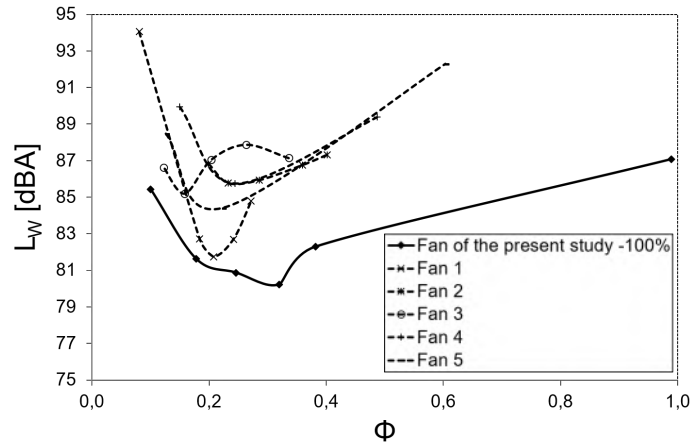


Figure 1.12 – Comparison of the overall sound power of the fan of the study and other commercial plenum fans, measurements at outlet

The fan of the current study behaves comparatively better than the other commercial fans of the same type, for all operating points. This suggests that the fan is well optimized in terms of its acoustic performance. Therefore, it is a challenging industrial platform for the study of serrations.

1.3.2.3 Noise spectra at operating points with the same flow coefficient $\bar{\delta}$

If we compare the sound power spectra for a given flow coefficient $\bar{\delta}$, we see that the spectra for the different speeds look quite similar. This can be seen in Figure 1.13 for $\bar{\delta} = 0.1$. In this case, there

is a significant hump centred in the 5000 Hz band for the 50 % speed, also present for other speeds at other frequencies, but less pronounced. The peaks at low frequency, below 100 Hz, do not correspond to the BPF, but to a subharmonic at around 0.75 BPF. This could be the trace of the interaction with some rotating instability, reducing the relative rotating speed between the impeller and the instability. This has been described, for instance, for a centrifugal fan with a volute by Sanjosé & Moreau [97].

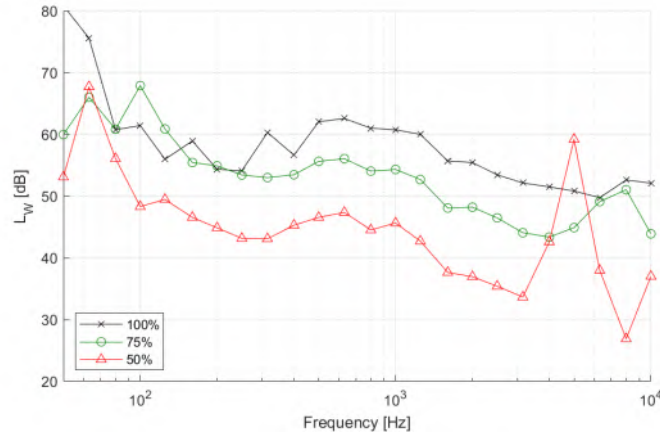


Figure 1.13 – Third-octave bands of sound power level at outlet as a function of the % of the nominal rotating speed, $\bar{\delta} = 0.1$

Plotting the results for all the operating points will be redundant because they show the same tendency. Nevertheless, it is always interesting to analyse the noise at the BEP, with $\bar{\delta} = 0.2$, displayed in Figure 1.14. It exhibits a similar trend as for $\bar{\delta} = 0.1$, without the peaks at high frequencies. Other peaks are observed at 1000 Hz, 5000 Hz and 8000 Hz for 50%, 75% and 100%, respectively, with that for 75% being particularly high and that for 100% rather weak. The third-octave peaks corresponding to the BPF are also easily identifiable. The sound power level for the nominal speed will be compared with an analytical prediction in Section 4.2.

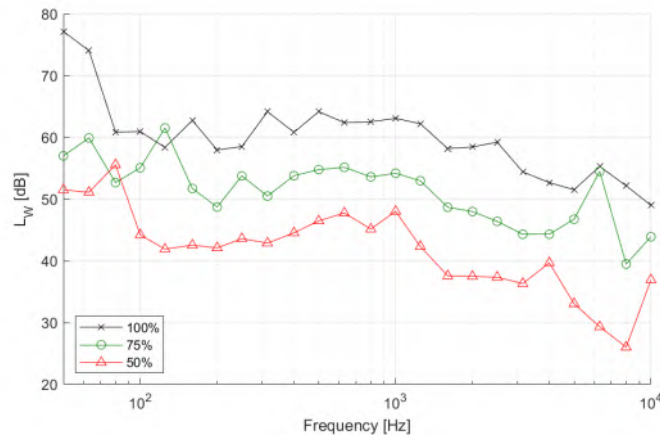


Figure 1.14 – Third-octave bands of sound power level at outlet as a function of the % of the nominal rotating speed, $\bar{\delta} = 0.2$

It is also relevant to show the chart for $\bar{\delta} = 0.3$ in Figure 1.15, for the extreme right characteristic of the curves, because an additional hump appears in the middle frequency range for the three speeds (1250 Hz for 50%, 2000 Hz for 75% and 3150 for 100%). The peaks at low frequency (80 Hz and 125 Hz for 50% and 75%, respectively) correspond again to the BPF.

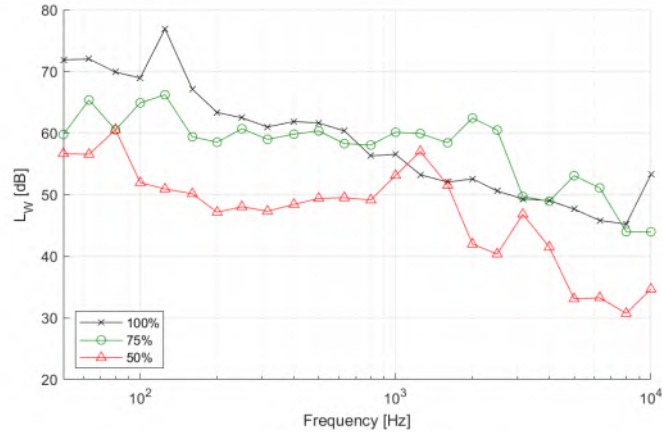


Figure 1.15 – Third-octave bands of sound power at outlet as a function of the % of the nominal rotating speed, $\bar{\delta} = 0.3$

Narrowband spectra, except for the highest speed, are needed to complement the information obtained with the third-octave spectra. In fact, the BPF at high speed is hard to see in all cases and the peak at 125 Hz for the high speed and $\bar{\delta} = 0.3$ in Figure 1.16 shows the raw data for the sound pressure level for the smallest flowrate of $\bar{\delta} = 0.1$. We can observe the large peaks responsible for the third-octave peaks at high frequencies in Figure 1.13. Furthermore, other smaller peaks appear at the same frequency regardless of the rotational speed (584 Hz, 872 Hz, 2144 Hz, 2720 Hz and 6048 Hz). They have been observed for other operating points, and also at the inlet. As they are independent of the rotational speed, they should be due to resonances, either mechanical or acoustic. In subsection 1.3.2.10 it will be checked if there is any relationship between them and the impeller geometry. The noise around 12 kHz, at the very right edge of the plot, is generated by the VFD.

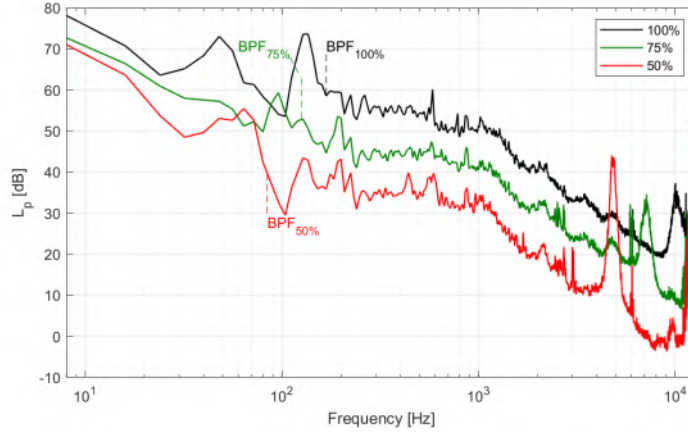


Figure 1.16 – Narrowband sound pressure spectra at outlet as a function of the % of the nominal rotating speed, $\bar{\delta} = 0.1$, $\Delta f = 8$ Hz

The large peaks at low (64, 96 and 128 Hz) and high frequencies (4800, 7100 and 10100 Hz) could be linked to the rotational speed. To investigate this, we apply a frequency conversion from Equation 1.11. The sound pressure level is also converted with Equation 1.10. This new representation (Figure 1.17) yields some interesting information. First, the peaks at low frequency are subharmonics of the BPF. They occurred at a frequency of around 0.75 BPF, and could be the trace of the interaction of the impeller with some rotating instability, reducing the relative rotating speed between both of them. Secondly, the peaks at high frequencies seem to scale with the rotational speed at around 58 BPF, albeit at such a high order multiple, the physical origin of the sound emission is probably not directly related to the rotation.

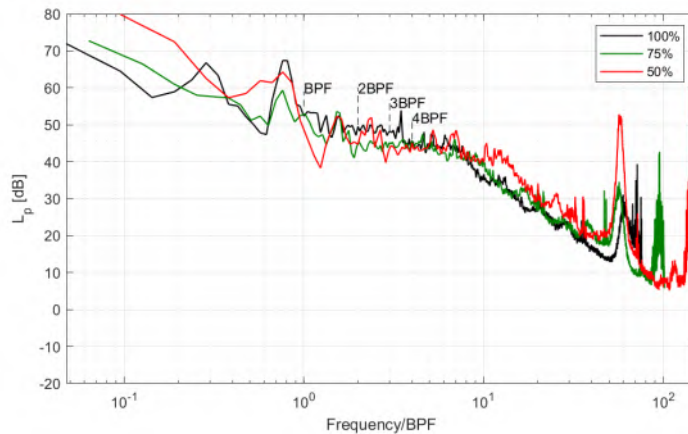


Figure 1.17 – Narrowband sound pressure spectra in reduced variables (reference speed $N=1080$ rpm) at outlet as a function of the % of the nominal rotating speed, $\bar{\delta} = 0.1$, $\Delta f = 8$ Hz

The spectrum for the larger flowrate at $\bar{\delta} = 0.3$ is reported in Figure 1.18. We observe similar features as for $\bar{\delta} = 0.1$. A major difference —and this is also the case for the other operating points— is that the peaks at low frequency do correspond to the first BPF (this is more clearly depicted in

Figure 1.19). Another difference is that now there are two peaks at high frequencies instead of only one. The peak at 7 kHz for the speed 100% seems to merge with the resonance at the very same frequency.

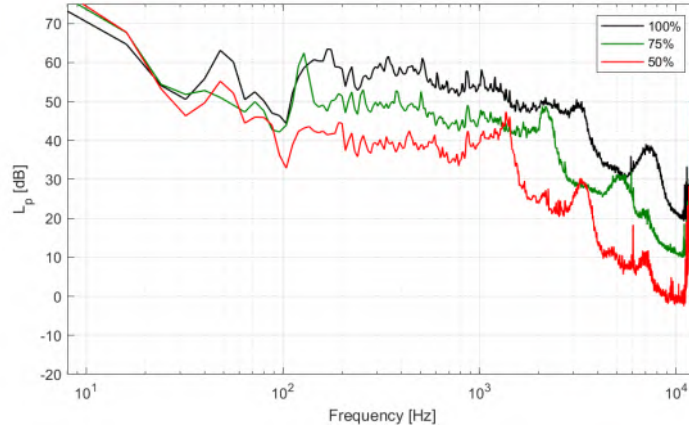


Figure 1.18 – Narrowband sound pressure spectra at outlet as a function of the % of the nominal rotating speed, $\bar{\delta} = 0.3$, $\Delta f = 8$ Hz

The aforementioned differences are better recognized using the reduced variables (Figure 1.19). Now the first three harmonics of the BPF are easily identified. We also see that the two peaks at mid-high frequencies seem to scale with the rotational speed, and correspond to a value of around 17 and 40 BPF. In this particular case, the inlet has been preferred to the outlet because the signal is less noisy.

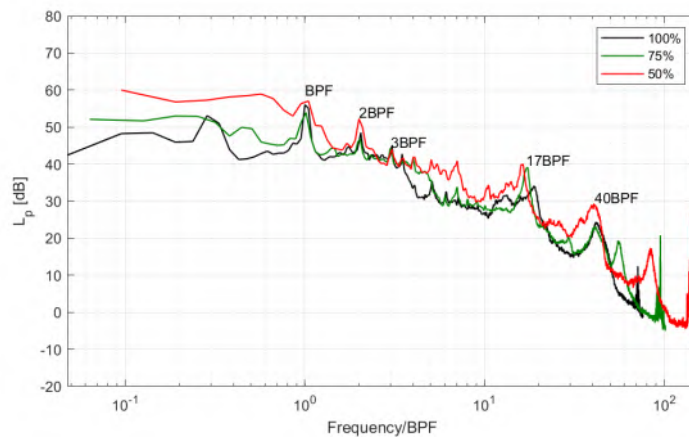


Figure 1.19 – Narrowband sound pressure spectra in reduced variables (reference speed $N=1080$ rpm) at inlet as a function of the % of the nominal rotating speed, $\bar{\delta} = 0.3$, $\Delta f = 8$ Hz

1.3.2.4 Inlet and outlet

The preceding analysis has shown the most relevant features, and their evolution when changing the rotating speed and the operating point. These features are common between inlet and outlet, and

the spectrum does not change that much from one to the other. However, the following differences can be pointed out:

- The sound at outlet is around 10 dB louder than the sound at inlet
- Some of the resonance peaks are less pronounced at the outlet, but the peaks at high frequencies are equal or bigger

As an example, the pressure spectra for inlet and outlet at the nominal speed and the BEP are presented in Figure 1.20. It can be argued that for radiation from inlet, sound has to be transmitted through a converging duct (from outer radius to inner radius). This difference is therefore somehow expected. It is even more expected if the dominant sources are at the trailing edges of the blades.

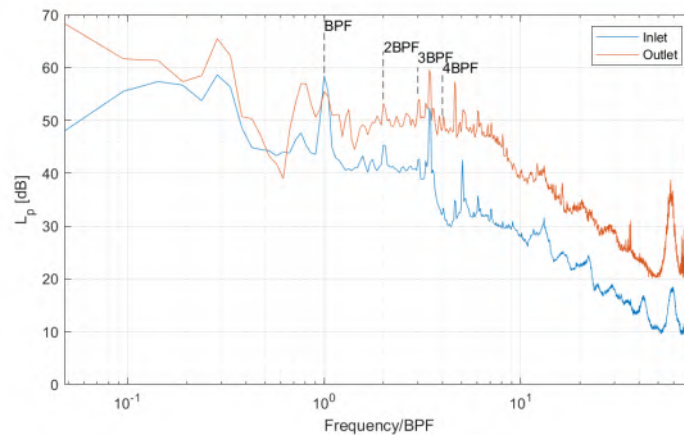


Figure 1.20 – Narrowband sound pressure spectra for inlet and outlet, $\bar{\delta} = 0.2$, $\Delta f = 8$ Hz, $N=1440$ rpm

1.3.2.5 Comparison of all operating points

A complementary way to display the data is to plot the spectra for all operating points at a given speed. To illustrate this, the nominal speed of 1440 rpm in Figure 1.21 is selected. As in Figure 1.19, the inlet is shown because the signal is less noisy.

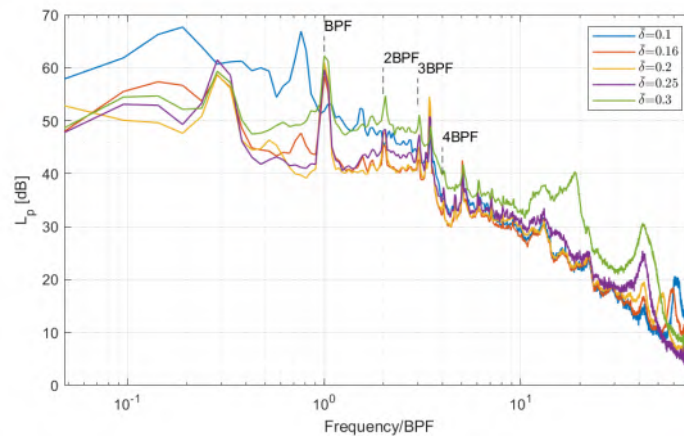


Figure 1.21 – Narrowband sound pressure spectra at inlet for all operating points, $\Delta f = 8$ Hz, $N=1440$ rpm

Most of the spectra are similar, a global minimum being almost achieved at the BEP (which is at $\bar{\delta} = 0.2$). Two special features are observed for the highest and lowest flowrates. One is the hump at around 3000 Hz (18 BPF), which only appears for $\bar{\delta} = 0.3$ (and also at $\bar{\delta} = 0.25$ for the speeds 75% and 50%, not shown here). The other is the low-frequency increase at the smallest flowrate. Besides, it is also noticeable that the amplitude of the resonance peak at 7000 Hz (40 BPF) effectively increases with the flowrate. However, this tendency has not been observed neither at the outlet nor for any other rotational speed.

1.3.2.6 Summary of the most prominent peaks

The following features are common to all operating points:

- A peak at 50 Hz (electrical network)
- The BPF and the second harmonic (and for some cases even the third and fourth), not apparent at the smallest flowrate $\bar{\delta} = 0.1$
- Small resonance peaks at mid to high frequencies (such as around 600, 900, 2000, 4000, 6000 and 7000 Hz)

For each operating point in particular:

- $\bar{\delta} = 0.1$
 - Subharmonic hump at $f \sim 0.75$ BPF (and a smaller harmonic of the subharmonic at 1.5 BPF)
 - Resonance at $f \sim 580$ Hz
 - Large peak at $f \sim 58$ BPF, especially at 50%
- $\bar{\delta} = 0.16$
 - Peaks at BPF (specially for 75% and 50%) and, to a lesser extent, at 2BPF
 - Resonance at $f \sim 580$ Hz, particularly visible at 100%
 - Big peak at $f \sim 58$ BPF, specially at 50%
- $\bar{\delta} = 0.2$
 - Peak at BPF and, to a lesser extent, at 2BPF and 3BPF
 - Resonance at $f \sim 580$ Hz, mainly at 100%
 - Peak at $f \sim 45$ BPF, only at 75% and 50% (so at a different frequency from the previous operating points)
- $\bar{\delta} = 0.25$
 - Peak at BPF and, to a lesser extent, at 2BPF, 3BPF and 4BPF
 - Resonance at $f \sim 580$ Hz, mainly at 100%
 - Hump at $f \sim 1.2$ kHz, only visible at 50%

- Narrow hump at $f \sim 40$ BPF, for all speeds but specially significant at 75%
- Resonance at 7 kHz, which overlaps with the hump at 40 BPF at 100%
- $\bar{\delta} = 0.3$
 - Peak at BPF and, to a lesser extent, at 2BPF and 3BPF
 - Hump at $f \sim 15$ BPF, mainly visible at 75% and 50%
 - Hump at $f \sim 40$ BPF
 - Resonance at 7 kHz, with a probable coincidence with the hump at 40 BPF at 100%

Spectral peaks or tones not related to the rotation may arise because of various mechanisms, shortly addressed in the following sections.

1.3.2.7 Laminar-boundary-layer-vortex-shedding

When at least one boundary layer of a blade remains laminar down to the trailing edge, with an adverse pressure gradient, laminar instabilities (often referred to as Tollmien-Schlichting waves) develop. Their scattering as sound at the trailing edge is responsible for narrow-band emergence, or even high-level tones in cases of acoustic feedback. The mechanism has been recently reviewed by Yakhina *et al.* [110]. The mechanism is referred to as LBL-VS for "laminar boundary-layer vortex shedding" by Brooks *et al.* [14].

To investigate if any of the peaks could be generated by a LBL-VS, a simplified analysis on the results is performed. For this, we apply the following equation, which expresses the frequency of the peak related to this mechanism [42]:

$$\frac{f \cdot T}{U_e} \approx 1 \quad (1.12)$$

where T is the blade thickness, f the frequency and U_e , the relative flow velocity outside the boundary layer, estimated from CFD simulations (Table 3.2). The LBL-VS mechanism is rather expected at low values of $\bar{\delta}$, for which the Reynolds number is lower. The simulation which fits better to this condition was carried out at $q_v = 1706 \text{ m}^3/h$, $\bar{\delta} = 0.16$ and $N = 1440 \text{ rpm}$. The flow velocity is around $U_e = 20 \text{ m/s}$. We will suppose that it scales with the rotational speed, so that:

$$U_{e2} = U_{e1} \frac{N2}{N1} \quad (1.13)$$

From these equations we obtain the potential frequencies, listed in Table 1.3.

N (rpm)	1440	1080	720
U_e (m/s)	20	15	10
Eq. 1.12 (Hz)	10000	7500	5000

Table 1.3 – Potential LBL-VS peak frequencies

The frequencies calculated with Equation 1.12 fit approximately with the peaks measured at $\bar{\delta} = 0.1$ and $\bar{\delta} = 0.16$. Therefore, we could identify LBL-VS as a noise source for low values of $\bar{\delta}$. However, low velocity is not the only necessary criterion for the existence of this phenomenon: a moderate loading condition is also necessary.

Another element which supports this hypothesis lays in Figure 1.22. In it, the noise is plotted for four different rotating speeds (100%, 75%, 65% and 50% of the nominal speed). When the rotating speed is reduced, the peak which appears roughly around 10 kHz at 100% of the nominal rotating speed is shifted towards lower frequencies and it increases in amplitude, scaling with the velocity to the power 1.5. This is consistent with the presence of laminar boundary layer vortex-shedding: if the noise is generated by a laminar instability, the reduction of the rotating speed could lead to an increase in the laminarity of the flow, therefore increasing the amplitude of the peak. The addition of trailing-edge serrations would mitigate or even completely cancel this phenomenon, as it is described in Section 1.5.3.

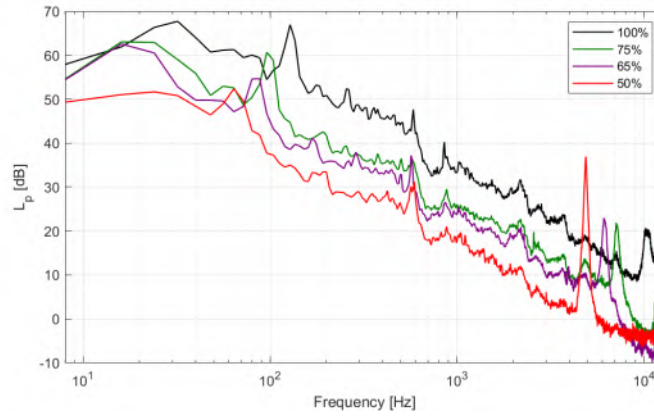


Figure 1.22 – Narrowband sound pressure spectra in reduced variables (reference speed $N=1080$ rpm) at inlet as a function of the % of the nominal rotating speed, $\bar{\delta} = 0.1$, $\Delta f = 8$ Hz

1.3.2.8 Von Karman vortex shedding

The von Karman vortex shedding at a blunted trailing edge is another well-known mechanism of narrow-band emission from a blade. For this, the blade thickness at the trailing edge must be large enough compared to the thickness of the boundary layer. The frequency of vortex shedding can be estimated with:

$$\frac{f \cdot T}{U_e} \approx 0.2 \quad (1.14)$$

T being again the blade thickness. It is worth noting that some "equivalent" thickness slightly larger than the physical thickness sometimes gives a better estimate based on a Strouhal number of 0.2. The value of U_e is estimated from the CFD simulations at 1440 rpm. For 1080 and 720 rpm, Equation

1.13 has been applied. Besides, the values of U_e for $\bar{\delta} = 0.3$ have been extrapolated. The results are displayed in Table 1.4:

N (rpm)	1440	1080	720
$\bar{\delta} = 0.16$	20	15	10
$\bar{\delta} = 0.2$	22	16.5	11
$\bar{\delta} = 0.25$	25	18.8	12.5
$\bar{\delta} = 0.3$	27	20.3	13.5

Table 1.4 – Estimation of U_e , in m/s

Applying Equation 1.14 yields the frequencies reported in Table 1.5.

N (rpm)	1440	1080	720
$\bar{\delta} = 0.16$	2000	1500	1000
$\bar{\delta} = 0.2$	2200	1650	1100
$\bar{\delta} = 0.25$	2500	1875	1250
$\bar{\delta} = 0.3$	2700	2025	1350

Table 1.5 – Vortex shedding frequencies, in Hz

For $\bar{\delta} = 0.25$, the frequencies correspond to peaks observed at 1080 and 720 rpm. For $\bar{\delta} = 0.3$, peaks have been detected at a higher frequency than the calculation (3200 Hz at 100% and 2200 Hz at 75%). This difference on the frequency could be due to the uncertainty of the estimation, which relies on CFD simulations, extraction of the velocity magnitude and extrapolations. On the other hand, the peaks are not necessarily originated by vortex shedding and could be generated by other mechanisms.

1.3.2.9 Analysis of the peaks at mid to high frequencies

The peaks at mid to high frequencies seem to depend on the rotational speed. To check this we will apply the following formula to the frequency of each peak:

$$F1 = F2 \left(\frac{N2}{N1} \right)^n \quad (1.15)$$

In the present case case, the frequencies of the peaks at 100% and 50% of the nominal speed are converted to 75%, which means that $N2 = 1080$ rpm. The values of n which yield a best fitting with the peaks at 75% are 1.3 for 100% and 1 for 50%.

Despite a partial fitting, the peaks remain shifted between some dozens and some hundreds of Hz. It is not possible to find a clear match between them. This suggests that the length scales involved in the scaling laws could have to be considered as variables. Indeed, if the physics changes — and with

$\bar{\delta}$	0.1	0.16	0.2	0.25	0.25	0.3	0.3
Raw frequency (100%)	10390	9744	8920		7000	3192	7448
Converted frequency (100%)	7148	6704	6137		4816	2196	5124
Raw frequency (75%)	7112	6838	6016	1768	5136	2168	5200
Raw frequency (50%)	4888	4672	3784	1072	3152	1360	3400
Converted frequency (50%)	7332	7008	5676	1608	4728	2040	5100

Table 1.6 – Scaling of the frequency of the peaks at mid-high frequencies, data from the outlet

it the boundary layer thickness — so does the Strouhal number, as it should be computed with the boundary layer thickness added to the blade thickness.

Whatever the physical origin of the spectral peaks can be, reduction means considered in the following sections will have an action, provided that their origin is around the edge at which modifications are applied.

1.3.2.10 Analysis of possible resonances

Some of the peaks which appear regardless of the rotating speed are likely due to acoustic resonances, only depending on the geometry. To check if they are generated by standing waves in the impeller, parallel or quasi-parallel faces are considered in this section, as annotated in Figure 1.23. Parallel faces can be defined between the front and back plates, the back plate and the motor, and between the front plate and the wall. Other distances correspond to quasi-parallel faces. For the channel between two blades, the minimum distance (leading edge-trailing edge) and the maximum (leading edge-leading edge) are considered.

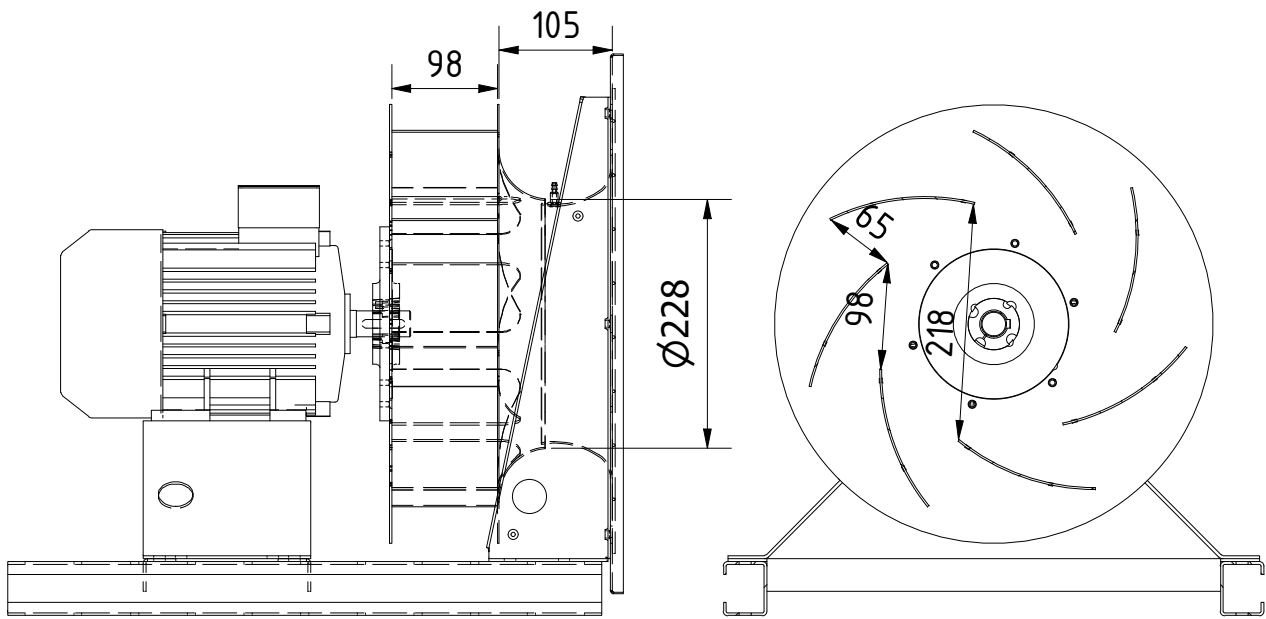


Figure 1.23 – Dimensions considered for the assessment of standing waves

At a resonance, if any, half the wavelength of the standing wave should be equal to the corresponding dimension. Table 1.7 shows the expected wavelengths and frequencies.

The computed frequencies are then compared with the peaks. As displayed in Figure 1.24, some peaks appear relatively close to the potential frequencies. Given the uncertainty of the method used in this section, some of the peaks are compatible with acoustic resonances. However, if this is the case, the observed peaks are unlikely to be due to one-dimensional standing waves. Instead, they could correspond to three-dimensional volume resonances, which is hard to verify in the present configuration. Furthermore, they could also be originated by vibrations.

Dimension	Length [mm]	Wavelength [m]	Frequency [Hz]
Nozzle diameter	228	0.456	746
Opposite blades	218	0.436	780
Front plate-wall	105	0.21	1619
Span	98	0.196	1735
Blade channel (LE-LE)	97	0.194	1753
Blade channel (LE-TE)	65	0.13	2615
Back plate-motor	65	0.13	2615

Table 1.7 – Possible standing waves: dimensions and expected wavelength and frequency

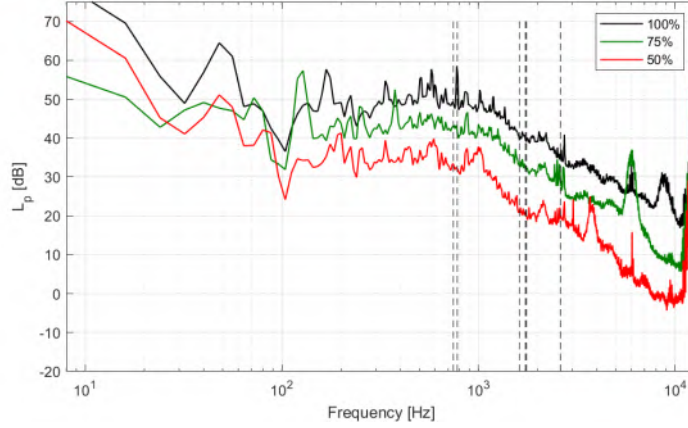


Figure 1.24 – Sound pressure level and potential resonances for $\bar{\delta} = 0.2$ at outlet $\Delta f = 8$ Hz

1.4 Leading-edge serrations

1.4.1 Serration design

This section addresses the aerodynamic and acoustic effect of leading-edge serrations on the blades of the impeller. The design is based on a sinusoidal shape, defined by two of the three following parameters: wavelength λ , amplitude $2h$ and angle θ . The geometry and parameters are shown in Figure 1.25.

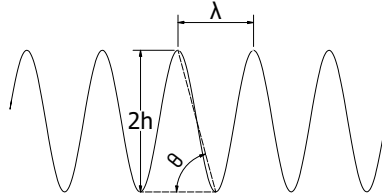


Figure 1.25 – Serrations parameters

To calculate the optimum serration angle θ_O , the model proposed by Chaitanya et al is used [18]. It is defined as a function of the turbulence integral length scale of the incident flow, L_t :

$$\theta_O = \tan^{-1}\left(\frac{2h}{L_t}\right) \quad (1.16)$$

The integral turbulence length scale is a parameter which represents the size of the biggest eddies in the flow. It is defined as [29]:

$$L_t = \int_0^{\infty} f(r) dr \quad (1.17)$$

where f is the longitudinal velocity correlation function of two points a distance r apart.

The turbulence integral length scale has been estimated from CFD simulations by using Equation 3.1, as described in Section 3.5.1. The average value is $L_t = 7.8mm$ for the best efficiency point (BEP), from which we can deduce an optimum wavelength $\lambda_O = 15.8mm \approx 16mm$.

There is no optimum criterion for the serration amplitude. However, empirical results usually show that the bigger it is, the better, as long as a compromise with the aerodynamic performance is kept [78, 18]. A value of $1/6$ of the chord has been taken, for it is similar to other values available in the bibliography [78, 12]. In our case, $2h = 1/6 C = 22\text{mm}$. The original blades of the plenum fan have been modified with leading-edge serrations as defined above. To perform a study on the influence of the serration geometry, in terms of $2h$ and λ , two other prototypes have been designed. In the first one, λ has been doubled while keeping the same $2h$. In the second one, $2h$ is twice as big while maintaining the same λ . The parameters for the three impellers are summarized in Table 1.8. The ratio $\lambda/2h$ has been added because it is commonly used to describe the sharpness of the serrations.

Table 1.8 – Parameters for impellers with leading-edge serrations

Designation	λ [mm]	h [mm]	$\lambda/2h$
LE_L8H11	8	11	0.36
LE_L16H11	16	11	0.73
LE_L16H22	16	22	0.36

The manufacturing of the prototypes, carried out by the company Ziehl-Abegg SE, was similar to that of the baseline fan. The only modification is the removal of material to carve the serrations on the blade. This has been done with a laser cutting tool, which slightly reduces the blade surface area, and thus may have an impact on the blade lift and therefore on the fan curve. This potential degradation of the fan performance will be taken into account in the comparison of the acoustic results of the different blade geometries by using the specific noise level. With this convention, any reduction of the specific noise level corresponds to a beneficial effect of the serrations. Figure 1.26 shows the three impeller prototypes. Appendix A shows drawings of each serrated blade.



Figure 1.26 – Impeller prototypes with leading-edge serrations

1.4.2 Aerodynamic results

The fan aerodynamic curves for the baseline impeller and the prototypes are shown in Figure 1.27a, where the fan total pressure p_f is plotted against the airflow q_v . For all the serration configurations there is a pressure decrease with respect to the baseline impeller at low flowrate, and a moderate pressure increase at high flowrate. In terms of fan pressure, the LE_L16H11 impeller is the best, followed by LE_L8H11 and LE_L16H22. The same hierarchy (Figure 1.27b) is observed for the overall efficiency.

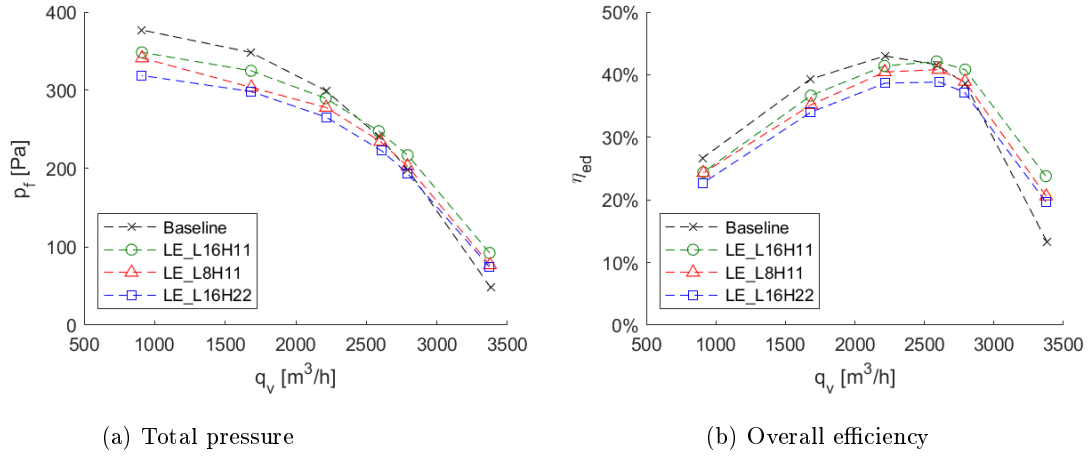


Figure 1.27 – Fan curves, $N=1440$ rpm

Figure 1.28 illustrates that the curves follow the same trend for the speed 720 rpm in terms of pressure and efficiency drop.

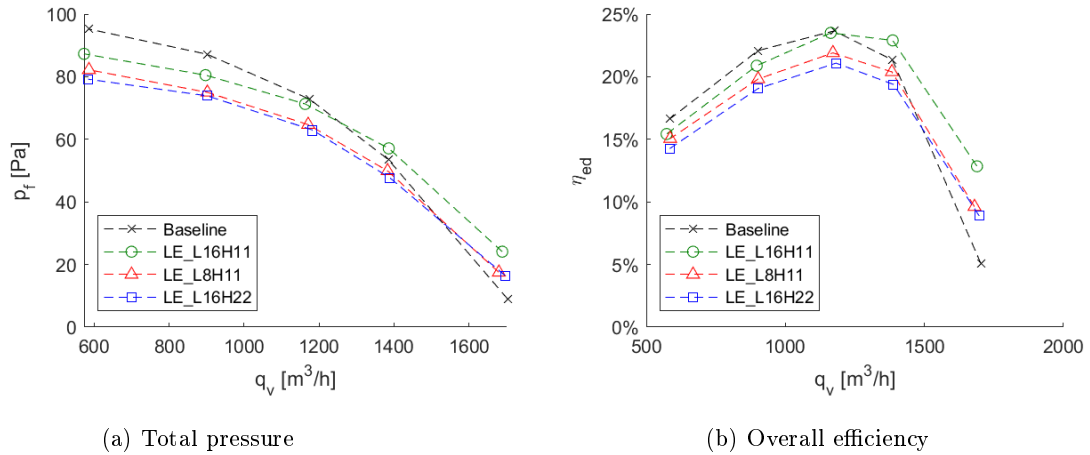


Figure 1.28 – Fan curves, $N=720$ rpm

The pressure drop induced by leading-edge serrations at low flowrate could be explained by the reduction on the blade surface. The slight pressure increase at high flowrate could be due to the generation of streamwise vortices in the serrations. This was proposed by Zenger *et al.* [113] for an axial fan. For a plenum fan, the vortices could reduce flow separation around the blade.

1.4.3 Acoustic results

1.4.3.1 1440 rpm

Due to changes in the experimental setup, measurements were noisier than results presented in section 1.3. In particular, many peaks are probably due to vibroacoustic phenomena, which can be noted in Figure 1.29 at the BEP. The BPF and its harmonics have been identified in the figure. The impact of the setup on the results is described in Annex B. The baseline impeller was retested to do a fair comparison with the prototypes. As we are only interested in characterizing the broadband noise, most of these peaks have been removed with a one-dimensional median filter, of order 14. Then, the biggest peaks which have not been treated by the filter have been trimmed manually. The peaks cannot be easily removed from the sound power levels, and thus from now on only sound pressure levels will be discussed. Anyhow, the sound pressure level measurements are the result of an average inside a reverberant room, so they are equivalent to the sound power as all directivity is lost. It should be taken into account that this is a spatial average in the corresponding reverberant room (big room for the inlet and pressure chamber for the outlet) and therefore any directivity effect is discarded.

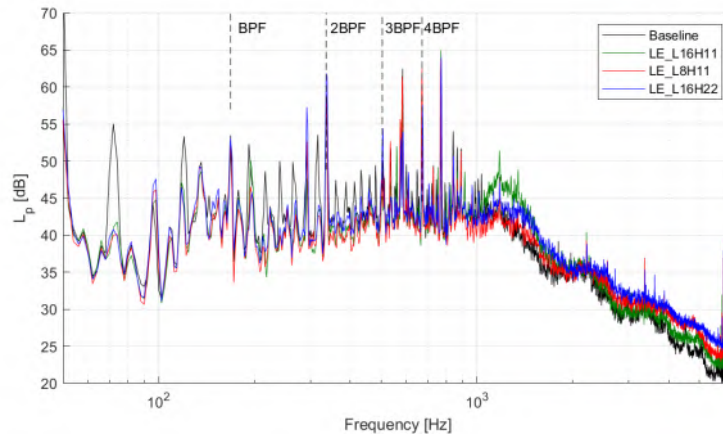


Figure 1.29 – Typical averaged narrowband sound pressure spectra at outlet for $q_v = 2200 \text{ m}^3/\text{h}$, $N=1440\text{rpm}$, $\Delta f = 2 \text{ Hz}$

The outcome of the filtering process is shown in Figure 1.30. Leading-edge serrations are found to reduce broadband noise at low and mid frequencies, under around 1000 Hz. However, at high frequencies, the serrated impellers are louder than the baseline.

To account for the difference in fan pressure due to serrations, the specific noise formula (Equation 1.3) must be used. The result for the best efficiency point ($q_v = 2196 \text{ m}^3/\text{h}$) is shown in Figure 1.31. It is similar to Figure 1.30, with the spectra corresponding to the serrated impellers being slightly shifted.

A more straightforward way to assess the impact of leading-edge serrations is to calculate the specific sound pressure reduction level $\Delta L_{p,spec}$. This is done by subtracting the spectrum of the

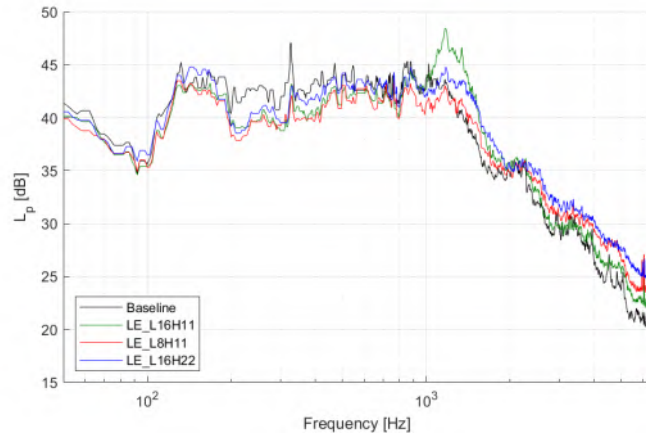


Figure 1.30 – Filtered narrowband sound pressure spectra at outlet for the BEP $q_v = 2200 \text{ m}^3/h$, $N=1440\text{rpm}$, $\Delta f = 2 \text{ Hz}$

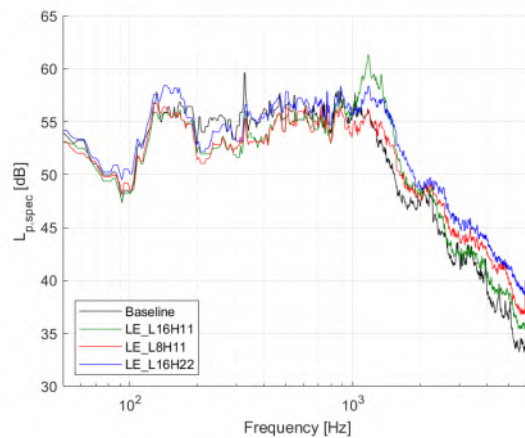


Figure 1.31 – Specific narrowband sound pressure spectra at outlet for the BEP, $q_v = 2200 \text{ m}^3/h$, $N=1440\text{rpm}$, $\Delta f = 2 \text{ Hz}$

baseline case from the spectra of the serrated configurations:

$$\Delta L_{p,spec} = L_{p,spec \text{ serrated impeller}} - L_{p,spec \text{ baseline}}$$

The result is plotted in Figure 1.32, with scattering removed and smoothed with the use of $1/12^{th}$ octave bands. At low frequencies (roughly under 1000 Hz), leading-edge serrations achieved some reduction of around 2-3 dB. However, noise is increased at high frequencies, between 2 and 4 dB depending on the impeller, which negates the gains at lower frequencies. This tendency has been observed for the rest of operating points, for both inlet and outlet. The results have to be considered at the light of A-weighted sound levels: around 1kHz and beyond, there is no modification in terms of dBA, whereas at lower frequencies, human hearing is less sensitive. This means that the benefit at low frequencies is even more crucially affected by the increase at high frequencies.

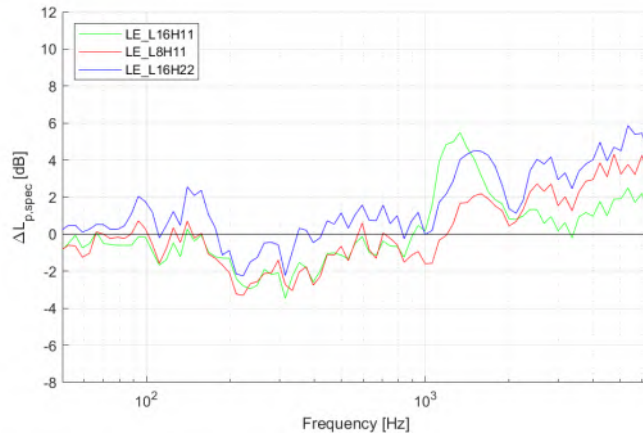


Figure 1.32 – Filtered sound pressure reduction level at outlet for the BEP $q_v = 2200 \text{ m}^3/h$, $N=1440\text{rpm}$

For a conventional assessment in an engineering context, and for each operating point, the narrow-band sound pressure levels are transformed to one-third octave levels, which are then A-weighted to obtain the overall A-weighted sound pressure levels between 100 Hz and 10 kHz. The frequencies under 100 Hz are not taken into account to remove low frequency vibrations and the peak from the power line at 50 Hz. The outcome, for both inlet and outlet levels as a function of the flowrate, is displayed in Figure 1.33. For the tested prototypes, leading-edge serrations only reduce noise at the point of maximum flowrate ($q_v = 3400 \text{ m}^3/h$). This is due to the increase in fan pressure with serrations at this operating point. The impeller LE_L16H11 also reduces noise for two other operating points ($q_v = 900 \text{ m}^3/h$ and $q_v = 1600 \text{ m}^3/h$). It is difficult to assess the impact of serration amplitude and wavelength on the noise reduction because the sound levels are very similar, regardless of the geometry. The impeller LE_16H22 is the least effective, but it is difficult to establish a hierarchy between LE_L16H11 and LE_L8H11.

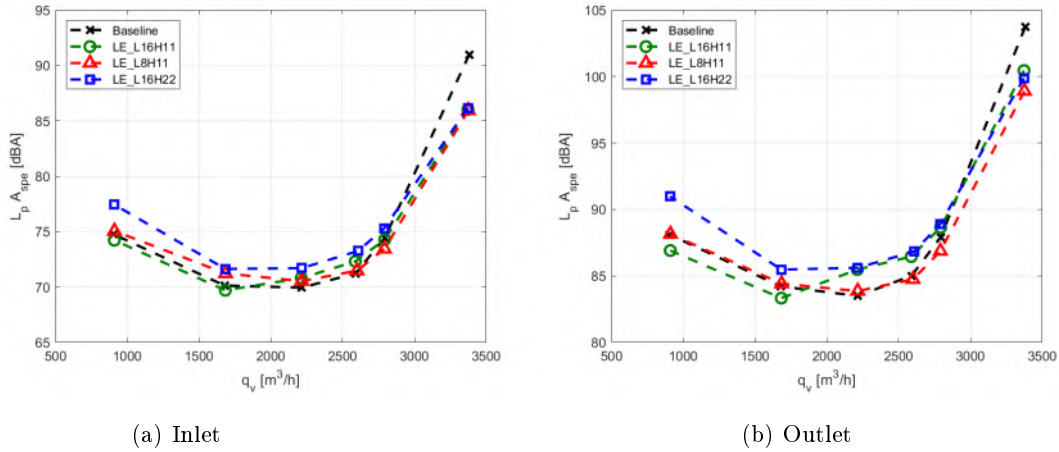


Figure 1.33 – Overall specific narrowband sound pressure spectra, $N=1440$ rpm

1.4.3.2 720 rpm

The overall sound pressure level at 50% of the nominal speed is displayed in Figure 1.34. The trend is somehow the same as for 1440 rpm: noise increase at most of the operating points and noise reduction at the point of maximum flowrate. A different feature is that noise is substantially reduced by the serrated impellers at the point of minimum flowrate ($q_v = 600 \text{ m}^3/h$), especially with LE_L16H22.

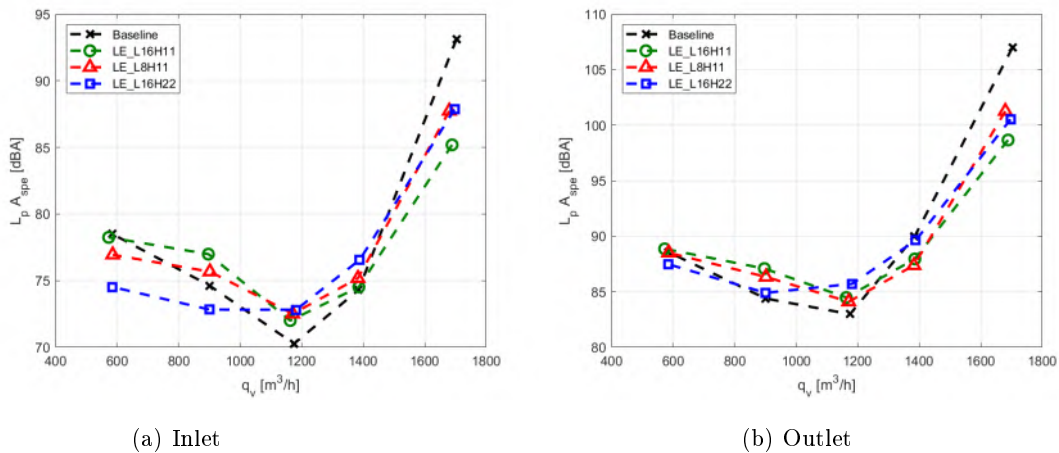


Figure 1.34 – Overall specific narrowband sound pressure spectra, $N=720$ rpm

To explain this particular effect, the specific noise pressure spectra at the minimum flowrate have been plotted in Figure 1.35. The difference is found to be due to the reduction of a peak around 5000 Hz. The maximum level of the peak for each impeller has been marked with a horizontal line which matches the colour of the spectrum. At this rotating speed, serrations do not reduce broadband noise: the prototypes either show the same broadband noise as the baseline (LE_L16H11) or higher noise (LE_L8H11 and LE_L16H22). Similar behaviour has also been observed for the operating point at $900 \text{ m}^3/h$.

The noise reduction spectra for the BEP are shown in Figure 1.36. Again, a 1/12th octave band

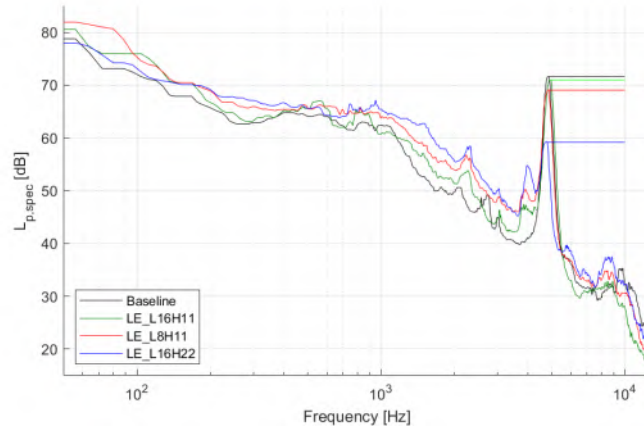


Figure 1.35 – Specific narrowband sound pressure spectra at outlet for the minimum flowrate operating point $q_v = 600 \text{ m}^3/h$, $N=720\text{rpm}$, $\Delta f = 2 \text{ Hz}$

representation has been used, for the sake of clarity. At low rotating speed, the serrated impellers are louder than the baseline for most of the frequency spectra, with the exception of the peak at 5 kHz, mainly for LE_L16H22.

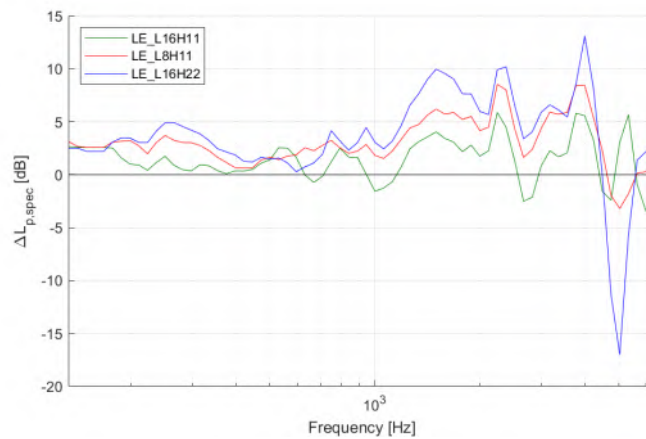


Figure 1.36 – Filtered sound pressure reduction level at outlet for the BEP $q_v = 600 \text{ m}^3/h$, $N=720\text{rpm}$

Given that leading-edge serrations were supposed to reduce turbulent impingement noise, the noise increase could come from a deterioration of the flow downstream of the edge (e.g. more disturbed and thicker boundary layers), inducing higher sources elsewhere.

1.4.4 Experiments with turbulence generator at inlet

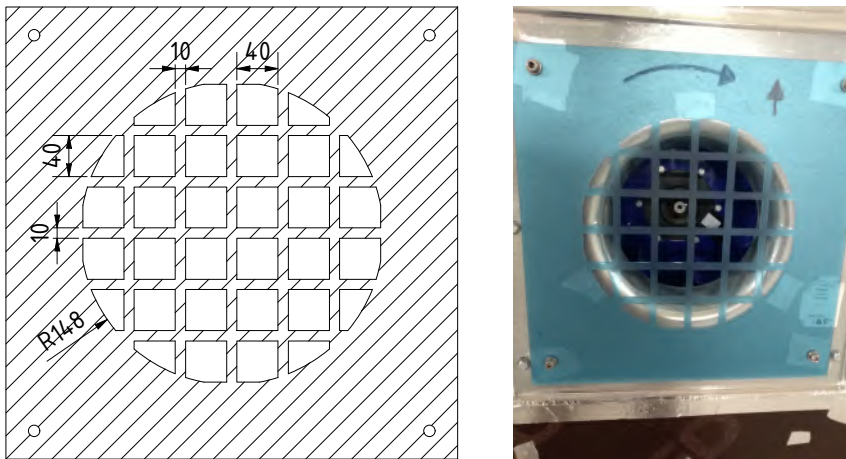
Leading-edge serrations have been tested up to now with an undisturbed inflow. The serrations were primarily aimed at reducing the turbulence impingement noise associated with upstream disturbances. In practical applications, upstream turbulence can be generated by obstacles, depending on fan installation details. This is why measurements have been repeated with an additional turbulence grid positioned at the inlet of the fan. The grid geometry was defined so it generates a turbulence

length scale tuned to the wavelength of our serrations, according to Equation 1.16. The value of 8 mm, used to design the serrations (see 1.4.1), has been used as a target for the grid. Empirical equation 1.18 predicts the turbulence downstream of a grid [86]:

$$\frac{L_t}{d} = I\left(\frac{x}{d}\right)^{1/2} \quad (1.18)$$

where I is an empirical constant (0.2 in the present case), d is the bar width of the grid and x is the distance downstream of the grid. This distance is defined between the grid and the midspan of the impeller (see Figure 2.9) and is equal to 154 mm. For our target turbulence length scale of 8 mm a bar width of 10 mm is required.

The bars were spaced of 50 mm, which implies a grid porosity of 36%. Figure 1.37a shows the grid and its main dimensions. The circular shape covers the inlet nozzle of the fan while keeping the stiffness of the sheet. The thickness of the grid is 3 mm and it has been made by laser cutting of a PMMA sheet. Figure 1.37b shows how the grid is installed directly on the inlet nozzle plate.



(a) Geometry and dimensions

(b) Installation at inlet

Figure 1.37 – Turbulence grid

The fan curves measured both with free inlet and grid, with a speed of 1440 rpm, are shown in Figure 1.38. A strong pressure drop is observed with the grid, due of course to its pressure loss. In terms of fan pressure p_f , the same hierarchy between the impellers is observed with grid, compared to the configuration with free inlet. However, there is no pressure increase induced by leading-edge serrations at maximum flowrate, so the beneficial effect of serrations on the pressure is deactivated by the grid. This suggests that the grid induces a fan system effect, in addition to a pressure drop.

Figure 1.39 illustrates that the curves follow the same trend for the speed 720 rpm.

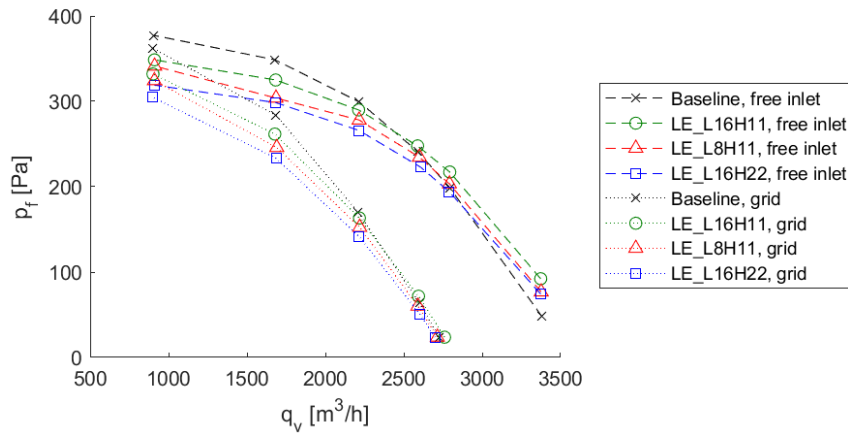


Figure 1.38 – Fan total pressure, $N=1440$ rpm

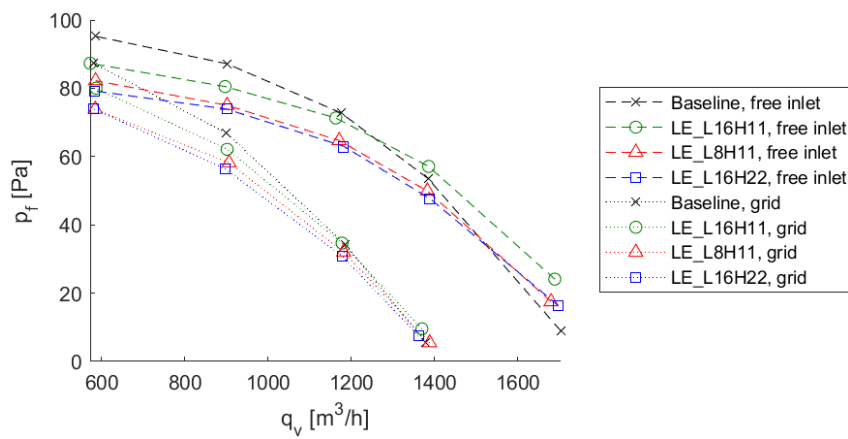


Figure 1.39 – Fan total pressure, $N=720$ rpm

The tests were carried out with a slightly different setup, which made that the peaks shown in Section 1.4.3 were not as prevalent. However, the impact of the setup on the measurements is limited and the changes on the results can be attributed to the turbulence generated by the grid. Figure 1.40a shows the comparison of the overall levels with and without the grid. With free inlet, there is a minimum on the noise level for the BEP, whereas with the grid the noise increases with the flowrate. This can be explained as follows: as the speed increases, so does the intensity of dipole sound - for fans it grows with the characteristic speed to the 5th power. This is verified in Figure 1.40b, where the noise is plotted versus the free-stream velocity to the power of 5: all curves describe roughly a straight line.

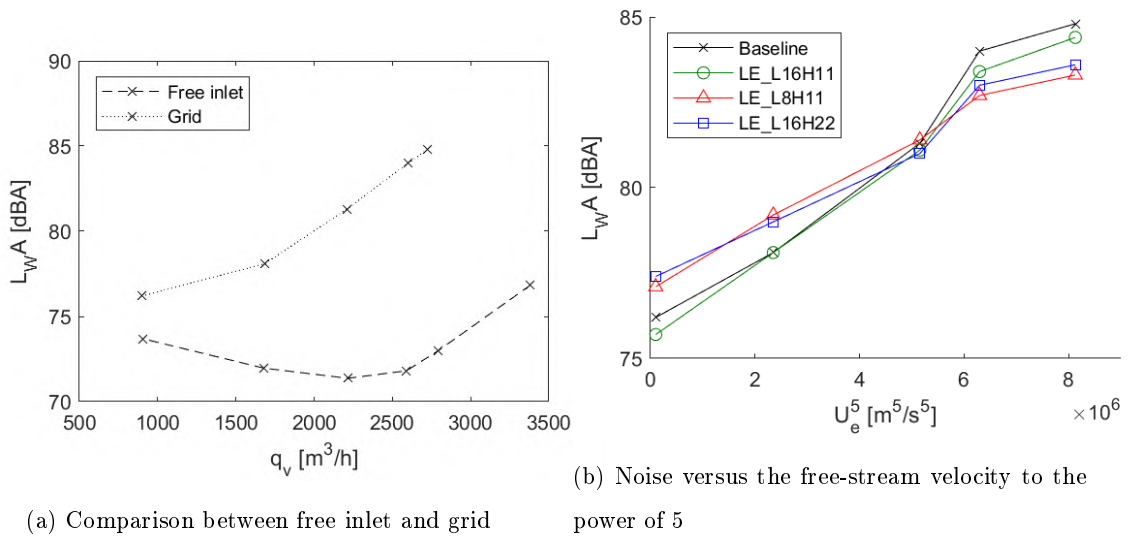


Figure 1.40 – Overall sound power level at outlet, $N=1440$ rpm

Figure 1.41 presents the overall sound power levels as a function of q_v . The grid at the inlet does not improve the noise reduction effectiveness of the prototypes. The grid is expected to generate suitable turbulence length scales, but the turbulent structures are likely to change as they enter the impeller. Furthermore, the flow changes its direction from axial at the inlet to radial at the outlet, which could also have an impact on the turbulence property.

The difference in overall levels between the baseline impeller and the serrated prototypes can be explained due to changes on the peaks and on the broadband levels at low and mid frequencies. The noise increase at high frequencies is only found at some operating points ($q_v = 900 m^3/h$ and $q_v = 1700 m^3/h$). The underlying mechanism seems to be affected by changes on the turbulence.

Figure 1.42 shows the sound pressure spectra for the BEP. All spectra almost collapse due to the noise increase induced by the grid. However, with the grid at inlet, there is still a slight noise increase with serrations at high frequencies. This is a general finding, for all the cases discussed in Section 1.4. This could be due to the generation of small-scale three-dimensional structures around the serrations

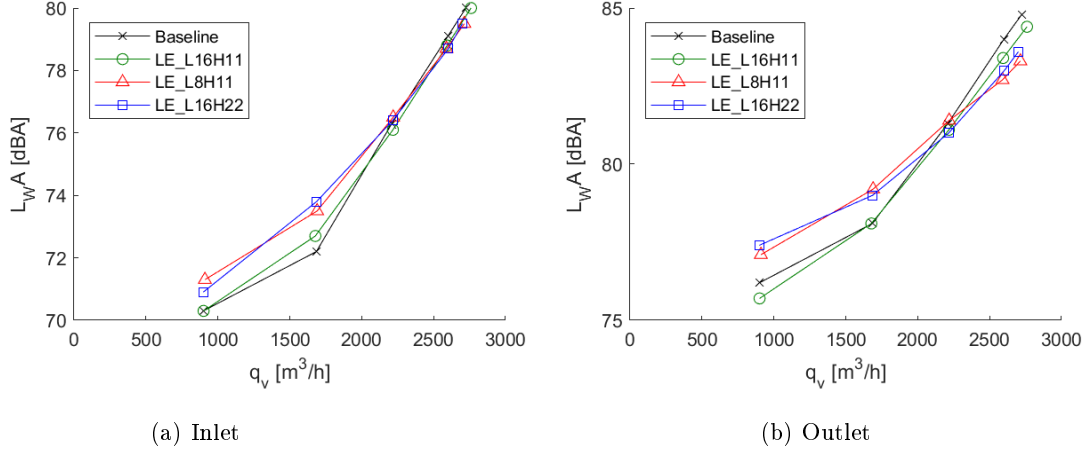


Figure 1.41 – Overall sound power level as a function of flowrate, $N=1440$ rpm

or to an indirect modification of trailing-edge noise.

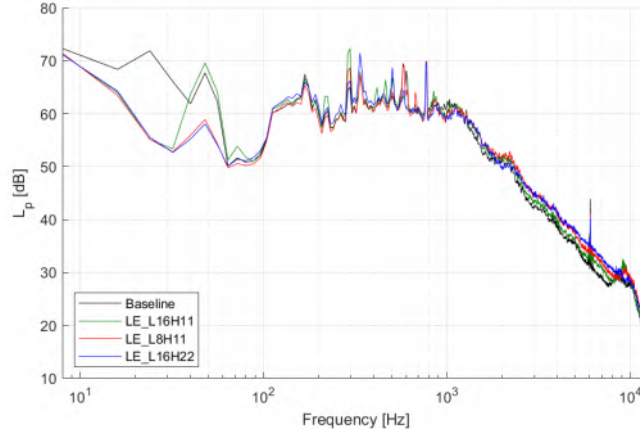


Figure 1.42 – Narrowband sound pressure spectra at outlet for the BEP $q_v = 2200$ m³/h, $N=1440$ rpm, $\Delta f = 8$ Hz

1.5 Trailing-edge serrations

1.5.1 Serration design

As for leading-edge serrations, the results of CFD simulations, described in Section 3.5.2, have been used to define the serration dimensions. In this case, the boundary layer thickness $\bar{\delta}$ is the significant parameter. Its value ranges from 1.7 to 8.7 mm along the spanwise location, for the suction side.

The design process relies on experimental results from Gruber [39], who made a parametric study with serrated insertions on the trailing edge of a NACA65(12)-10 airfoil. For the serration amplitude $2h$, [39] proposed that at least $h > 0.25\bar{\delta}$. The value of $h = 2\bar{\delta}$ used by Arce León *et al.* [5] has been taken as reference. In order for serrations to be narrow, h should be as big as possible, so the maximum value of $\bar{\delta}$ has been considered. It has been rounded to 8.5 mm, so $h = 2\bar{\delta} = 17$ mm.

For an efficient noise reduction, it was proposed in [39] that $\lambda < 2h$, and it was also suggested that a value of $\lambda < h/6.5$ should yield even better results. If this extreme criterion was applied in our case, it would yield a result of 2.6 mm, which is extremely small and will cause manufacturing issues. As a compromise between the dimension of λ and manufacturing feasibility, a value of $\lambda = 4\text{ mm}$ has been taken.

A third design criterion regarding the serration shape has been used. Ragni *et al.* [85] proposed that "iron-shaped" serrations can reduce by up to 2 dB with respect to conventional sawtooth serrations in the range $5 < Sc < 15$, where Sc is the Strouhal number based on the chord. This geometry has been taken into account for the serration design (see Figure 1.43). It is defined with a spline curve perpendicular to the baseline trailing edge at the root and tangent to the line which passes through the tip forming an angle ϖ with the streamwise direction. The angle ϖ is defined as:

$$\varpi = \tan^{-1} \left(\frac{\lambda/2}{h/2} \right)$$

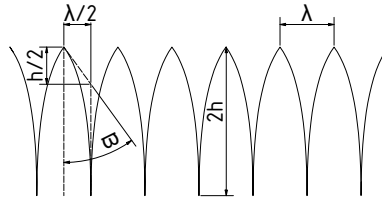


Figure 1.43 – Iron-shaped serrations

As it has been done for leading-edge serrations, two other impeller prototypes have been manufactured. This has allowed to assess the effect of each parameter, as one of them ($2h$ or λ) has been modified at a time. It is to be noted that, as the angle of the serrations valley is very narrow, the laser cutting tool used for manufacturing could not cut all the way through. Therefore, the effective amplitude h_e is shorter than the design amplitude h . The impellers designation, in Table 1.9, takes into account this effective amplitude.

Table 1.9 – Parameters for impellers with trailing-edge serrations

Designation	λ [mm]	h [mm]	h_e	$\lambda/2h_e$
TE_L4H12	4	17	12	0.17
TE_L8H12	8	17	12	0.33
TE_L8H8	8	11	8	0.5

Figure 1.44 shows the three prototypes. Drawings of the final geometry of each blade, as built, can be seen in Appendix A.



Figure 1.44 – Impeller prototypes with trailing-edge serrations

Figure 1.45 shows a view of an impeller with trailing-edge serrations when installed with the inlet cone and motor.

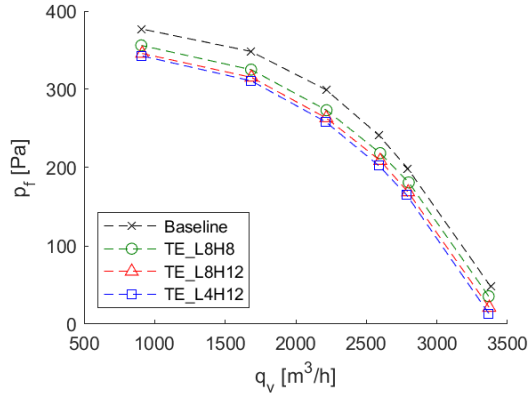


Figure 1.45 – Impeller with trailing-edge serrations mounted on the shaft

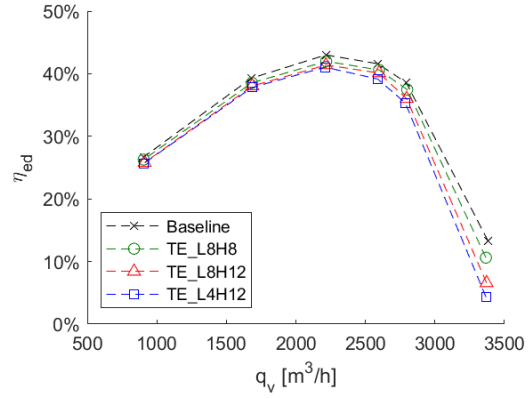
1.5.2 Aerodynamic results

The fan total pressure curves for the baseline impeller and the prototypes are shown in Figure 1.46a. In this case, there is a pressure drop for all the serrated configurations, with no pressure increase whatsoever. A similar effect is found for the overall efficiency, depicted in Figure 1.46b.

The pressure curve at 50% of the nominal speed is shown in Figure 1.47a. The overall efficiency is depicted in Figure 1.47b. In both cases, the same tendency as for the nominal speed has been observed.

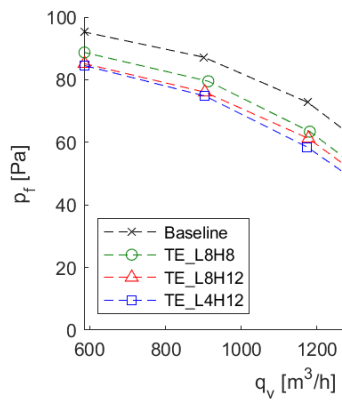


(a) Total pressure

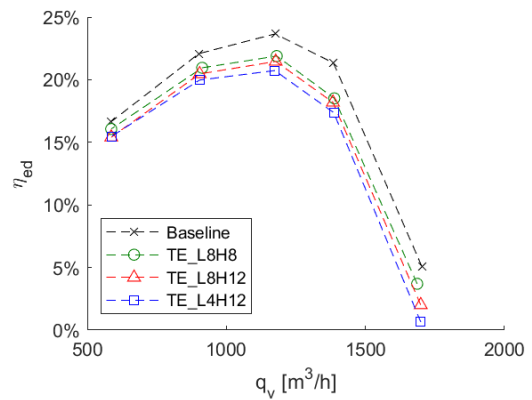


(b) Overall efficiency

Figure 1.46 – Fan curves for impellers with trailing-edge serrations, $N=1440$ rpm



(a) Total pressure



(b) Overall efficiency

Figure 1.47 – Fan curves for impellers with trailing-edge serrations, $N=720$ rpm

1.5.3 Acoustic results

The overall specific sound pressure levels, presented in Figure 1.48, provide an overview of the acoustic footprint of each impeller. The same filtering algorithm used on the leading-edge serrations raw data has been applied, and then the spectra are integrated and A-weighted. A noise reduction of up to 2 dBA is measured at some operating points, the impeller TE_L8H12 being slightly more effective. For the tested configurations, the impact on the noise reduction of changes in the serration geometry is small: in other words, noise reduction does not seem to be very sensitive to changes in the serration geometry. The specific noise is increased at higher flowrates for the TE_L8H12 and TE_L4H12 configurations, but this is only due to the fan pressure drop.

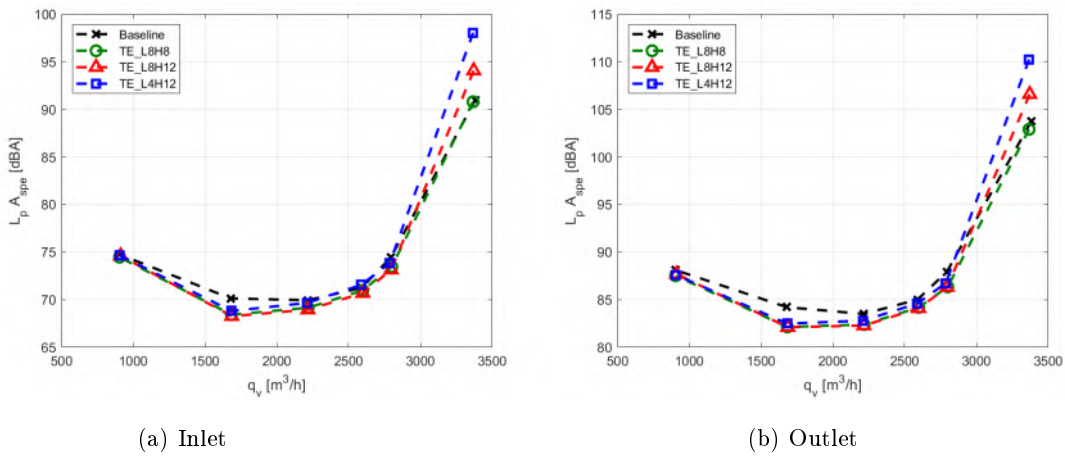


Figure 1.48 – Overall specific narrowband sound pressure spectra, $N=1440$ rpm

The specific sound pressure spectra at the best efficiency point ($q_v = 2200 m^3/h$) are shown in Figure 1.49. The noise reduction is broadband and more important for low and mid frequencies, but this is better described in the noise reduction plot (Figure 1.50).

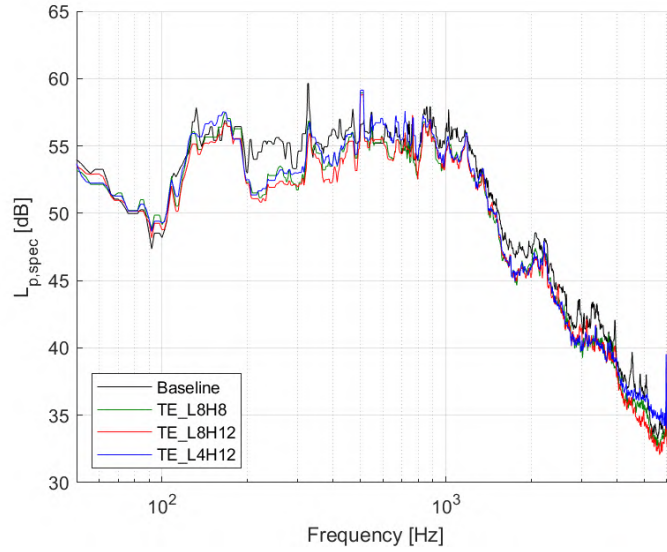


Figure 1.49 – Specific narrowband sound pressure spectra at outlet for the best efficiency point, $\Delta_f = 2Hz$, $N=1440$ rpm, $q_v = 2200 m^3/h$

The noise reduction at the BEP is shown in Figure 1.50, again the scattering smoothed with the use of $1/12^{th}$ octave bands. The noise reduction is broadband, with some fluctuations due to peaks which have not been removed by the filtering algorithm. The reduction ranges between 4 dB and -1 dB (noise increase), with an average value of around 2 dB.

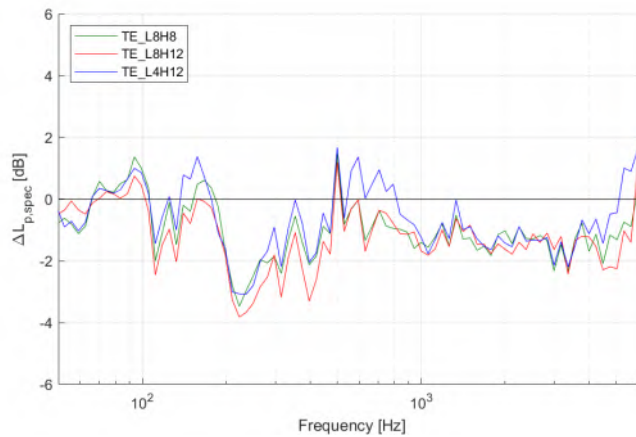


Figure 1.50 – Filtered sound pressure reduction level at outlet for the BEP $q_v = 2200 m^3/h$, $N=1440$ rpm

From Figure 1.48, it seems that impellers TE_L8H12 and TE_L4H12 increase noise with respect to the baseline at $3400 m^3/h$. However, this result is due to the relative difference between the total pressure at this particular operating point ($p_f = 48$ Pa for the baseline, $p_f = 36$ Pa for TE_L8H8, $p_f = 21$ Pa for TE_L8H812 and $p_f = 14$ Pa for TE_L4H12). If we plot the narrowband filtered noise instead of the specific noise at $q_v = 3400 m^3/h$ (Figure 1.51), all serrated prototypes generate less noise than the baseline.

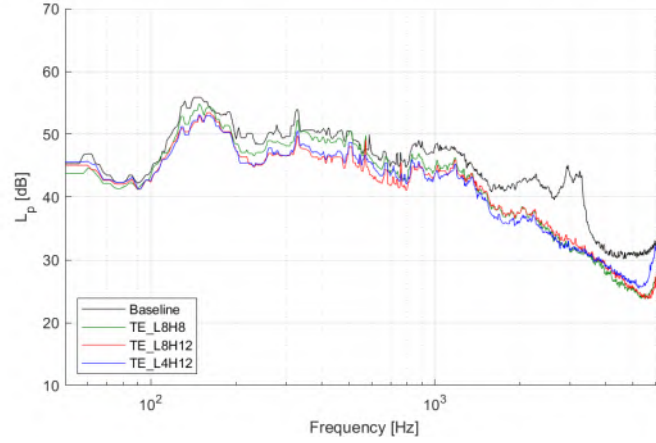


Figure 1.51 – Specific narrowband sound pressure spectra at outlet for $q_v = 3400 \text{ m}^3/\text{h}$, $\Delta_f = 2 \text{ Hz}$, $N=1440$ rpm

An interesting result is observed at 50% of the nominal rotating speed (720 rpm), as shown in Figure 1.52. At the operating points on the left of the BEP, a considerable noise reduction is observed. This can be explained by looking at the spectra at $q_v = 585 \text{ m}^3/\text{h}$, displayed in Figure 1.53. The spectrum of the baseline impeller shows a peak with a considerable emergence around 5000 Hz. As shown in Figures 1.16 and 1.22, this peak also appears at 1080 rpm and 1440 rpm and is proportional to the frequency. Serrations highly reduce its amplitude (TE_L8H8) or practically cancel it (TE_L8H12 and TE_L4H12). A similar effect has already been observed with the leading-edge serrations (Figure 1.35), but with less impact on the peak. As described in Section 1.3.2.7, the peak seems to scale with the air velocity to the power 1.5.

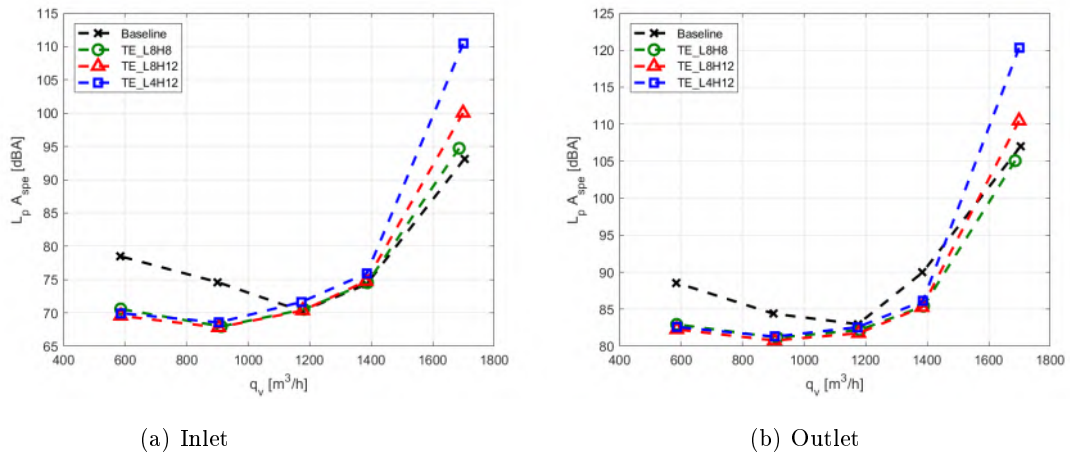


Figure 1.52 – Overall specific narrowband sound pressure spectra, $N=720$ rpm

Laminar boundary layer vortex-shedding is suspected *priori*, but von Kármán vortex shedding could also be present. When generated from trailing-edge bluntness it would correspond to equation 1.14. But this holds only for purely homothetic flows, which would need to be verified in the present

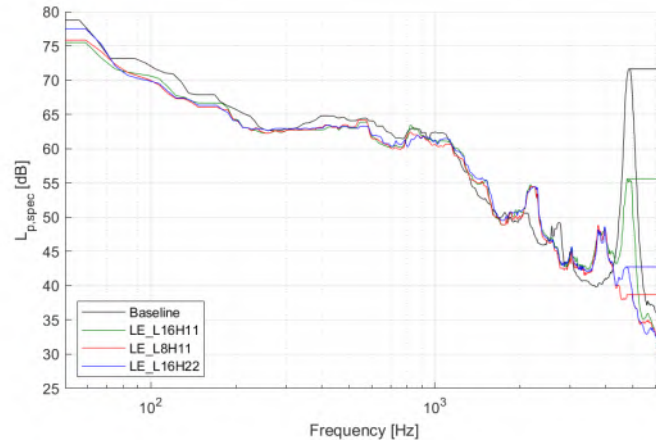
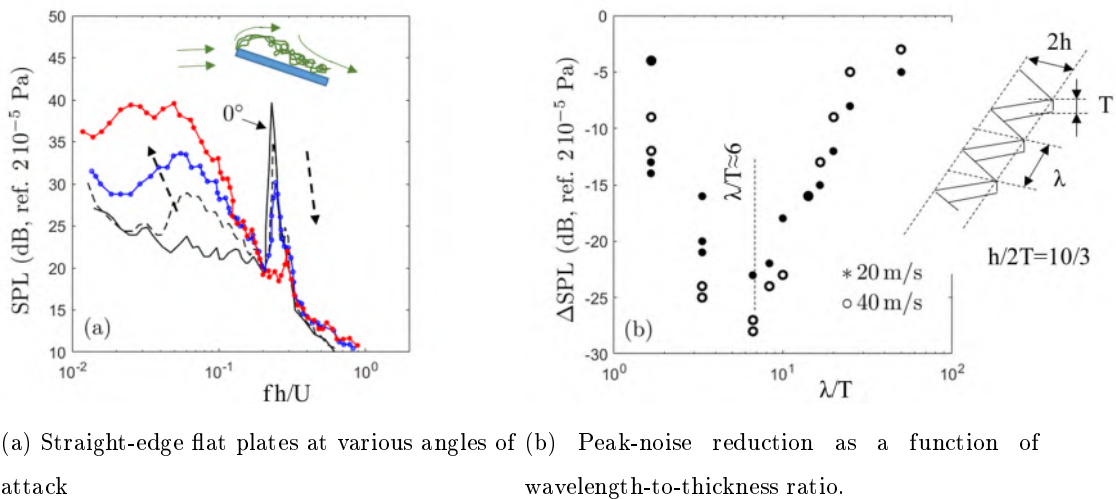


Figure 1.53 – Specific narrowband sound pressure spectra at outlet for $q_v = 585 \text{ m}^3/h$, $\Delta_f = 2 \text{ Hz}$, $N=720 \text{ rpm}$

case. Serrations are known to reduce both mechanisms. This has been reported for instance by Burgain [15], from the observation of flat plates tested in an open-jet anechoic facility. Key results are shown in Figure 1.54, produced from the reference.



(a) Straight-edge flat plates at various angles of attack (b) Peak-noise reduction as a function of wavelength-to-thickness ratio.

Figure 1.54 – Flat-plate sound spectra and vortex-shedding sound reduction by trailing-edge serrations, adapted from [15]

Figure 1.54a first displays far-field sound spectra measured normal to the flow direction in the mid-span plane at various angles of attack. The plates have a 10 cm chord and a 3 mm thickness. At zero angle of attack, boundary-layers are quite thin and the vortex shedding is highly coherent. The spectrum includes a peak of high-amplitude and low-level broadband noise (trailing-edge noise). As the angle of attack is increased, the growing separation bubble formed at the leading edge triggers reattached turbulent flow of higher intensity and thicker boundary layers on the suction side. The broadband noise is increased at lower frequencies, with a progressive decrease of the vortex-shedding peak. This suggests that, depending on the loading conditions of a blade with a blunted trailing edge, the vortex-shedding sound can be heard or not.

The second set of results, in Figure 1.54b, refers to versions of the same flat plate at zero angle of attack which differ by the shape of trailing-edge serrations. The plotted quantity is the reduction of vortex-shedding sound level achieved by the serrations, as a function of the parameter λ/T for a fixed value $2h/T$, where $2h$ and λ are the length and wavelength of the serrations, and T the plate thickness. The most efficient reduction of about 25 dB is achieved as λ is 6 times the thickness, which also corresponds to a typical spanwise correlation length of the vortex shedding.

To compare our results with [15], we need to calculate the ratio λ/T . This is 4 for TE_L8H12 and TE_L8H8 and 2 for TE_L4H12. According to Figure 1.54b we would expect a bigger peak reduction with the ratio $\lambda/T = 4$. However, according to Figure 1.53, the highest peak mitigation is achieved with TE_L8H12 and TE_L4H12, which have a ratio of 4 and 2 respectively. It seems that a ratio of 4 is slightly better, but this is contradicted by TE_L8H8, which has a ratio of 4 and a much lower impact on the peak than TE_L4H12. This could be explained by a dependence of the peak size not only on the ratio λ/T but also on the ratio $\lambda/2h$.

1.6 Conclusion

A design process for leading-edge and trailing-edge serrations for a plenum fan has been carried out aimed at reducing the noise. Six impeller prototypes with serrations were manufactured and tested to investigate their aerodynamic and acoustic performances. For both solutions, a noticeable degradation of the aerodynamic performance has been measured, which is expected from the reduced area of the blades.

The fan of the study is well-optimized in terms of acoustic performance. This has allowed us to test the serrations on a realistic and challenging industrial platform. Regarding the noise spectra, different potential noise sources have been identified: BPF (or subharmonics for the minimum flow), resonances, laminar-boundary-layer-vortex-shedding, vortex-shedding and rotation-related peaks at high frequencies.

Leading-edge serrations tend to reduce noise below 1000 Hz but can increase the noise at higher frequencies, depending on the operating point. The impact on the overall sound level is rather limited and serrations actually increase the overall noise if we take into account the aerodynamic degradation. All the impeller prototypes have been designed to yield substantial noise reductions. The discrepancies between the measured and expected values could be due to the uncertainty of the simulations, the inaccuracy of the turbulence estimation and averaging or the fact that the inlet flow of a 2D airfoil is not the same than that of the blade of a centrifugal fan. The latter is done over a rectangular spanwise area, whereas using the maximum value of the turbulence length scale instead could be a better serration design strategy. Installing a grid at the inlet which is tuned to the serration dimensions did not improve noise reduction. This could be due to the change in the direction of the flow as it goes through the impeller, which is expected to have an impact on the turbulent structures which are sucked in by the fan.

Trailing-edge serrations reduce noise for all frequencies at some operating points, with a maximum decrease of about 1-2 dBA at nominal speed. For low flow rates and low rotating speed, a substantial noise reduction of up to 8 dBA is observed due to the mitigation or even cancellation of a high-frequency peak. This peak is generated by a source near the trailing edge. The most likely hypothesis points towards laminar boundary-layer vortex shedding, but this yet needs to be confirmed. The ratios $\lambda/2h$ and λ/T could both have an influence on the magnitude of the peak reduction.

Chapter 2

Analytical modelling of the broadband noise of the baseline fan

As shown in Chapter 2, serrations on the leading and the trailing edge of the fan blades reduce broadband noise under certain conditions. This suggests that leading-edge noise and trailing-edge noise could be significant noise sources of this fan. An analytical approach would allow us to assess these contributions. In the current chapter, Amiet’s analytical models will be adapted to our geometry and operating conditions. They were developed to predict the noise generated by an airfoil inside a wind-tunnel [1, 3]. The trailing-edge noise model was later completed with a leading-edge back-scattering correction [88]. It has also been adapted to rotating blades, such as helicopter rotors [101] or low-speed fans [90, 103]. In [98], Amiet’s model was adapted to a centrifugal fan with volute, but the application to a plenum fan was still missing.

Amiet’s models make the assumption of a flat plate with zero thickness and camber within uniform mean flow. This is reasonable for fans and compressors, which typically feature relatively low turbulence rates, small relative thickness and moderate cambers ([89]). In our case, they will be implemented with the application of the strip theory to account for the spanwise flow variability. Finally, it will also be required to add extra analytical and empirical models to account for the turbulence and boundary layer input data.

2.1 Amiet’s far-field models

Leading-edge noise is generated by the impingement of upstream turbulence, whereas trailing-edge noise is produced by the boundary-layer eddies interacting with the trailing edge. In both cases there is a change of the boundary conditions on a convected vortical field and thus they can be solved mathematically in a similar way. The objective is to obtain the fluctuating flow velocity for

the prediction of the leading-edge noise and THE wall-pressure fluctuations for the prediction of the trailing-edge noise. The following steps are needed [89]:

1. Expand the fluctuating quantities in Fourier components (gusts) of spanwise wavenumber k_2 , the chordwise/streamwise wavenumber being fixed by Taylor's hypothesis of frozen incident turbulence
2. Apply an iterative technique to calculate the pressure jump along the airfoil, assimilated to a rigid, zero-thickness flat plate. This is required to account for the finiteness of the chord.
 - (a) Apply Schwarzschild's technique, which assumes a semi-infinite plate in the opposite direction of the edge of interest. The formulation of the problem is adapted to obtain the canonical solution:
 - i. Each gust is solution of a modified 2D Helmholtz equation. Reduce the convected Helmholtz operator to a stationary one by a suited change of variables
 - ii. Transpose the solution to original variables by applying inverse transformations
 - (b) Apply a second-order correction by assuming a semi-infinite plate in the direction of the opposite edge. It has been shown that these two iterations are enough [4].
 - (c) Calculate the acoustic far-field through a radiation integral, according to Ffowcs Williams-Hawkings analogy [35]
3. Sum all gusts contributions and take an ensemble average.

This technique is common to the trailing-edge and leading-edge problems. However, they have to be solved separately because the scales are very different. Indeed, leading-edge noise is most often associated with larger scales (and therefore lower frequencies), whereas trailing-edge noise is generated by the smaller scales formed within the boundary layer (and thus higher frequencies). Both sources are not correlated, so they may be modeled separately and the outcomes of the models combined.

Amiet's observer coordinate system for a flat plate is presented in Figures 2.1 and 2.2. Changing from trailing-edge to leading-edge noise simply shifts the reference frame from one edge to the other. In fact, because the formulation is based on a geometrical far-field assumption, the origin of the reference frame can be put at the LE, at the TE or at the mid-chord, without any effect. The problem is solved for skewed gusts, defined by their streamwise (k_1) and spanwise (k_2) wavenumbers.

2.1.1 Trailing-edge noise

Amiet's original model [3] has been adapted by Roger and Moreau ([88, 76]) and extended to account for all effects of a finite chord and to allow the estimation of radiation off the mid-span plane. This was validated experimentally on a flat-plate based airfoil by Bampanis and Roger [11].

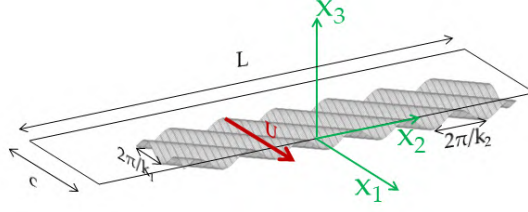


Figure 2.1 – Flat plate reference frame for the trailing-edge problem, and main notations. Gust featured by the undulated surface

The fundamental expression of the far-field acoustic PSD, with coordinates and aerodynamic wavenumbers defined in Figure 2.1.1, is:

$$S_{pp} = \left(\frac{kcx_3}{4\pi S_0^2} \right)^2 2c \int_{-\infty}^{\infty} \Pi_0 \left(\frac{\omega}{U_c}, k_2 \right) \frac{\sin^2 \left[\frac{L}{c} \left(k_2^* - \bar{k} \frac{x_2}{S_0} \right) \right]}{\left(k_2^* - \bar{k} \frac{x_2}{S_0} \right)^2} \left| \mathcal{I} \left(\frac{\bar{\omega}}{U_c}, k_2^* \right) \right|^2 dk_2^* \quad (2.1)$$

The formula involves the wall-pressure wavenumber spectral density, as estimated closely upstream of the trailing edge, used as input data and given by:

$$\Pi_0 \left(\frac{\omega}{U_c}, k \frac{x_2}{S_0} \right) = \frac{1}{\pi} \phi_{pp}(\omega) l_y(k_2^*, \omega) \quad (2.2)$$

where $\phi_{pp}(\omega)$ is the wall-pressure PSD induced by the incident turbulence and $l_y(k_2^*, \omega)$ is the associated correlation length. The model assumes that the wall-pressure statistics is homogeneous, especially in the spanwise direction.

The following wavenumbers, dimensional and dimensionless, are used:

$$k = \frac{\omega}{c_0} \quad \bar{k} = \frac{kc}{2} \quad k_1 = \frac{\omega}{U} \quad \bar{K}_1 = \frac{\omega c}{2U_c} = K_1 \frac{c}{2} \quad k_1^* = \frac{k_1 c}{2} \quad k_2^* = \frac{k_2 c}{2}$$

and k_2^* takes any possible value ($-\infty < k_2^* < \infty$), as the gusts can take any given skew angle. S_0 is the corrected distance for the convection effect (see definition in Appendix C.1) and U_c is the convection velocity.

For large aspect ratios (L/c), k_2^* becomes $k_2^* = \bar{k} \frac{x_2}{S_0}$ and Equation 2.1 can be reasonably simplified as:

$$S_{pp} = \left(\frac{kcx_3}{4\pi S_0^2} \right)^2 2\pi L \left| \mathcal{I} \left(\frac{\bar{\omega}}{U_c}, \bar{k} \frac{x_2}{S_0} \right) \right|^2 \Pi_0 \left(\frac{\omega}{U_c}, k \frac{x_2}{S_0} \right) \quad (2.3)$$

Depending on the angle, a gust can be supercritical or subcritical. When the angle is small and the gust wavefronts are nearly parallel to the edge, they are supercritical and generate radiating waves. Bigger angles yield subcritical gusts, which produce evanescent waves and are inefficient noise sources. Graham's parameter allows us to differentiate between both types of gusts $\Theta_0 = k_1^* M / (\beta k_2^*)$: when it takes values smaller than 1 they are supercritical, being subcritical otherwise. The simplified

Equation 2.3 is only considering the particular wavenumber $k_2^* = k x_2/S_0$, which always corresponds to a supercritical gust.

The tridimensional radiation integral \mathcal{I} is given by $\mathcal{I} = \mathcal{I}_1 + \mathcal{I}_2$. Its expression can be found in Appendix C.1.

2.1.2 Leading-edge noise

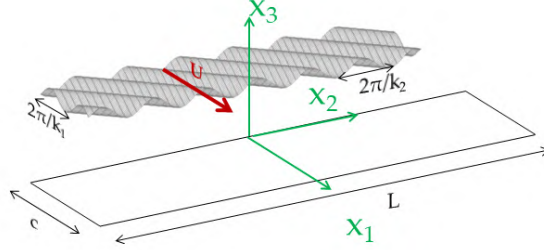


Figure 2.2 – Flat plate reference frame for leading-edge problem, and main notations. Velocity gust featured by the undulated surface

Leading-edge noise is generated by the impingement of turbulence velocity gusts, defined as the Fourier components of the incident velocity component normal to the airfoil surface. The turbulence is assumed frozen. The gusts are again defined by the streamwise k_1 and the spanwise k_2 wavenumbers. The fundamental equation of the far-field acoustic PSD for turbulence-impingement noise of a flat plate is:

$$S_{pp} = \left(\frac{k\rho_0 c x_3}{2S_0^2} \right)^2 \pi U_0 \frac{L}{2} \int_{-\infty}^{\infty} \Phi_{ww} \left(\frac{\omega}{U_0}, k_2 \right) \left| \mathcal{L} \left(x_1, \frac{\omega}{U_0}, k_2 \right) \right|^2 \frac{\sin^2 \left[\left(\frac{kx_2}{S_0} - k_2 \right) \frac{L}{2} \right]}{\pi \frac{L}{2} \left(\frac{kx_2}{S_0} - k_2 \right)^2} dk_2 \quad (2.4)$$

with the same notations as in 2.1.1. Analogously to k_2^* from the trailing edge, k_2 takes any possible value ($-\infty < k_2 < \infty$).

Assuming a large aspect ration L/b , the simplified expression for the far-field acoustic PSD becomes

$$S_{pp} = \left(\frac{k\rho_0 c x_3}{2S_0^2} \right)^2 \pi U_0 \frac{L}{2} \Phi_{ww} \left(\frac{\omega}{U_0}, \frac{kx_2}{S_0} \right) \left| \mathcal{L} \left(x_1, \frac{\omega}{U_0}, \frac{kx_2}{S_0} \right) \right|^2 \quad (2.5)$$

Here \mathcal{L} is the non-dimensional chordwise aeroacoustic transfer function. As for the trailing edge, it is the sum of two contributions: $\mathcal{L} = \mathcal{L}_1 + \mathcal{L}_2$. The full expression is shown in Appendix C.2.

2.1.3 Application to a fan blade

Before applying Amiet's model to the fan of our study, we need to extract the required geometrical parameters, shown in Figure 2.3. The blade is cambered and the chord line will be used to define the

flat plate length required as an input for the analytical model. The blade is double-clamped by the front and the back plates, which have an impact in terms of aerodynamics and acoustics. Furthermore, the span is not constant along the whole chord due to the curved shape of the front plate. It is easy to measure at the trailing edge, where both plates are parallel. However, it widens at the leading edge and there is also a curved part, defined by a quarter of a circle of 17 mm of radius. This area, albeit relatively short, needs to be taken into account for the noise estimation.

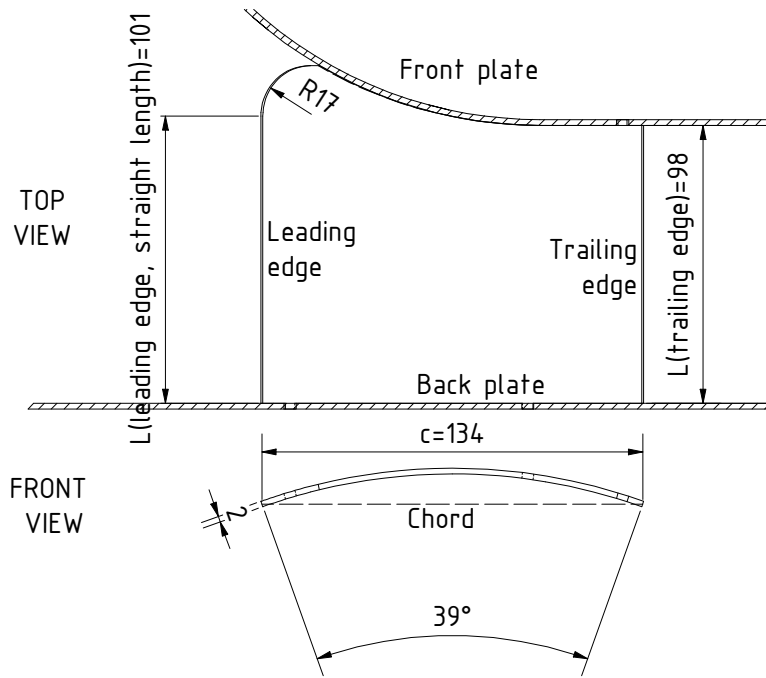


Figure 2.3 – Blade geometrical parameters for noise calculation (dimensions in mm)

2.1.4 Spanwise segmentation

The previous formulation, albeit considering limited span, assumes that the flow conditions are homogeneous along the whole span. However, for an industrial application such as ours, there is a considerable spanwise variation of the flow conditions. This will be taken into account with the application of the classical strip theory. The blade is divided into spanwise strips. For each of them, the flow conditions are averaged and the analytical model is then applied. A compromise needs to be found: if the number of strips is too large, it will reduce the aspect ratio and therefore impact the applicability of Amiet’s model; if it is too small, the flow spanwise evolution will not be accurately taken into consideration. This will be assessed in section 3.6. Furthermore, too narrow segments are logically hardly compatible with the large-span approximation. Yet previously reported studies state that it is relevant for rotating blades [99].

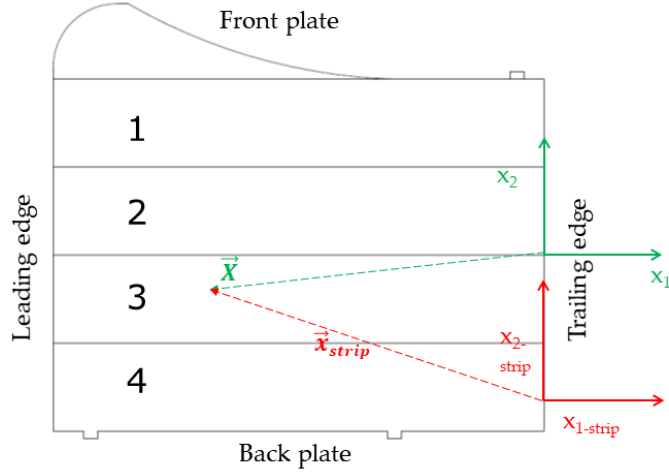


Figure 2.4 – Strips for trailing-edge noise calculation and projected observer positions

It is straightforward to segment the fan blade for a trailing-edge noise calculation, as depicted in Figure 2.4. The use of strips implies doing a slight change of coordinates, from the geometrical center of the whole trailing edge to the center of the trailing edge of each strip. This correction only concerns the spanwise coordinate x_2 :

$$x_{2-strip}(s) = x_2 - \frac{L}{2} + \frac{L}{2n} + \frac{(s-1)L}{n} \quad (2.6)$$

where n is the number of strips, s is the strip number (an integer between 1 and n) and L is the span.

For the leading-edge noise, the situation is different, as depicted in Figure 2.5. Its curved part, at the level of the front plate enlargement, should be taken into account because it is likely to contribute to the blade leading-edge noise. Indeed, boundary-layer turbulence is expected on the front wall. However, defining strips on this area appears questionable. The leading edge is straight along most of the span direction, but it describes a quarter of a circle before joining the front plate of the impeller. This curvature has been designed by the fan manufacturer in order to have the leading edge mainly normal to the streamlines in this part of the blade. This is so due to the axial component of the flow, which predominates in the area close to the front plate, but decreases as we move away from it (see section 3.6.2). To account for this, an additional skewed strip has been added, which requires a more complex transformation than Equation 2.6 (which is still used for the parallel strips). This special strip could be crucial because inlet turbulence is often of higher intensity close to curved walls:

$$\left. \begin{aligned} x_{1-curve} &= x_1 \cos(\beta) - x_2 \sin(\beta) - r \cos(\alpha) \\ x_{2-curve} &= x_1 \sin(\beta) + x_2 \cos(\beta) - r \sin(\alpha) \end{aligned} \right\} \quad (2.7)$$

with r being 65.1 mm, $\alpha = 130$ and $\beta = 45$. The skewed strip has a span of 26.7 mm, equal to the length of the circular leading edge. The chord is the same as for the parallel strips. This transformation is not really needed because the strips are independent and the observer is on the far-field, but it has been included for the sake of completeness.

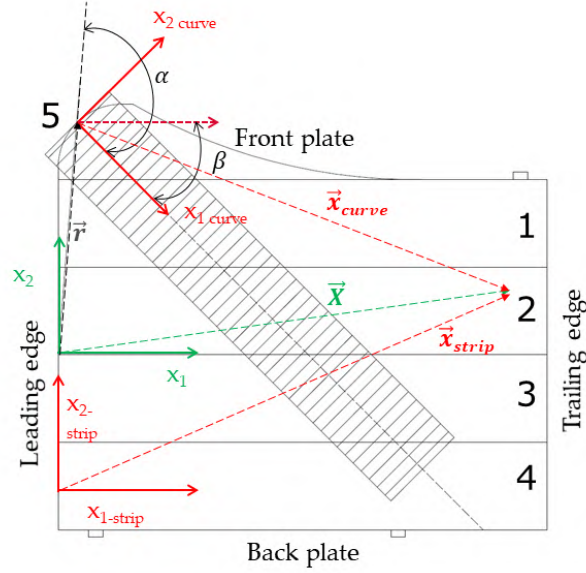


Figure 2.5 – Strips for leading-edge noise calculation

One correction is added to account for the effect of the front and back plates. Indeed, when the noise sources are close to a plate, the latter will behave as a wall which reflects the sound. This is equivalent to an image source which is symmetric with respect to the wall. A simple way to include this in the analytical model is the addition of 3 extra dB to the strips closer to the front and the back plates. For example, for the case represented in Figure 2.4, 3 dB would be added to the noise levels of strips 1 and 4. Conversely, the same would be done for strips 1 and 5 in Figure 2.5.

The last step is to add the noise from the different strips: $S_{ppblade} = \sum_{s=1}^n S_{pp}(s)$. Such a procedure is valid as long as the span of each strip is larger than the local spanwise correlation length of the addressed mechanism.

2.1.5 Change of coordinates and rotating blades

Sections 2.1.1 and 2.1.2 show the expressions for the far-field noise generated by both the trailing edge and the leading edge of a flat plate divided into strips, in a reference frame attached to the plate. It is necessary to adapt them to the geometry and the conditions of the blades of a centrifugal fan. This will be done by assimilating the blade to a flat plate tangent to the blade at the corresponding edge. Indeed, induced lift fluctuations acting as sources concentrate at the leading edge for turbulence-impingement noise, and at the trailing edge for trailing-edge noise. So, the errors due to the ignored

curvature are assumed negligible. The circular motion is assimilated to a rectilinear motion locally tangent to the circular trajectory at a given angular position. As shown by Sinayoko *et al.* [103], this simplification leads to similar predictions when compared to an exact formulation taking the circular motion into account. It is required to perform a change of coordinates from the general system of reference (X, Y, Z) , centred on the axis of rotation, to a local system (x_1, x_2, x_3) , centred on the edge of the plate (Figure 2.6).

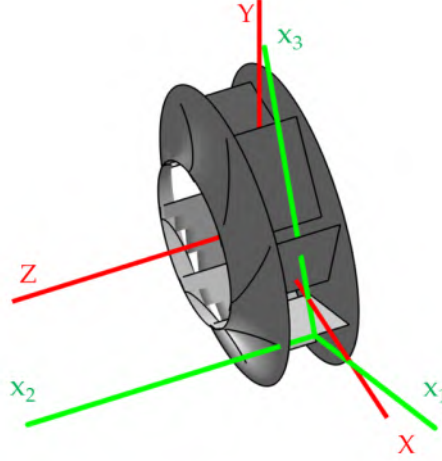


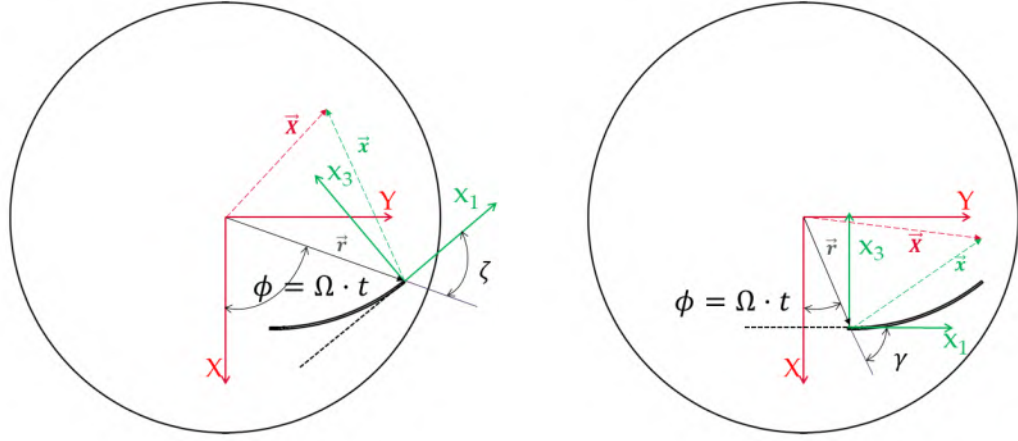
Figure 2.6 – Rotating (green) and fixed (red) reference frames, trailing-edge model

For an axial flow machine, the change of coordinates can be quite complex (e.g. [2, 103]), as there are one translation and up to three rotations involved. However, given the simpler geometry of our case, the problem is reduced to two dimensions (the coordinates x_2 and Z are equivalent). We will consider a generic angular position of the blade, at which its edge forms an angle ϕ with the X axis. The angle changes as the fan rotates with angular velocity Ω (see Figure 2.7). We can express the position of an observation point in local coordinates $\vec{x}(x_1, x_2, x_3)$ or in absolute coordinates $\vec{X}(X, Y, Z)$. Converting from the former to the latter requires a translation, expressed by the vector \vec{r} , and a rotation, an angle ζ for the trailing edge or γ for the leading edge. The vectorial expression of the conversion is thus: $\vec{x} = \vec{X} - \vec{r}$. The value of r is 179 mm for the trailing edge and 113 mm for the leading edge. The angles are $\zeta = 59^\circ$ and $\gamma = 67^\circ$.

The equations for the change of coordinates are:

$$\left. \begin{aligned} x_1 &= X \cos(\phi + \zeta) + Y \sin(\phi + \zeta) - r \cos(\zeta) \\ x_2 &= Z \\ x_3 &= Y \cos(\phi + \zeta) - X \sin(\phi + \zeta) + r \sin(\zeta) \end{aligned} \right\} \quad (2.8)$$

with the angle γ replacing ζ for the leading-edge formulation. As for Equation (2.7), for uncorrelated



(a) Trailing-edge model

(b) Leading-edge model

Figure 2.7 – Rotating and fixed reference frames

sources and an observer on the far-field, the radius-translation plays no role. The whole expression is shown here for the sake of clarity.

Using this transformation we can apply Equations (2.1), (2.3), (2.4) and (2.5) to obtain S_{pp} for any given angular position of the impeller. Then we average the acoustic PSD over all azimuthal positions ϕ to account for the rotation of the impeller:

$$S_{pp_{impeller}} = \frac{B}{2\pi} \int_0^{2\pi} \left(\frac{\omega_e(\phi)}{\omega} \right)^2 S_{pp_{blade}}(\phi, \omega_e) d\phi \approx \frac{B}{2\pi} \int_0^{2\pi} S_{pp_{blade}}(\phi) d\phi \quad (2.9)$$

where $(\omega_e(\phi)/\omega)$ is the Doppler factor and B the number of blades. This procedure, introduced by Paterson & Amiet [84] with a simple Doppler ratio, has been corrected for the squared frequency ratio by Sinayoko *et al.* [103]. As the Mach number is quite low ($M = 0.06$ for the BEP) and we are interested in modelling the broadband noise, the Doppler factor can be approximated by 1. The integral is calculated numerically using the trapezoidal rule. A convergence study (see section 4.1) has shown that the interval $[0, 2\pi]$ can be accurately discretized with $N = 10$ angular steps for all frequencies. Increasing this number has hardly any effect on the result of the integration. Equation (2.9) then becomes:

$$S_{pp_{impeller}} \approx \frac{B}{2\pi} \frac{\pi}{N} \sum_{i=1}^N [S_{pp_{blade}}(\phi_i) + S_{pp_{blade}}(\phi_{i+1})] \quad (2.10)$$

where $\phi_i = \frac{2\pi}{N-1}(i-1)$.

2.1.6 Calculation of sound power level

In order to compare the analytical predictions with the experimental results, it is required to compute the sound power level. If the directivity was not known, it would be needed to integrate the far-field sound pressure level over a hemisphere which encompasses the outlet fan side. As our problem is axisymmetric, we can replace the hemisphere by a semicircle (see Figure 2.9b). The equation to compute the sound power level is given by:

The equation to compute the sound power is given by:

$$P = \int_0^{2\pi} S_{pp_{impeller}(\theta)} 2\pi R^2 \sin(\theta) d\theta = 8\pi R^2 \int_0^{\pi/2} S_{pp_{impeller}} \sin(\theta) d\theta \approx 8\pi R^2 \sum_{i=1}^N S_{pp_{impeller}} \sin(\theta_i) \Delta\theta \quad (2.11)$$

where $\Delta\theta = \frac{\pi R}{2N}$

Finally the sound power level is obtained with:

$$L_W = 10 \log_{10}(P) + S_{PP_{correction}} \quad (2.12)$$

where $S_{PP_{correction}}$ is a correction function to account for the reflection of the sound on the wall between both reverberant rooms, because the source is close to the wall in terms of acoustic wavelength. The latter is equivalent to an image source symmetric with respect to the wall. At low frequency, both the real and the image sources are assumed correlated and 6 extra dB should be added. This assumption is essentially made because of the increasing effect of multiple scattering by surfaces, expected as frequency increases. However, for higher frequencies, the sources are decorrelated and only 3 extra dB should be added. The frequency dependency is reflected by defining a limit frequency f_{lim} , above and under which 3 and 6 dB will be added, respectively. Though the procedure is somehow arbitrary, a smooth transition between both levels is allowed with the adaptation of the tanh function:

$$S_{PP_{correction}}(f) = 9 - \{4.5 + 1.5 \tanh[0.005(f - f_c)]\} \quad (2.13)$$

The critical frequency f_c is calculated considering that the distance between the midspan of the impeller and the wall equals half of our critical wavelength, which yields a result of 1104 Hz. The curve generated by Equation (2.13) is shown in Figure 2.8.

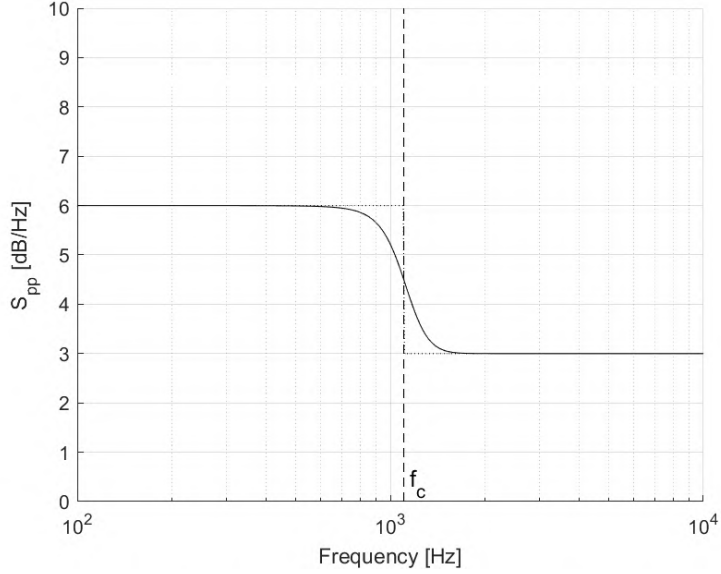
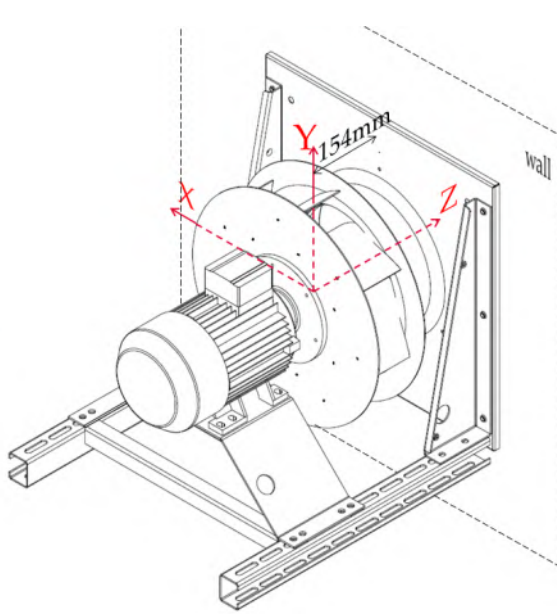


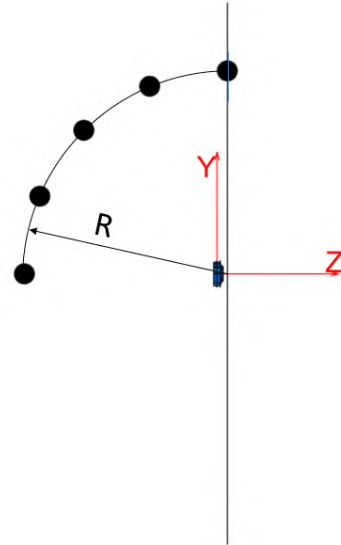
Figure 2.8 – Correction of sound level to account for the wall reflection

Another effect is that part of the sound generated in the outer part of the impeller and propagating towards the inlet is reflected back because of the geometrical contraction of the wave passage in this upstream direction. This, a priori, increases the noise at outlet. This effect is not accounted for in the present study because of the lack of available prediction method for it, at least at the engineering level.

The fan inlet noise has not been calculated because the sound transmission is much more complex due to the propagation of the sound waves through the inlet nozzle. A convergence study shows that 5 points over the semicircle are enough (see 3.6). Another numerical assessment showed that L_W converges with a radius of $R = 3\text{ m}$, which ensures the conditions of acoustic and geometrical far-field. This result also confirms that the radius related translation in the change of coordinates can be ignored (Equation (2.8)). The circle is normal to the wall, which is situated 154 mm away from the midplane of the impeller (see Figure 2.9a). Therefore, the center of the circle is at $(X=0, Y=0, Z=-0.154\text{ m})$, with respect to the reference frame of the fan.



(a) Positioning of the impeller with respect to the wall power



(b) Semicircle for the computation of the fan outlet sound

Figure 2.9 – Two views of the area for the noise computing

2.1.7 Noise radiation model for front-plate and back-plate trailing edges

The radial component of flow at the outlet of a plenum fan may generate noise at the edges of the front and back plates. Furthermore, the rotation of the impeller also induces a boundary layer on the outer part of the plates, the radial component of which could also radiate noise. Therefore, the edges of the front and back plates might be an additional noise source. The noise of a rotating disk was investigated experimentally in [21]. More recently, it was investigated numerically [71]. Some analytical work has also been carried out, but it was focused on the vibratory modes of a disk [61], a disk with constant thickness [60] and a disk with variable thickness [22]. This research was mainly aimed at applications to brakes, hard disk drives or saw blades, but studies on impellers are missing.

As a first assessment of the noise of the plates and in order to state about the ability of the circular edges to contribute to the total fan noise, Amiet's trailing-edge model was adapted to our geometry (see 2.1.1). Both inner and outer sides of the front and back plates are considered, as designated in Figure 2.10.

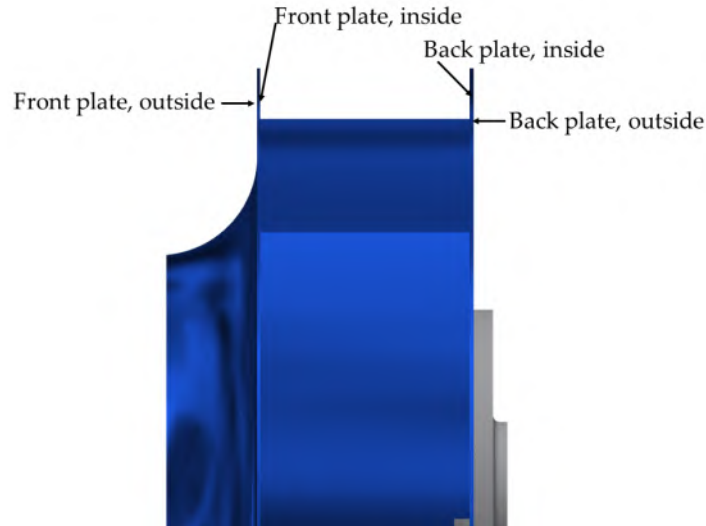
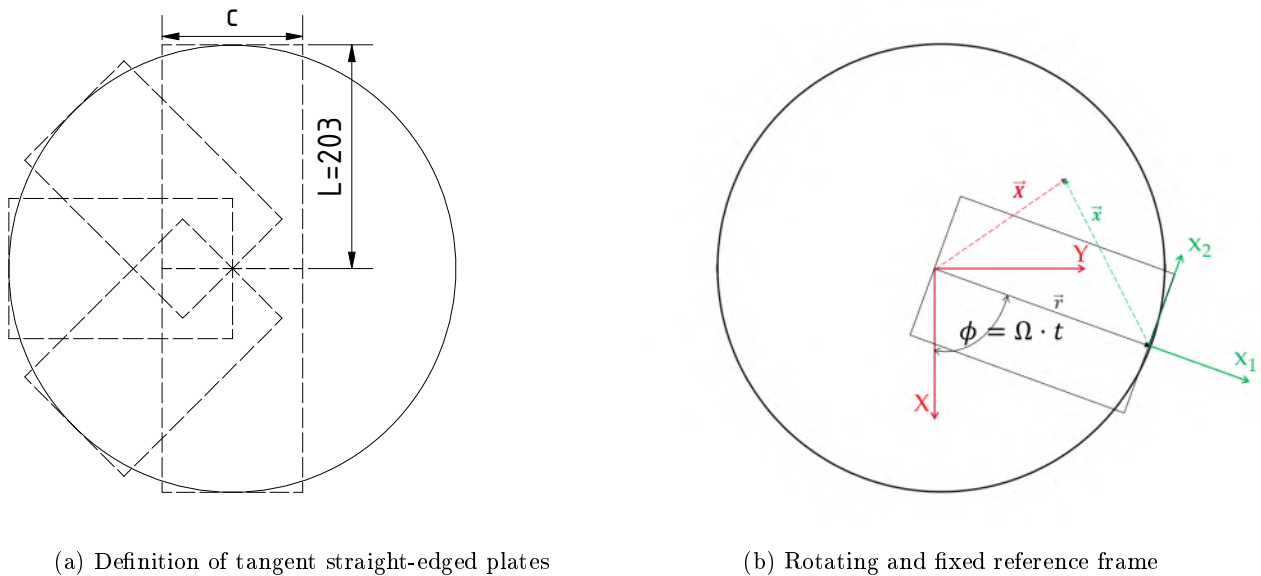


Figure 2.10 – Sides of front and back plates to be considered

For each side, the disk is divided into rectangular sectors, as shown in Figure 2.11a. For the sake of clarity and due to axisymmetry of the geometry, only the sectors on the left side of the disk is represented. The span of each sector correspond to the length of the perimeter of the flat plate (of radius R) divided by the number of sectors N : $L = 2\pi R/N$. The equivalent chord L equals the radius: $L = R = 203\text{ mm}$ and the leading edge always passes through the centre of the disk. Such an approximation artificially increases the total area of radiating surfaces, because of the overlap of adjacent rectangles. This is not believed a serious drawback for order-of-magnitude estimates. Indeed, the lift fluctuations acting as equivalent sound sources concentrate at the trailing edge.



(a) Definition of tangent straight-edged plates

(b) Rotating and fixed reference frame

Figure 2.11 – Disk model geometry

A similar derivation as in Section 2.1.5 is required. The same change of coordinates is used, with $\zeta = 0^\circ$ and the dimension x_3 being swapped with x_2 . Equation (2.8) is then rewritten as:

$$\left. \begin{aligned} x_1 &= X \cos(\phi) + Y \sin(\phi) - r \\ x_2 &= Y \cos(\phi) - X \sin(\phi) \\ x_3 &= Z \end{aligned} \right\} \quad (2.14)$$

The new change of coordinates is depicted in Figure 2.11b.

Similarly, Equation (2.9) then becomes Equation (2.15):

$$S_{pp_{disk}} = \frac{N}{2\pi} \int_0^{2\pi} S_{pp_{sector}}(\phi) d\phi \quad (2.15)$$

where $S_{pp_{sector}}$ is the far field PSD of a disk sector, computed with Equation (2.3). Finally, Equation (2.12) can be applied, with $S_{pp_{sector}}$ again replacing $S_{pp_{blade}}$.

2.2 Input data

2.2.1 Leading edge: wavenumber spectrum of the turbulence

A mathematical expression of the turbulence spectrum is required as an input for Equation 2.2. For simplicity, we will assume that the turbulence is locally homogeneous and isotropic. This allows the use of simple analytical models, such as Liepmann's or Von Kármán's. These have been satisfactorily combined with Amiet's model [1, 87]. The two-dimensional wavenumber spectrum of the turbulence Φ_{ww} adapted from Von Kármán's spectrum is:

$$\Phi_{ww}(k_1, k_2) = \frac{4\bar{u}^2}{9\pi k_e^2} \frac{\hat{k}_1^2 + \hat{k}_2^2}{(1 + \hat{k}_1^2 + \hat{k}_2^2)^{7/3}} \quad (2.16)$$

where \bar{u} is the streamwise *RMS* fluctuating velocity and \hat{k}_i are the wavenumbers, made dimensionless by k_e :

$$k_e = \frac{\sqrt{\pi}\Gamma(5/6)}{L_t\Gamma(1/3)}, \quad \hat{k}_1 = \frac{k_1}{k_e}, \quad \hat{k}_2 = \frac{k_2}{k_e},$$

L_t being the integral turbulence length scale and Γ the Gamma function. When the large aspect ratio approximation is used (Equation 2.5), $k_2 = kx_2/S_0$. The parameters are tuned on the CFD RANS data, as described in subsection 3.6.2

2.2.2 Trailing edge

The following models are required as an input for Equation 2.2. The definition of the boundary layer parameters used in this subsection can be found in Appendix D.1

2.2.2.1 Wall-pressure spectrum

In experimental studies, wall pressure fluctuations are typically measured with sensors embedded on the surface of the airfoil or blade. When this is not possible, a numerical, analytical or empirical approach is required. In the present study, two different empirical models will be used.

2.2.2.1.1 Rozenberg's model This model, presented in [94], extends Goody's model ([38]) by including an adverse pressure gradient. This is done by changing some of the boundary layer normalization parameters (displacement thickness δ^* instead of boundary layer thickness δ and τ_{max} instead of τ_w).

The fundamental equation of the model is:

$$\frac{\Phi_{pp} U_e}{\tau_{max}^2 \delta^*} = \frac{[2.82\Delta^2(6.13\Delta^{-0.75} + F_1)^{A_1}] \left(4.2\frac{\Pi}{\Delta} + 1\right) St^2}{[4.76St^{0.75} + F_1]^{A_1} + (C'_3 St)^{A_2}} \quad (2.17)$$

where $St = \omega\delta^*/U$ is the Strouhal number based on the displacement thickness . The parameters $A_1, A_2, F_1, \Delta, \beta_c, \Pi, C'_3$ are defined in Appendix D.2. Figure 2.12 shows a dimensionless wall pressure spectrum computed with Rozenberg's model. The following values, typical of our study (as estimated in 3.6.1), have been used: $\Delta = 5, \beta_c = 8, u_\tau = 1, R_T = 20$.

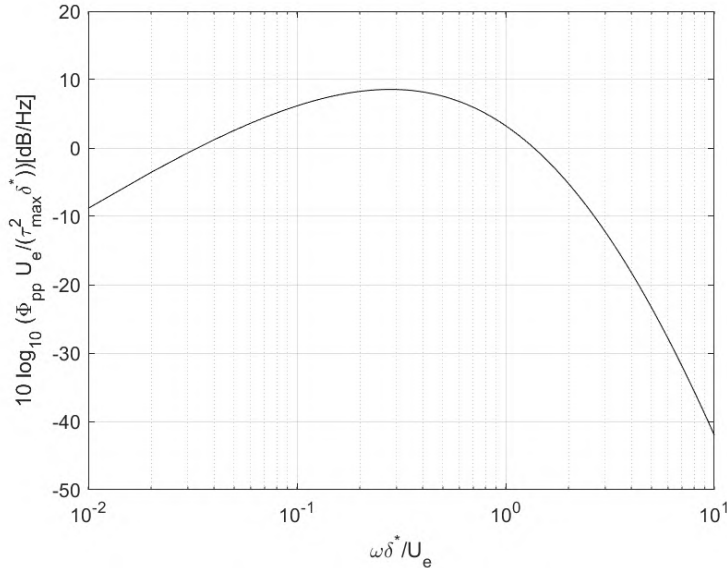


Figure 2.12 – Dimensionless wall pressure spectrum with Rozenberg's model. Parameters deduced from 3.6.1 and given in the main text.

2.2.2.1.2 Guédel's model The previous model, albeit empirical, involves many physical parameters. These parameters require that a RANS simulation is available, providing inner and outer boundary-layer variables. In this section, we present a purely empirical model. It was proposed

in [44], defined by averaging several wall pressure measurements, carried out on different axial fan blades. The results were made dimensionless by $\pi U_e^3 \delta^* \rho^2$, where δ^* and U_e have been estimated from RANS simulations. The corresponding spectral shape is presented in Figure 2.13.

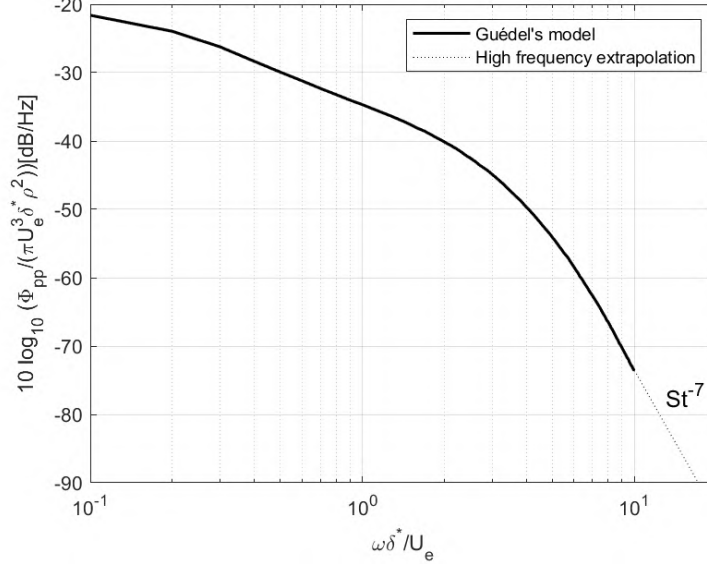


Figure 2.13 – Dimensionless wall-pressure spectrum according to Guédel's model

One drawback of the model is that its range is limited between $0 < St < 10$. This means that for low δ^* and high U we could end up with a maximum frequency which is excessively low for the desired application. For higher frequencies, the wall-pressure is extrapolated with a slope of St^{-7} : $\Phi_{pp}/(\pi U_e^3 \delta^* \rho^2) = 0.4386 \cdot St^{-7}$.

2.2.2.1.3 Dimensionless wall pressure spectrum for flow separation The previous models assume a developed and attached boundary layer. However, CFD simulations predict that the flow could detach on an area of the suction side of the blade (see Section 3.6.1). Due to the lack of a proper analytical model to predict a wall pressure spectrum with flow separation, an empirical approach is instead adopted. For this, previous spectra measured on a flat plate with a 10° angle of attack, placed inside a wind tunnel with a 20 m/s flow [43] and made dimensionless, are redimensionalised. In this configuration, detachment of the boundary layer on the suction side of the plate was observed. The boundary layer parameters δ^* and U_e were estimated from CFD simulations.

The results are approximated with a mathematical expression, Equation 2.18.

$$\Phi_{pp}/(\pi U_e^3 \delta^* \rho^2) = \begin{cases} a \omega' & \omega' < \omega'_1 \\ b \omega'^{-2} & \omega'_1 < \omega' < \omega'_2 \\ c \omega'^{-5} & \omega' > \omega'_2 \end{cases} \quad (2.18)$$

where $\omega' = \omega \delta^*/U_e$, $\omega'_1 = 0.577$, $\omega'_2 = 21.202$ and the constants a, b and c are, respectively, 0.0013,

$2.59 \cdot 10^{-4}$ and 2.467. The spectrum is displayed in Figure 2.14.

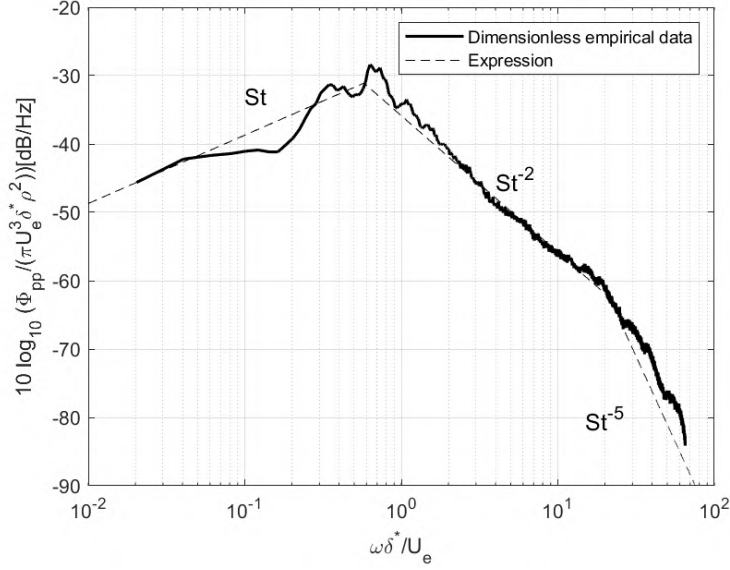


Figure 2.14 – Dimensionless wall-pressure spectrum for a flat plate with detached flow

As it is common with wall-pressure spectra (see [62] for more details), there are three different intervals where the slope changes. The slope is positive at low frequencies and then it shows decay rates of, respectively, ω^{-2} at mid frequencies and ω^{-5} at high frequencies. Many analytical wall-pressure models exhibit a decay rate of $\omega^{-0.75}$ [62]; the difference is likely to be due to the hump centered around $\omega' = 0.7$, probably induced by the flow detachment.

2.2.2.2 Correlation length

In a similar way as for Φ_{pp} , the correlation length needs to be estimated with the help of a mathematical model. Among other proposed ones, Corcos' model is quite popular [26]:

$$l_y(\omega, k_2^*) = \frac{\frac{\omega}{bU_c}}{(k_2^*)^2 + \left(\frac{\omega}{bU_c}\right)^2} \quad (2.19)$$

For parallel gusts, $k_2^* = 0$, Equation 2.19 becomes

$$l_y(\omega) = \frac{bU_c}{\omega} \quad (2.20)$$

where b is a model constant. However, the model is expected to be abusive when predicting the correlation length at low frequencies. Indeed, the inverse frequency dependance is unrealistic as the frequency goes to zero, and some experiments report a decrease below some characteristic frequency [95, 44]. An alternative model, proposed by Efimtsov [31], accounts for this:

$$l_y(Sh) = \delta \left[\left(\frac{a_1 Sh}{U_c/U_\tau} \right)^2 + \frac{a_2^2}{Sh^2 + (a_2/a_3)^2} \right]^{-1/2} \quad (2.21)$$

where $Sh = \omega\delta/u_\tau$ is the Strouhal number defined by the boundary layer thickness and the friction velocity. For high frequencies ($\omega \rightarrow \infty$), Equation 2.21 becomes Equation 2.20, with $a_1 = b$. The coefficients a_i are defined empirically. For the original model, they take the values $a_1 = 0.1$, $a_2 = 72.8$ and $a_3 = 1.54$ for the streamwise correlation length (not used in the present mathematical model) and $a_1 = 0.77$, $a_2 = 548$ and $a_3 = 13.5$ for the spanwise direction. Further investigations, such as [83], have recalculated them for different values of the Mach number. Nevertheless, an accurate measurement of the coefficients for low M , such as the case of the present study, is still missing.

An empirical model also proposed in [44] is preferred. As for the wall pressure spectrum, it is the result of averaging several measurements performed on rotating blades. The result is presented in Figure 2.15.

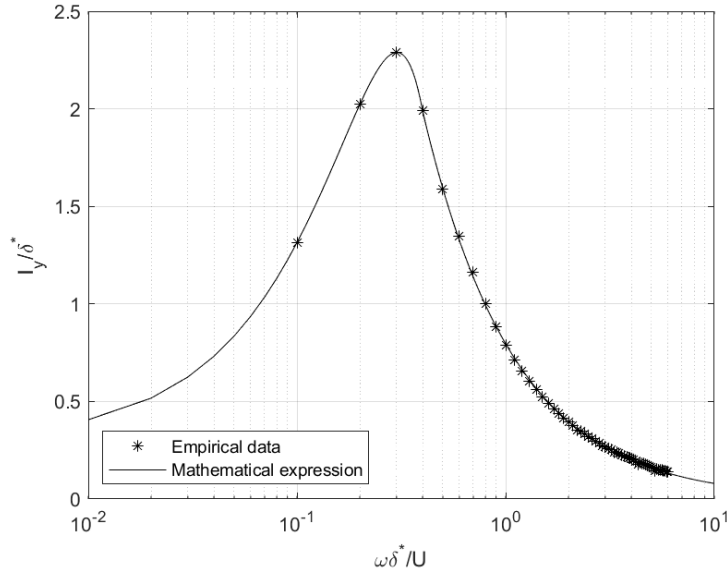


Figure 2.15 – Dimensionless correlation length with Guedel’s model

As it was the case for the wall pressure empirical model, it may be required to extrapolate the curve at high frequencies. Furthermore, in some cases, it could instead be needed to extrapolate it at low frequencies, because the lowest Strouhal number is 0.1. The empirical curve can be adjusted with the following expression:

$$l_y/\delta^*(St) = \begin{cases} -21.2612St^3 - 9.2583St^2 + 11.3431St + 0.2938, & \text{if } St < 0.4 \\ \frac{1.137\alpha}{St}, & \text{if } St \geq 0.4 \end{cases} \quad (2.22)$$

where the Strouhal number is defined based on the displacement thickness $St = \omega\delta^*/U$ and α is the free stream to convection speed ratio. The equation for $St \geq 0.4$ corresponds to Corcos’ model for parallel gusts (2.19) with a coefficient $b = 1.137$. In this study, the value $\alpha = 1/0.7$ will be used systematically.

2.3 Conclusion

This chapter describes how Amiet's model was adapted to the geometry of the plenum fan. As the flow features over the blade change along the spanwise direction, a strip segmentation of the blade has been done. This is straightforward for the trailing-edge noise, but the curved part of the leading edge requires the definition of a skewed strip. To account for the rotation of the impeller, a change of coordinates was introduced. The effect of the wall which separates both reverberant rooms is taken into account by introducing a correction function depending on frequency. Empirical and analytical functions used to estimate wall pressure spectra, correlation length or turbulence are also presented.

Chapter 3

CFD simulations

The objectives of this chapter are threefold. First, RANS simulations of the baseline fan are used to describe and analyse the main flow features at several operating points. Second, some results are extracted so they can be used to define the serrations in Chapter 1. And third, flow parameters are extracted to be used as input for the analytical model of the baseline fan described in Chapter 2 and applied in Chapter 4. Steady RANS was used instead of unsteady simulations like LES or even LBM to perform the study within the industrial constraints of this thesis

3.1 CFD: an overview

CFD is an acronym for *Computational fluid dynamics*, which is a technique aimed to solve the Navier-Stokes equations of mass, momentum and energy conservation. Typically, the equations are solved with the finite volume method, which requires discretising the domain of interest into small volumes, integrating the equations in each volume to obtain the discrete equations and solving the discretized equation.

The discretisation of the domain is done through meshing. The mesh resolution of the grid is critical, especially in areas of high gradients, so the physics of the fluid is accurately captured. There are three types of meshes:

- Structured mesh: the domain is divided into basic shapes (quadrilaterals in 2D and hexahedrons in 3D). This approach is cost-effective in terms of number of elements and is robust when the flow is aligned with the mesh. However, it is difficult to use with complex geometries and it usually requires the subdivision of the domain into simplified geometries, which are meshed independently.
- Unstructured mesh: it is based on triangles for 2D and tetrahedrons for 3D flows, but arbitrary

polyhedrons can also be used. This approach suits complex geometries better than structural meshes and can be automated easily.

- Hybrid meshes: it merges both structured and unstructured meshes, combining the advantages of both methods. However, it is difficult to implement, particularly on the interface between the structured and unstructured meshes.

Boundary conditions are required to solve the aforementioned governing equations. For turbomachinery applications, these are typically: pressure at inlet, velocity at inlet, mass flow at inlet, pressure at outlet, walls (usually associated with a no-slip condition) and/or periodicity [111]. There is a relative movement between the rotating and the static parts. There are three different approaches which can simplify this problem:

- Simple reference frame (SRF). Applicable to axial machines without singularities, it uses a reference which rotates with the impeller.
- Multiple reference frame (MRF). It divides the domain in two parts: a rotating domain which turns with the impeller and a fixed domain. The rotating domain is static from the computational point of view; the method is also known as frozen rotor. It averages the flow features and is thus valid for flows with weak rotor-stator interaction.
- Moving mesh. It is the most accurate method and captures rotor-stator interactions accurately. The mesh is similar to that of a MRF, but the flow is considered unsteady. For each time step, the rotating domain turns and the interface with the fixed domain is recalculated.

Turbulence is a phenomenon characterized by a huge range of scales. The biggest eddies are geometry-dependant and have a large lifetime. The smallest eddies are viscosity dependent and show a small lifetime. The turbulence kinetic energy is transferred from the biggest to the smallest ones, where it is finally dissipated. With the current computational means, "we are still a long way from performing *direct numerical simulations* (DNS) of flows of direct interest to the engineer" [29]. Instead, the instantaneous solution of the turbulence is averaged and the small scales are removed.

The Reynolds Averaged Navier-Stokes (RANS) is a cost-effective approach for industrial applications. It is based on the application of the Reynolds decomposition to the Navier-Stokes equations. This adds unknowns to the system, which require the use of turbulence models, such as Spalart-Allmaras, $k - \epsilon$ (and variants), $k - \omega$ (and variants) or RSM. In this work, both the $k - \epsilon$ [58] and the $k - \omega$ SST (Shear Stress Transport) [73] models have been used. The latter is a merge between the $k - \omega$ model, for the near wall, and the $k - \epsilon$ model, for the outer flow.

In the $k - \epsilon$ model, the integral turbulence length scale is given by

$$L_t = C_\mu^{3/2} \frac{k^{3/2}}{\epsilon}, \quad (3.1)$$

where k is the turbulent kinetic energy, ϵ is the rate of dissipation of the turbulent kinetic energy C_μ is a model constant which in the standard version of the model has a value of 0.09. The definition of integral turbulence length scale is given in 1.17. In the $k - \omega$ model, the integral turbulence length scale is computed from:

$$L_t = \frac{\sqrt{k}}{C_\mu \omega}, \quad (3.2)$$

where ω is the specific dissipation rate and C_μ is also 0.09.

3.2 Geometry description and parameters

Simulations were carried out in order to gain better insight into the fluid dynamics within the fan impeller. For this, the conditions of the tests of the baseline fan described in Section 1.2 were reproduced. The geometry of the simulation, described in Figure 1.5, can be seen in Figure 3.1. The reverberant room was replaced by a hemisphere, which allows the flow to enter uniformly through the impeller. The pressure chamber has been fully reproduced. Furthermore, a two-meter long extension of the room has been added so the boundary conditions do not disturb our area of interest.

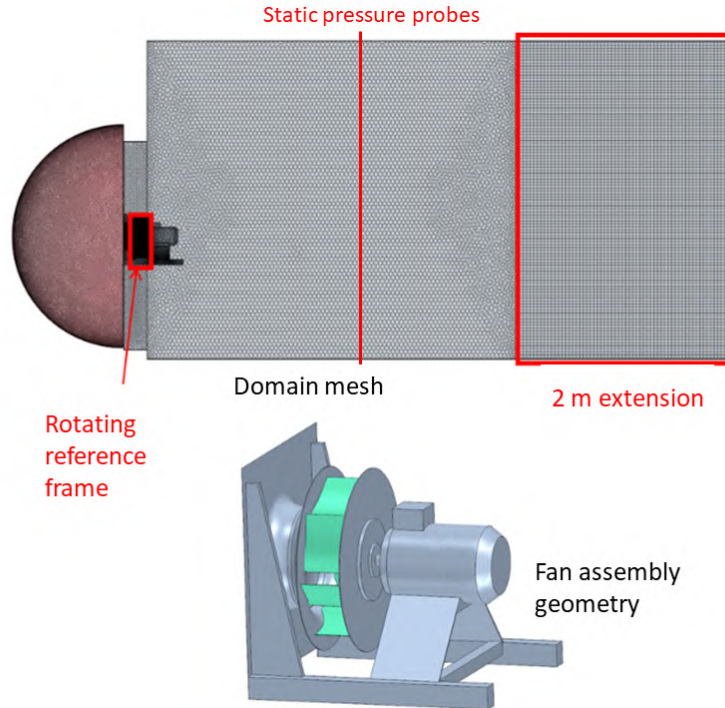


Figure 3.1 – Overview of the simulation domain and the fan

The boundary conditions were a uniform velocity over the hemisphere and zero static pressure at the outlet. The velocity was imposed so the desired flowrate is retrieved, as $q_v = U \cdot S$, where S is the surface of the hemisphere $S = 2\pi R^2$. Imposing zero static pressure at the end of the room guarantees

Label	Turbulence model	Polyhedral elements	Polyhedral elements in rotating domain	Length of surface meshing of impeller	Layers in boundary layer
Coarse $k - \epsilon$	$k - \epsilon$	3.75 M	1.51 M	0.8 mm	6
Coarse $k - \omega$	$k - \omega$ SST	3.75 M	1.51 M	0.8 mm	6
Refined $k - \epsilon$	$k - \epsilon$	9.39 M	5.22 M	0.5 mm	5
Refined-layers $k - \epsilon$	$k - \epsilon$	12.38 M	6.97 M	0.5 mm	15
Refined-layers $k - \omega$	$k - \omega$ SST	12.38 M	6.97 M	0.5 mm	15

Table 3.1 – Simulation mesh parameters

that it behaves as an outlet. The simulation used 3D steady RANS with a Multiple Reference Frame (MRF) approach. Values of the flow q_v , taken from the experimental fan curve, have been used as input. The simulations were carried out with the commercial software Star CCM+. Several configurations, with different mesh refinement and turbulence models ($k - \epsilon$ and $k - \omega$ SST), were simulated. Their main features can be seen in Table 3.1. First, a coarse mesh was used. In a next stage, it was refined. Finally, the number of boundary layer elements was increased.

Figure 3.2 shows the mesh around the fan assembly. It is refined around the impeller. The MRF can be distinguished: it is delimited by a rectangle that contains the impeller. The motor, the shaft, the support, the inlet nozzle and the wall can also be seen.

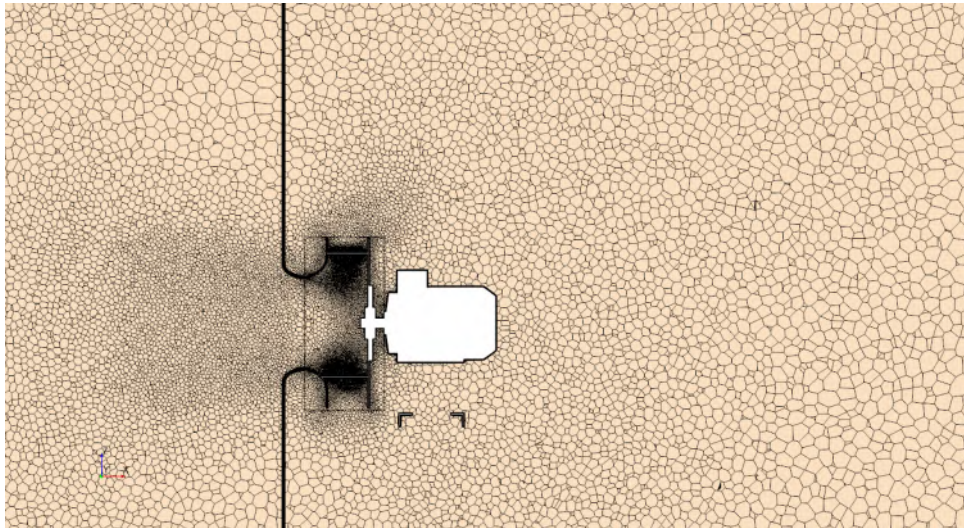
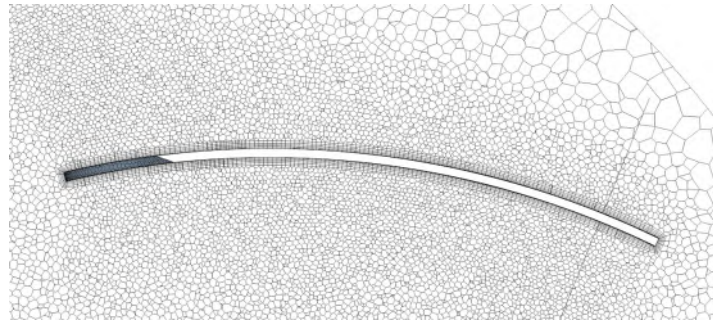


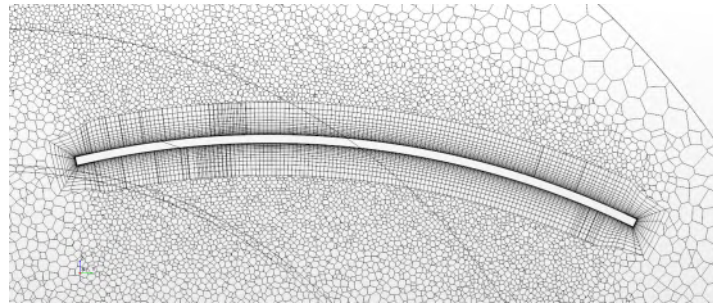
Figure 3.2 – Mesh around the fan assembly

Figures 3.3a and 3.3b show the mesh around a blade for the refined geometry and the refined geometry with extra layers, respectively. The difference between the number of layers is appreciable.

As an unstructured mesh is used, the value of the dimensionless wall distance y^+ over the blade



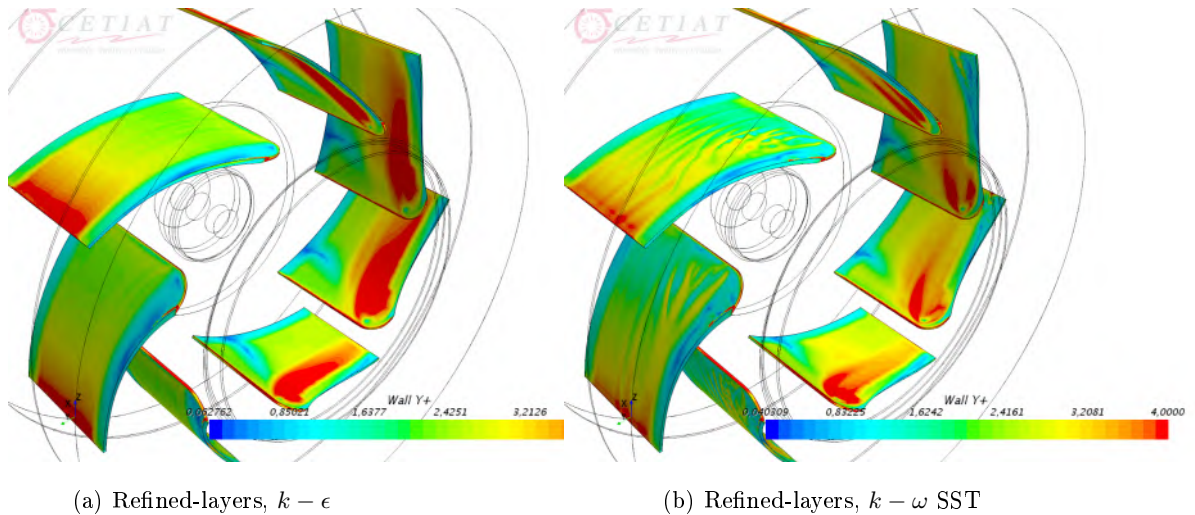
(a) Refined mesh



(b) Refined mesh with extra layers

Figure 3.3 – Mesh around a blade

should be below 1 [30]. Albeit this was not achieved, everywhere, the values are quite reasonable. As an example, Figure 3.4 shows the result for the refined simulations with extra layers on the boundary layers. Over most of the blade surface, the values are below 4.



(a) Refined-layers, $k - \epsilon$

(b) Refined-layers, $k - \omega$ SST

Figure 3.4 – Values of y^+ over the blades, $N=1440$ rpm

As an overview of the simulations, Figure 3.5 shows the velocity magnitude around the fan-motor assembly. The velocity magnitude is limited to 2.5 m/s (over this value it is cropped). It should be taken into account that the room physically ends at the level of the black vertical line. Right of it, there is an extension to ensure that the boundary condition does not affect the flow inside the room.

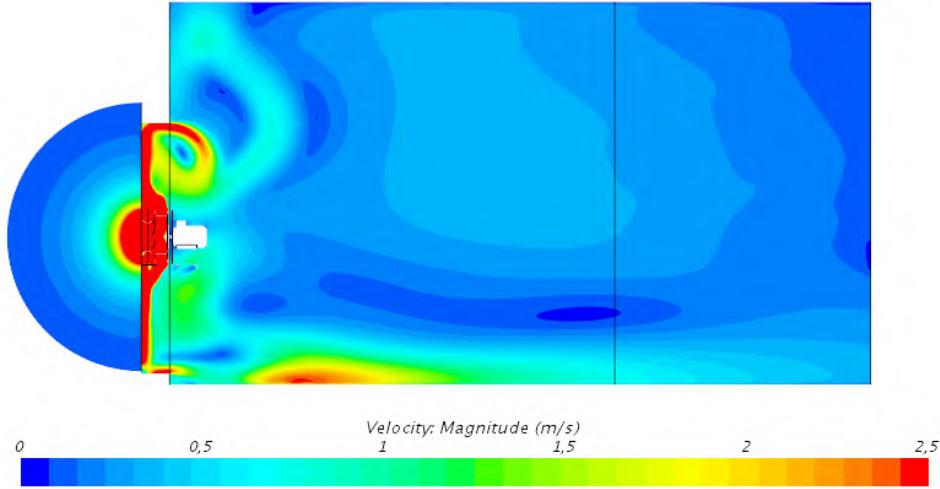


Figure 3.5 – Velocity magnitude inside the room, vertical cut, $q_v = 2196 \text{ m}^3/\text{h}$, $N=1440 \text{ rpm}$

From Figure 3.5, we can draw the following conclusions:

- The flow converges very uniformly towards the inlet nozzle. This is due to the simplification of the room as a hemisphere.
- The velocity gradient at the outlet of the impeller is very big, but it rapidly becomes uniform.
- There are four eddies generated by the corners of the section change on the left side of the room (only two are visible on Figure 3.5).
- The flow velocity is quite high near the floor of the room downstream of the impeller.

3.3 Pressure-flow curves

3.3.1 Baseline fan

The fan curves obtained from the simulations give an overview of the results and can be compared with the experimental results. Figure 3.6a shows the total pressure curves measured and predicted with the coarse and refined mesh. Three operating points have been simulated: the BEP ($q_v = 2196 \text{ m}^3/\text{h}$) and the points to the left ($q_v = 1706 \text{ m}^3/\text{h}$) and to the right ($q_v = 2584 \text{ m}^3/\text{h}$) of it. In all cases, the simulations underpredict the fan pressure. The experimental error bars have been added to the plots ($\pm 2.5\%$ of p_f and $\pm 1 \text{ m}^3/\text{h}$) and their length is shorter than the pressure underprediction. As far as the turbulence model is concerned, the prediction is slightly closer to the measured data with the $k - \epsilon$ model. It was therefore decided to use this model for the case with a refined mesh, which slightly raised the pressure prediction. Figure 3.6b shows the overall efficiency for the different simulations (see Equation 1.2), which follows the same tendency than the pressure. The measured overall efficiency accounts for the motor and VFD efficiency, which is obviously not the case for the predicted efficiency.

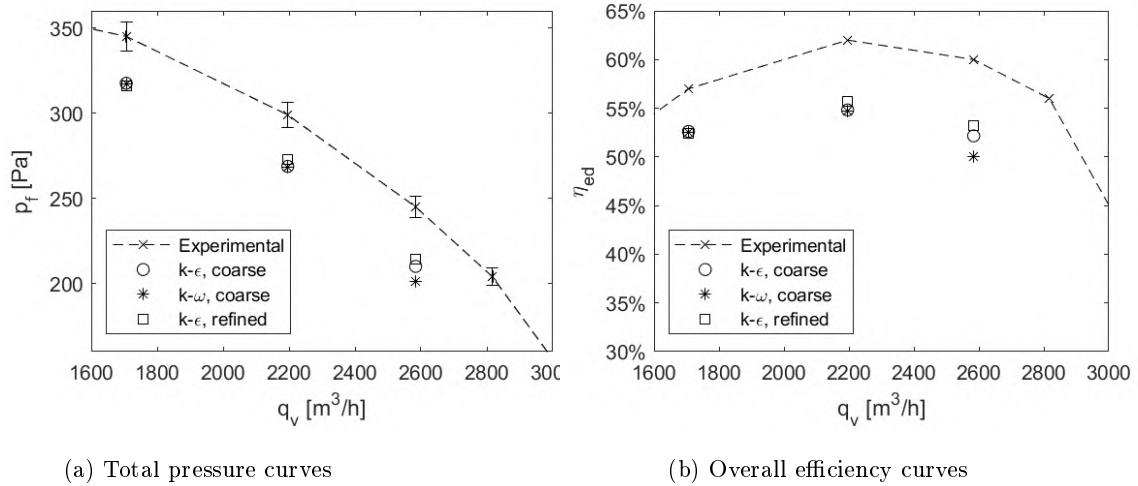


Figure 3.6 – Results with coarse and refined mesh, N=1440 rpm

The number of layers of the boundary layers was increased to extract the input information required to apply the analytical model, as described in Section 2.2. As it is shown in figure 3.13, there is flow detachment close to the front plate. This motivated to change the turbulence model from $k-\epsilon$ to $k-\omega$ SST because the latter is better suited for flow separation simulations. Figures 3.7a and 3.7b show the fan pressure and efficiency curves with the extra layers, respectively. The results for the refined mesh have been shown again for the sake of comparison. Only one point with extra layers was simulated with the $k-\epsilon$ model: the BEP. The same point was simulated with the $k-\omega$ SST model, to which two more were added, with $q_v = 903 \text{ m}^3/\text{h}$ and $q_v = 2795 \text{ m}^3/\text{h}$.

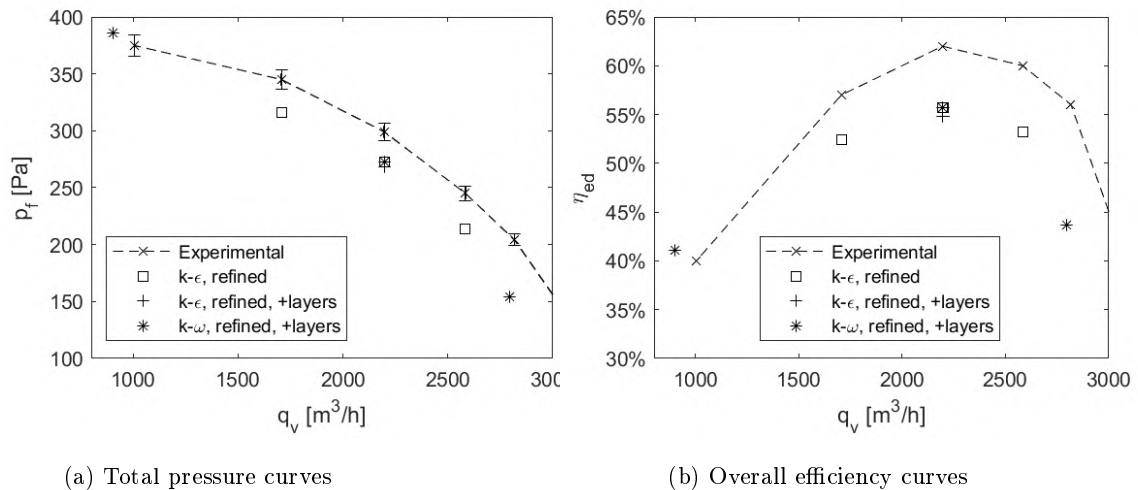


Figure 3.7 – Results with refined mesh and extra layers, N=1440 rpm

Simulations were also carried out for the rotation speed of 720 rpm. The fan curves, depicted in Figure 3.8, show the same underprediction seen for the nominal speed.

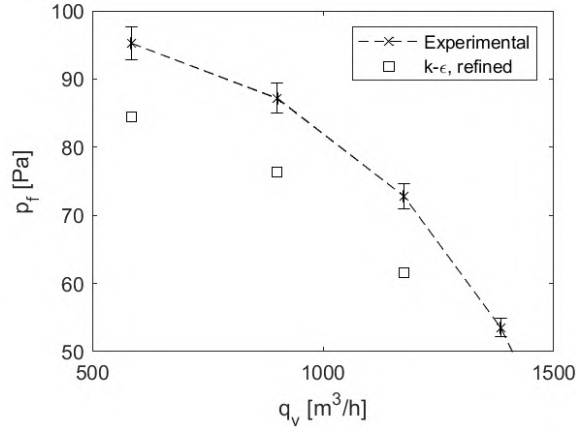
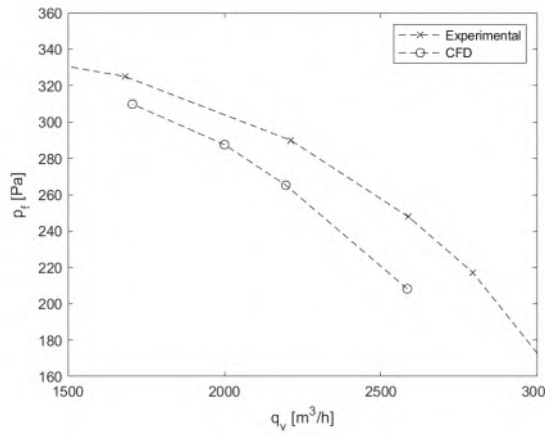


Figure 3.8 – Total pressure with $k - \epsilon$ model and refined mesh, $N=720$ rpm

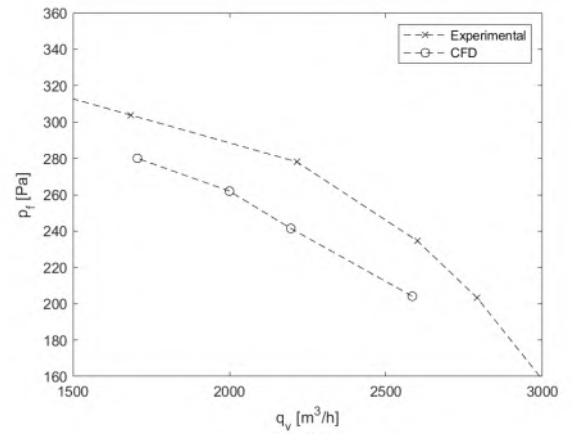
This consistent underprediction of the fan pressure has been observed for axial fans simulated with RANS [44]. A possible cause which may explain the underprediction could be the recirculating flow through the gap between the impeller and the inlet nozzle [81].

3.3.2 Leading-edge serrations

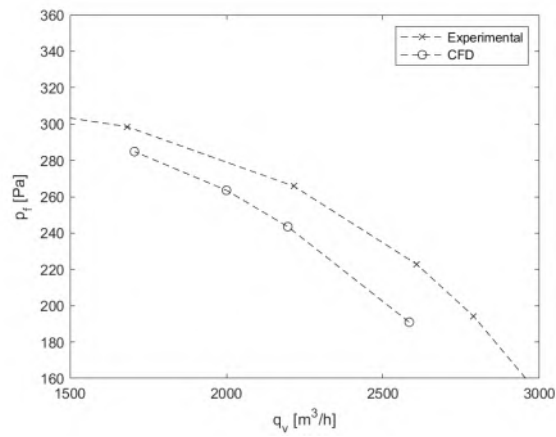
The three impeller prototypes were simulated at nominal speed, with the $k - \epsilon$ model and refined mesh. As it was the case for the baseline fan, the simulations slightly underpredict the fan pressure with respect to the experimental results (see Figure 3.9).



(a) LE_L16H11 prototype



(b) LE_L8H11 prototype



(c) LE_L16H22 prototype

Figure 3.9 – Total pressure for the impellers with leading-edge serrations, $k-\epsilon$ model and refined mesh, $N=1440$ rpm

3.3.3 Trailing-edge serrations

The prototype TE_ L8H12 was also simulated, for the rotating speed of 720 rpm. The outcome, shown in Figure 3.10, is consistent with the previous results: there is a slight underprediction of the fan pressure.

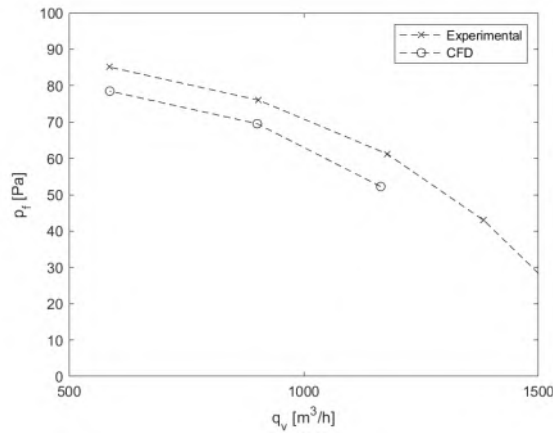


Figure 3.10 – Total pressure for the TE_ L8H12 impeller, $k - \epsilon$ model and refined mesh, $N=720$ rpm

3.4 Analysis of the flow features

The results presented in this subsection correspond to the refined mesh, with the $k - \epsilon$ turbulence model, for a rotating speed of $N=1440$ rpm.

3.4.1 Mean blade pressure field

The static pressure on the blades, displayed in Figure 3.11, has a similar distribution regardless of the operating point of the fan. In all three cases, the pressure increases when we move from the leading edge to the trailing edge, for both the pressure side and the suction side. The minimum value is located close to the inlet nozzle and the leading edge due to the high flow velocity around this area.

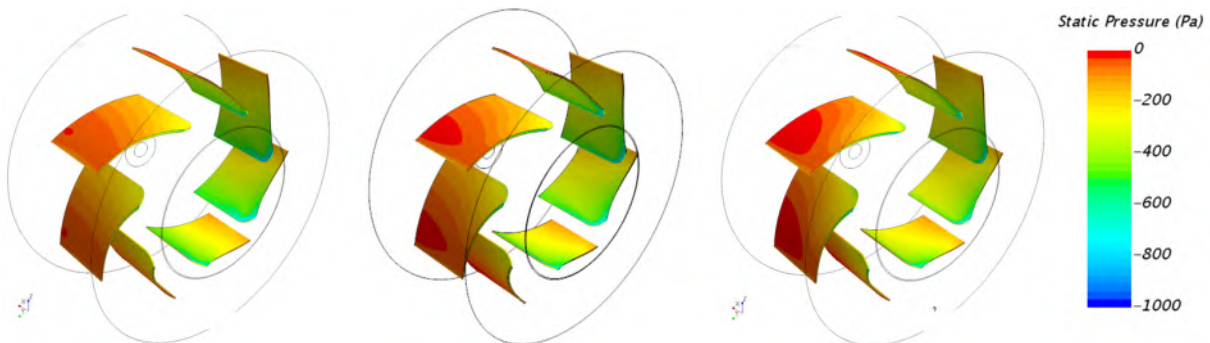


Figure 3.11 – Static pressure on the blades ($q_v = 1706, 2196, 2584 \text{ m}^3/h$), $N=1440$ rpm

3.4.2 Velocity field

We have used three transversal sections for the flow visualization, as it can be seen in Figure 3.12. The first section is 5 mm from the front plate, the second is in the middle and the third is 5 mm from the back plate.

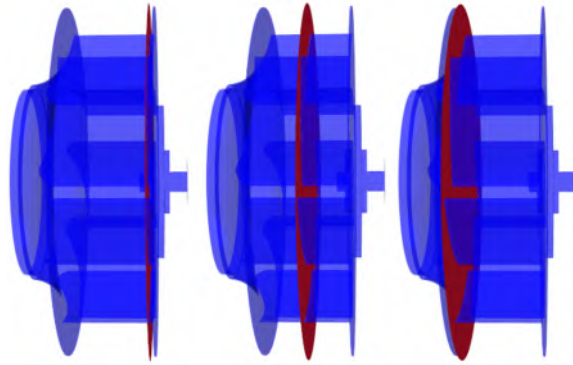


Figure 3.12 – Sections of the impeller

3.4.2.1 Relative mean velocity magnitude through the impeller

The velocity distribution is presented in Figures 3.13, 3.14 and 3.15. Here are some remarks:

- The flow around the blades is mainly axisymmetrical, with some asymmetry for one of the blades at $q_v = 1706$ and $q_v = 2196$, m^3/h (the lower blade in Figure 3.14).
- Close to the front plate there is a flow separation zone on the suction side. As we move away from it and towards the back plate (from Figure 3.13 towards Figures 3.14 and 3.15), the size of the zone is reduced, and it disappears more or less at the level of the middle plane. When the airflow is reduced, the size and length of the separation zone tend to grow, almost reaching the hub for the minimum flow of 1706 m^3/h .
- The velocity increases and becomes uniform as the flow leaves the impeller.

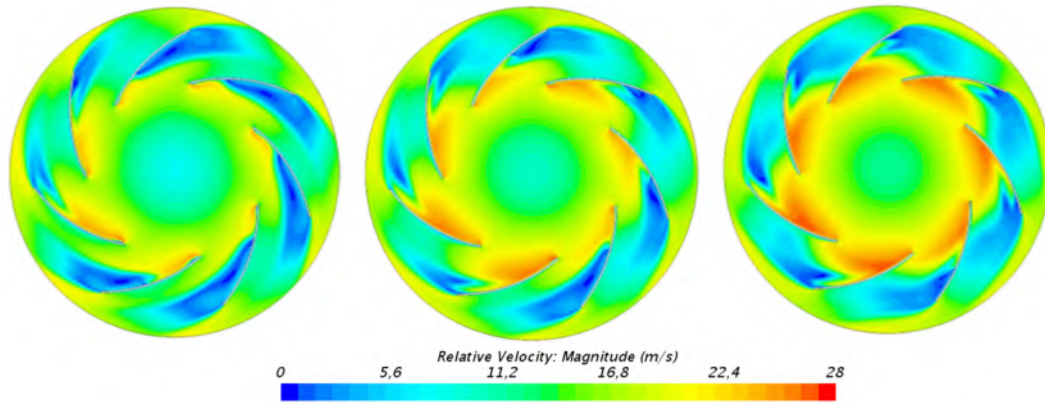


Figure 3.13 – Magnitude of relative velocity 5 mm from the front plate ($q_v = 1706, 2196, 2584 \text{ m}^3/\text{h}$), $N=1440$ rpm

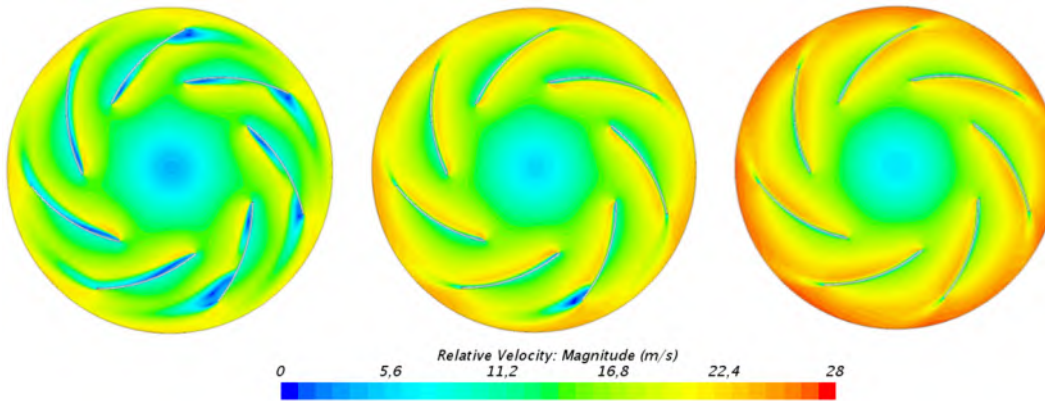


Figure 3.14 – Magnitude of relative velocity at the middle plane ($q_v = 1706, 2196, 2584 \text{ m}^3/\text{h}$), $N=1440$ rpm

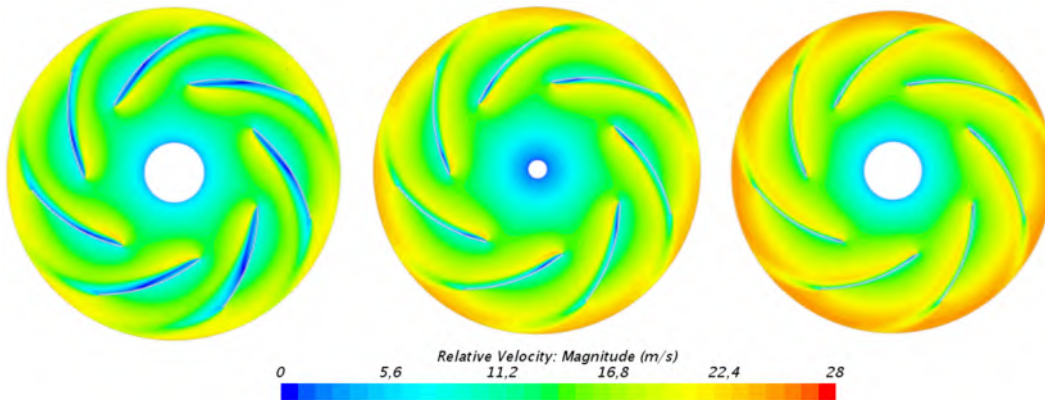


Figure 3.15 – Magnitude of relative velocity 5 mm from the hub ($q_v = 1706, 2196, 2584 \text{ m}^3/\text{h}$), $N=1440$ rpm

3.4.2.2 Visualization between two blades

To better reflect the evolution of the different parameters along the axial and tangential direction, a section between two blades has been used. As there is little dependency on the value of the airflow, we only show here results for the intermediate value $q_v = 2196 \text{ m}^3/h$. This section can be visualized in Figure 3.16.

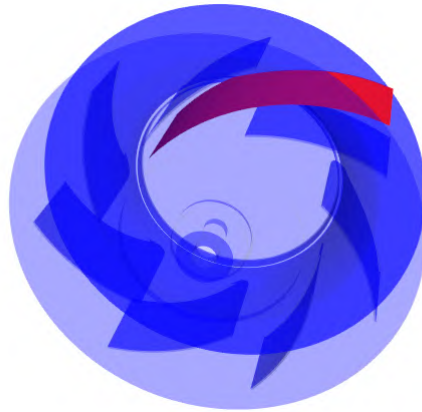


Figure 3.16 – View of the visualization area

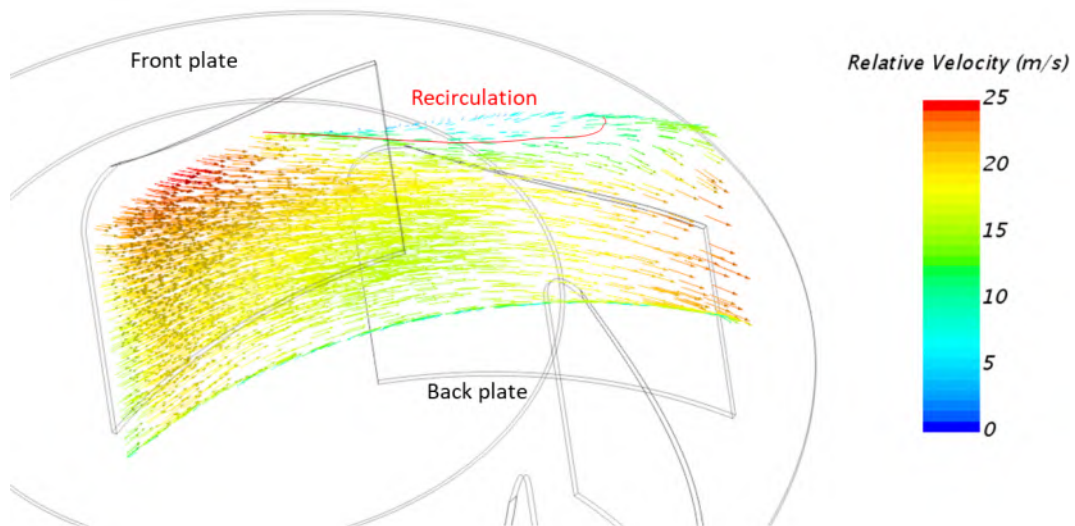


Figure 3.17 – Velocity field between two blades, $q_v = 2196 \text{ m}^3/h$, $N=1440 \text{ rpm}$

In Figure 3.17 it can be seen that the velocity is very high close to the inlet, with an important axial component. As the flow moves towards the back plate this axial component is gradually reduced. The velocity vectors close to the front plate are quite small, which is evidence of flow recirculation.

To complement the previous figure, we display in Figure 3.18 the flow through the inlet nozzle and the impeller. For the sake of clarity, the nozzle and front plate have been made transparent. In

general, there is a good guidance of the flow by the nozzle and the impeller. However, the vectors close to the front plate still have a significant axial component, which is complementary evidence of the recirculation shown in Figure 3.17. There is also a small recirculation of flow through the gap between the nozzle and the impeller.

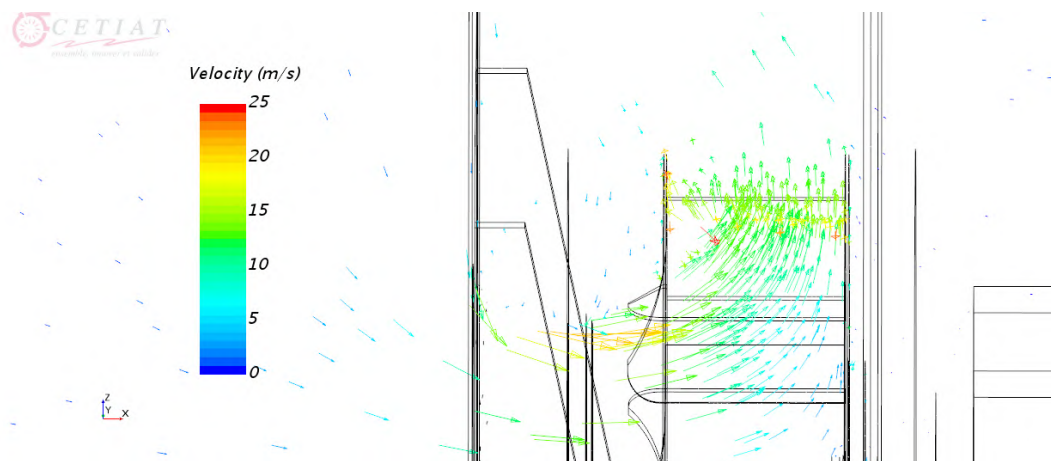


Figure 3.18 – Velocity vectors around the fan assembly, $q_v = 2196 \text{ m}^3/h$, $N=1440 \text{ rpm}$

3.4.2.3 Flow around a blade at midspan

3.4.2.3.1 Minimum flow ($q_v = 1706 \text{ m}^3/h$) To have a better insight on the flow pattern around a blade we have plotted a zoom of the relative velocity vectors in Figure 3.19. Now the swirls in the areas with flow separation over the suction side are easily identified.

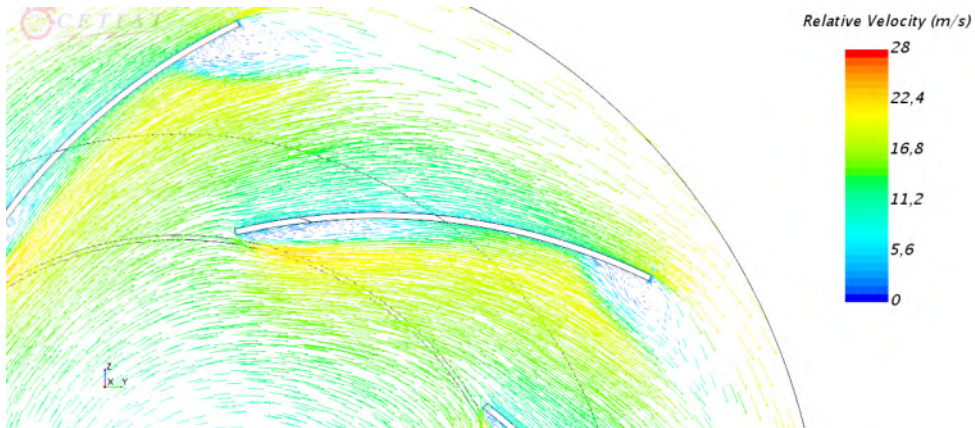


Figure 3.19 – Velocity field around the blade, $q_v = 1706 \text{ m}^3/h$

The relative total pressure around the blade, plotted on Figure 3.20, allows us to better estimate the boundary layer thickness. In this particular case, on the suction side, it has a rough value of 4 mm close to the leading edge and 12 mm close to the trailing edge (due to flow separation). The boundary layer is more uniform on the pressure side and is around 0.5 mm thick.

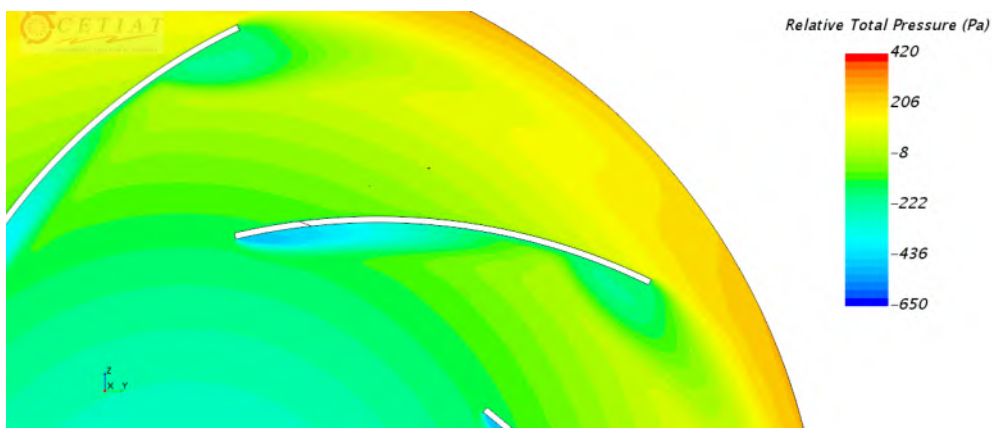


Figure 3.20 – Relative total pressure around a blade, $q_v = 1706 \text{ m}^3/h$, $N=1440 \text{ rpm}$

3.4.2.3.2 Intermediate flow ($q_v = 2196 \text{ m}^3/h$) In Figure 3.21 we can appreciate that the recirculation zones on the suction side have become much smaller. From Figure 3.22 we can estimate a boundary layer thickness of 2 mm on the suction side and 0.5 mm on the pressure side.

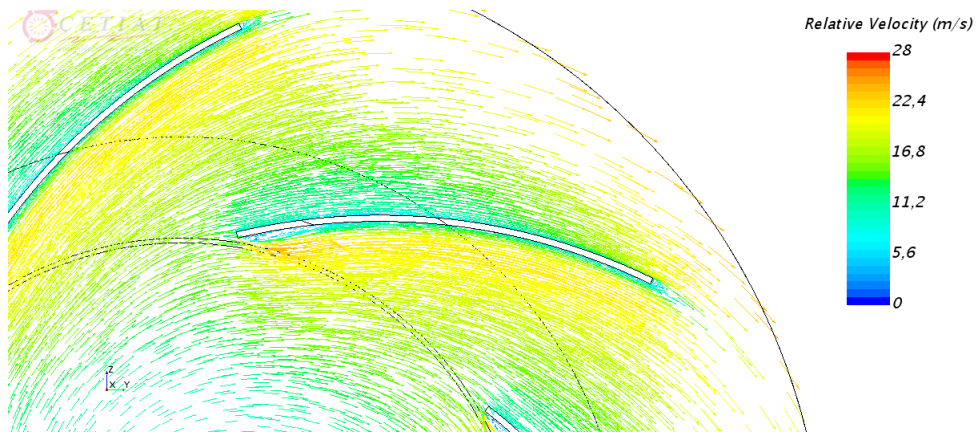


Figure 3.21 – Velocity field around the blade, $q_v = 2196 \text{ m}^3/h$, $N=1440 \text{ rpm}$

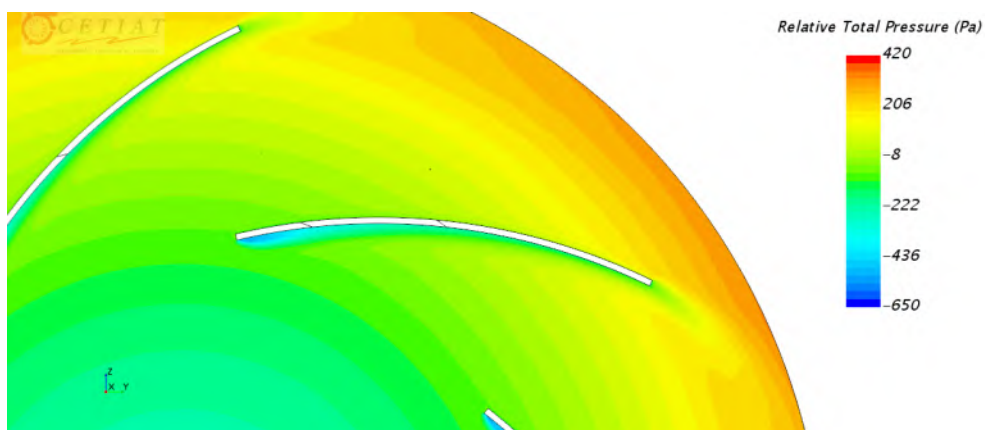


Figure 3.22 – Relative total pressure around a blade, $q_v = 2196 \text{ m}^3/h$, $N=1440 \text{ rpm}$

3.4.2.3.3 Maximum flow ($q_v = 2584 \text{ m}^3/h$) The velocity field (see Figure 3.23) looks very similar to the previous case, with an even smaller recirculation area close to the leading edge. The boundary layer thickness on the suction side at the trailing edge is almost the same as for $q_v = 2196 \text{ m}^3/h$.

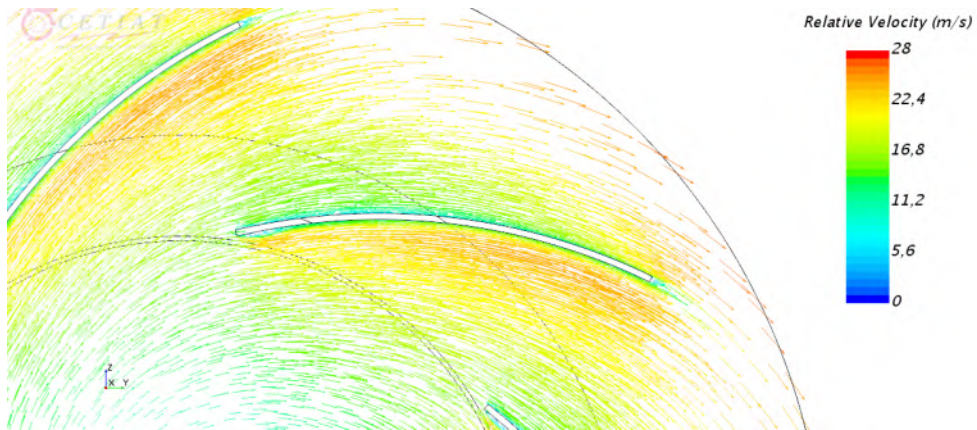


Figure 3.23 – Velocity field around the blade, $q_v = 2584 \text{ m}^3/h$, $N=1440 \text{ rpm}$

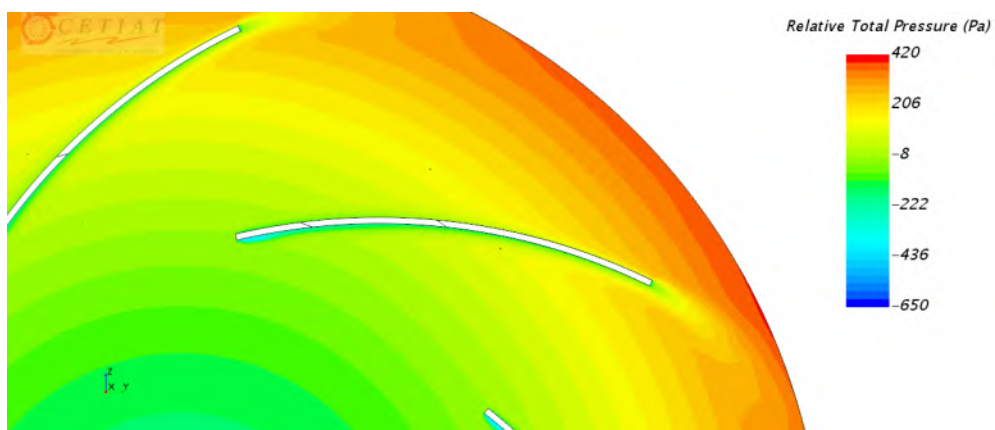


Figure 3.24 – Relative total pressure around a blade, $q_v = 2584 \text{ m}^3/h$, $N=1440 \text{ rpm}$

3.5 Flow parameters for serration design

3.5.1 Estimation of the turbulence length scale from RANS simulations

The results of the simulations with the refined mesh and the $k - \epsilon$ model were used to estimate the integral turbulence length scale, required to apply Equation 1.16. Equation 3.1 was applied upstream of the leading edge of a blade, to assess the integral length scale, for the best efficiency point ($q_v = 2196 \text{ m}^3/h$). We defined a rectangle perpendicular to the curved surface which goes through the middle of the blade (see Figure 3.25). It was placed upstream of the leading edge, at a distance equal to one fourth of the chord ($0.25 c$), with a height of 7 times the blade thickness ($7 T$) and a length equal to the span. It was verified that the rectangular area was not influenced by the potential flow around the leading edge.

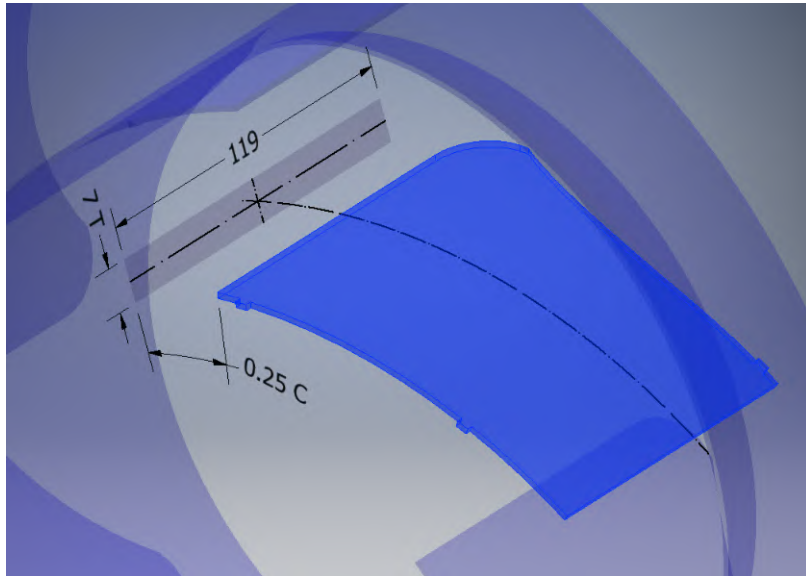


Figure 3.25 – Area for the calculation of the turbulent length scale, $q_v = 2196 \text{ m}^3/h$, $N=1440 \text{ rpm}$

The application of Equation 3.1 yields the result shown in Figure 3.26. The average of L_t on the rectangle is 7.8 mm, and the maximum is around 25 mm, close to the back plate. The turbulence evolves axially

3.5.2 Boundary layer thickness

The boundary layer thickness needs to be estimated to define the trailing-edge serrations, as described in Section 1.5.1. A rectangular area has been defined to visualise it. It is perpendicular to the blade and is located at a distance of 10% of the chord upstream of the leading edge Figure 3.27a. Even when the boundary layer thickness may be defined from the velocity field, it can be more easily observed on the relative total pressure field. This has been done in Figure 3.27b, and δ on the suction

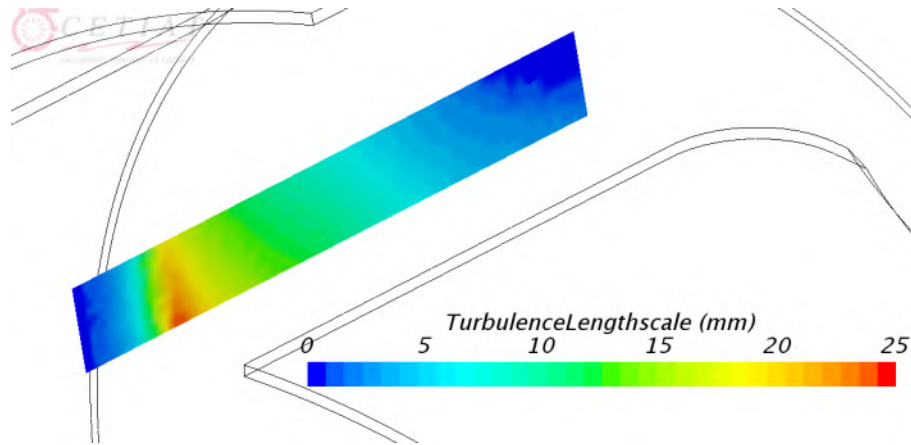
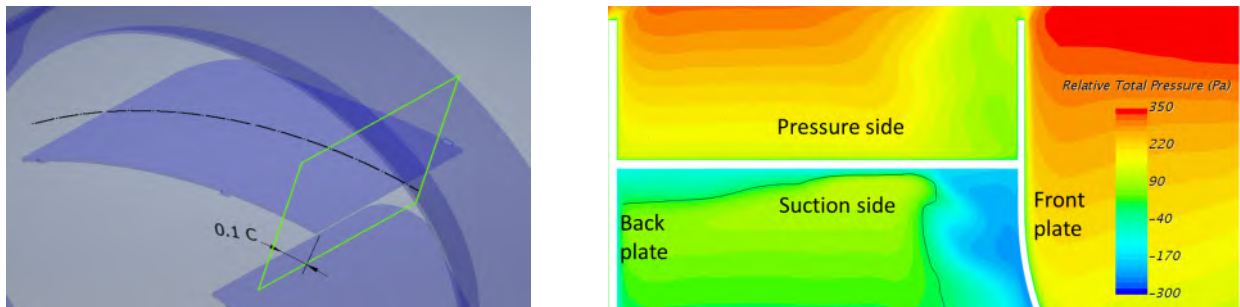


Figure 3.26 – Estimation of the integral turbulence length scale, $q_v = 2196 \text{ m}^3/h$, $N=1440 \text{ rpm}$

side ranges between 8.7 and 1.7 mm, depending on the spanwise location (without considering the flow separation area close to the front plate).



(a) Visualisation area

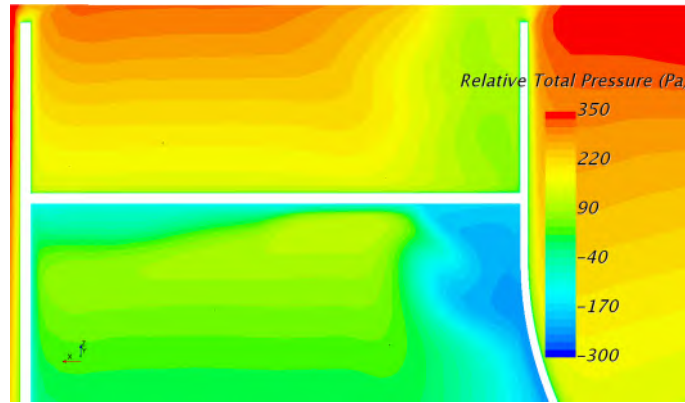
(b) Relative total pressure field. The estimated boundary layer is marked with a black line

Figure 3.27 – Visualisation of boundary layer thickness, $q_v = 2196 \text{ m}^3/h$, $N=1440 \text{ rpm}$

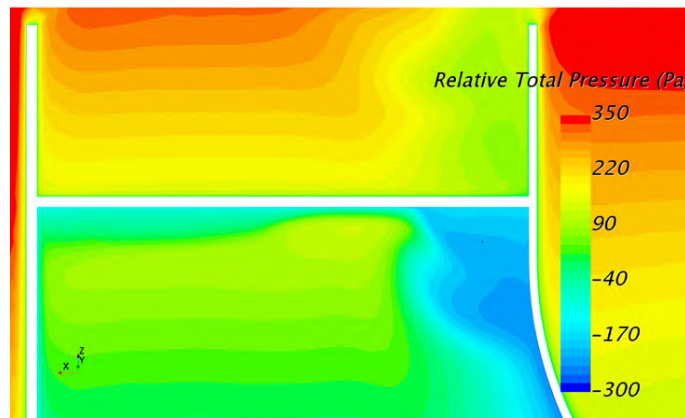
3.6 Input data for analytical model

3.6.1 Trailing-edge noise

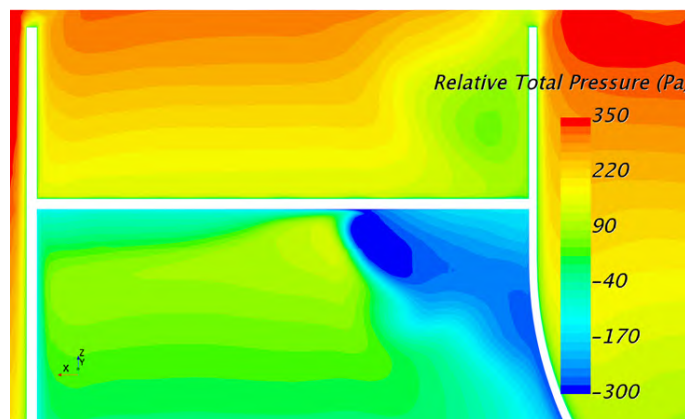
A set of boundary layer parameters is required to apply the analytical model described in Chapter 3 (see 2.2.2). As summarised by Table 3.1, the turbulence model was changed to $k - \omega$ SST and the number of layers of the boundary layer was increased. Figure 3.28a shows the relative total pressure for the initial configuration ($k - \epsilon$ model with fewer BL layers). Increasing the number of layers does not change much the flow features, as shown in Figure 3.28b. However, if we change the turbulence model to $k - \omega$ SST, the recirculation area close to the front plate doubles in size and now takes one third of the span of the blade on the suction side, as depicted in Figure 3.28c.



(a) Relative total pressure, $k - \epsilon$ model, refined



(b) Relative total pressure, $k - \epsilon$ model, refined and extra BL layers



(c) Relative total pressure, $k - \omega$ SST model, refined and extra BL layers

Figure 3.28 – Visualisation of the effect of the turbulence model and the number of layers of the boundary layer, $q_v = 2196 \text{ m}^3/h$, $N=1440 \text{ rpm}$

The boundary layer parameters are extracted on the rectangular area already described in 3.27a, for the best efficiency point. To capture the spanwise flow variability, eight "virtual" probes normal to the blade surface have been evenly distributed along the span, for both the pressure and the suction side (see 3.29). A general system of coordinates is placed in the middle of the blade, colinear with the back plate (black axis on Figure 3.29). Then, for each probe, for both the pressure and the suction side, a local system of coordinates is defined (red axis on Figure 3.29). For all cases, x, y, z represent the streamwise, normal and spanwise directions, respectively. The probes are numbered from 1 to 8. It is to be noted that this procedure is more accurate than the boundary layer thickness estimation described in 3.5.2.

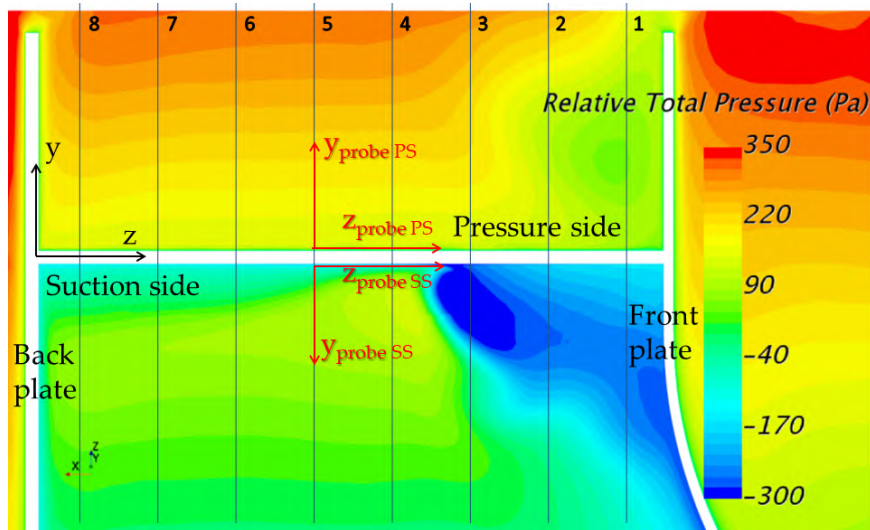


Figure 3.29 – Probes for boundary layer extraction

Along each probe, the relative velocity components and the relative total pressure are extracted. Furthermore, the static pressure and the wall shear stress are also extracted on the blade surface, for eight span sections which match the position of the probes. As far as the analytical model is concerned, only the streamwise component of the velocity is required. It is verified that the latter component is several orders of magnitude bigger than the other two (spanwise and normal), which therefore can be neglected (see Figure 3.30).

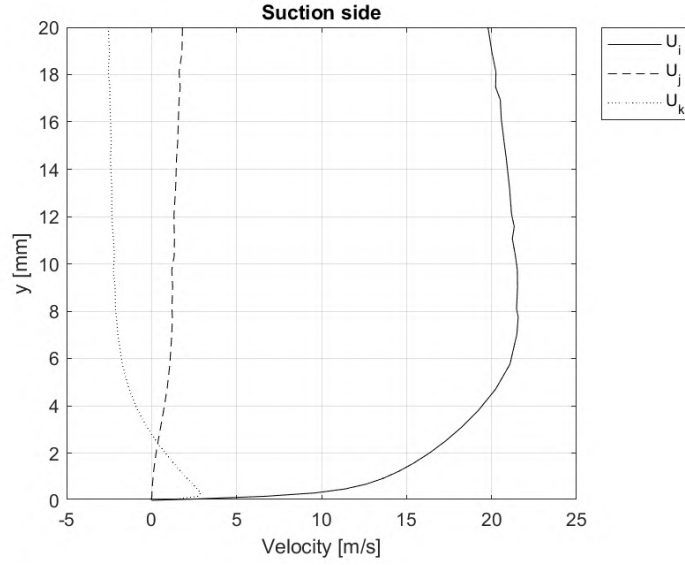


Figure 3.30 – Components of relative velocity: streamwise (U_i), normal (U_j) and spanwise (U_k), probe 5 ($z=55.1$ mm)

For each probe, a free stream velocity U_e is defined. For the suction side, this is done by finding the maximum of the streamwise velocity. The y coordinate where 99% of its value is reached is used to define the boundary layer thickness δ (see Figure 3.32). Then δ^* and Θ are obtained by integration (see D.1 for more details). As there are some fluctuations on the velocity and relative total pressure, a 5-point moving average is performed.

For the pressure side, there is not a maximum of velocity, as it is monotonically increasing with the normal coordinate y . Instead, we look for a maximum on the second derivative of the relative total pressure with respect to y : $\frac{d^2 P_{totrel}}{dy^2}$. The evolution of the relative total pressure and the first and second derivatives is shown in Figure 3.31, for a particular probe.

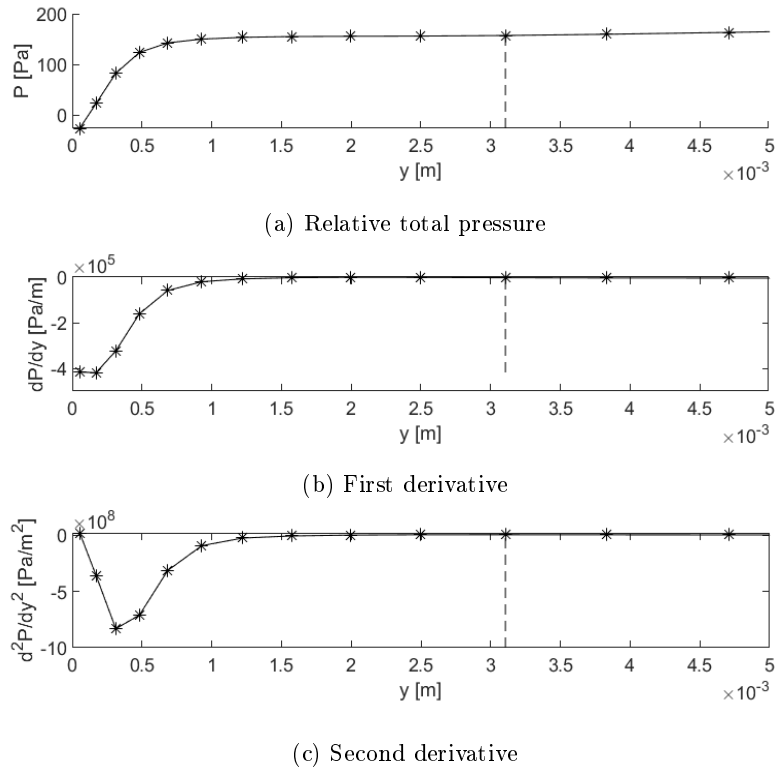


Figure 3.31 – Evolution of the relative total pressure and derivatives, probe 5 ($z=55.1$ mm)

The outcome of this process, for both sides of the blade, is the free stream velocity U_e and it is shown in Figure 3.32. Once U_e is obtained, the process to compute the rest of the parameters is the same as for the suction side.

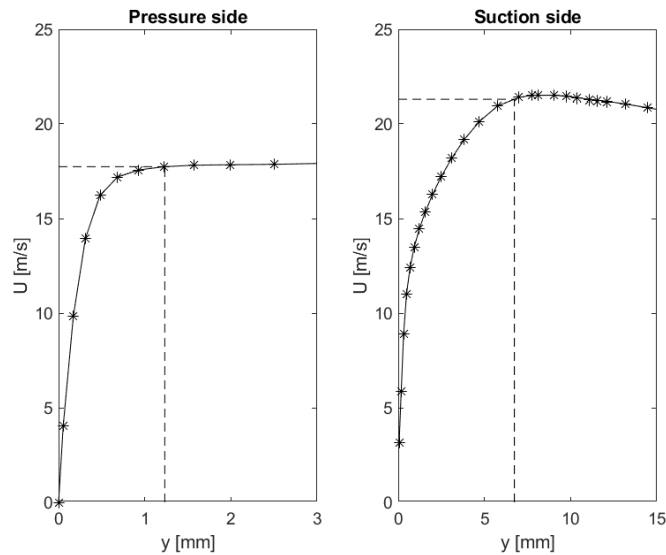


Figure 3.32 – Profile of streamwise velocity, pressure side and suction side, with U_{99} marked with a dashed line, probe 5 ($z=55.1$ mm)

In Figure 3.33 the spanwise evolution of the boundary layer thickness is shown. As it could already

be ascertained from Figure 3.29, δ is much more uniform in the pressure side than the suction side. This is due to the flow detachment on the suction side, close to the front plate. It also explains the big values of the boundary layer thickness for the first three probes, which have an impact on δ^* and Θ .

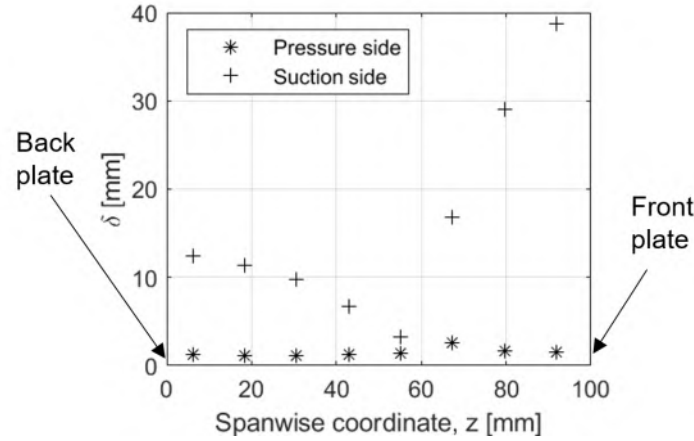


Figure 3.33 – Spanwise evolution of boundary layer thickness

The wall static pressure and wall shear stress are extracted on the surface of the blade, at a constant spanwise coordinate z which matches the position of the probes. Rozenberg’s model (2.17) uses the maximum shear stress instead of the value on the wall, but in the present study, it was verified that these were equivalent. This model also uses the streamwise wall pressure gradient at the probe location dP/dx . Figure 3.34 shows the streamwise evolution of the static pressure and the shear stress on the blade surface. The pressure has been smoothed with a 5-point moving average to mitigate some fluctuations in the results of the simulations. The plots show the evolution of the pressure and the shear stress along the blade, but only the values at our point of interest are used (at a distance of 10% of the chord upstream of the trailing edge, with a coordinate of $x=0$).

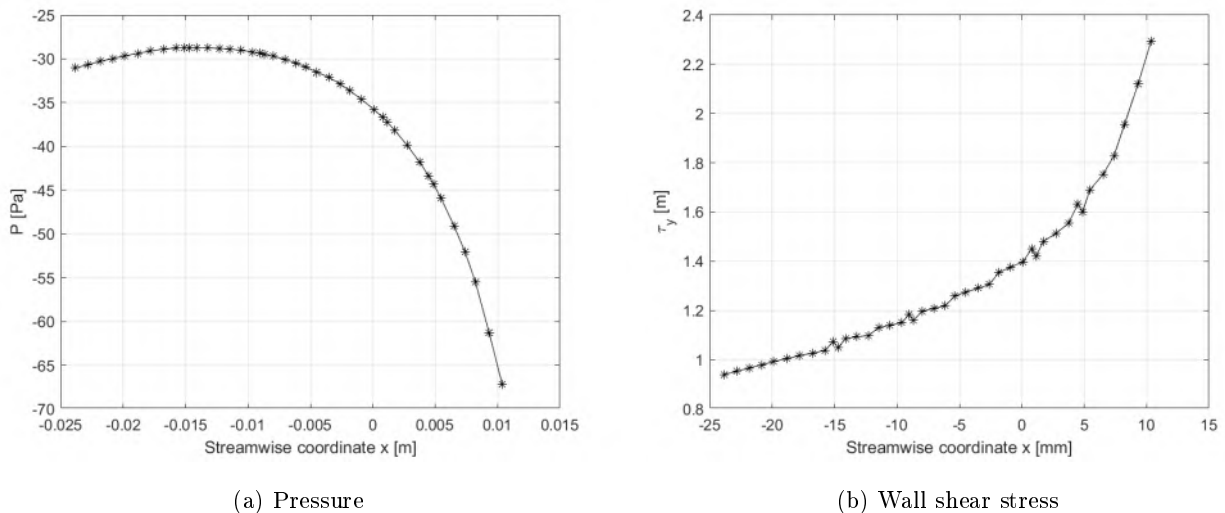


Figure 3.34 – Pressure and wall shear stress on the pressure side of the blade, for probe 5 ($z=55.1$ mm)

The data extracted with the procedures described in this subsection are compiled in Tables 3.2 and 3.3.

Probe	1	2	3	4	5	6	7	8
U_e (m/s)	15.9	18.4	21.6	24.8	21.5	20.3	19.7	19.2
δ (mm)	38.8	29.0	16.8	3.2	6.7	9.7	11.3	12.4
δ^* (mm)	26.6	20.6	12.5	0.6	1.2	2.1	2.4	2.8
Θ (mm)	-0.04	-0.15	-0.29	0.34	0.78	1.34	1.55	1.75
τ_w (Pa)	-1.0	-0.9	-1.8	1.2	0.8	0.7	0.8	0.5
$\frac{dP}{dx}$ (Pa/m)	6106	5039	14747	8485	3313	2932	2984	2793

Table 3.2 – Boundary layer values for BEP, suction side

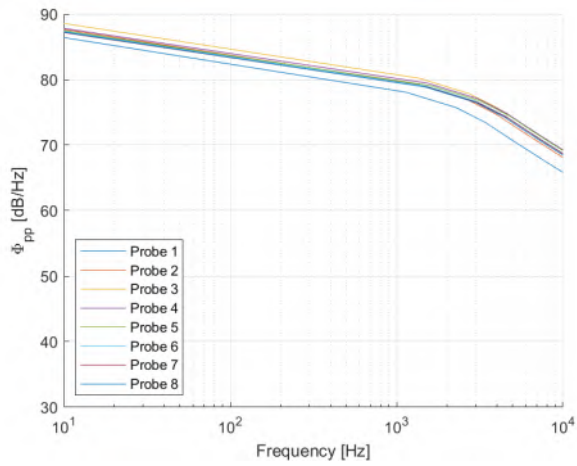
Probe	1	2	3	4	5	6	7	8
U_e (m/s)	15.6	17.3	18.4	18.1	17.9	17.6	17.5	17.4
δ (mm)	1.4	1.7	2.5	1.4	1.2	1.2	1.2	1.2
δ^* (mm)	0.23	0.23	0.23	0.22	0.21	0.22	0.21	0.20
Θ (mm)	0.11	0.12	0.12	0.10	0.10	0.10	0.10	0.09
τ_w (Pa)	1.1	1.3	1.5	1.4	1.4	1.3	1.3	1.3
$\frac{dP}{dx}$ (Pa/m)	-775	-1153	-1563	-1448	-1283	-1299	-1159	-1019

Table 3.3 – Boundary layer values for BEP, pressure side

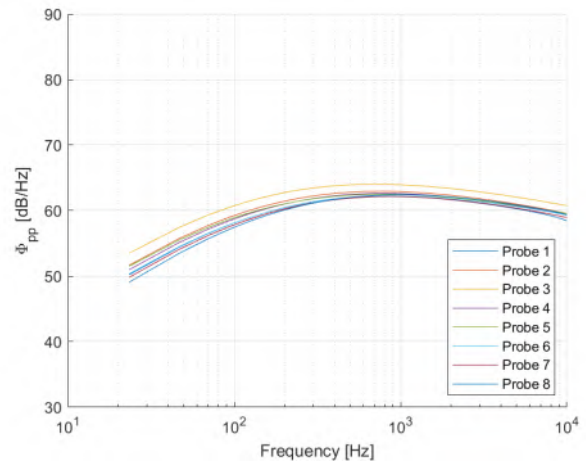
3.6.1.1 Wall-pressure spectrum

The results from the previous section have been used to feed Rozenberg’s and Guedel’s models (see 2.2.2.1.1 and 2.2.2.1.2). For probes 1,2 and 3 on the suction side (the closest to the front plate), the redimensionalised spectra of the detached flow on a flat plate have been used instead (2.2.2.1.3). The outcome is shown in Figure 3.35 for the pressure side, and in Figure 3.36 for the suction side.

The wall pressure spectra obtained with Rozenberg’s model are much lower than the spectra calculated with Guedel’s model, especially at low frequencies. For the suction side, the levels of the redimensionalised spectra for probes 1,2 and 3 are closer to those obtained with Guedel’s model for the rest of the strips. This is because the redimensionalisation is done based on the same parameters in both cases, whereas Rozenberg’s model uses another set of values. The difference at low frequencies is justified by the fundamentally different shape of the adimensional spectra: as the frequency is reduced, Rozenberg’s model tends to 0 whereas Guedel’s tends to its maximum value (see Figure ??).

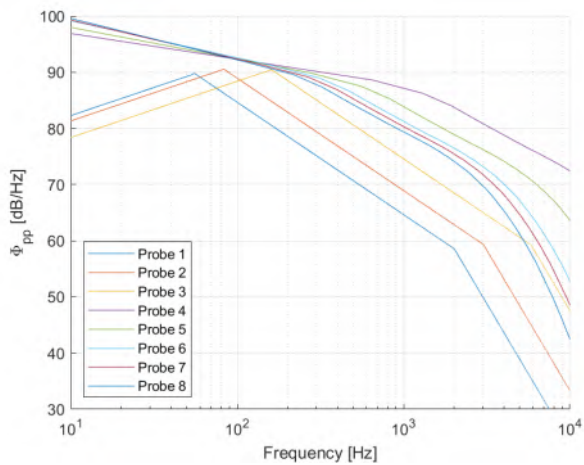


(a) Guedel's model

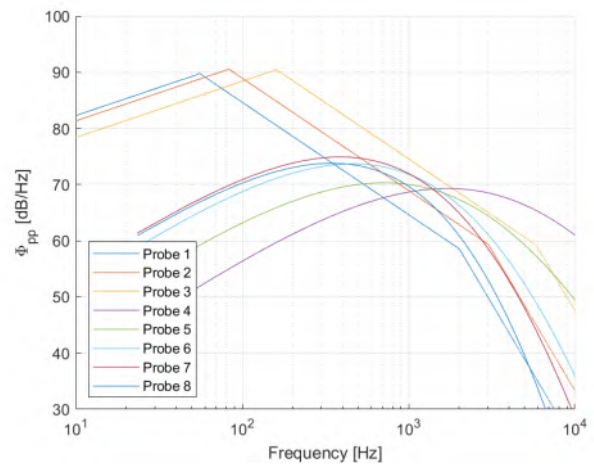


(b) Rozenberg's model

Figure 3.35 – Wall pressure spectra on the pressure side



(a) Flat plate + Guedel's model



(b) Flat plate + Rozenberg's model

Figure 3.36 – Wall pressure spectra on the suction side

3.6.1.2 Correlation length

The correlation length spectra are also obtained for each probe on both the pressure and the suction sides, as displayed in Figure 3.37. The correlation length seems to tend to infinity, but this is just an effect due to the lowest frequency set to 100 Hz. An important criterion for applying the spanwise segmentation strategy described in 2.1.4 is that the semispan of each strip should be bigger than the maximum of the correlation length at this strip (mathematically $\max(l_y) \leq 1/2L_{strip}$). For the pressure side, this implies a minimum strip span of 1.1 mm and 54 mm for the suction side. This criterion will be taken into account to define the number of trailing-edge strips in 4.1.

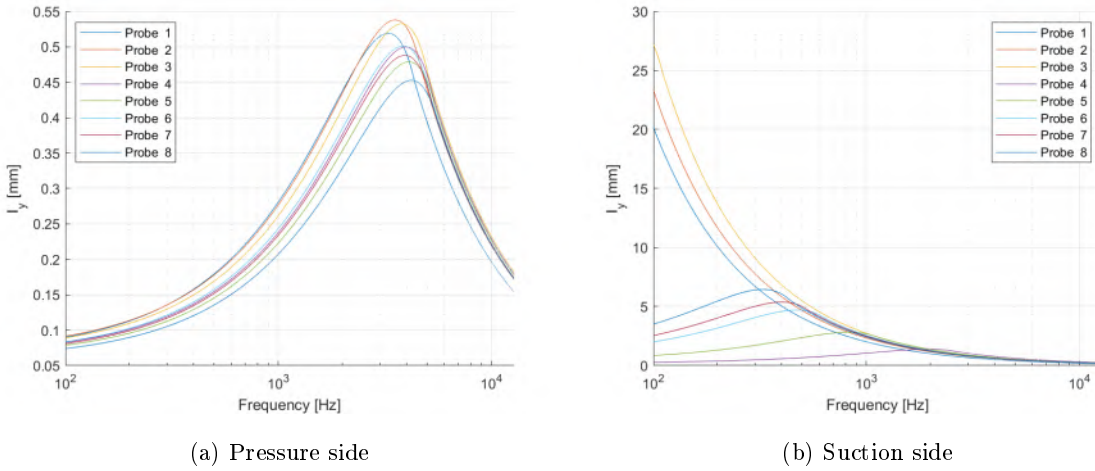


Figure 3.37 – Correlation length

3.6.2 Leading-edge noise

The application of the leading-edge analytical model (4.2.2) requires the flow velocity, the integral length scale and the turbulence intensity as input data. These will be extracted over a surface normal to the continuation of the blade midplane arc, situated upstream at a distance of 10% of the chord (see Figure 3.38 and Figure 2.3 for blade dimensions and geometry). Its width equals seven times the blade thickness ($7T$). It is similar to the surface used in Section 3.5.1, but it has been placed closer to the leading edge because it also has to cover the curved part of the leading edge. This would be impractical if it was at a distance of $0.25c$ of the leading edge, for the radius of the curved part of the visualisation area increases as we move away from the edge. The surface is normal to the leading edge, which means that it will be rectangular along the 101 mm long straight edge, but will become curved to follow the circular part of the edge. This is an important difference with respect to the estimation of the turbulence for the serration design, which only considered the straight part of the leading edge (see 3.26 and 3.25). The top corner of the curved part of the surface is trimmed because it intersects the flat plate.

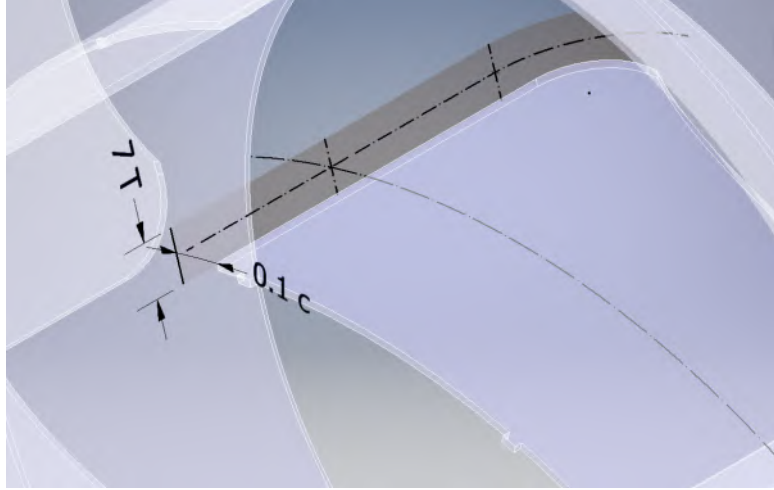


Figure 3.38 – Surface for extraction of leading-edge noise input

The data are extracted over the area and averaged along its height. The spanwise coordinate z is defined along the length of the extraction area, with the origin on the back plate. The outcome for the turbulence is displayed in Figure 3.39. There are two turbulence spots: close to the back plate ($z = 15\text{mm}$) and on the curved area of the blade, near the front plate ($113 < z < 150$). It is expected that these areas will be the main sources of leading-edge noise. The strips used for the spanwise segmentation of the blade should be bigger than twice the maximum turbulence length scale ($\max(L_t) \leq 1/2L_{strip}$). As the latter is 2.7 mm, the strips should be at least 5.4 mm wide.

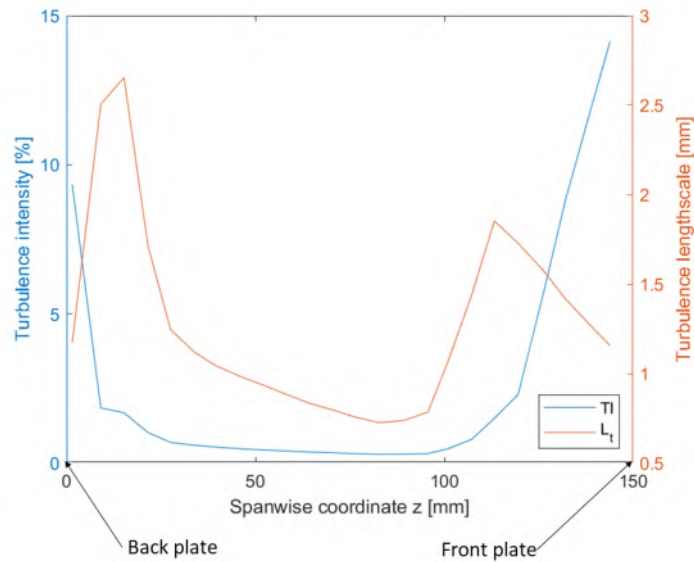


Figure 3.39 – Spanwise evolution of the leading-edge turbulence parameters

The curvature of the leading edge is also taken into account to extract the velocity components, depicted in Figure 3.40. The streamwise and spanwise directions are defined as normal and tangent to the leading edge, respectively. The streamwise velocity is dominant over the other two, albeit the normal velocity U_j being relatively high around $z = 100\text{mm}$. Only the streamwise velocity will be

used for the noise calculation.

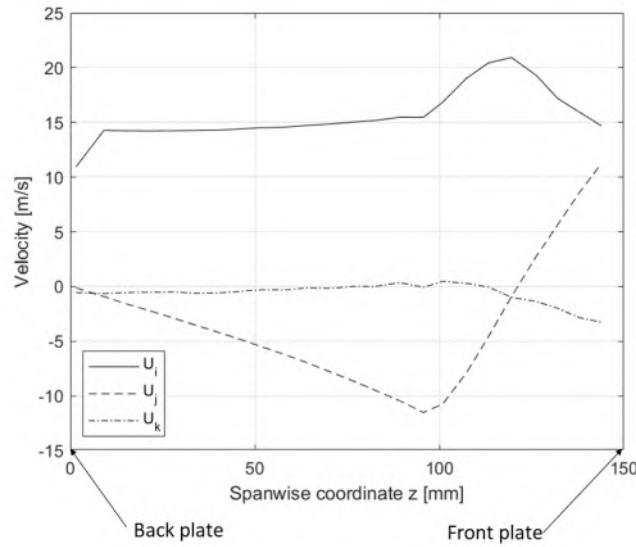


Figure 3.40 – Spanwise evolution of the velocity components upstream of the leading edge: streamwise (U_i), normal (U_j) and spanwise (U_k)

3.6.3 Front and back plates noise

Similarly to Section 3.6.1, the parameters required to apply Amiet’s trailing-edge model are extracted from the RANS simulations. A cylindrical surface coaxial with the front and back plates has been used for this purpose. It has the same radius as the plates, minus a distance of 10 mm to avoid the effect of the wake, which makes a radius of 193 mm. As an example, a visualisation of the magnitude of the relative velocity is shown in Figure 3.41.

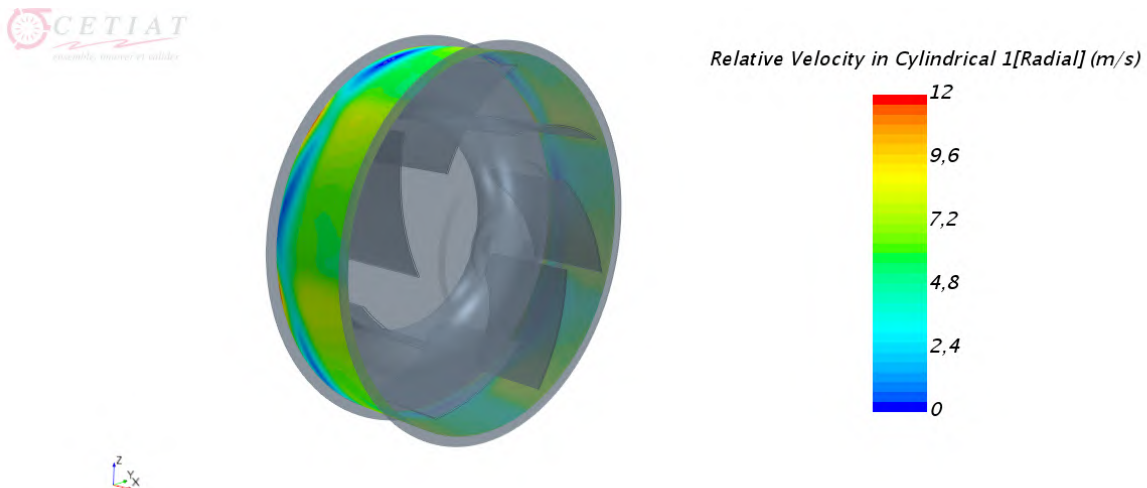


Figure 3.41 – Visualisation of the magnitude of the axial velocity, $q_v = 2196 \text{ m}^3/h$, $N=1440 \text{ rpm}$

The radial component of the velocity, which is normal to the edges of the plates, has been extracted on the cylinder. From these data, for each plate side, U_e, δ, δ^* and Θ have been estimated. The radial

	Inside		Outside	
	Front plate	Back plate	Front plate	Back plate
U_e (m/s)	8.0	8.1	4.1	3.8
δ (mm)	0.7	1.1	0.5	0.5
δ^* (mm)	0.1	0.1	0.1	0.1
Θ (mm)	0.05	0.06	0.02	0.02
τ_w (Pa)	1.0	1.0	0.7	0.7
$\frac{dP}{dr}$	999	1119	98	-34

Table 3.4 – Boundary layer values for BEP, impeller plates

component of the shear stress τ_w and the radial gradient of pressure dP/dr have been obtained on the surface of the plates, at a distance of 193 mm from the centre, and then averaged over 360 °. All the boundary layer parameters are displayed in Table 3.4.

With these parameters, the wall pressure spectra can be estimated with Rozenberg’s model (Equation 2.17) and the correlation length can be obtained with Guédél’s model (Equation 2.22).

3.7 Conclusion

The CFD simulations have replicated the tests of the baseline fan. Despite an underprediction of the total pressure, the tendency of the fan curve has been well replicated. The flow guidance through the impeller is quite good, albeit flow separation close to the front plate on the suction side. There is also a small recirculation through the gap between the inlet nozzle and the impeller. Besides, it is significant that the boundary layer is thicker on the suction side than on the pressure side.

The results for the best efficiency point have been used to estimate the turbulence integral length scale and the boundary layer thickness. These have been used in Chapter 1 to define the leading-edge and trailing-edge serrations. In both cases, an average value has been used. This strategy should be re-evaluated. For the leading edge, the maximum values of the turbulence are expected to be dominant in terms of turbulence impingement noise production. because it is not the average, but the maximum value which will be dominant in terms of noise production.

Several input parameters for the analytical model of the fan noise spectrum have been estimated from the simulations. For the trailing edge, the boundary layer parameters and the velocity profiles have been obtained along eight virtual probes, for both the pressure and the suction side. The longitudinal pressure gradient and the shear stress have also been estimated. Upstream of the leading edge, the turbulence intensity and integral length scale have also been extracted. The analytical noise prediction which uses these results as input is presented in Chapter 4.

Chapter 4

Validation of the noise prediction

This chapter presents the results of the analytical model developed in Chapter 2. Before these are discussed, a study is performed to evaluate the convergence of the model based on several numerical parameters. The results allow assessing the contribution of each part of the blade, as well as the hierarchy of the noise sources which have been modelled. Finally, the prediction is compared with the experimental results from Chapter 2. The noise of the trailing edges of the front and back plates of the impeller is also discussed.

4.1 Convergence study

There are some parameters of the analytical model which need to be adjusted. In this subsection, a numerical assessment will be performed so the values which ensure proper convergence of the analytical results are found out. Equation 2.12 will be applied while changing some of its variables: number of strips, number of points on the semicircle, semicircle radius and semicircle angle.

The analytical model is expected to yield an axisymmetric noise distribution. To verify this, the circular arc displayed in Figure 4.1 will be rotated around the Z axis. The **circular arc angle** is designated as ϕ , with 0° being horizontal and 90° vertical (albeit the distinction between both is irrelevant due to the axisymmetry).

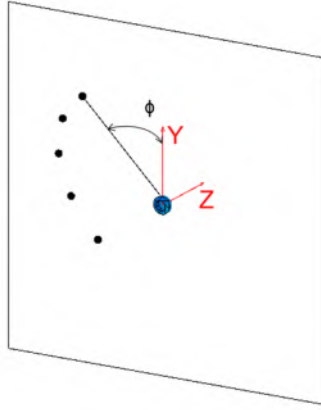


Figure 4.1 – Definition of the angle of the circular arc ϕ

The comparison of the sound power level spectra for three values of ϕ is shown in Figure 4.7a for the trailing-edge noise and in Figure 4.7b for the leading-edge noise. In both cases, the axisymmetry of the model is verified.

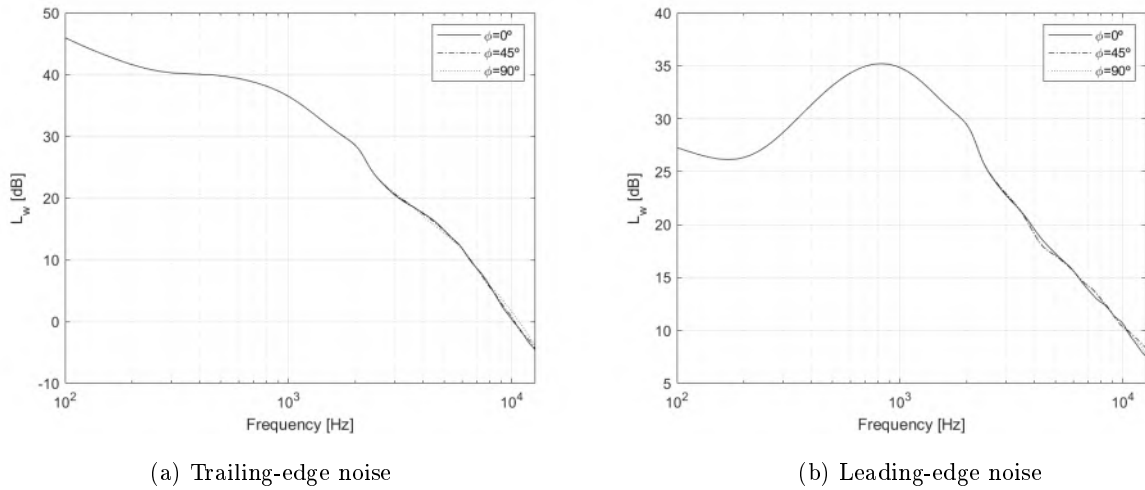
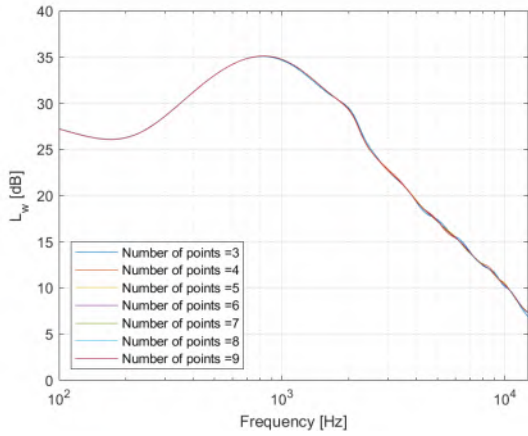


Figure 4.2 – Effect of the circular arc angle on the convergence of the analytical model ($R_{circulararc} = 3 \text{ m}$)

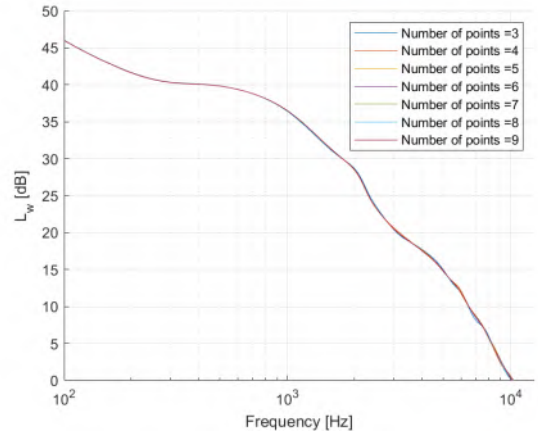
The **number of points along the circular arc** is another parameter to be tested. The points are evenly distributed, the sound pressure level is computed for each of them and at the end the sound power level is retrieved. As depicted in Figure 4.3, four points are enough in both cases to ensure the convergence of the calculation.

The study of the **radius of the circular arc** is shown in Figure 4.4. In both cases a value of 2 m is enough.

A very important parameter is the **number of strips**. There are other criteria to be taken into account besides the convergence. The strips should be as wide as possible to mitigate the distortion induced by the large aspect ratio approximation (Equations 2.3 and 2.5). On the other hand, the number of strips should be large enough to capture the spanwise evolution of the flow. A third

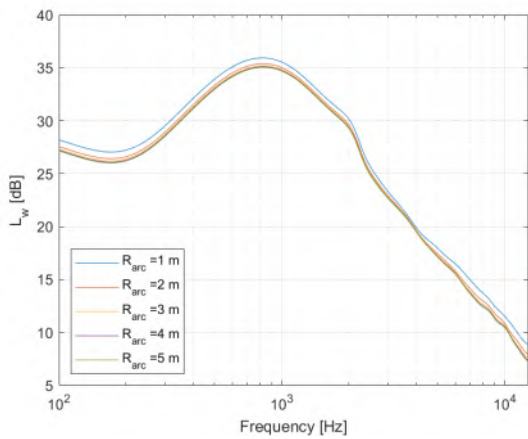


(a) Leading-edge noise

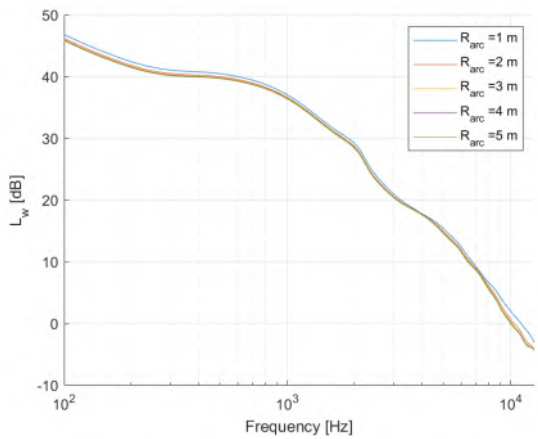


(b) Trailing-edge noise

Figure 4.3 – Effect of the discretisation of the circular arc on the convergence of the analytical model



(a) Leading-edge noise



(b) Trailing-edge noise

Figure 4.4 – Effect of the the circular arc radius on the convergence of the analytical model

criterion, already described in 3.6.1.2 and 3.6.2, sets a minimum strip width based on the maximum turbulence length scale for the leading edge and correlation length for the trailing edge.

For the trailing edge, the convergence study needs to be carried out for both pressure and suction sides. As shown in 3.6.1.2, the turbulence length scale imposes a minimum strip span of 1.1 mm for the former, whereas the correlation length sets 54 mm for the latter. However, the value for the suction side is too high, for it would imply only one or two strips. It is due to the high correlation length in probes 1, 2 and 3, where the flow detaches. If we ignore them and only consider the remaining probes, the maximum length is 6.5 mm, which yields a minimum span width of 13 mm. This sets a maximum number of strips of 7.5. The noise will be calculated with 8, 6, 4 and 2 strips, interpolating the input values calculated for 8 probes (see 3.6.1). The outcome appears in Figure 4.5. For both the pressure and the suction side, using 4 strips seems a good compromise among all the aforementioned reasons.

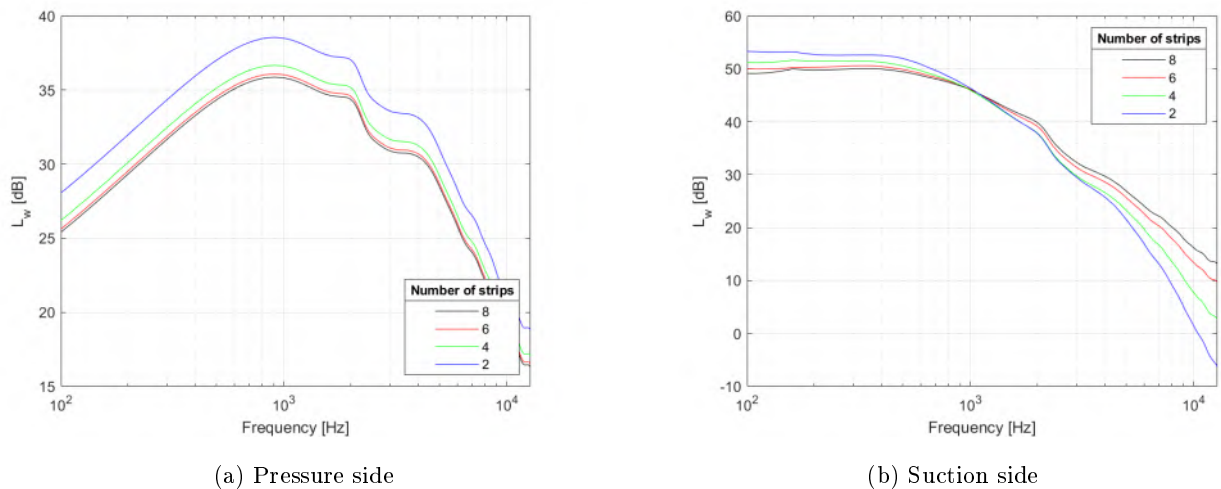


Figure 4.5 – Effect of the number of strips on the convergence of the analytical trailing-edge noise model

The study of the number of strips for the leading-edge noise calculation is slightly different. Instead of evenly dividing the whole blade into strips, this will only be done on the straight part of the leading edge (see Figure 2.3), while keeping the skewed strip undivided. The outcome of the study is depicted in Figure 4.6. Convergence is attained with 5 strips.

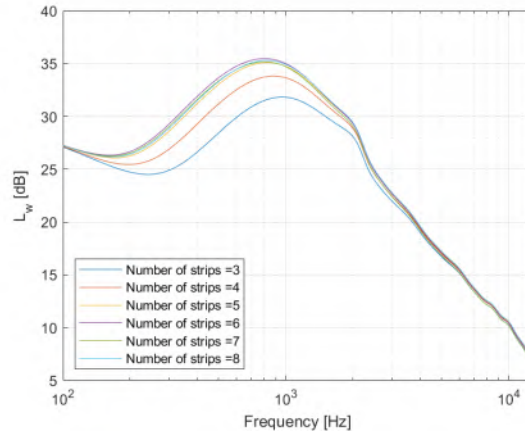


Figure 4.6 – Effect of the number of strips on the convergence of the analytical leading-edge noise model

The final division of the blade into strips, with the corresponding numbering, is depicted in Figure 4.7.

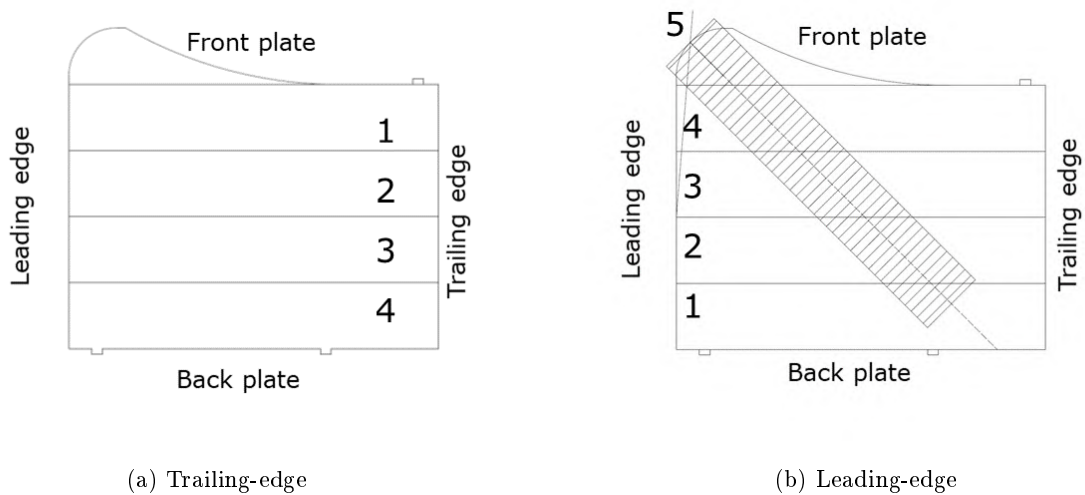


Figure 4.7 – Strips for noise calculation

As a summary, Table 4.1 shows the final parameters used for the analytical calculation.

	Trailing edge	Leading edge
Angle of the circular arc, ϕ [°]	0	0
Number of points on circular arc	4	4
Circular arc radius [m]	2	2
Number of strips	4	5

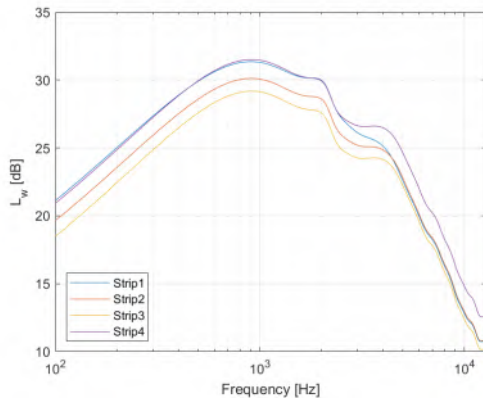
Table 4.1 – Parameters for analytical model

4.2 Analysis of results

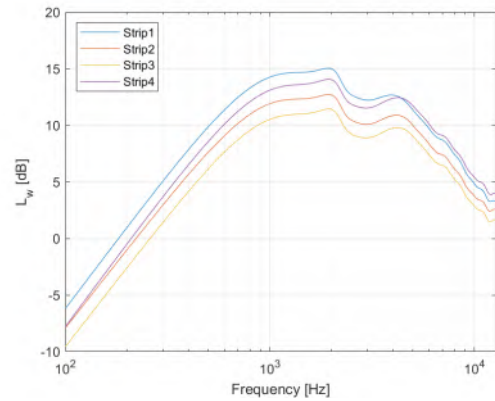
4.2.1 Trailing-edge noise

An assessment of the trailing-edge noise requires to compare pressure side with suction side and Rozenberg's model with Guedel's model. It is interesting to perform this analysis strip by strip, depicted in Figure 4.8. For the pressure side, Guedel's model yields higher noise levels, with a smaller slope at low frequencies and a bigger slope at high frequencies.

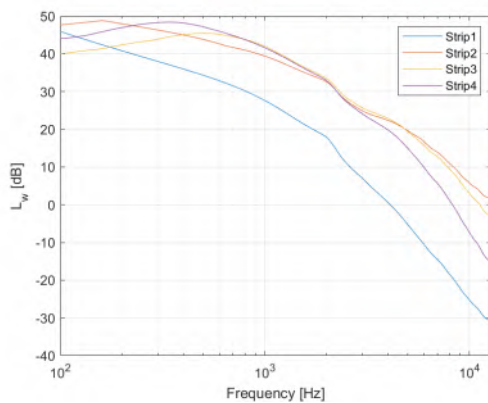
For the suction side, the situation is different. The levels for Strip 1 are the same for both cases because the wall pressure spectra input is also the same (redimensionalised spectra of a flat plate). Strip 2 is also rather similar because it is the result of interpolating between probe 3 (which is the same) and probe 4. For strips 3 and 4 we appreciate more clearly the difference between Guedel's model (with its higher level and plateau at low frequency) and Rozenberg's model (lower level and a hump at mid frequency).



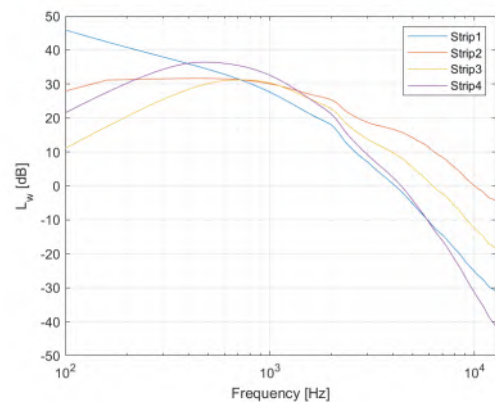
(a) Pressure side, Guedel's model



(b) Pressure side, Rozenberg's model



(c) Suction side, Guedel's model



(d) Suction side, Rozenberg's model

Figure 4.8 – Noise generated per strip: pressure side with Guedel's model (top left), pressure side with Rozenberg's model (top right), suction side with Guedel's model (bottom left), suction side with Rozenberg's model (bottom right)

The notable discrepancies between both wall-pressure models could be due to the different parameters used by each one to make the spectra dimensionless. Furthermore, Rozenberg’s model is based on measurements on static airfoils, whereas Guedel’s model was developed from measurements on fan blades.

The next stage is to combine the noise of all strips to obtain the blade noise from each side of the blade, which will be finally summed. The outcome appears in Figure 4.9. Guedel’s model yields a higher spectrum than Rozenberg’s. In both cases, the noise coming from the pressure side only contributes to the blade noise at higher frequencies.

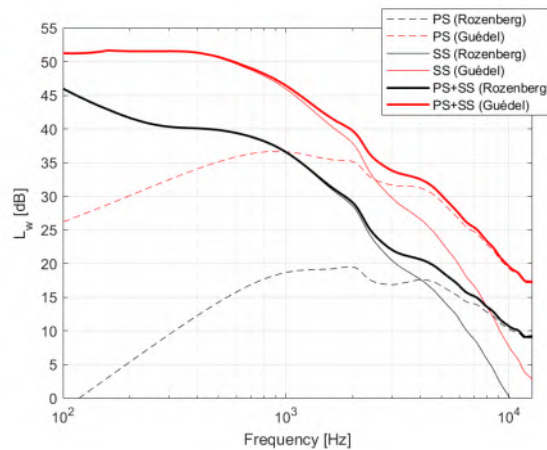


Figure 4.9 – Trailing-edge noise, results from analytical model

4.2.2 Leading-edge noise

The same strip assessment will also be performed for the leading-edge noise, illustrated in Figure 4.10. For this case, most of the noise is generated in strip 1 and, at low frequency, strip 5. The former, close to the back plate, radiates mostly at mid and high frequencies; the latter, near the front plate, generates noise at low frequencies. The remaining strips do not contribute to the blade noise, as they are at least 15 dB lower.

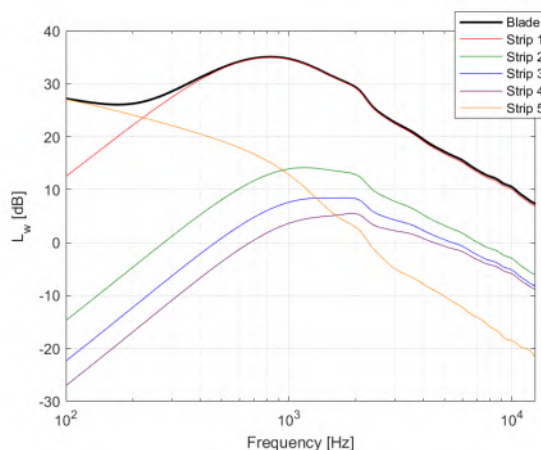


Figure 4.10 – Noise generated per strip and global blade noise

4.2.3 Combination of leading and trailing-edge noise

The final stage is to combine leading and trailing-edge noise. The result is shown in Figure 4.11. According to the model, trailing-edge noise is dominant over leading-edge noise. The latter slightly contributes to the spectra at high frequencies, and this only when combined with Rozenberg’s model, which is lower than Guedel’s.

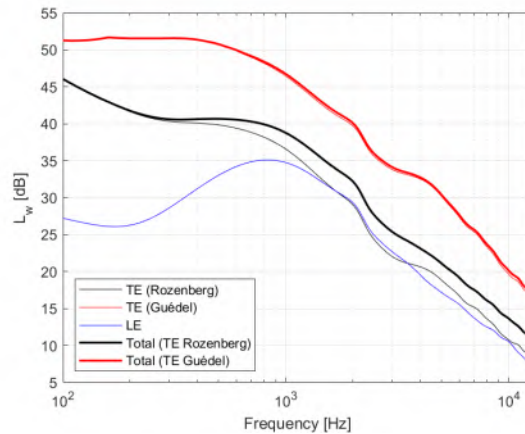


Figure 4.11 – Blade noise (trailing edge and leading edge)

4.3 Comparison with experimental results

The predicted results shown in Figure 4.12 are integrated into third-octave bands so they can be compared with the measurements from the baseline fan at the BEP (see Figure 1.14). The noise prediction obtained with Guedel’s model at the trailing edge shows a quite good agreement. In general, the experimental results are underpredicted by around 2 dB (and up to 7 dB at high frequencies), with an overprediction of 1 dB for the third-octave bands centred in 200, 250 and 400 Hz. Rozenberg’s model for the trailing edge strongly underpredicts the fan noise, being around 11 dB lower than the experimental data. The general underprediction of the results hints that other noise sources could be present inside the impeller. Yet the effectiveness of trailing-edge serrations in reducing the noise confirms that trailing-edge noise dominates.

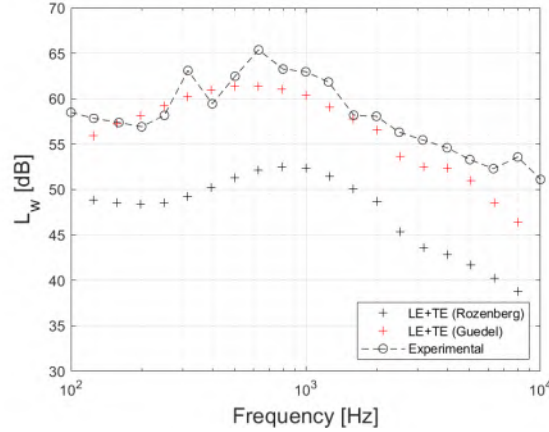


Figure 4.12 – Comparison with experimental results (trailing-edge and leading-edge noise)

Furthermore, the analytical model is based on a series of assumptions, which may contribute to the reported underprediction:

- Use of RANS simulations (estimation of the average flow values, boundary layer and turbulence parameters)
- Use of wall-pressure models (Rozenberg, Guédél) and redimensionalised empirical data (flat plate with high incidence)
- Use of a correlation length model
- Limitations on the use of the large aspect-ratio approximation

The influence of the first three points of the previous list could be assessed with a more accurate turbulence model for the CFD simulations. This is done in Section 4.6, where the previous wall-pressure spectra are compared with those obtained with LBM simulations. Besides, the flow detachment would ideally require the application of an analytical noise model specific to stall noise, such as the one proposed by Moreau *et al.* [77]. The last point could be tackled by using the full equations 2.1 and 2.4, albeit it has been shown that this is not always consistent when applied to strips with small span [99].

4.4 Noise prediction with empirical response of the impeller

Aforementioned predictions do not account for a possible resonance effect of the confined environment of the blades. A rough estimate of this effect has been obtained by measuring the transfer function between points inside and outside the impeller. The analytical prediction of the fan noise was calculated considering the empirical response of the impeller. The procedure is described in Annex E. The measurements were taken in three points for both the trailing and the leading edge: close to the front plate, close to the back plate, and at mid span. The response function was then interpolated for each strip and summed to the PSD of each strip $S_{pp}(s)$. The rest of the parameters and equations of

the analytical model have not been modified. The outcome is displayed in Figure 4.13, where TF in the legend stands for the transfer function response of the impeller.

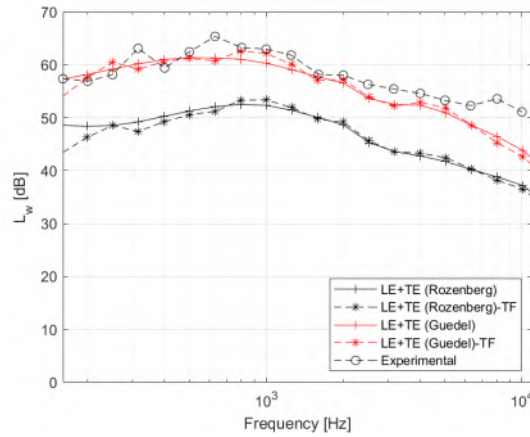


Figure 4.13 – Comparison of analytical model prediction, analytical model prediction including response of the impeller and experimental results (trailing edge and leading-edge noise)

The analytical model still slightly underpredicts the sound power level, but the shape of the spectra seems to capture some of the measured humps and dips. This gives us a hint on the possible effect of the envelope of the impeller on the noise.

4.5 Contribution of front and back plates

The estimation of the noise generated by the front and back plates is displayed in Figure 4.14. The back plate generates more noise than the front plate, and in both cases the inner side of the disk is dominant.

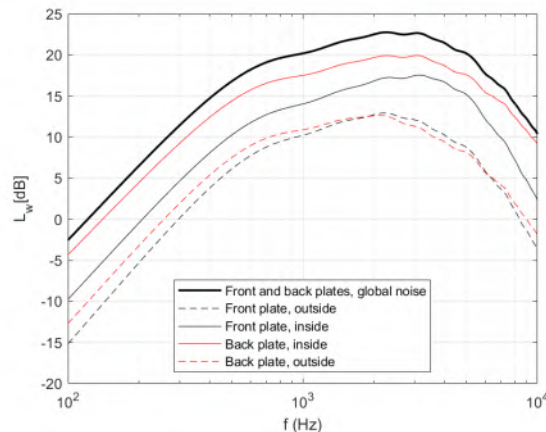


Figure 4.14 – Contribution of each side of the front and back plates and overall noise

Figure 4.15 shows that the contribution of the noise generated by the plates to the overall noise of the impeller is negligible, as it is at least 15 dB lower. Therefore, the plates do not appear to be a

noise source. The support of the fan has also been ruled out as a significant noise source, as detailed in Annex F.

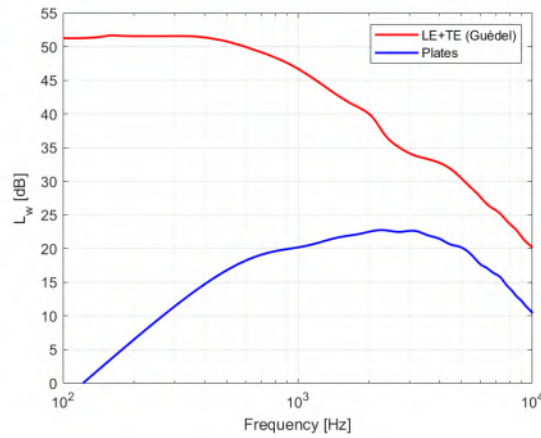


Figure 4.15 – Comparison of blade noise (trailing-edge and leading-edge noise) with the front and back plates noise

4.6 Comparison with LBM simulations

In this section, the wall-pressure spectra estimated in 3.6.1.1 for the BEP will be compared with simulations performed on the same fan with the Lattice Boltzmann Method (LBM). The setup and results are described and discussed by Sanjose *et al.* [100]. The overall numerical domain counts 98 million cells and 7 million surface elements, with a resolution around the impeller of 1 mm. A view of the mesh is displayed in Figure 4.16.

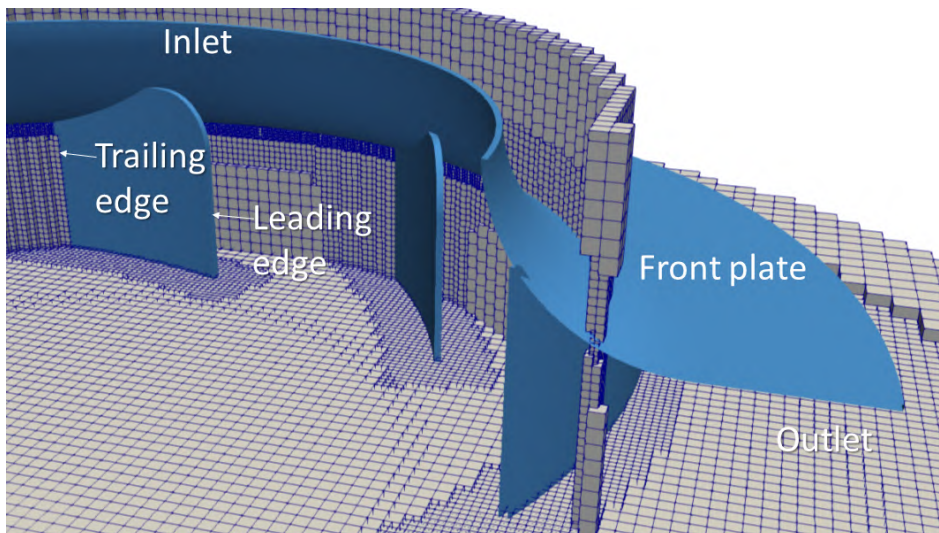


Figure 4.16 – Mesh visualization of the LBM simulations, adapted from [100]

As the simulations were performed for a rotating speed of 2975 rpm, the results need to be scaled to 1440 rpm. This is done both for the frequency and the amplitude of the PSD of the wall-pressure

fluctuations. The frequency is converted with Equation 1.9. For the amplitude of the PSD, a dependency of the air velocity to the power of 3 is used [93]. This means that the ratio of rotating speeds (N_2/N_1) will also be to the power of 3:

$$PSD_2 = PSD_1 + 10 \cdot \log_{10}((1440/2975)^3) = PSD_1 + 30 \cdot \log_{10}(1440/2975) \quad (4.1)$$

The transposition to another speed assumes some self-similarity in the flow. After applying Equations 1.9 and 4.1, the spectra of wall-pressure fluctuations obtained with the LBM simulations can be compared with the estimation from RANS. For the latter case, three different models have been used: an empirical dimensionless spectrum for the area of the blade with flow detachment and Rozenberg's or Guédél's models for the rest (see 2.2.2.1). Figure 4.17a shows the results for Probe 2, close to the front plate (see definition of probes in 3.29). With respect to the LBM, the RANS estimation based on the empirical model for flow detachment tends to underpredict wall-pressure fluctuations at low frequencies and to overpredict them at high frequencies. The results for probe 6, in the area of the blade without flow detachment, are shown Figure 4.17b. Guédél's model matches the LBM prediction at low frequencies, whereas it is up to 30 dB above it at high frequencies. Rozenberg's model is way below the LBM estimation at low frequencies but it overpredicts it by between 10 and 20 dB at high frequencies.

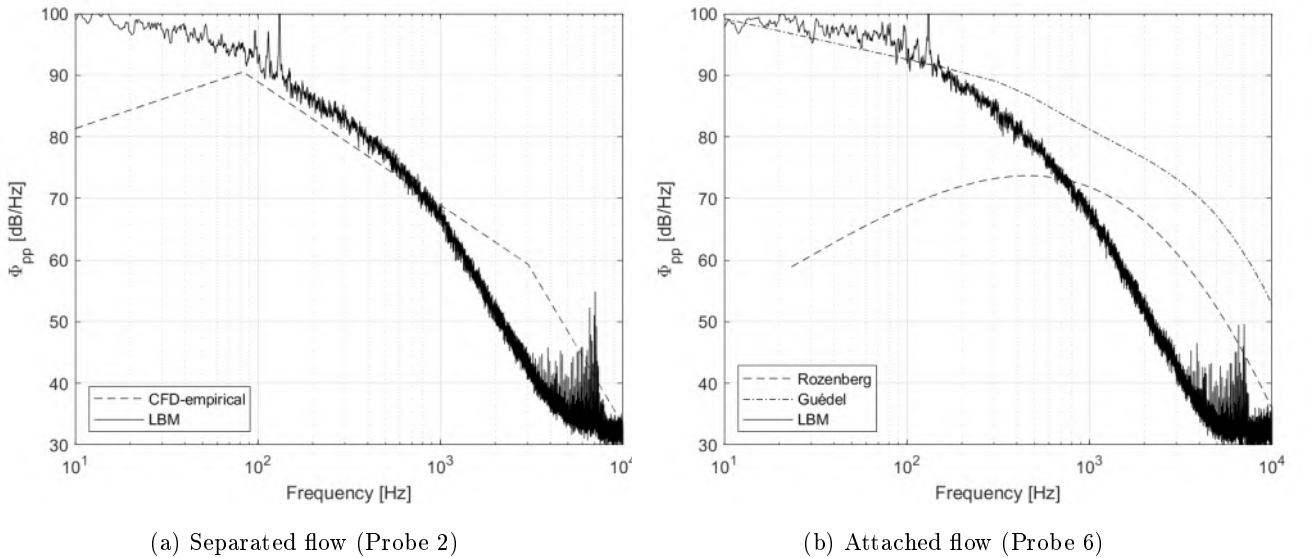


Figure 4.17 – Comparison of the wall-pressure spectra, suction side

A similar comparison has been performed for the pressure side, displayed in Figure 4.18. The tendency at low frequencies is similar to the pressure side. However, the LBM prediction is quite different to the RANS estimation at high frequencies, in terms of both amplitude and slope. This may be explained, among other causes, by the fact that the boundary layer meshing of the RANS simulations is rather coarse for its order of magnitude.

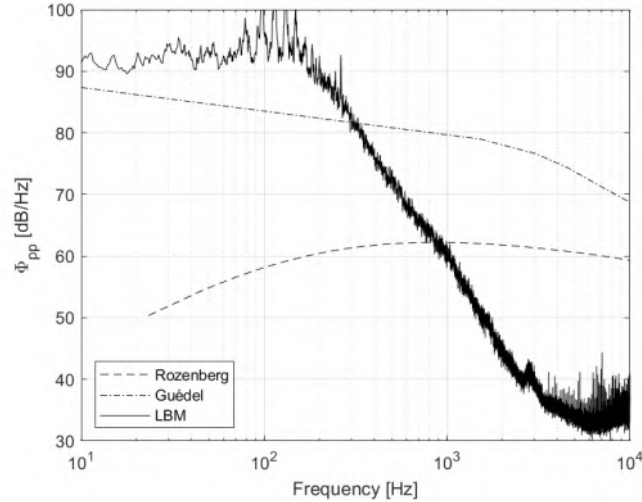


Figure 4.18 – Comparison of the wall-pressure spectra, pressure side (probe 6)

To conclude, the comparison between the LBM simulations and the RANS estimation of the wall-pressure fluctuations shows remarkable differences. The LBM spectra are, in general, similar or lower than the RANS prediction, so they could not solve the question of the underprediction of the noise described in 4.3. This also supports the hypothesis that other noise sources apart from trailing-edge noise might be present in the impeller.

4.7 Conclusion

The comparison of the analytical noise predictions with experimental results shows a certain agreement when Guédel’s model for the wall-pressure fluctuations near the trailing edge is used. Overall, the model underpredicts the fan noise by about 2 dB, with a slight overprediction between 200 and 400 Hz, which seems a reasonable performance in view of underlying assumptions and simplifications. It is worth noting that the modeling is aimed at producing very fast estimates in engineering context, when some flow features are unknown. When Rozenberg’s model is used to estimate the wall-pressure spectra, the noise is strongly underpredicted, by 11 dB on average, whatever the frequency.

There are several possible reasons behind the general tendency to underpredict the noise. First, other noise sources apart from trailing-edge and leading-edge noise could be present. Rotating stall, investigated by Sanjosé et al [100], could be one of them, but if it was the case this would only account for the low frequencies. There is also uncertainty on the data extracted from the RANS simulations. Furthermore, the use of analytical and empirical models to predict the wall pressure fluctuations, the correlation length and the turbulence intensity and integral length scale also adds uncertainty to the prediction.

The analytical results suggest that trailing-edge noise is dominant over leading-edge noise. This is

consistent with the experimental results, which show that trailing-edge serrations are more effective than leading-edge serrations in our particular application. In view of the results, the outer edges of the front and back plates are not a significant noise source for the impeller

Conclusion and perspectives

Conclusion

A bibliography review of the use of leading-edge and trailing-edge serrations on fixed airfoils and axial fans allowed to identify the most relevant variables involved in the noise reduction. This previous experience, in combination with some data extracted from CFD simulations, was used to define a design strategy to machine leading-edge and trailing-edge serrations on the blades of a plenum fan. Six different prototypes were manufactured and tested.

Experimental results for leading-edge serrations show a noise reduction at mid frequency, but an increase at high frequencies. If the degradation of the air performances is taken into account, leading-edge serrations increase noise for most of the tested configurations and operating points. This brings the serration design process into question. Instead of using the average value of the integral turbulence length scale, its maximum should have been used. Indeed, the dominant sources of leading-edge noise are associated to the areas of highly turbulent flow.

The test of impeller prototypes with trailing-edge serrations yielded a noise reduction at all frequencies for some operating points, with a maximum decrease of around 2 dBA at the nominal speed ($N = 1440$ rpm). At low flowrate and reduced speed ($N = 720$ rpm), a substantial noise reduction of up to 8 dBA is observed, due to the mitigation or even cancellation of a high-frequency peak. This peak is generated by a source near the trailing edge. The most likely hypothesis points towards laminar boundary-layer vortex shedding, maybe issued in the pressure side blade boundary layer, but this yet needs to be confirmed.

Amiet's model was adapted to the geometry of a plenum fan. The analytical results suggest that trailing-edge noise is dominant over leading-edge noise. This is consistent with the experimental results, which show that trailing-edge serrations are more effective than leading-edge serrations in this fan configuration. Furthermore, applying Amiet's model to predict the noise of the trailing edges of the front and back plates shows that this is not a significant noise source as compared with the blade trailing edge.

The comparison of the predicted and experimental results shows that the analytical model shows

a reasonable agreement, with a tendency to underpredict the noise. There are several possible reasons behind this. First, other noise sources apart from trailing-edge and leading-edge noise could be present. There is also uncertainty on the data extracted from the RANS simulations. Furthermore, the analytical and empirical models to predict the spectra and correlation lengthscales of the wall pressure fluctuations, which are the input data of the trailing-edge noise model, as well as the data to predict the leading-edge noise, also add uncertainty to the prediction.

Perspectives

The experimental results obtained with the leading-edge serrations and the experience of other investigations [12] show that characterizing the turbulence upstream of the trailing edge is paramount for their noise reduction effectiveness. However, this constitutes a challenge for industrial applications because there is a high variability of the turbulence parameters depending on the installation, the inlet configuration including the inlet nozzle and the operating conditions. For the particular case of centrifugal impellers, the change from axial to radial direction of the flow makes this problem more difficult than for axial fans. The application of trailing-edge serrations to a plenum fan has shown some success. This results might be improved by increasing the serration amplitude or by including new geometries, such as slits [7] or ogee-shaped serrations [67].

The serration design strategy described in this work, based on steady RANS, could be validated by unsteady CFD simulations, like LBM or LES. This might also help to explain the underprediction of the analytical model. To account for other noise sources, the impact of rotating stall could be assessed [74, 100]. The procedure proposed by Tetu [106] could also be an interesting alternative.

The robustness of the analytical model should be assessed by applying it to other operating points, different from the BEP. The final stage of the analytical modelling of the broadband noise of a plenum fan would be the addition of serrations. The model presented here could be completed with an existing model for leading and trailing-edge serrations [66, 45]. Even if there is a difference between the prediction and the experiment on the baseline fan, the validation of the model with serrations could be assessed by comparing the predicted and measured difference in levels between unserrated and serrated blade impellers.

Bibliography

- [1] R. K. Amiet. « Acoustic radiation from an airfoil in a turbulent stream ». In: *Journal of Sound and Vibration* 41.4 (1975), pp. 407–420. ISSN: 10958568. DOI: [10.1016/S0022-460X\(75\)80105-2](https://doi.org/10.1016/S0022-460X(75)80105-2).
- [2] R. K. Amiet. *Frame of Reference Considerations for the Forward Flight Noise Problem*. Tech. rep. East Hartford: United Aircraft Research Laboratories, 1974, pp. 1–12.
- [3] R. K. Amiet. « Noise due to turbulent flow past a trailing edge ». In: *Journal of Sound and Vibration* 47.3 (1976), pp. 387–393. ISSN: 10958568. DOI: [10.1016/0022-460X\(76\)90948-2](https://doi.org/10.1016/0022-460X(76)90948-2).
- [4] R. K. Amiet. « High frequency thin-airfoil theory for subsonic flow ». In: *AIAA Journal* (1976). ISSN: 00011452. DOI: [10.2514/3.7187](https://doi.org/10.2514/3.7187).
- [5] C. Arce Leon et al. « PIV Investigation of the Flow Past Solid and Slitted Sawtooth Serrated Trailing Edges ». In: *54th AIAA Aerospace Sciences Meeting*. January. San Diego, California: American Institute of Aeronautics and Astronautics, 2016. ISBN: 978-1-62410-393-3. DOI: [10.2514/6.2016-1014](https://doi.org/10.2514/6.2016-1014).
- [6] *Autodesk Inventor Professional 2019*. Build: 136, Release: 2019, 64-Bit Edition, 2018.
- [7] F. Avallone et al. « Noise reduction mechanisms of sawtooth and combed-sawtooth trailing-edge serrations ». In: *Journal of Fluid Mechanics* 848 (2018), pp. 560–591. ISSN: 14697645. DOI: [10.1017/jfm.2018.377](https://doi.org/10.1017/jfm.2018.377).
- [8] L. J. Ayton and P. Chaitanya. « An analytical and experimental investigation of aerofoil-turbulence interaction noise for plates with spanwise-varying leading edges ». In: *Journal of Fluid Mechanics* (2019). ISSN: 14697645. DOI: [10.1017/jfm.2019.78](https://doi.org/10.1017/jfm.2019.78).
- [9] L. J. Ayton and J. W. Kim. « An analytic solution for the noise generated by gust–aerofoil interaction for plates with serrated leading edges ». In: *Journal of Fluid Mechanics* 853 (2018), pp. 515–536. ISSN: 0022-1120. DOI: [10.1017/jfm.2018.583](https://doi.org/10.1017/jfm.2018.583).

- [10] M. Azarpeyvand, M. Gruber, and P. F. Joseph. « An analytical investigation of trailing edge noise reduction using novel serrations ». In: *19th AIAA/CEAS Aeroacoustics Conference*. 2013. ISBN: 9781624102134. DOI: [10.2514/6.2013-2009](https://doi.org/10.2514/6.2013-2009).
- [11] G. Bampanis and M. Roger. « Three-dimensional effects in the reduction of turbulence-impingement noise of aerofoils by wavy leading edges ». In: *Euronoise 2018*. Vol. 1. 2018.
- [12] T. Biedermann et al. « On the Transfer of Leading Edge Serrations from Isolated Aerofoil to Ducted Low-Pressure Fan Application ». In: *2018 AIAA/CEAS Aeroacoustics Conference (2018)*. DOI: [10.2514/6.2018-2956](https://doi.org/10.2514/6.2018-2956). URL: <https://arc.aiaa.org/doi/10.2514/6.2018-2956>.
- [13] K. Braun et al. « Serrated trailing edge noise (STENO) ». In: *Proceedings of the European Wind Energy Conference (1999)*, pp. 180–183. URL: <http://books.google.dk/books?id=TGbZHWAAAJ>.
- [14] T. F. Brooks, D. S. Pope, and M. A. Marcolini. *Airfoil self-noise and prediction*. Tech. rep. NASA, 1989.
- [15] T. Burgain. « Contribution du bruit propre des pales au bruit à large bande des ventilateurs centrifuges ». PhD thesis. École Centrale de Lyon, 1998.
- [16] L. Cardillo et al. « The use of serrated leading edge for inflow conditioning in centrifugal fan ». In: *Fan 2018 (2018)*.
- [17] F. M. Catalano and L. D. Santana. « Airfoil self noise reduction by application of different types of trailing edge serrations ». In: *28th International Congress of the Aeronautical Sciences September (2012)*. URL: <http://www.icas-proceedings.net/ICAS2012/PAPERS/778.PDF>.
- [18] P. Chaitanya et al. « Broadband noise reduction through leading edge serrations on realistic aerofoils ». In: *21st AIAA/CEAS Aeroacoustics Conference June (2015)*. DOI: [10.2514/6.2015-2202](https://doi.org/10.2514/6.2015-2202).
- [19] P. Chaitanya et al. « Leading edge serration geometries for significantly enhanced leading edge noise reductions ». In: *22nd AIAA/CEAS Aeroacoustics Conference August (2016)*. DOI: [10.2514/6.2016-2736](https://doi.org/10.2514/6.2016-2736). URL: <http://arc.aiaa.org/doi/10.2514/6.2016-2736>.
- [20] P. Chaitanya et al. « Performance and mechanism of sinusoidal leading edge serrations for the reduction of turbulence-aerofoil interaction noise ». In: *Journal of Fluid Mechanics* 818 (2017), pp. 435–464. ISSN: 14697645. DOI: [10.1017/jfm.2017.141](https://doi.org/10.1017/jfm.2017.141).
- [21] R. C. Chanaud. « Experimental Study of Aerodynamic Sound from a Rotating Disk ». In: *The Journal of the Acoustical Society of America* 45 (1969), pp. 392–397. ISSN: 0001-4966. DOI: [10.1121/1.1911386](https://doi.org/10.1121/1.1911386).

- [22] A. Chatterjee et al. « Theoretical and numerical estimation of vibroacoustic behavior of clamped free parabolic tapered annular circular plate with different arrangement of stiffener patches ». In: *Applied Sciences (Switzerland)* (2018). ISSN: 20763417. DOI: [10.3390/app8122542](https://doi.org/10.3390/app8122542).
- [23] T. P. Chong et al. « Self-Noise Produced by an Airfoil with Nonflat Plate Trailing-Edge Serrations ». In: *AIAA Journal* 51.11 (2013), pp. 2665–2677. ISSN: 0001-1452. DOI: [10.2514/1.J052344](https://doi.org/10.2514/1.J052344). URL: <http://arc.aiaa.org/doi/10.2514/1.J052344>.
- [24] V. Clair et al. « Experimental and Numerical Investigation of Turbulence-Airfoil Noise Reduction Using Wavy Edges ». In: *AIAA Journal* 51.11 (2013), pp. 2695–2713. ISSN: 0001-1452. DOI: [10.2514/1.J052394](https://doi.org/10.2514/1.J052394). URL: <http://arc.aiaa.org/doi/10.2514/1.J052394>.
- [25] F. H. Clauser. « Turbulent Boundary Layers in Adverse Pressure Gradients ». In: *Journal of the Aeronautical Sciences* (1954). DOI: [10.2514/8.2938](https://doi.org/10.2514/8.2938).
- [26] G. M. Corcos. « Resolution of Pressure in Turbulence ». In: *The Journal of the Acoustical Society of America* 33.2 (1963), pp. 192–199. ISSN: 0001-4966. DOI: [10.1121/1.1918431](https://doi.org/10.1121/1.1918431).
- [27] A. Corsini, G. Delibra, and A. G. Sheard. « On the Role of Leading-Edge Bumps in the Control of Stall Onset in Axial Fan Blades ». In: *Journal of Fluids Engineering* 135.8 (2013), p. 081104. ISSN: 0098-2202. DOI: [10.1115/1.4024115](https://doi.org/10.1115/1.4024115). URL: <http://fluidsengineering.asmedigitalcollection.asme.org/article.aspx?doi=10.1115/1.4024115>.
- [28] T. Dassen et al. « Results of a wind tunnel study on the reduction of airfoil self-noise by the application of serrated blade trailing edges ». In: *Proceeding of the European Union Wind Energy Conference and Exhibition* September (1996), pp. 800–803.
- [29] P. Davidson. *Turbulence: An Introduction for Scientists and Engineers*. Oxford, United Kingdom: Oxford University Press, 2004. ISBN: 9780198529484.
- [30] V. Dippold. « Investigation of wall function and turbulence model performance within the wind code ». In: 2005. DOI: [10.2514/6.2005-1002](https://doi.org/10.2514/6.2005-1002).
- [31] B. Efimtsov. « Characteristics of the field of turbulent wall pressure fluctuations at large reynolds numbers ». In: *Akusticheskiy zhurnal* 4 (1982), pp. 491–497.
- [32] *Environmental noise guidelines for the European Region*. Copenhagen, Denmark: World Health Organization, 2018. ISBN: 978 92 890 5356 3.
- [33] European Commision. *COMMISSION REGULATION (EU) No 327/2011: implementing Directive 2009/125/EC of the European Parliament and of the Council with regard to ecodesign requirements for fans driven by motors with an electric input power between 125 W and 500 kW*. Brussels, 2011. URL: <http://data.europa.eu/eli/reg/2011/327/oj>.

- [34] *FE2owlet*. URL: <https://www.ziehl-abegg.com/en-de/products/fe2owlet{\#}overview> (visited on 02/25/2021).
- [35] J. E. Ffowcs Williams and D. L. Hawkings. « Sound generation by turbulence and surfaces in arbitrary motion ». In: *Philosophical Transactions of the Royal Society of London. Serie A, Mathematical and Physical Sciences* 264.1151 (1969), pp. 321–342. ISSN: 1364-503X.
- [36] A. Finez et al. « Broadband noise reduction with trailing edge brushes ». In: *Proceedings of the 16th AIAA/CEAS aeroacoustics conference* (2010), pp. 1–13.
- [37] F. E. Fish et al. « The tubercles on humpback whales’ flippers: Application of bio-inspired technology ». In: *Integrative and Comparative Biology*. Vol. 51. 1. 2011, pp. 203–213. ISBN: 1557-7023 (Electronic)\n1540-7063 (Linking). DOI: [10.1093/icb/icr016](https://doi.org/10.1093/icb/icr016).
- [38] M. Goody. « Empirical spectral model of surface pressure fluctuations ». In: *AIAA Journal* (2004). ISSN: 00011452. DOI: [10.2514/1.9433](https://doi.org/10.2514/1.9433).
- [39] M. Gruber. « Airfoil noise reduction by edge treatments ». Thesis for the degree of Doctor of Philosophy. University of Southampton, 2012. URL: <https://eprints.soton.ac.uk/349012/>.
- [40] M. Gruber, M. Azarpeyvand, and P. Joseph. « Airfoil trailing edge noise reduction by the introduction of sawtooth and slitted trailing edge geometries ». In: *Proceedings of 20th International Congress on Acoustics, ICA 10*. August (2010), pp. 1–9. URL: http://www.acoustics.asn.au/conference/{_}proceedings/ICA2010/cdrom-ICA2010/papers/p686.pdf.
- [41] M. Gruber, P. Joseph, and M. Azarpeyvand. « An experimental investigation of novel trailing edge geometries on airfoil trailing edge noise reduction ». In: *19th AIAA/CEAS Aeroacoustics Conference* (2013), p. 10. DOI: [10.2514/6.2013-2011](https://doi.org/10.2514/6.2013-2011). URL: <http://www.scopus.com/inward/record.url?eid=2-s2.0-84883726260{\&}partnerID=tZ0tx3y1>.
- [42] A. Guédel. *Les ventilateurs: Bruit et techniques de réduction*. Paris: Dunod, 2015, p. 192. ISBN: 9782100725250.
- [43] A. Guédel et al. « Prediction of fan broadband noise ». In: *International conference on fans : 9-10 November 2004*. Ed. by Fluid Machinery Group of the Institution of Mechanical Engineers (IMEchE). IMechE headquarters, London, UK, 2004, pp. 25–34. DOI: [C631/009/2004](https://doi.org/10.1093/imech/9780007252500_009).
- [44] A. Guedel et al. « Prediction of the blade trailing-edge noise of an axial flow fan ». In: *Proceedings of the ASME Turbo Expo 4*. January 2011 (2011), pp. 355–365. DOI: [10.1115/GT2011-45256](https://doi.org/10.1115/GT2011-45256).
- [45] A. Halimi, B. G. Marinus, and S. Larbi. « Analytical prediction of broadband noise from mini-RPA propellers with serrated edges ». In: *International Journal of Aeroacoustics* (2019). ISSN: 20484003. DOI: [10.1177/1475472X19859889](https://doi.org/10.1177/1475472X19859889).

- [46] K. Hansen, R. Kelso, and C. Doolan. « Reduction of flow induced airfoil tonal noise using leading edge sinusoidal modifications ». In: *Acoustics Australia* 40.3 (2012), pp. 172–177. ISSN: 08146039.
- [47] S. M. Hasheminejad et al. « Airfoil Self-Noise Reduction Using Fractal-Serrated Trailing Edge ». In: *2018 AIAA/CEAS Aeroacoustics Conference*. Reston, Virginia: American Institute of Aeronautics and Astronautics, 2018. ISBN: 978-1-62410-560-9. DOI: [10.2514/6.2018-3132](https://doi.org/10.2514/6.2018-3132). URL: <https://arc.aiaa.org/doi/10.2514/6.2018-3132>.
- [48] M. Herr. « Experimental Study on Noise Reduction through Trailing Edge Brushes ». In: *New Results in Numerical and Experimental Fluid Mechanics V. Notes on Numerical Fluid Mechanics and Multidisciplinary Design (NNFM)*. Vol. 92. 2006, pp. 365–372. DOI: [10.1007/978-3-540-33287-9_45](https://doi.org/10.1007/978-3-540-33287-9_45). URL: http://link.springer.com/10.1007/978-3-540-33287-9_{ }45.
- [49] A. S. Hersh et al. « Investigation of acoustic effects of leading-edge serrations on airfoils ». In: *Journal of Aircraft* 11.4 (1974), pp. 197–202. ISSN: 00218669. DOI: [10.2514/3.59219](https://doi.org/10.2514/3.59219). URL: <http://arc.aiaa.org/doi/10.2514/3.59219>.
- [50] M. S. Howe. « Aerodynamic noise of a serrated trailing edge ». In: *Journal of Fluids and Structures* 5.1 (1991), pp. 33–45. ISSN: 10958622. DOI: [10.1016/0889-9746\(91\)80010-B](https://doi.org/10.1016/0889-9746(91)80010-B).
- [51] M. S. Howe. « Noise produced by a sawtooth trailing edge ». In: *The Journal of the Acoustical Society of America* 90.1 (1991), pp. 482–487. ISSN: 0001-4966. DOI: [10.1121/1.401273](https://doi.org/10.1121/1.401273). URL: <http://asa.scitation.org/doi/10.1121/1.401273>.
- [52] *ISO 13347: Determination of fan sound power levels under standardized laboratory conditions — Part 2: Reverberant room method*. 2004. DOI: [ISO/FDIS13347-3:2004\(F\)](https://doi.org/10.31030/ISO/FDIS13347-3:2004(F)). URL: <https://www.iso.org/standard/29753.html>.
- [53] *ISO 5801: Performance testing using standardized airways*. 2017. URL: <https://www.iso.org/standard/39542.html>.
- [54] R. Jaron et al. « Optimization of Trailing-Edge Serrations to Reduce Open-Rotor Tonal Interaction Noise ». In: *ISROMAC 2016 International Symposium on Transport Phenomena and Dynamics of Rotating Machinery*. 2016.
- [55] P. Kholodov and S. Moreau. « Optimization of trailing-edge serrations with and without slits for broadband noise reduction ». In: *Journal of Sound and Vibration* (2021). ISSN: 10958568. DOI: [10.1016/j.jsv.2020.115736](https://doi.org/10.1016/j.jsv.2020.115736).
- [56] J. W. Kim, S. Haeri, and P. Joseph. « On the reduction of aerofoil-turbulence interaction noise associated with wavy leading edges ». In: *Journal of Fluid Mechanics* 792 (2016), pp. 526–552. ISSN: 14697645. DOI: [10.1017/jfm.2016.95](https://doi.org/10.1017/jfm.2016.95).

- [57] A. S. Lau, S. Haeri, and J. W. Kim. « The effect of wavy leading edges on aerofoil–gust interaction noise ». In: *Journal of Sound and Vibration* 332.24 (2013), pp. 6234–6253. ISSN: 0022460X. DOI: [10.1016/j.jsv.2013.06.031](https://doi.org/10.1016/j.jsv.2013.06.031). URL: <http://linkinghub.elsevier.com/retrieve/pii/S0022460X13005713>.
- [58] B. E. Launder and B. I. Sharma. « Application of the energy-dissipation model of turbulence to the calculation of flow near a spinning disc ». In: *Letters in Heat and Mass Transfer* (1974). ISSN: 00944548. DOI: [10.1016/0094-4548\(74\)90150-7](https://doi.org/10.1016/0094-4548(74)90150-7).
- [59] H. M. Lee, K. M. Lim, and H. P. Lee. « Reduction of ceiling fan noise by serrated trailing edge ». In: *Fluctuation and Noise Letters* 17.3 (2018). ISSN: 02194775. DOI: [10.1142/S0219477518500268](https://doi.org/10.1142/S0219477518500268).
- [60] H. Lee and R. Singh. « Acoustic radiation from out-of-plane modes of an annular disk using thin and thick plate theories ». In: *Journal of Sound and Vibration* (2005). ISSN: 0022460X. DOI: [10.1016/j.jsv.2004.02.059](https://doi.org/10.1016/j.jsv.2004.02.059).
- [61] M. ran Lee and R. Singh. « Analytical formulations for annular disk sound radiation using structural modes ». In: *Journal of the Acoustical Society of America* (1994). ISSN: NA. DOI: [10.1121/1.409993](https://doi.org/10.1121/1.409993).
- [62] S. Lee. « Empirical wall-pressure spectral modeling for zero and adverse pressure gradient flows ». In: *AIAA Journal* 56.5 (2018), pp. 1818–1829. ISSN: 00011452. DOI: [10.2514/1.J056528](https://doi.org/10.2514/1.J056528).
- [63] M. Lighthill. « On sound generated aerodynamically I. General theory ». In: *Proceedings of the Royal Society of London. Series A. Mathematical and Physical Sciences* 211.1107 (1952), pp. 564–587. ISSN: 0080-4630. DOI: [10.1098/rspa.1952.0060](https://doi.org/10.1098/rspa.1952.0060).
- [64] M. Lighthill. « On sound generated aerodynamically II. Turbulence as a source of sound ». In: *Proceedings of the Royal Society of London. Series A. Mathematical and Physical Sciences* 222.1148 (1954), pp. 1–32. ISSN: 0080-4630. DOI: [10.1098/rspa.1954.0049](https://doi.org/10.1098/rspa.1954.0049).
- [65] B. Lyu and M. Azarpeyvand. « On the noise prediction for serrated leading edges ». In: *Journal of Fluid Mechanics* 826 (2017), pp. 205–234. ISSN: 14697645. DOI: [10.1017/jfm.2017.429](https://doi.org/10.1017/jfm.2017.429). arXiv: [1706.04509](https://arxiv.org/abs/1706.04509).
- [66] B. Lyu, M. Azarpeyvand, and S. Sinayoko. « Prediction of noise from serrated trailing edges ». In: *Journal of Fluid Mechanics* 793 (2016), pp. 556–588. ISSN: 14697645. DOI: [10.1017/jfm.2016.132](https://doi.org/10.1017/jfm.2016.132). arXiv: [1508.02276](https://arxiv.org/abs/1508.02276).
- [67] B. Lyu, L. Ayton, and P. Chaitanya. « Leading- and trailing-edge noise reduction using serrations of new geometry ». In: *Proceedings of the 23rd International Congress on Acoustics* 1 (2019), pp. 5359–5366.

- [68] B. Lyu and L. J. Ayton. « Rapid noise prediction models for serrated leading and trailing edges ». In: *Journal of Sound and Vibration* 469.July (2019), p. 115136. ISSN: 10958568. DOI: [10.1016/j.jsv.2019.115136](https://doi.org/10.1016/j.jsv.2019.115136). arXiv: 1906.02645. URL: <http://arxiv.org/abs/1906.02645><https://doi.org/10.1016/j.jsv.2019.115136>.
- [69] B. Lyu, L. J. Ayton, and P. Chaitanya. « On the acoustic optimality of leading-edge serration profiles ». In: *Journal of Sound and Vibration* 462 (2019). ISSN: 10958568. DOI: [10.1016/j.jsv.2019.114923](https://doi.org/10.1016/j.jsv.2019.114923).
- [70] B. Lyu, M. Azarpeyvand, and S. Sinayoko. « Noise Prediction for Serrated Leading-edges ». In: *22nd AIAA/CEAS Aeroacoustics Conference*. 2016. ISBN: 978-1-62410-386-5. DOI: [10.2514/6.2016-2740](https://doi.org/10.2514/6.2016-2740). URL: <http://arc.aiaa.org/doi/10.2514/6.2016-2740>.
- [71] M. Maeder et al. « Numerical analysis of sound radiation from rotating discs ». In: *Journal of Sound and Vibration* (2020). ISSN: 10958568. DOI: [10.1016/j.jsv.2019.115085](https://doi.org/10.1016/j.jsv.2019.115085).
- [72] *MATLAB*. R2018.
- [73] F. R. Menter. « Two-equation eddy-viscosity turbulence models for engineering applications ». In: *AIAA Journal* (1994). ISSN: 00011452. DOI: [10.2514/3.12149](https://doi.org/10.2514/3.12149).
- [74] L. Mongeau, D. E. Thompson, and D. K. McLaughlin. « Sound generation by rotating stall in centrifugal turbomachines ». In: *Journal of Sound and Vibration* (1993). ISSN: 10958568. DOI: [10.1006/jsvi.1993.1145](https://doi.org/10.1006/jsvi.1993.1145).
- [75] D. Moreau, L. Brooks, and C. Doolan. « On the noise reduction mechanism of a flat plate serrated trailing edge at low-to-moderate Reynolds number ». In: *18th AIAA/CEAS Aeroacoustics Conference (33rd AIAA Aeroacoustics Conference)* June (2012), pp. 1–20. DOI: [10.2514/6.2012-2186](https://doi.org/10.2514/6.2012-2186). URL: <http://arc.aiaa.org/doi/abs/10.2514/6.2012-2186>.
- [76] S. Moreau and M. Roger. « Back-scattering correction and further extensions of Amiet’s trailing-edge noise model. Part II: Application ». In: *Journal of Sound and Vibration* 323.1-2 (2009), pp. 397–425. ISSN: 0022460X. DOI: [10.1016/j.jsv.2008.11.051](https://doi.org/10.1016/j.jsv.2008.11.051).
- [77] S. Moreau, M. Roger, and J. Christophe. « Flow features and self-noise of airfoils near stall or in stall ». In: *15th AIAA/CEAS Aeroacoustics Conference (30th AIAA Aeroacoustics Conference)*. 2009. ISBN: 9781563479748. DOI: [10.2514/6.2009-3198](https://doi.org/10.2514/6.2009-3198).
- [78] S. Narayanan et al. « Airfoil noise reductions through leading edge serrations ». In: *Physics of Fluids* 27.2 (2015). ISSN: 10897666. DOI: [10.1063/1.4907798](https://doi.org/10.1063/1.4907798).
- [79] S. Oerlemans et al. « Reduction of Wind Turbine Noise Using Optimized Airfoils and Trailing-Edge Serrations ». In: *AIAA Journal* 47.6 (2009), pp. 1470–1481. ISSN: 0001-1452. DOI: [10.2514/1.38888](https://doi.org/10.2514/1.38888). URL: <http://arc.aiaa.org/doi/10.2514/1.38888>.

- [80] S. Oerlemans et al. « Reduction of Wind Turbine Noise Using Optimized Airfoils and Trailing-Edge Serrations ». In: *AIAA Journal* 47.6 (2009), pp. 1470–1481. ISSN: 0001-1452. DOI: [10.2514/1.38888](https://doi.org/10.2514/1.38888). URL: <http://arc.aiaa.org/doi/10.2514/1.38888>.
- [81] M. Ottersten, H. Yao, and L. Davidson. « Unsteady simulation of tonal noise from isolated centrifugal fan ». In: *Fan 2018*. 2018, pp. 1–10.
- [82] T. Pagliaroli et al. « Aeroacoustic Study of small scale Rotors for mini Drone Propulsion: Serrated Trailing Edge Effect ». In: *2018 AIAA/CEAS Aeroacoustics Conference* (2018), pp. 1–13. DOI: [10.2514/6.2018-3449](https://doi.org/10.2514/6.2018-3449). URL: <https://arc.aiaa.org/doi/10.2514/6.2018-3449>.
- [83] D. Palumbo. « Determining correlation and coherence lengths in turbulent boundary layer flight data ». In: *Journal of Sound and Vibration* 331.16 (2012), pp. 3721–3737. ISSN: 0022460X. DOI: [10.1016/j.jsv.2012.03.015](https://doi.org/10.1016/j.jsv.2012.03.015). URL: <http://dx.doi.org/10.1016/j.jsv.2012.03.015>.
- [84] R. W. Paterson and R. K. Amiet. « Noise and surface pressure response of an airfoil to incident turbulence ». In: *Journal of Aircraft* 14.8 (1977), pp. 729–736. ISSN: 00218669. DOI: [10.2514/3.58845](https://doi.org/10.2514/3.58845). URL: <https://arc.aiaa.org/doi/abs/10.2514/3.58845>.
- [85] D. Ragni, F. Avallone, and W. C. van der Velden. « Concave serrations on broadband trailing edge noise reduction ». In: *23rd AIAA/CEAS Aeroacoustics Conference* June (2017). DOI: [10.2514/6.2017-4174](https://doi.org/10.2514/6.2017-4174). URL: <https://arc.aiaa.org/doi/10.2514/6.2017-4174>.
- [86] P. E. Roach. « The Generation of Nearly Isotropic Turbulence by Means of Grids ». In: *International Journal of Heat and Fluid Flow* 8.2 (1987), pp. 82–92.
- [87] M. Roger and S. Serafini. « Interaction noise from a thin annulus in a circular jet ». In: *Collection of Technical Papers - 11th AIAA/CEAS Aeroacoustics Conference*. 2005. ISBN: 1563477300. DOI: [10.2514/6.2005-2958](https://doi.org/10.2514/6.2005-2958).
- [88] M. Roger and S. Moreau. « Back-scattering correction and further extensions of Amiet’s trailing-edge noise model. Part 1: Theory ». In: *Journal of Sound and Vibration* 286.3 (2005), pp. 477–506. ISSN: 0022460X. DOI: [10.1016/j.jsv.2004.10.054](https://doi.org/10.1016/j.jsv.2004.10.054).
- [89] M. Roger and S. Moreau. « Extensions and limitations of analytical airfoil broadband noise models ». In: *International Journal of Aeroacoustics* 9.3 (2010), pp. 273–305. DOI: [10.1260/1475-472X.9.3.273](https://doi.org/10.1260/1475-472X.9.3.273). URL: <https://hal.archives-ouvertes.fr/hal-00566057>.
- [90] M. Roger, S. Moreau, and A. Guedel. « Broadband fan noise prediction using single-airfoil theory ». In: *Noise Control Engineering Journal* (2006). ISSN: 07362501. DOI: [10.3397/1.2888773](https://doi.org/10.3397/1.2888773).

- [91] M. Roger, C. Schram, and L. D. Santana. « Reduction of Airfoil Turbulence-Impingement Noise by Means of Leading-Edge Serrations and / or Porous Materials ». In: *19th AIAA/CEAS Aeroacoustics Conference* (2013), pp. 1–20. DOI: [doi:10.2514/6.2013-2108](https://doi.org/10.2514/6.2013-2108).
- [92] N. Rostamzadeh et al. « The effect of undulating leading-edge modifications on NACA 0021 airfoil characteristics ». In: *Physics of Fluids* 25.11 (2013). ISSN: 10706631. DOI: [10.1063/1.4828703](https://doi.org/10.1063/1.4828703).
- [93] Y. Rozenberg. « Modélisation analytique du bruit aérodynamique à large bande des machines tournantes : utilisation de calculs moyennés de mécanique des fluides ». PhD thesis. École Centrale de Lyon, 2007.
- [94] Y. Rozenberg, G. Robert, and S. Moreau. « Wall-pressure spectral model including the adverse pressure gradient effects ». In: *AIAA Journal* (2012). ISSN: 00011452. DOI: [10.2514/1.J051500](https://doi.org/10.2514/1.J051500).
- [95] Y. Rozenberg, M. Roger, and S. Moreau. « Rotating blade trailing-edge noise: Experimental validation of analytical model ». In: *AIAA Journal* (2010). ISSN: 00011452. DOI: [10.2514/1.43840](https://doi.org/10.2514/1.43840).
- [96] R.R.Graham. « The silent flight of owls ». In: *The Journal of the Royal Aeronautical Society* 38.286 (1934), pp. 837–843.
- [97] M. Sanjosé, S. Magne, and S. Moreau. « Aeroacoustic predictions of a low speed radial fan ». In: *15th International Symposium on Transport Phenomena and Dynamics of Rotating Machinery, ISROMAC 2014* (2014).
- [98] M. Sanjosé and S. Moreau. « Unsteady numerical simulations of a low-speed radial fan for aeroacoustics predictions ». In: *ISROMAC 2012 - 14th International Symposium on Transport Phenomena and Dynamics of Rotating Machinery* (2012).
- [99] M. Sanjosé and S. Moreau. « Fast and accurate analytical modeling of broadband noise for a low-speed fan ». In: *The Journal of the Acoustical Society of America* (2018). ISSN: 0001-4966. DOI: [10.1121/1.5038265](https://doi.org/10.1121/1.5038265).
- [100] M. Sanjosé et al. « Noise mechanisms in a radial fan without volute ». In: *ISROMAC 2020 - 18th International Symposium on Transport Phenomena and Dynamics of Rotating Machinery*. 2020.
- [101] R. H. Schlinker and R. K. Amiet. « Helicopter rotor trailing edge noise ». In: *7th Aeroacoustics Conference*. NASA. Palo Alto, CA: American Institute of Aeronautics and Astronautics, 1981. DOI: [10.2514/6.1981-2001](https://doi.org/10.2514/6.1981-2001). URL: <https://ntrs.nasa.gov/archive/nasa/casi.ntrs.nasa.gov/19820003986.pdf>.

- [102] *Simcenter STAR-CCM+*. 2019.1.
- [103] S. Sinayoko, M. Kingan, and A. Agarwal. « Trailing edge noise theory for rotating blades in uniform flow ». In: *Proceedings of the Royal Society A: Mathematical, Physical and Engineering Sciences* 469.2157 (2013). ISSN: 14712946. DOI: [10.1098/rspa.2013.0065](https://doi.org/10.1098/rspa.2013.0065).
- [104] S. Sinayoko, M. Azarpeyvand, and B. Lyu. « Trailing edge noise prediction for rotating serrated blades ». In: *20th AIAA/CEAS Aeroacoustics Conference* June (2014). DOI: [10.2514/6.2014-3296](https://doi.org/10.2514/6.2014-3296). URL: <http://arc.aiaa.org/doi/10.2514/6.2014-3296>.
- [105] A. Skillen et al. « Flow over a Wing with Leading-Edge Undulations ». In: *AIAA Journal* 53.2 (2015), pp. 464–472. ISSN: 0001-1452. DOI: [10.2514/1.J053142](https://doi.org/10.2514/1.J053142). URL: <http://arc.aiaa.org/doi/10.2514/1.J053142>.
- [106] L. G. Tetu. « Experiments and analysis of the trailing edge aeroacoustics of centrifugal turbomachinery ». PhD thesis. The Pennsylvania State University, 1996, p. 298. URL: <https://dissexpress.proquest.com/dxweb/results.html?QryTxt={\&}By=tetu{\&}Title=experiments+and+analysis+of+the+trailing+edge+aeroacoustics{\&}pubnum=9702400>.
- [107] E. A. Van Nierop, S. Alben, and M. P. Brenner. « How bumps on whale flippers delay stall: An aerodynamic model ». In: *Physical Review Letters* 100.5 (2008). ISSN: 00319007. DOI: [10.1103/PhysRevLett.100.054502](https://doi.org/10.1103/PhysRevLett.100.054502).
- [108] Y. Wang et al. « Bio-inspired aerodynamic noise control: A bibliographic review ». In: *Applied Sciences* 9.11 (2019). ISSN: 20763417. DOI: [10.3390/app9112224](https://doi.org/10.3390/app9112224). URL: <https://doi.org/10.3390/app9112224>.
- [109] C. Weckmüller and S. Guérin. « On the influence of trailing-edge serrations on open-rotor tonal noise ». In: *18th AIAA/CEAS Aeroacoustics Conference (33rd AIAA Aeroacoustics Conference)*. 2012. ISBN: 9781600869327. DOI: [10.2514/6.2012-2124](https://doi.org/10.2514/6.2012-2124).
- [110] G. Yakhina et al. « Experimental and Analytical Investigation of the Tonal Trailing-Edge Noise Radiated by Low Reynolds Number Aerofoils ». In: *Acoustics* (2020). DOI: [10.3390/acoustics2020018](https://doi.org/10.3390/acoustics2020018).
- [111] M. Younsi. « Aeroacoustique et Aerodynamique Instationnaire, Numerique Et Experimentale Des Ventilateurs Centrifuges à Action ». PhD thesis. École Nationale Supérieure d’Arts et Métiers, 2007. URL: <https://tel.archives-ouvertes.fr/pastel-00003220/>.
- [112] M. V. Zagarola and A. J. Smits. « Mean-flow scaling of turbulent pipe flow ». In: *Journal of Fluid Mechanics* (1998). ISSN: 00221120. DOI: [10.1017/S0022112098002419](https://doi.org/10.1017/S0022112098002419).

- [113] F. Zenger and S. Becker. « Experimental investigation of the sound reduction by leading edge serrations on a flat-plate axial fan ». In: *2018 AIAA/CEAS Aeroacoustics Conference* (2018). ISSN: 2017-3387. DOI: [10.2514/6.2017-3387](https://doi.org/10.2514/6.2017-3387). URL: <https://arc.aiaa.org/doi/10.2514/6.2017-3387>.
- [114] F. Zenger, A. Renz, and S. Becker. « Experimental Investigation of Sound Reduction by Leading Edge Serrations in Axial Fans ». In: *23rd AIAA/CEAS Aeroacoustics Conference* June (2017), pp. 1–13. DOI: [10.2514/6.2017-3387](https://doi.org/10.2514/6.2017-3387). URL: <https://arc.aiaa.org/doi/10.2514/6.2017-3387>.
- [115] M. M. Zhang, G. F. Wang, and J. Z. Xu. « Aerodynamic Control of Low-Reynolds-Number Airfoil with Leading-Edge Protuberances ». In: *AIAA Journal* 51.8 (2013), pp. 1960–1971. ISSN: 0001-1452. DOI: [10.2514/1.J052319](https://doi.org/10.2514/1.J052319). URL: <http://arc.aiaa.org/doi/10.2514/1.J052319>.

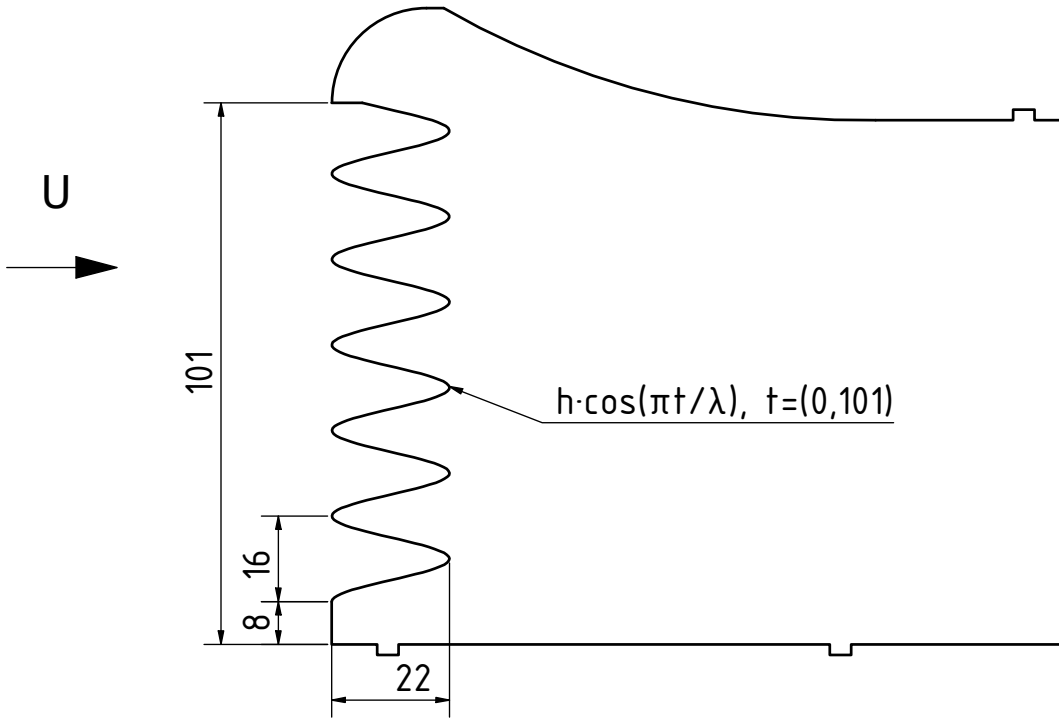
Appendix A

Drawings of serrated flat blades

Impeller LE_L16H11

$\lambda=16$ mm

$2h=22$ mm

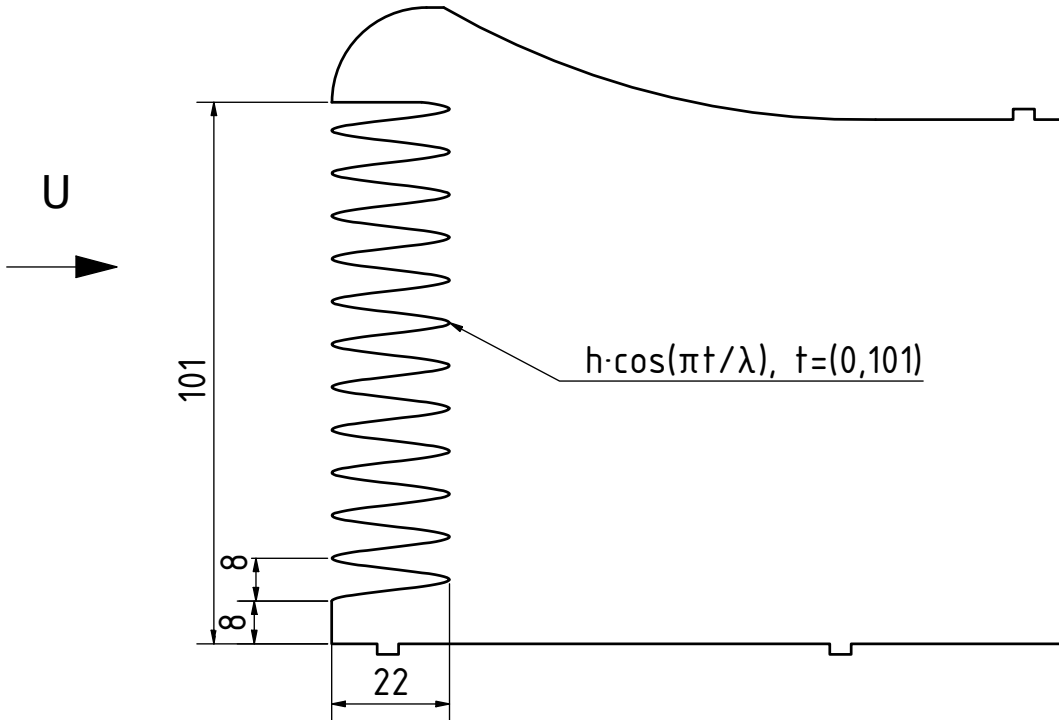


SCALE 1:2

Impeller LE_L8H11

$\lambda=8$ mm

$2h=22$ mm

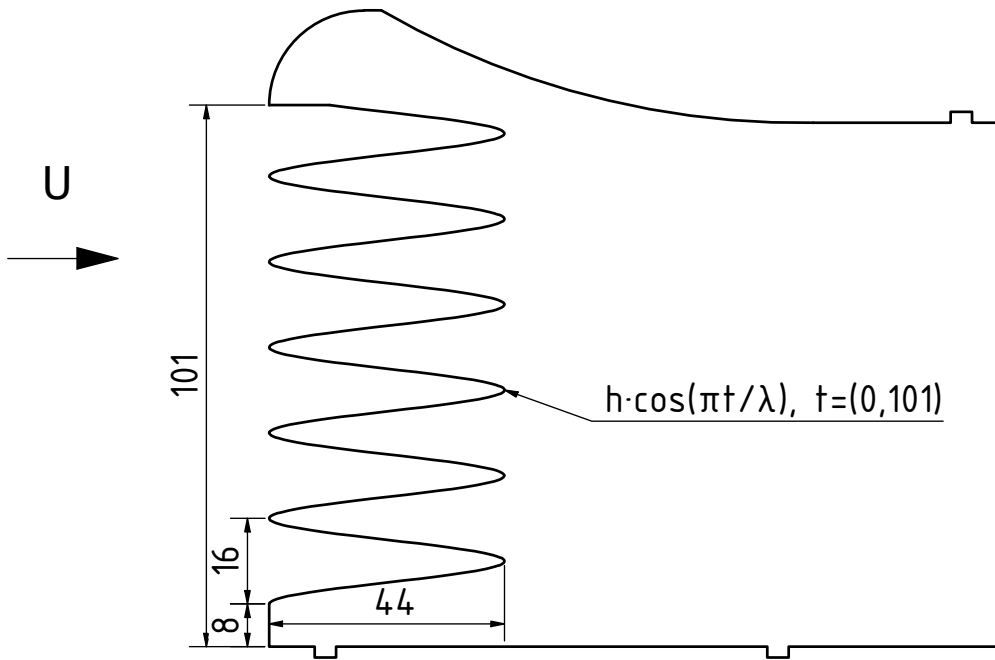


SCALE 1:2

Impeller LE_L16H22

$\lambda=16$ mm

$2h=44$ mm

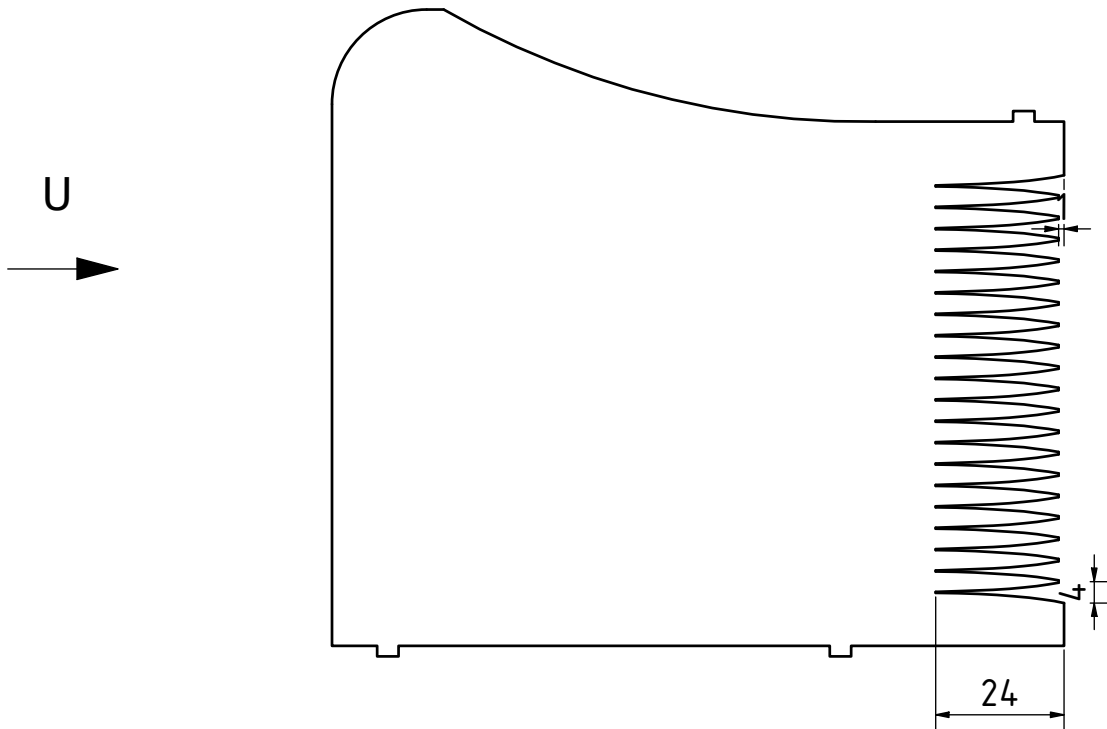


SCALE 1:2

Impeller TE_L4H12

$\lambda=4$ mm

$2h=24$ mm



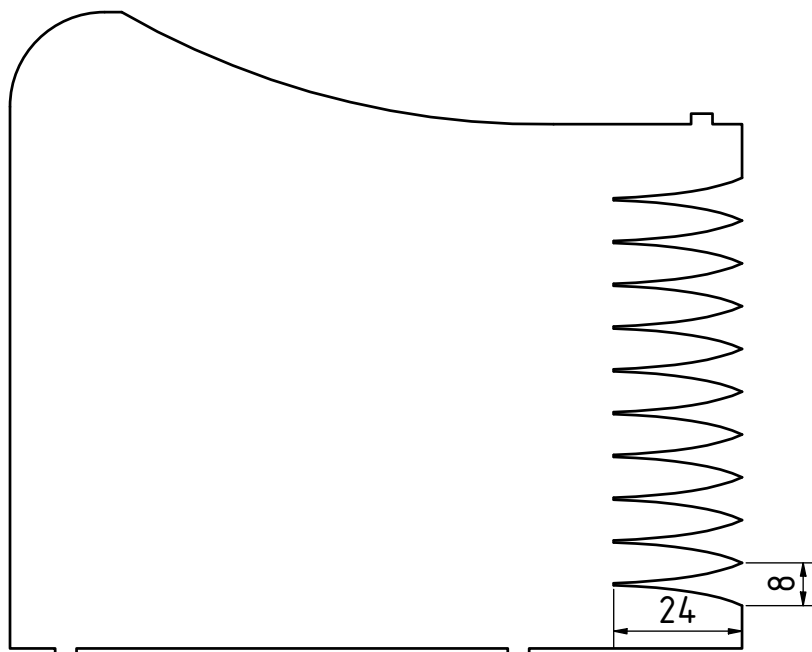
SCALE 1:2

Impeller TE_L8H12

$\lambda=8$ mm

$2h=24$ mm

U
→



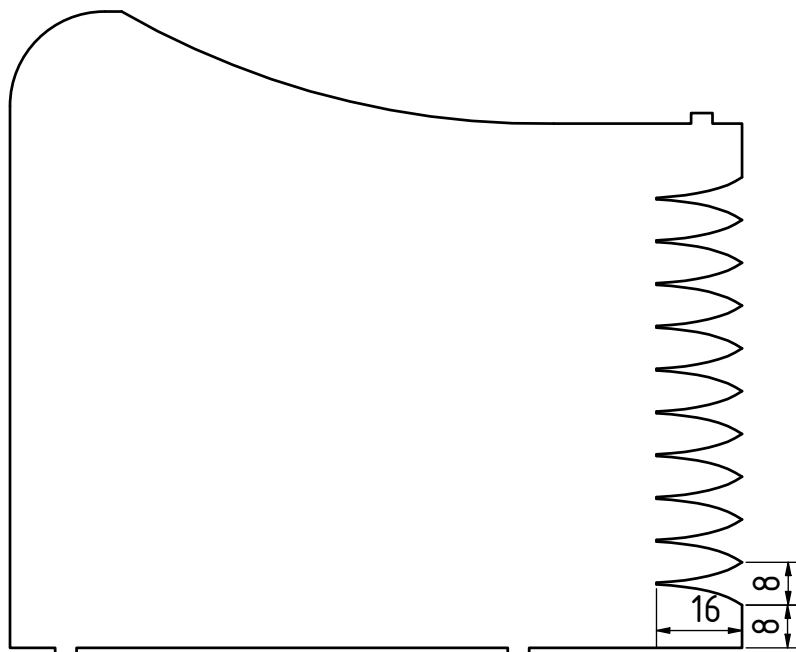
SCALE 1:2

Impeller TE_L8H8

$\lambda=8$ mm

$2h=16$ mm

U
→



SCALE 1:2

Appendix B

Impact of fan assembly on acoustics

During the project, different assemblies of the fan were used. This proved to have an important impact on the noise generated by the whole system due to vibroacoustic issues. Four different setups were used: a table with two boards separated by two concrete blocks (Figure B.1a), a board supported by a tripod (Figure B.1b), a table clamped on one side to the wall of the room (Figure B.1c) and the same clamped table but vibration-decoupled (Figure B.1d).

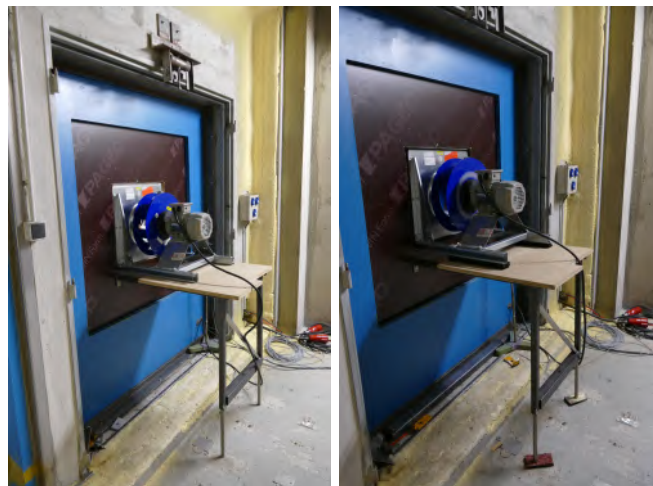
B.1 Nominal speed: 1440 rpm

The overall sound power level (Figure B.2) appears to be relatively high for the setup with the table. If we add some vibration decoupling elements, we can reduce the noise up to a level similar to the double table. The level of the assembly with the tripod falls somewhere in between.



(a) Double table

(b) Tripod



(c) Table

(d) Decoupled table

Figure B.1 – Different fan assemblies

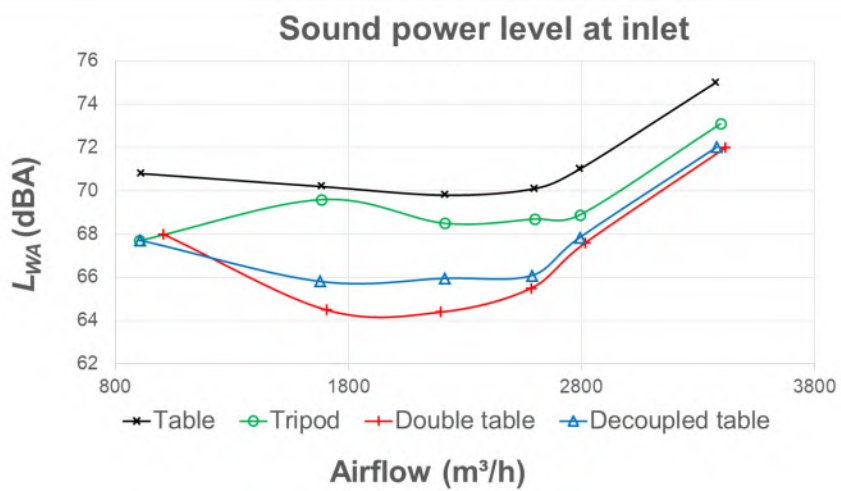


Figure B.2 – Overall sound power level at the fan inlet for the different assemblies

In Figure B.3, third octave band sound power spectra complement the overall levels. The higher levels of the table and tripod setups are mainly due to a peak centred at 630 Hz (and at 315 Hz for the table). Despite showing the lowest levels, the double table and decouple table assemblies have rather high levels at low frequencies, but their contribution is mitigated by the A-weighting. The

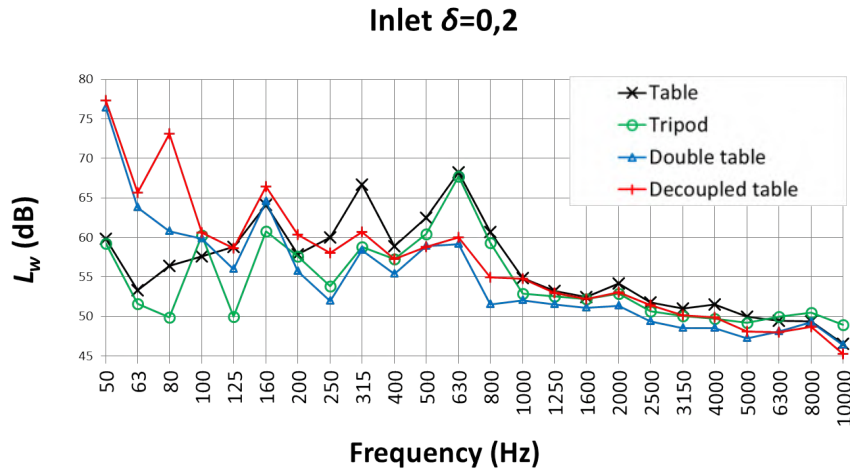


Figure B.3 – Third octave band plots for the different assemblies

comparison of the table and the decoupled table is available in Figure B.4. It is to be noted that the L16H11 impeller was not tested with the table assembly and only results with the tripod assembly are available. The same tendencies as for the baseline impeller are observed: decoupling the table significantly reduces the overall level and replacing the tripod by the decoupled table slightly reduces the noise.

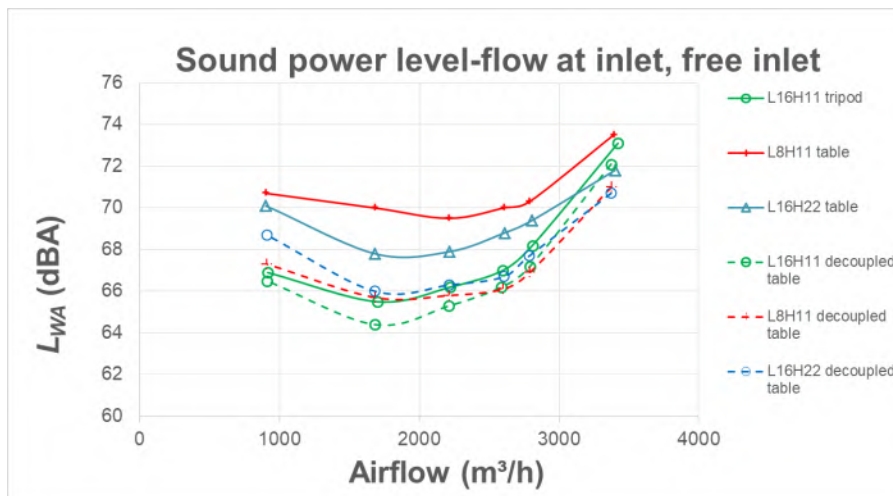


Figure B.4 – Sound power level at inlet for the serrated impellers with different assemblies

B.2 Partial speed: 720 rpm

At 720 rpm, only results for the double table and tripod setups are available. However, for the second configuration, two different experimental campaigns were carried out, in September 2018 and in April 2019. As shown in Figure B.5, there is a big difference between the results for the double table and the tripod setups, specially at the inlet. This actually motivated the tests in September.

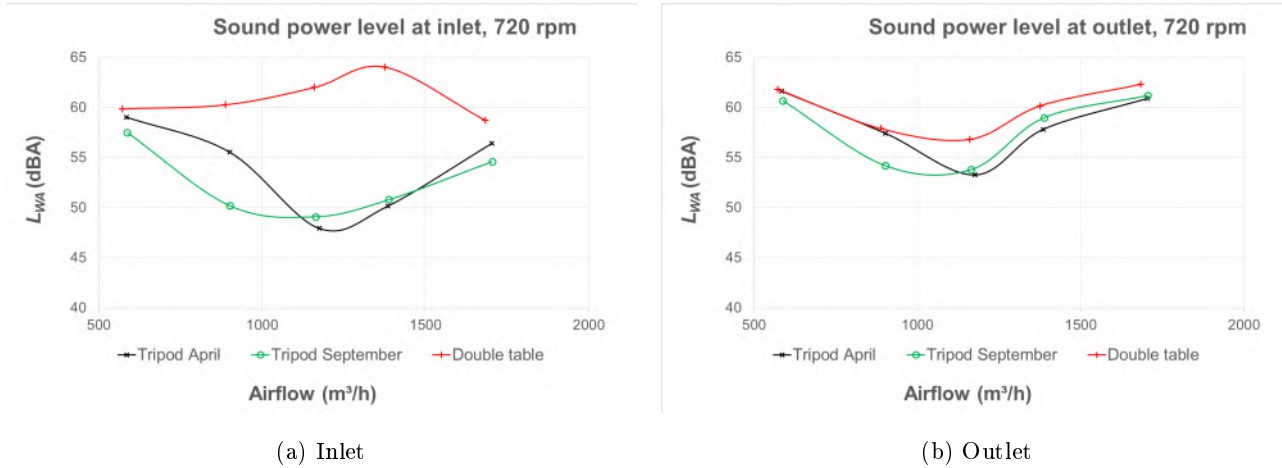


Figure B.5 – Overall sound power level

Figure B.6 presents the sound power spectra in third octave bands for the setups from Figure B.5. There is an overall increase on the noise at inlet for the double table setup, and an increase at low frequencies at outlet. On the other hand, there is a very good agreement between the results of April and September.

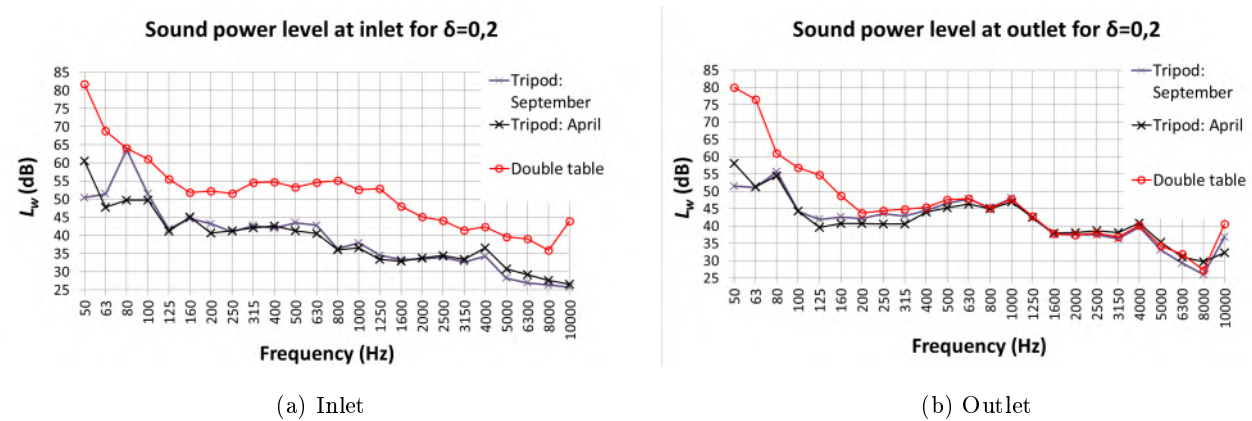


Figure B.6 – Third octave bands for $N=720$ rpm, $\delta = 0.1$

B.3 Conclusion

The test setup and the assembly of the fan plays an important role on the noise. It is paramount to carefully assure that it does not disrupts the noise measurements.

Appendix C

Aeroacoustic transfer functions

The notation of this appendix follows the publication by Roger & Moreau [89].

C.1 Trailing edge

The tridimensional radiation integral \mathcal{I} is given by $\mathcal{I} = \mathcal{I}_1 + \mathcal{I}_2$. The first-order term (trailing-edge solution) for a supercritical gust ($\Theta_0 < 1$) is calculated from

$$\mathcal{I}_1 = -\frac{e^{2iC}}{iC} \left\{ (1+i)e^{-2iC} \sqrt{\frac{B}{B-C}} E^*[2(B-C)] - (1+i)E^*(2B) + 1 \right\}$$

with

$$E^*(x) = \int_0^x \frac{e^{-it}}{\sqrt{2\pi t}} dt$$

$$C = \bar{K}_1 - \bar{\mu} \left(\frac{x_1}{S_0} - M \right) \quad B = \bar{K}_1 + M\bar{\mu} + \bar{\kappa}$$

with $M = U/c_0$ $X = \frac{x}{b}$ $Y = \frac{y}{b}$ $Z = \frac{\beta z}{b} \beta^2 = 1 - M^2$ $\bar{\mu} = \frac{kc}{2\beta^2} = \frac{k_1^* M}{\beta^2}$ $\bar{\kappa}^2 = \bar{\mu}^2 - \frac{\bar{K}_2^2}{\beta^2}$ and the corrected distance for convection effect

$$S_0^2 = x_1^2 + \beta^2 (x_2^2 + x_3^2)$$

The leading-edge back-scattering correction for supercritical gusts ($\Theta_0 < 1$) is given by:

$$\mathcal{I}_2 = \left\{ \left\{ e^{4i\bar{\kappa}} [1 - (1+i)E^*(4\bar{\kappa})] \right\}^c - e^{2iD} + i[D + \bar{K}_1 + M\bar{\mu} - \bar{\kappa}]G \right\} H$$

where

$$H = \frac{(1+i)e^{-4i\bar{\kappa}} (1 - \Theta^2)}{2\sqrt{\pi}(\alpha - 1)\bar{K}_1\sqrt{B}} \quad D = \bar{\kappa} - \bar{\mu}x_1/S_0 \quad \Theta = \sqrt{\frac{\bar{K}_1 + \bar{\mu}M + \bar{\kappa}}{\bar{K}_1 + \bar{\mu}M + \bar{\kappa}}} \quad \alpha = \frac{U_0}{Uc}$$

and

$$G = (1 + \epsilon)e^{i(2\bar{\kappa}+D)} \frac{\sin(D - 2\bar{\kappa})}{D - 2\bar{\kappa}} + (1 - \epsilon)e^{i(-2\bar{\kappa}+D)} \frac{\sin(D + 2\bar{\kappa})}{D + 2\bar{\kappa}} + \frac{(1 + \epsilon)(1 - i)}{2(D - 2\bar{\kappa})} e^{4i\bar{\kappa}} E^*(4\bar{\kappa})$$

$$- \frac{(1 - \epsilon)(1 + i)}{2(D + 2\bar{\kappa})} e^{-4i\bar{\kappa}} E(4\bar{\kappa}) + \frac{e^{2iD}}{2} \sqrt{\frac{2\bar{\kappa}}{D}} E^*(2D) \left[\frac{(1 - \epsilon)(1 + i)}{D + 2\bar{\kappa}} - \frac{(1 + \epsilon)(1 - i)}{D - 2\bar{\kappa}} \right]$$

and the notation $\{\cdot\}^C$ means that the imaginary part must be multiplied by the factor $\epsilon = 1/\sqrt{1 + 1/(4\bar{\mu})}$

For sub-critical gusts ($\Theta_0 > 1$ and $\bar{\kappa}'^2 < 0$), the terms of the aeroacoustic transfer function take the form

$$\mathcal{I}_1 = -\frac{e^{-2iC}}{iC} \left\{ e^{-2iC} \sqrt{\frac{A'_1}{\bar{\mu}(x_1/S_0) - i\bar{\kappa}'}} \Phi^o([2i(\bar{\mu}(x_1/S_0) - i\bar{\kappa}')]^{1/2}) - \Phi^o([2iA'_1]^{1/2}) + 1 \right\}$$

and

$$\mathcal{I}_2 = \frac{e^{-2iB'}}{B'} H' \left\{ A' \left(e^{2iB'} [1 - \text{erf}(\sqrt{4\bar{\kappa}'})] - 1 \right) + \sqrt{2\bar{\kappa}'} \left(k_1^* + \left(M - \frac{x_1}{S_0}\right)\bar{\mu} \right) \frac{\Phi^0\sqrt{-2iB'}}{\sqrt{-iB'}} \right\} H$$

where Φ^o is the complementary error function of complex argument and

$$H' = \frac{(1+i)(1-\Theta'^2)}{2\sqrt{\pi}(\alpha-1)k_1^*\sqrt{A'_1}}, \quad A'_1 = \bar{K}_1 + M\bar{\mu} - i\bar{\kappa}'$$

$$A' = k_1^* + M\bar{\mu} - i\bar{\kappa}', \quad \Theta' = \sqrt{\frac{A'_1}{A'}}, \quad B' = \bar{\mu} \left(\frac{x_1}{S_0} \right) - i\bar{\kappa}'$$

C.2 Leading edge

As for the trailing edge, the transfer function is the sum of two contributions: $\mathcal{L} = \mathcal{L}_1 + \mathcal{L}_2$. For subcritical gusts its expression reads:

$$\mathcal{L}_1 = -\frac{1}{\pi} \sqrt{\frac{2}{(k_1^* + i\beta^2\bar{\kappa}')i\Theta_3}} e^{i\Theta_2} E[2i\Theta_3]$$

$$\mathcal{L}_2 = \frac{e^{-i\Theta_2}}{\pi\sqrt{2\pi(k_1^* + i\beta^2\bar{\kappa}')}\Theta_3} \left\{ 1 - e^{-2\Theta_3} - \text{erf}(\sqrt{4\bar{\kappa}'}') + 2e^{-2\Theta_3} \sqrt{\frac{\bar{\kappa}'}{i\bar{\kappa}' + \bar{\mu}x_1/S_0}} E[2(i\bar{\kappa}' + \bar{\mu}x_1/S_0)] \right\}$$

with

$$\Theta_2 = \bar{\mu}(M - x_1/S_0) - \frac{\pi}{4}, \quad \Theta_3 = \bar{\kappa}' + i\bar{\mu}\frac{x_1}{S_0}, \quad \bar{\kappa}' = \sqrt{\frac{k_2^{*2}}{\beta^2} - \bar{\mu}^2}, \quad \bar{\kappa}'^2 = \bar{\mu}^2 \left(\frac{1}{\Theta_0^2} - 1 \right)$$

E is related to Fresnel integrals: $E(\xi) = \int_0^\xi \frac{e^{it}}{\sqrt{2\pi t}} dt$

For a supercritical oblique gust ($\Theta_0 > 1$ and $\bar{\kappa}'^2 < 0$), the aeroacoustic transfer function is deduced by changing $i\bar{\kappa}'$ by $i\bar{\kappa}$ and by replacing the error function $\text{erf}(\sqrt{\cdot})$ by the function $(1-i)E$: $\mathcal{L} = \mathcal{L}_1 + \mathcal{L}_2$.

Its expression then reads:

$$\mathcal{L}_1 = -\frac{1}{\pi} \sqrt{\frac{2}{(k_1^* + \beta^2\bar{\kappa})\Theta_1}} e^{i\Theta_2} E[2\Theta_4]$$

$$\mathcal{L}_2 = \frac{e^{-i\Theta_2}}{\pi\sqrt{2\pi(k_1^* + \beta^2\bar{\kappa})}\Theta_4} \left\{ i(1 - e^{2i\Theta_1}) - (1+i) \left[E(4\bar{\kappa}) - e^{2i\Theta_1} \sqrt{\frac{2\bar{\kappa}}{\bar{\kappa} + \bar{\mu}x_1/S_0}} E[2(\bar{\kappa} + \bar{\mu}x_1/S_0)] \right] \right\}$$

Appendix D

Trailing-edge noise input parameters

D.1 Boundary layer

The classical equations for the boundary layer parameters of a flat plate with incompressible flow have been used. The boundary layer thickness δ is defined as the value of the normal coordinate y where 99% of the free stream velocity U_e is reached

$$\delta = y : U(y) = 0.99U_e = U_{99}$$

From δ we can compute the displacement thickness δ^* :

$$\delta^* = \int_0^\delta \left(1 - \frac{U(y)}{U_{99}}\right) dy$$

as well as the momentum thickness Θ :

$$\theta = \int_0^\delta \frac{U(y)}{U_{99}} \left(1 - \frac{U(y)}{U_{99}}\right) dy$$

D.2 Rozenberg model parameters [94]

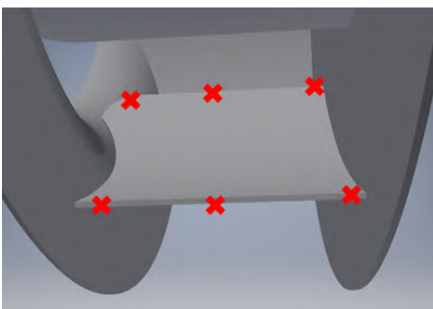
$$A_1 = 3.7 + 1.5\beta_c, \quad A_2 = \min(3.19/\sqrt{R_T}) + 4, \quad F_1 = 4.76 \left(\frac{1.4}{\Delta}\right)^{0.75} [0.375A_1 - 1]$$

In the previous expressions Zagarola and Smith's [112] parameter ($\Delta = \delta/\delta^*$), as well as Clauser's [25] ($\beta_C = (\delta^*/\tau_w)(dp/dx_1)$), have been used, where τ_w is the wall shear stress and (dp/dx_1) is the mean pressure gradient on the blade wall in the streamwise direction. The wake parameter is modelled with $\Pi = 0.8(\beta_c + 0.5)^{3/4}$ and $C'_3 = 8.8R_T^{-0.57}$ is a parameter from Goody's model. The ratio of the outer to inner boundary layer time scale is $R_T = (\delta/U_E)/(\nu/u_\tau^2)$, where ν is the kinematic viscosity. The friction velocity is given by $u_\tau = \sqrt{\tau_w/\rho}$, where ρ is the air density.

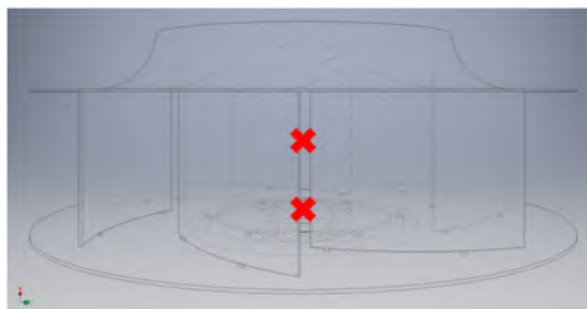
Appendix E

Measurement of the response of the isolated stationary impeller

The effect of the geometry of the impeller on the noise sources was measured experimentally inside Cetiat's *Reverb2* reverberant room. The objective of this experiment was to assess the correction described in Section 2.1.4, where 3 extra dB were added to the strips adjacent to the front and back plates. The noise close to the blade was measured at different positions, as described in Figure E.1. A reciprocity method was used: a broadband noise signal was emitted inside the room, and a microphone would measure it in the vicinity of a blade. This is equivalent to emitting the noise close to the blade and measuring it in the far field. The broadband noise inside the reverberant room was also measured.



(a) Leading and trailing edge of the blade

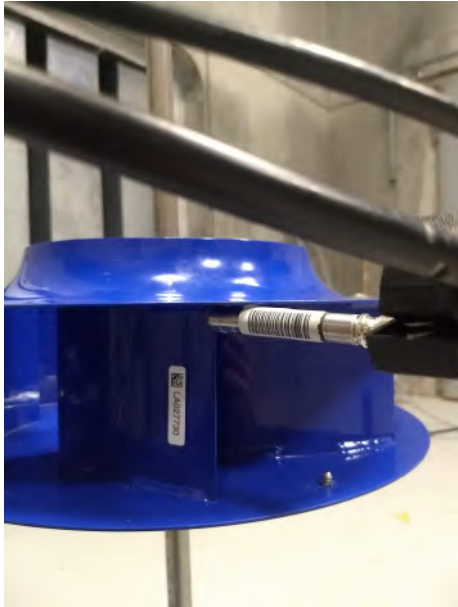


(b) Rotating axis of the impeller

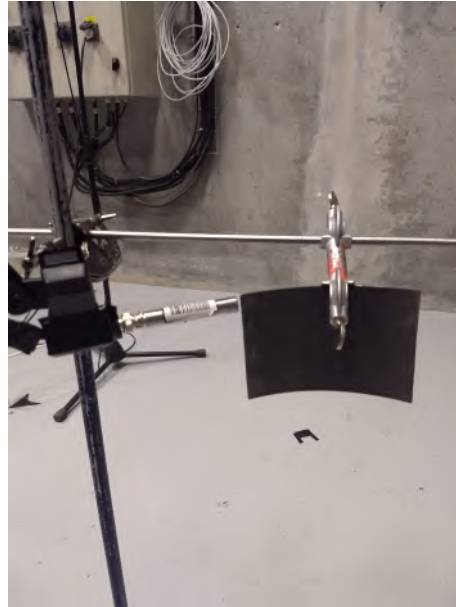
Figure E.1 – Positions of the microphone

To assess the contribution of the blade alone, measurements on a mock-up of an isolated blade were also carried out. Figure E.2 compares the measurement of a point for the impeller and the blade mock-up.

The response of the impeller is obtained by subtracting the noise measured without the impeller to the noise measured for each position (Figure E.3). This is combined in 4.4 with the impeller analytical model.

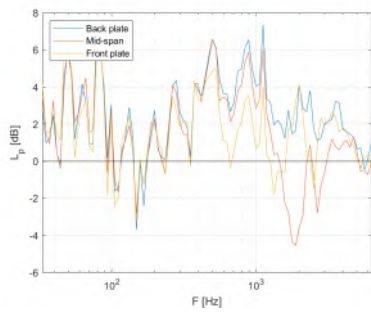


(a) Impeller

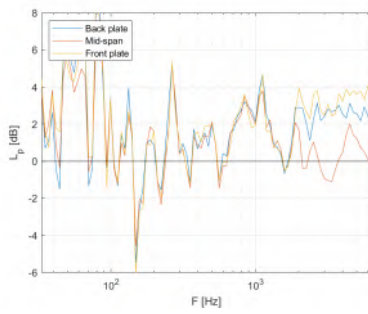


(b) Blade mock-up

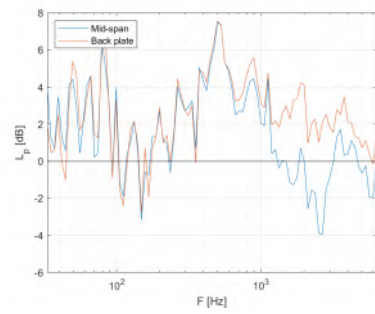
Figure E.2 – Example of a measurement point close to the trailing edge



(a) Leading edge



(b) Trailing edge



(c) Axis

Figure E.3 – Response of the impeller

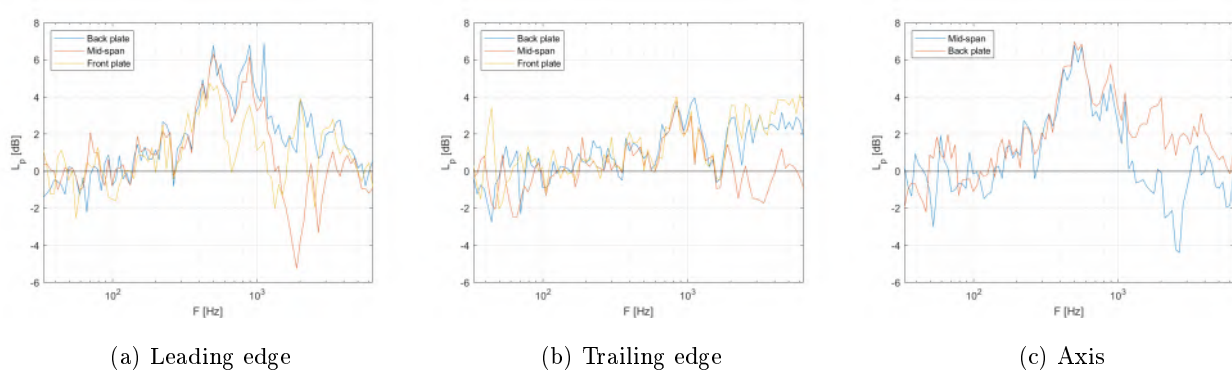


Figure E.4 – Response of the impeller-response of the isolated blade

The result of subtracting the response of the isolated blade from the impeller, described in Figure E.4, shows that, over 200 Hz, the spectra are similar to those of Figure E.3. Therefore, the response as described in the latter figure can be used to account for the effect of the impeller blade.

Appendix F

Contribution of the fan support

Another potential noise source is the fan support. Indeed, the outlet flow of the impeller impacts the longitudinal bars of the support and could generate noise. The bars have a rectangular cross section of 40 x 50 mm. Figure F.1 shows a rendering of the fan assembly, with the longitudinal bars highlighted in red.



Figure F.1 – Fan assembly with potential noise sources highlighted

The simulated aforementioned outlet flow is depicted in Figure F.2, for the BEP ($q_v = 2196 \text{ m}^3/h$, $N=1440 \text{ rpm}$). The flow is represented over a cylinder of 297 mm of radius. This dimension has been defined so it is slightly smaller than the distance between the impeller's axis of rotation and the longitudinal bar (302 mm). This difference equals to 10 % of the biggest dimension of the bar cross section (50 mm). As it was to be expected, the air velocity is high around the impeller and next to zero everywhere else. The velocity magnitude of the wake has a maximum value of 11 m/s for the BEP.

Velocity: Magnitude (m/s)

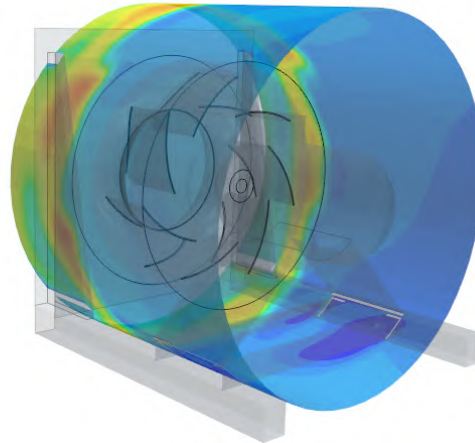
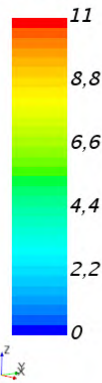


Figure F.2 – Velocity magnitude slightly upstream of the fan support over a cylinder coaxial with the impeller

To assess the noise generated by the support, a wind tunnel experiment was carried out in the low-speed anechoic open-jet wind tunnel of École Centrale de Lyon (ECL). A rectangular nozzle with a vertical outlet cross-section of $15\text{ cm} \times 30\text{ cm}$ was used to deliver a uniform flow into the anechoic chamber with a constant speed. The contraction ratio of the nozzle is 2:1 (from an initial section of $30\text{ cm} \times 30\text{ cm}$). The measurements have been performed at a flow speed of 11 m/s , the top value upstream of the support. A wooden bar with the same cross-section as the support was installed in the test section. The setup is displayed in Figure F.3.

The acquisition of the acoustic pressure has been made with a microphone connected to an external unit *PXI – 1036* averaging on 30 samples of 1 second, with a sampling frequency of 51.2 kHz and a frequency resolution of 1 Hz . The sound power level spectra is displayed in Figure F.4. The level is quite low, so we can rule out the fan support as a relevant noise source.

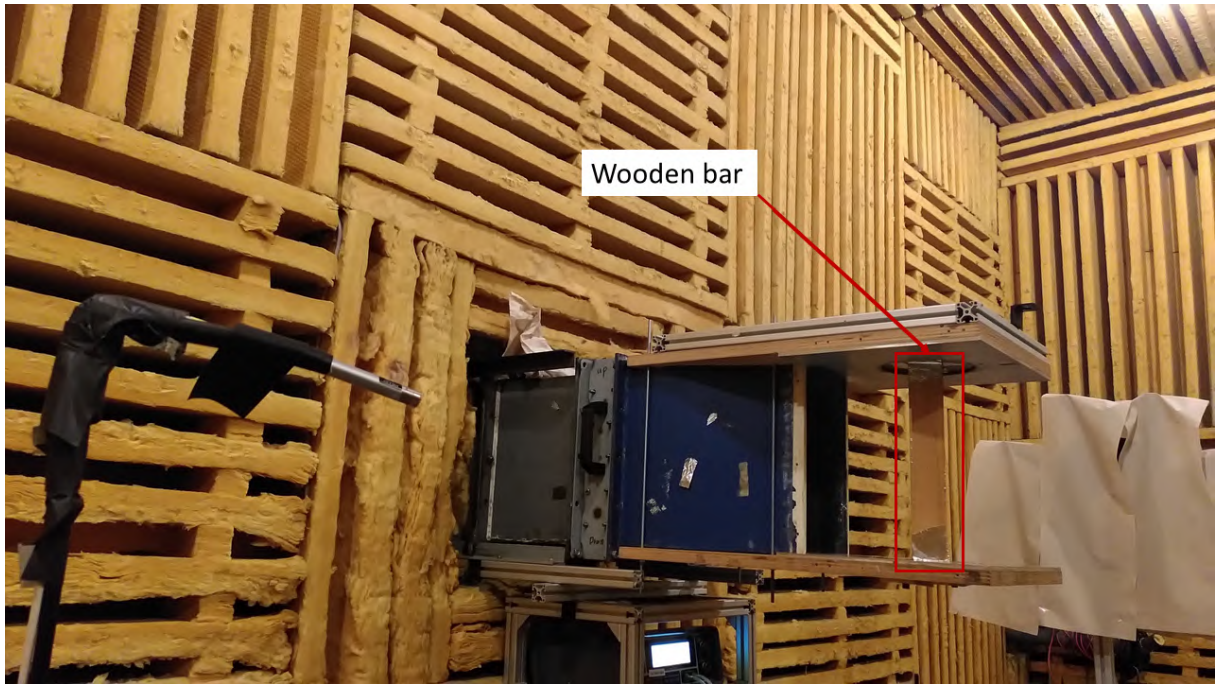


Figure F.3 – Windtunnel setup

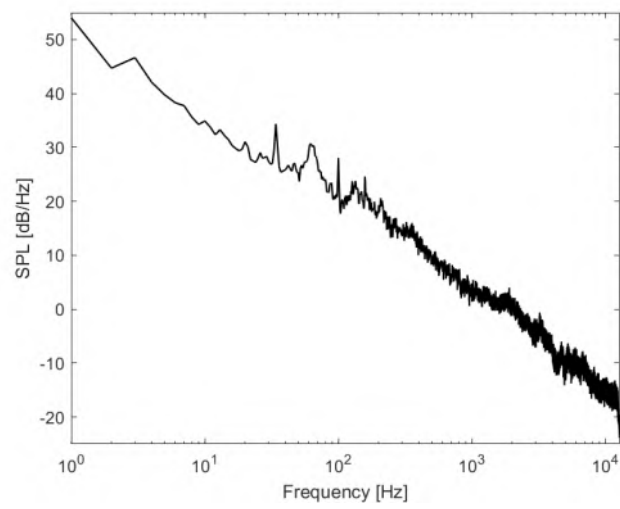


Figure F.4 – PSD of the noise of the support

